GEOCHEMISTRY OF LUNAR GRANULITES AND IMPLICATIONS FOR THE COMPOSITION AND HISTORY OF THE LUNAR CRUST

A Thesis

Presented to

the Faculty of the Department

of Earth and Atmospheric Sciences

University of Houston

In Partial Fulfillment

of the Requirements for the Degree of

Master of Science

By

Jeremy J. Kent

May, 2013

GEOCHEMISTRY OF LUNAR GRANULITES AND IMPLICATIONS FOR THE COMPOSITION AND HISTORY OF THE LUNAR CRUST

_____

Jeremy James Kent

APPROVED:

_____

Dr. Alan Brandon, Chairman

_____

Dr. Thomas Lapen

_____

Dr. Katherine Joy
University of Manchester

_____

Dean, College of Natural Sciences and Mathematics

Acknowledgements:

First I would like to thank Dr. Alan Brandon for giving me the amazing opportunity to study lunar meteorites, and for his guidance and advice which have been invaluable resources. He has always been open, available, and encouraging. Thank you to Dr. John Shafer for his immense help with preparing my thesis proposal, to Dr. Tom Lapen for his expertise on all things petrology and geochemistry, and to both Dr. Lapen and Barry Shaulis for their assistance with the LA-ICP-MS. Thank you to Dr. Katie Joy for sharing her exhaustive knowledge and resources on lunar meteorites and for being superhumanly fast and thorough with all questions I've had and feedback she's given – this paper would not be what it is today without her singular help. I am grateful to Dr. Tony Irving, curator of meteorite type specimens archived at the University of Washington, Seattle, for access to the samples of NWA 5744, upon which much of this thesis is based. I also need to thank Dr. Anne Peslier for all of her great feedback and all of the training she gave me on the electron microprobe. Dr. Daniel "Kent" Ross is largely responsible for the BSE and elemental maps I obtained from the scanning electron microscope, and for that I owe him a debt of gratitude. I sincerely thank the Lunar and Planetary Institute for funding, NASA-JSC for access to their SEM and EMP, Shell International E&P for the use of their X-ray micro-CT scanner, and Dan Coleff for all of his help with the CT scans. Thank you to Steve Braun for the data he collected on MAC 88104. I want to give special thanks to my parents and brother. Lastly, Dr. Veronica Sanchez has kept me sane during the extended process of writing this thesis,

and although I could never hope to match the extraordinary levels of dedication she has for everything she does, she has served and continues to serve as my ultimate role model and I cannot thank her enough.

GEOCHEMISTRY OF LUNAR GRANULITES AND IMPLICATIONS FOR THE COMPOSITION AND HISTORY OF THE LUNAR CRUST

A Thesis

Presented to

the Faculty of the Department

of Earth and Atmospheric Sciences

University of Houston

In Partial Fulfillment

of the Requirements for the Degree of

Master of Science

By

Jeremy J. Kent

May, 2013

Abstract:

Lunar meteorites originate from random locations on the Moon, and therefore can serve as tools to study lithologies from locations other than the area covered by the Apollo and Luna missions. This study is based on the geochemical compositions of lunar granulites Northwest Africa (NWA) 5744, MacAlpine Hills (MAC) 88105, and Queen Alexandra Range (QUE) 93069.

NWA 5744 is a magnesian lunar meteorite with bulk Mg# = 79, and may have been a monomict or genomict crustal rock prior to metamorphism. This meteorite does not fit into the established lunar classification scheme for primary crustal rocks, with major element relationships that best fit the Apollo Mg-suite but trace elements better fitting the Apollo ferroan anorthosite (FAN) suite. NWA 5744 could represent a distinct type of crustal lithology formed on the far side of the Moon. This would imply that bulk lunar crust models primarily based on Apollo samples from the Procellarum region may need revision. Metamorphism appears to have been intense but brief enough in NWA 5744 to prevent complete re-equilibration among the different minerals, and likely occurred near the lunar surface relating to an impact melt sheet or high shock event.

Both MAC 88105 and QUE 93069 are polymict lunar regolith breccias containing clasts of granulite. Most of these clasts have Mg#'s < 70 and match the Apollo FAN suite more closely than the Mg-suite in both major and trace element composition. MAC 88105 contains a broad range of FAN granulites and is likely to originate from some depth below the lunar surface in a well-mixed regolith. QUE 93069 has two to four distinct compositional populations among its

granulite clasts and is likely to originate at or near the lunar surface in a regolith that was less well-mixed than MAC 88105.

Due to the geochemical makeup of the lunar surface, it is more likely that both MAC 88105 and QUE 93069 originated from the nearside of the Moon than the far side. NWA 5744 is conversely more likely to have originated on the far side of the Moon. All three meteorites likely originated far from the Apollo and Luna mission sites.

Table of Contents:

Table of Figures:

Table of Tables:

Chapter 1: Lunar Crustal Geology, Methods, and Analytical Challenges

1.1. Lunar Crustal Geology

1.1.1. Lunar Magma Ocean

The most presently favored model for the origin of the lunar crust involves a magma ocean spanning the entire globe of the Moon early in its history. In a lunar magma ocean (LMO) model, the high temperatures sustained by the Moon shortly after its formation would have caused most of the crust to be molten. As this magma ocean cooled, minerals would have crystallized in a predictable sequence, sink, and be removed from the system. That sequence would depend on the composition of the magma, but in general olivine would crystallize early followed by orthopyroxene, then clinopyroxene, until plagioclase crystallization would have begun (Shearer and Papike, 1999; Elkins-Tanton *et al.,* 2002; Elardo *et al.,* 2011). Plagioclase would only appear on the solidus after 70-80% crystallization (Snyder *et al.,* 1992). As crystallization proceeded, the magma ocean would become increasingly ferroan and flotation of comparatively less dense plagioclase would occur (Warren, 1985). The last of the melt to crystallize would be rich in ilmenite (Shearer and Papike, 1999). The end result of these models would be a lunar crust on the near side composed mostly of ferroan anorthosite, which was confirmed by the Apollo missions to be the composition of the bulk of the lunar Highlands.

1.1.2. Structure of the Lunar Crust

Based on what is known about the surface of the Moon (Fig. 1) from the Apollo and Luna missions, remote sensing, and models developed to explain these observations, it has been generally believed that the global average crust is roughly 40-50 km thick (Toksöz, 1979; Wieczorek *et al.,* 2006), although the recent GRAIL gravity measurements now indicate a thinner average thickness of 34-43 km (Wieczorek *et al.,* 2013). The oldest, likely primary, highlands crust is anorthositic, and based on the composition of pristine Apollo 16 samples, may be 50% comprised of the Ferroan Anorthosite suite (FAN) (Warren, 1985), typically having cataclastic textures, Ca-rich plagioclase (95% or more anorthite)(Warren, 1985), low bulk Mg# <70 (Mg# = molar Mg / [Mg + Fe]) (Lindstrom and Lindstrom, 1986), and believed to have originated as floatation cumulates from a lunar magma ocean (e.g., Wood, 1975; Warren, 1985; Warren, 1990; Snyder *et al.,* 1992; Shearer and Papike, 1999; Elkins-Tanton *et al.,* 2002; Arai *et al.,* 2008; Elardo *et al.,* 2011). The other 50% of the highlands crust is possibly comprised of the Mg-Suite, which tend to have cumulate or granulitic textures (Warner *et al.,* 1976) and bulk Mg# >70 (Lindstrom and Lindstrom, 1986), usually contain a greater proportion of mafic silicates than FAN suite material (Warren, 1985), and have plagioclase that is typically less dominated by anorthite (while anorthite can still be as high as 98%, it can also be as low as 80%)(Warren, 1985). It has been suggested that both groups could have originated as cumulates from an LMO (Arai, 2008). However, it is very widely accepted that Mg-suite material would not have floated in an LMO and

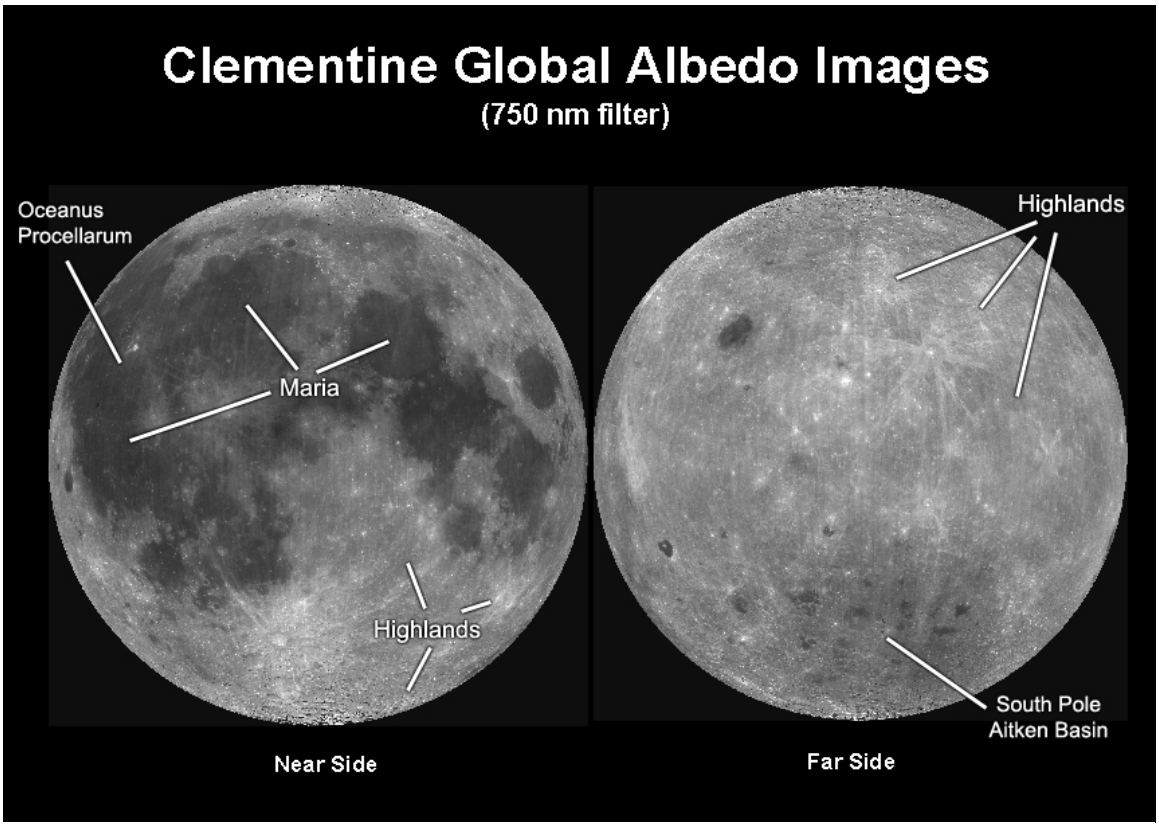

Figure 1: Map of the lunar nearside (left) and farside (right) based on spectral imaging from the NASA-sponsored 1994 Clementine surveys. The feldspathic highlands are light colored compared to the darker maria, and the highlands represent a much larger portion of the farside lunar crust than the nearside. Image modified from the Lunar and Planetary Institute website, The Clementine Mission, April 22nd, 2012 http://www.lpi.usra.edu/lunar/missions/clementine/images/

instead represents secondary crust formed in subsequent igneous intrusive episodes (Warren, 1985; Wieczorek *et al.,* 2006).

The other major crustal features are the mare basalts, which are younger features than the highlands, and the Procellarum KREEP Terrane, an area associated with the Oceanus Procellarum mare region which is rich in Potassium, Rare Earth Elements, and Phosphorus (KREEP) in comparison to the rest of the lunar crust (Wieczorek *et. al.* 2006).

On the nearside of the Moon (as sampled by the Apollo missions), Mg-suite intrusives likely assimilated some KREEP-rich material during ascent (Shearer and Papike, 1999; Shearer et al., 2006 *and refs. therein*). For this reason, the nearside lunar crust is believed to be more magnesian below a depth of about 19-25 km, the greatest depth of origin indicated for FAN rocks (Spudis and Davis, 1986; McCallum and O'Brien, 1996). Mg-suite rocks are considered to have formed at a greater depth, ranging from 20 to 50 km below the lunar surface on the lunar nearside, or roughly from the lower half of the crust (McCallum and Schwartz, 2001). Mg-rich rocks akin to the Mg-Suite from the farside may also originate from deeper than the nearside, because the nearside crust is approximately 13-17 km thinner (Wieczorek and Zuber, 2001). This difference in thickness could indicate the magma ocean cooled asymmetrically (Arai *et al.,* 2008).

Rock and dust samples returned from the Apollo and Luna missions provide invaluable data on the composition and structure of the lunar crust, but they represent only about 4.7% of the lunar surface and may not be representative of the entire surface of the Moon (Warren *et al.,* 1989). Lunar meteorites are rocks that originate from random locations on the Moon's surface, many of which are likely far away from the sites of the Apollo and Luna missions (see Korotev, 2005 for a review). Therefore, they potentially provide a more comprehensive record of global lunar geological diversity, shedding new light on the Moon's geological evolution (e.g., Korotev *et al.,* 2003; Cahill *et al.,* 2004; Warren *et al.,* 2005; Arai *et al.,* 2008; Joy *et al.,* 2010; Gross *et al.,* 2012).

1.2. Methods

I studied a thin section and a small polished chip of Northwest Africa (NWA) 5744 weighing 527 mg, a single thick section each of paired meteorites MacAlpine Hills (MAC) 88104 and MAC 88105, and a thick section of Queen Alexandra Range (QUE) 93069. The chip of NWA 5744 was a wedge-shaped slab approximately 1.5 cm in length, 1 cm in width, and thickness ranging from 0.5 to 2 mm (Fig. 2). These samples were analyzed by four different techniques in order to obtain two- and three-dimensional maps and major and trace element concentrations of all phases.

1.2.1. Sample mapping

X-ray Computed Tomography (CT) is a non-destructive process to acquire a digital volume which can be manipulated to reveal subsurface structure, texture, grain boundaries, and major fracture patterns that are not visible from the surface of a sample. The method used was similar to that of Tsuchiyama *et al.* (2002). We performed this analysis on the slab of NWA 5744 using an XTECH (Nikon) XT H 225 machine at Shell BTC Research Facility in Houston. The following settings were used: 60 kV for penetration, 100 μA for brightness, optimized at 2947 projections, exposure of 1 frame per second, with 16 frames per projection. Indexing with a 3-pixel offset was used to minimize ring artifacts due to stage rotation. Raw data were compiled into a 3D volume using Nikon Metrology CT Pro 3D XT software, using a medium beam-hardening setting of 3 and a light noise reduction of 2, both of which are unit-less values on a scale

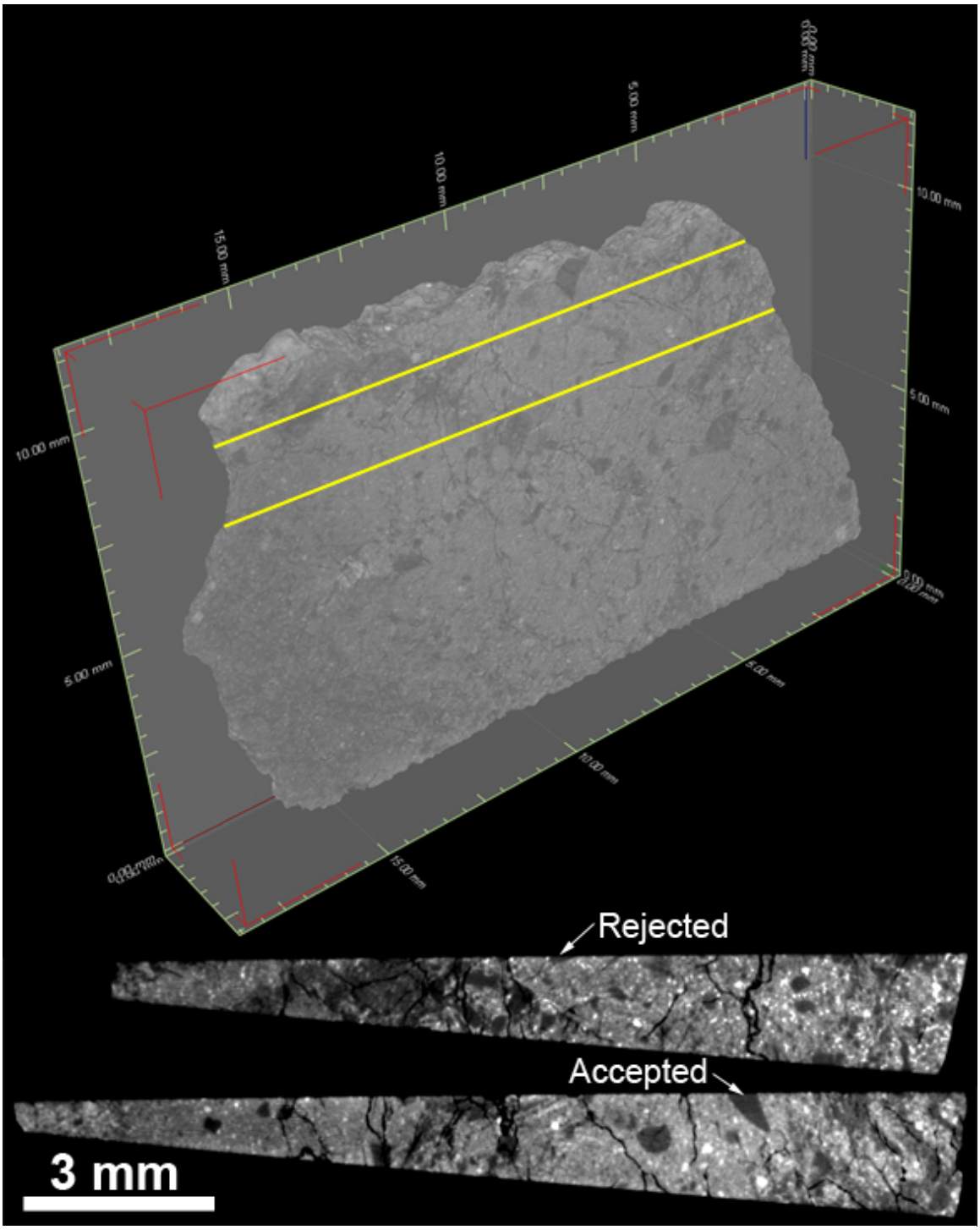

Figure 2: Above: 3D density volume of the slab of NWA 5744, obtained by X-ray CT scan. Higher density materials are lighter in color. The tick marks on the scale bars are 500 µm. Below: Example of two plagioclase grains on the slab of NWA 5744 considered for laser ablation. Using slices through the CT volume, candidates were rejected if they did not extend deep enough below the surface of the slab to ensure the laser would not ablate through the grain entirely. Locations of the two slices are shown on the 3D volume (above) in yellow.

from 1 to 6. Volumetric rendering was done with VGStudioMAX software. This was done prior to any destructive analyses, and produced a 3D volumetric density model. A digital 3-dimensional density model was produced from the CT scan with spatial resolution of 10.4 µm (Fig. 2). This resolution is too coarse to image the small mafic phases embedded in the matrix, but it was sufficient to identify the large plagioclase and olivine crystals.

Backscatter and elemental maps of all samples were obtained on a JEOL JSM-7600F field emission scanning electron microscope at NASA-Johnson Space Center using a <0.01 micrometer electron beam and 15 kV, 30 nA beam conditions which were monitored using an equipped faraday cup. The spatial resolution of the resulting backscatter maps was ~3.3 microns per pixel, and count times were ~6 milliseconds per pixel. A silicon drift X-ray detector (SSD) with ultra-thin window was used to acquire all data, and Thermoelectron NSS software was used to collect and reduce the data. All elemental maps were extracted from the hyper-spectral image data sets and were background corrected.

1.2.2. In Situ *Mineral Analysis*

The slab of NWA 5744 was separated into two similarly sized pieces and each was mounted on a 1-inch (2.54 cm) round slide using carbon tape. Because of the wedge shape, more carbon tape was used under one end of each slab piece than the other, in order to have the sample surface perpendicular to the electron beam of the

electron microprobe. The ramp and slab section placements were adjusted until the slab surface could be viewed in focus at one end under an optical microscope and remain in focus across the entire upper surface, ensuring it was horizontal.

Additional BSE images of the slab of NWA 5744 and the thick sections of MAC 88105 and QUE 93069 were acquired and major element concentrations of all principal mineral phases were measured via wavelength dispersive X-ray spectroscopy (WDS) using a Cameca SX100 electron microprobe (EMP) at NASA-Johnson Space Center. Beam conditions of 15 kV and 20 nA and a beam size of 1 μm were applied to all phases. The following well-characterized standards were used for calibration of EMP measurements on all phases: troilite for S, apatite for P, rutile for Ti, chromite for Cr, NiO for Ni, rhodonite for Mn, cobalt metal for Co, and oligoclase for Na. For plagioclase or maskelynite (a glass with the same composition as plagioclase, formed by shock melting): orthoclase for K and Si, oligoclase for Al and Na, hypersthene for Fe, diopside for Mg, plagioclase for Ca. For olivine: fayalite for Si and Fe, forsterite for Mg, chromite for Al, and diopside for Ca. For pyroxene: diopside for Si, Ca, and Mg, oligoclase for Al, and hypersthene for Fe. For chromite: chromite for Al, Fe, Cr and Mg, olivine for Si, and diopside for Ca. Sodium, potassium, and phosphorus were always measured simultaneously first to minimize the effect of their loss from beam interaction with the sample.

Trace element concentrations were determined by laser ablation inductively coupled plasma mass spectrometry (LA-ICP-MS) at the University of Houston on a Varian *810* quadrupole ICP-MS with a Photon Machines *Analyte.193* ArF excimer laser. Helium gas was used to carry ablated material to the ICP-MS. Ablations were performed on the same mineral phases measured by EMP on the slab of NWA 5744 and the thick sections of MAC 88105 and QUE 93069. In preparation for trace element analysis, the CT volume of the NWA 5744 slab was used in this study to help select desirable ablation locations with low risk of breaching a grain boundary (e.g. Figure 2). Suitable candidate grains were selected from BSE images, and these grains were located in the CT volume. Any candidates that appeared to be only surficial and did not extend at least 50 µm below the surface of the slab were not ablated.

For all trace element measurements calcium concentrations measured by EMP were used as internal standards for plagioclase, while magnesium contents measured by EMP were used for olivine, pyroxene, and bulk ablations. The United States Geological Survey (USGS) standard reference material BHVO-2G glass was used to correct for instrumental fractionation and drift using the commercial data reduction software package Glitter (http://www.glitter-gemoc.com). Where multiple ablations were averaged together, either for two or more ablations on a single crystal, or when estimating bulk rock composition, precision or reproducibility was measured with percent relative standard deviation (%RSD), which is the standard deviation of all measured concentrations divided by the average of those concentrations. Cracks that

contained greater levels of calcium than the surrounding plagioclase (as seen in elemental mapping) were avoided for all ablation sites to minimize the chance of contamination by terrestrial calcite. The USGS SRM BIR-1G glass was used to monitor external reproducibility. The BIR glass data is given for trace element measurements, with the averaged measurements compared to the reference values as a means of assessing accuracy. Precision or reproducibility of the BIR data is reported via %RSD for each element. The %RSD is between 2-10 percent for all elements except tantalum, thorium, and uranium, meaning BIR measurements were reproducible to within 2 to 10 percent for all other elements.

Chapter 2: The Origin and Compositional Dichotomy of Lunar Granulite Northwest Africa 5744

J. J. Kent[1], A. D. Brandon[1], T. J. Lapen[1], K. H. Joy[2], A. H. Peslier[3,4], A. J. Irving[5], and D. M. Coleff[1,6]

[1]University of Houston, Department of Earth and Atmospheric Sciences, USA (jjkent@uh.edu).

[2]School of Earth, Atmospheric and Environmental Sciences, University of Manchester, Oxford Road, Manchester, M13 9PL UK.

[3] Jacobs Technology, E.S.C.G., Mail Code JE23, 2224 Bay Area Blvd, Houston, TX 77058, USA.

[4] Astromaterials Research and Exploration Science, NASA-Johnson Space Center, Houston TX 77058, USA.

[5]University of Washington, Seattle, USA.

[6]Outsource Research Consultants (Shell International E&P Resident Contractor), Shell Technology Center Houston, USA.

Keywords: lunar-meteorite, lunar-crust, granulite, LA-ICP-MS

Running header: Lunar meteorite NWA 5744

2.1. Introduction

Northwest Africa (NWA) 5744 is an anorthositic troctolitic lunar meteorite with a metamorphic texture. It was found in Mali in February 2009 (Weisberg *et al.,* 2009), and is composed entirely of granulitic breccia. This lunar meteorite was originally classified

via petrography and geochemistry by EMP, X-ray fluorescence (XRF), and instrumental neutron activation analysis (INAA) (Weisberg *et al.,* 2009; Kuehner *et al.,* 2010), and is composed primarily of plagioclase (partially shocked to maskelynite), olivine, and low-Ca pyroxene (clinoenstatite), with accessory high-Ca pyroxene (augite, and Ti-chromite). Few studies have been previously conducted on NWA 5744 aside from initial cursory analysis (Weisberg *et al.,* 2009; Kuehner *et al.,* 2010; Kent *et al.,* 2012).

NWA 5744 has a magnesian composition with bulk molar Mg/(Mg+Fe) of ~ 0.79 and is potentially monomict (Weisberg *et al.,* 2009; Kuehner *et al.,* 2010), i.e., it may have been formed from only one parent rock type. According to Kuehner *et al.,* (2010), NWA 5744 has a general lack of metal grains and a bulk Ni/Co ratio of ~3.5 (compared to chondritic ratios ranging between 19.4 and 21.1; Wasson and Kallemeyn, 1998). Kuehner *et al.* (2010) also found that NWA 5744 has lower concentrations of incompatible trace elements (ITEs) than what is generally seen in Apollo granulites (e.g. Ma and Schmitt, 1982; Goodrich *et al.,* 1984; Lindstrom and Lindstrom, 1986; Salpas *et al.,* 1988). Thus NWA 5744 appears to be a distinct crustal lithology from those present at the Apollo and Luna sites.

Lunar granulites are particularly intriguing because they appear un-related to the two main known pristine lithologies of the anorthosite crust, the ferroan and Mg-suite lithologies. Moreover they are present as clasts in many lunar meteorites (e.g. Allan Hills 81005, Queen Alexandra Range 93069, MacAlpine Hills 88104 and 88105; Maloy *et al.,* 2005; Koeberl 1996; Lindstrom *et al.,* 1991) and Apollo rocks (e.g. 60035, 67415,

67955, 72275, 76503, 79215; Ma and Schmitt 1982; Lindstrom and Lindstrom 1986; Salpas *et al.* 1988; Jolliff *et al.,* 1996; Hudgins *et al.,* 2008), suggesting they are an important component of the ancient lunar crust. Magnesian granulites in particular are believed to have originated from a chemically-different source material than the ferroan anorthosites, and mare basalts that are prevalent at the Apollo and Luna landing sites, and are therefore likely to have formed in a region distant from those sites with differing local geology (Lindstrom and Lindstrom, 1986; Korotev *et al.,* 2003).

The overall goals of this study are to perform a detailed petrological and elemental analysis characterization of the NWA 5744 in order to classify this and other magnesian granulites within accepted lunar crustal classification schemes. These data will also allow to constrain the igneous formation process of the parent rock of NWA 5744, the degree and type of metamorphism that affected it, and to improve our knowledge of the composition and evolution of the lunar crust.

2.2. Results

NWA 5744 has been subjected to metamorphic conditions and contains some relict mineral clasts that did not fully recrystallize. It has a porphyroblastic texture consisting of >80 μm subhedral to anhedral relict plagioclase and olivine crystals surrounded by interstitial <30 μm olivine and <10 μm pyroxene phases embedded within a matrix of maskelynite (Fig. 3). Back-scattered and elemental map images of the entire sections (Fig. 4) reveal that olivine and relict plagioclase are distributed relatively

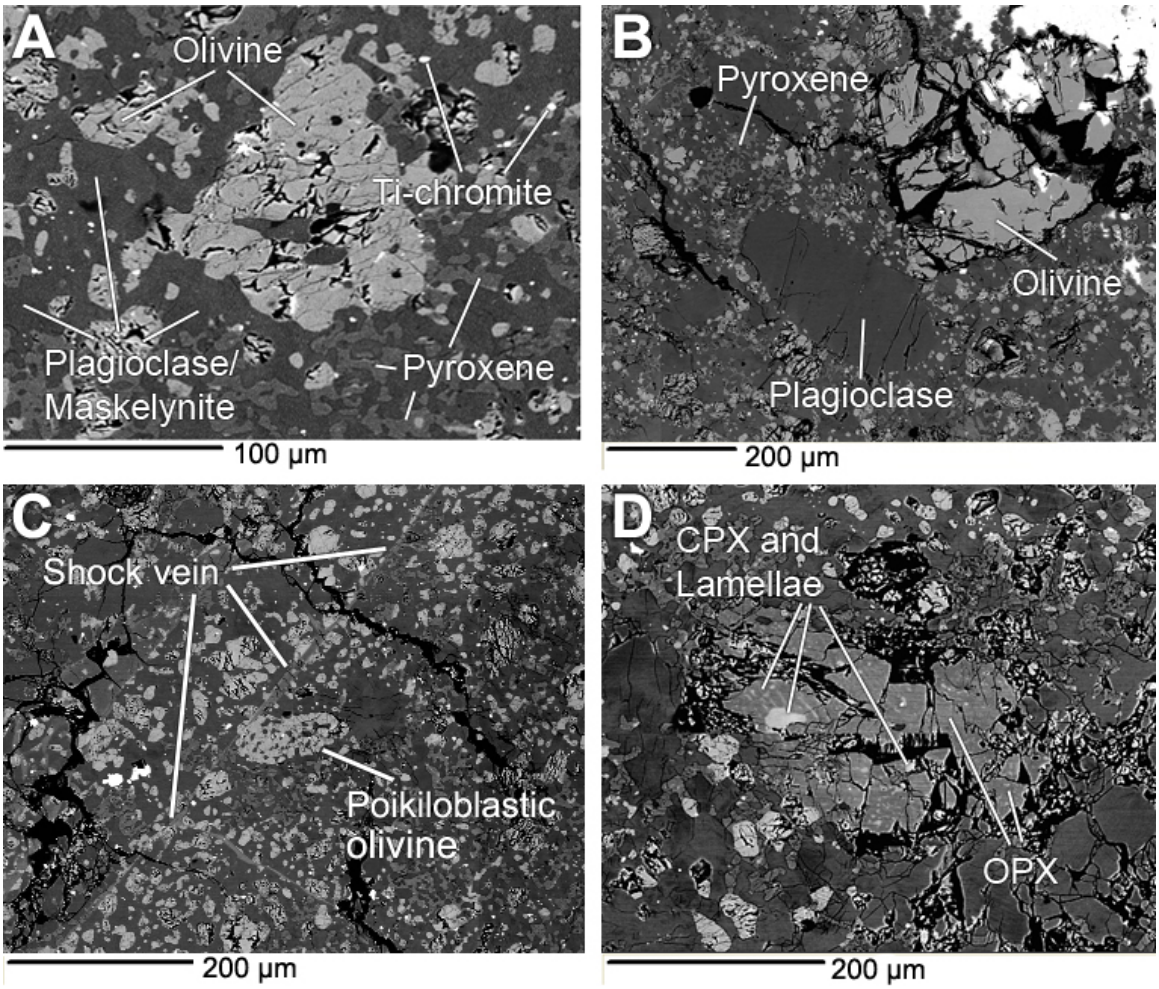

Figure 3: (A) Back Scattered Electron (BSE) image of an olivine within NWA 5744, surrounded by plagioclase/maskelynite matrix, darker pyroxene, lighter smaller olivines, and white specks of Ti-chromite exhibiting schlieren texture. **(B)** BSE image of one plagioclase and one olivine grain which were ablated in this study for trace element analyses. The plagioclase has rounded edges and is typical of most of the relict plagioclase crystals analyzed. The olivine is among the largest seen on the surface of the NWA 5744 slab, measuring about 400 µm across. Compositionally it was similar to others ablated, but all others were 150 µm across or less. The white areas around the olivine are where the carbon coating on the slab had been damaged. **(C)** BSE image of a rare poikiloblastic olivine within the slab of NWA 5744 enclosing <5 µm plagioclase or maskelynite. A small shock vein cuts diagonally through the image, skirting the edge of the poikiloblastic olivine. **(D)** BSE image of the largest pyroxene found in the slab of NWA 5744. Its composition is primarily low-Ca pyroxene (~95%) with some lighter colored high-Ca pyroxene within it, both in small amorphous blebs and thin parallel lamellae-like structures.

evenly throughout the meteorite. Pyroxene generally has a less even distribution, with some areas having more concentrated pyroxene abundances.

All <100 μm olivine and pyroxene grains exhibit a high degree of metamorphism which occur as rounded, amoeboid, or elongated, amorphous grains that appear to have been in a semi-fluid state (schlieren) (Fig. 3). Plagioclase matrix is fully transformed into maskelynite (full extinction under cross polarized light) and fractures within the matrix maskelynitic plagioclase are often present radiating outward from olivine crystals. This indicates that the rock was subjected to high pressure shock (Johnson and Hörz, 2003; Hiesinger and Head, 2006). Larger crystals of each mineral show fewer melting and metamorphic characteristics than smaller crystals

Modal proportions were estimated from BSE images processed in Adobe Photoshop software. Each mineral in the image has a distinct range in color between black and white or red/green/blue, and the percentage of pixels falling within each of those ranges was taken to be the percentage of the mineral that range represents. Repeating the selection of pixels within each color range for these images yields estimates which are identical to within one decimal place. However, it does not distinguish between matrix maskelynite and relict plagioclase. This method was used on both BSE images and elemental maps for the slab and thin section. The modal composition of NWA 5744 (Table 1) is estimated to be 67.1% plagioclase and maskelynite, 26.3% olivine, and 6.6% pyroxene, with minor accessory phases totaling less than 0.1%. As such it can be classified as a fine grained troctolitic granulite.

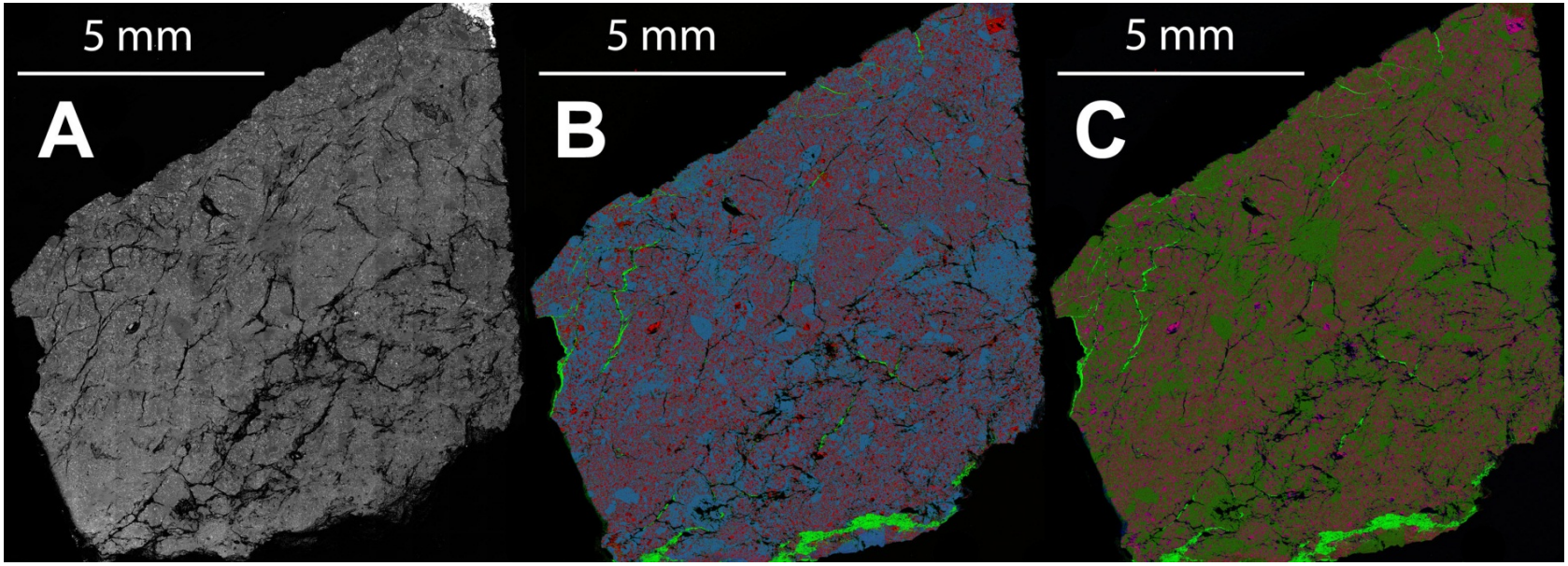

Figure 4: (A) Back scattered electron image of a portion of the slab of NWA 5744 studied here. **(B)** Elemental map of the same slab portion with Mg colored in red, Ca in green, and Al in blue. Plagioclase is light blue, olivine is bright red, pyroxene is dark burgundy, and terrestrial calcite in the major cracks is bright green. **(C)** Elemental map of the same slab portion with Mg in red, Ca in green, and Fe in blue. Plagioclase is dull green, olivine is bright pink, pyroxene is darker purple, and terrestrial calcite in the major cracks is bright green.

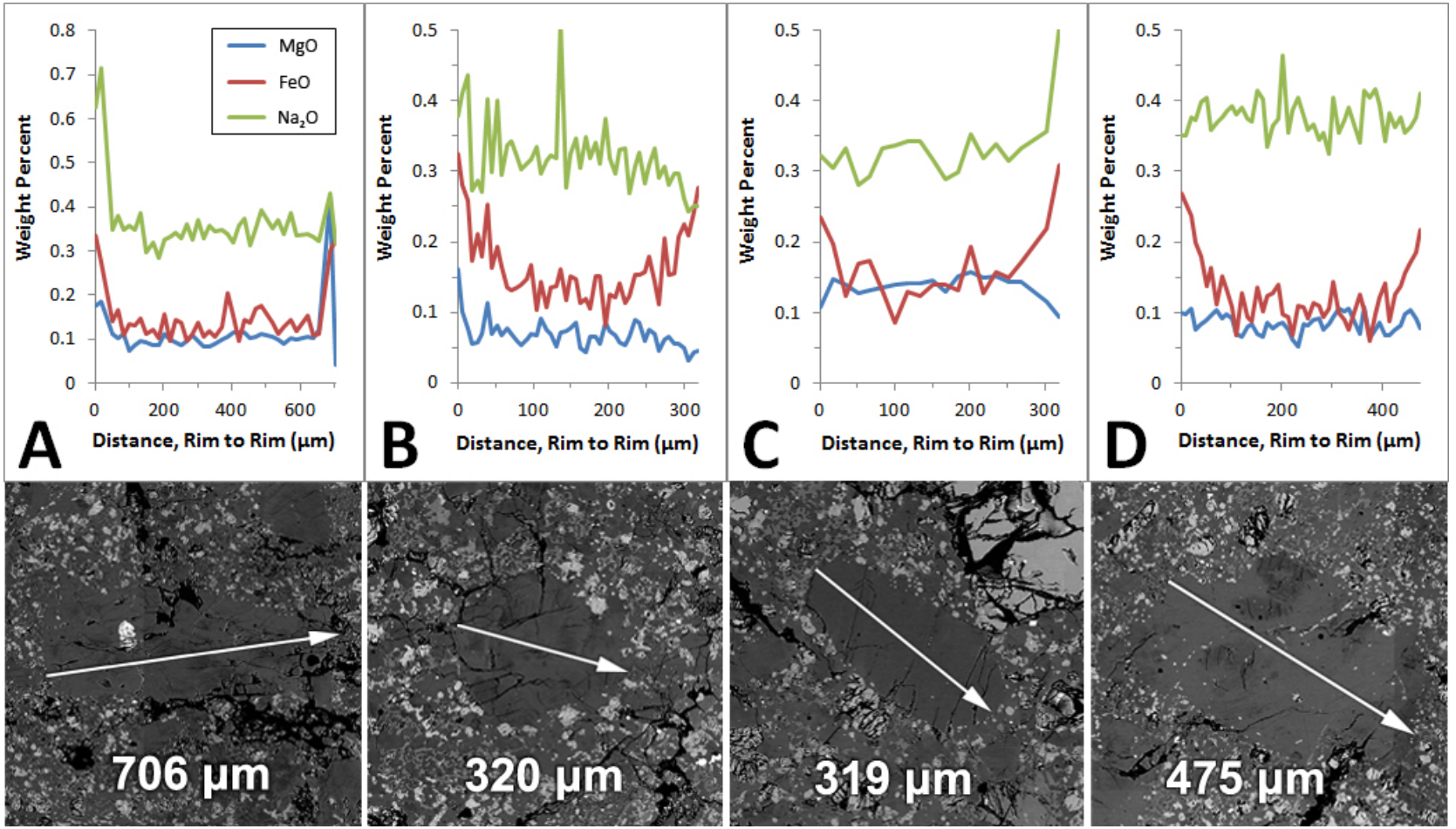

Figure 5: Top: Typical examples of EMP-measured MgO, FeO, and Na_2O wt% composition along relict plagioclase profiles in the longest dimension from rim to rim, through the core. Bottom: BSE image of the plagioclase grain detailed directly above, showing the location and direction of the profile and the length of that profile. Numbers in BSE images indicate distance in microns. **A:** Example of a plagioclase with parallel MgO, FeO and Na2O at its rim. **B:** Rim enrichment of FeO with little or zoning of MgO or Na_2O. **C:** Rim enrichment of FeO, enrichment of Na_2O in one rim but not the other, and depletion of MgO in at least one rim. **D:** Enrichment of FeO in both rims, while MgO and Na_2O exhibit slight enrichment in one rim and depletion in the other.

Table 1. Calculated average major element composition for NWA 5744 primary minerals and bulk rock

	Analyses	Na_2O	MgO	Al_2O_3	SiO_2	P_2O_5	K_2O	SO_2	CaO	TiO_2	MnO	FeO	Cr_2O_3	NiO	Total	Proportion
Plag (wt. %)	842	0.42	0.09	35.00	44.69	0.02	0.02	0.01	19.09	0.02	0.01	0.34	0.01	0.01	99.73	67.1
C-En	52	0.01	27.67	0.92	54.97	0.01	0.01	0.01	2.55	0.45	0.26	13.09	-	-	99.96	6.3
Aug	19	0.05	18.62	2.14	52.27	0.04	0.01	0.02	18.47	1.09	0.18	6.45	-	-	99.32	0.3
Olv	145	0.02	41.75	0.12	38.54	0.01	0.02	0.01	0.19	0.16	0.24	18.86	-	-	99.92	26.3
Bulk		0.30	12.26	23.91	44.03	0.02	0.02	0.01	13.29	0.09	0.09	5.78	0.01	<0.01	99.79	-

Table 2a: Plagioclase major element data. Values are in weight percent.

	Plag 1	1σ	Plag 2	1σ	Plag 3	1σ	Plag 4	1σ	Plag 5	1σ	Plag 6	1σ	Plag 7	1σ	Plag 8	1σ	Plag 9	1σ
SiO_2	44.41	0.31	44.57	0.32	45.23	0.32	44.84	0.32	44.60	0.03	44.44	0.31	43.59	0.27	43.93	0.28	44.30	0.24
Al_2O_3	35.31	0.21	35.24	0.20	35.08	0.20	35.21	0.20	35.20	0.20	35.05	0.20	35.63	0.27	35.58	0.27	35.43	0.42
FeO	0.11	0.05	0.14	0.05	0.13	0.05	0.11	0.05	0.11	0.05	0.11	0.05	0.16	0.05	0.14	0.05	0.16	0.05
MgO	0.07	0.01	0.10	0.01	0.13	0.02	0.09	0.01	0.08	0.01	0.07	0.01	0.07	0.01	0.07	0.01	0.14	0.02
CaO	19.27	0.30	19.28	0.30	19.20	0.30	19.25	0.30	19.20	0.30	19.27	0.30	19.79	0.44	19.76	0.44	19.67	0.39
Na_2O	0.29	0.04	0.35	0.04	0.39	0.04	0.36	0.04	0.37	0.04	0.36	0.04	0.32	0.04	0.33	0.04	0.33	0.04
K_2O	0.02	0.02	0.02	0.02	0.02	0.02	0.02	0.02	0.02	0.02	0.03	0.02	0.02	0.02	0.02	0.02	0.03	0.02
Total	99.48		99.70		100.17		99.87		99.59		99.34		99.57		99.84		100.05	
An	97.28		96.75		96.38		96.62		96.55		96.54		97.04		96.91		96.89	
Mg#	54.49		55.46		64.25		58.80		57.54		54.66		42.64		48.31		60.29	

Errors reported are the averaged 1-sigma analytical errors for all EMP measurements on the specific crystal.

Table 2b: Plagioclase trace element data

	BIR Ref	BIR Avg	%RSD	Plag 1	1σ	%RSD	Plag 2	1σ	%RSD	Plag 3	1σ	%RSD	Plag 4	1σ	%RSD
Spot (μm)				30			30			30			30		
Ablations				6			8			14			12		
Co (ppm)	52.5	52.90	1.58	1.16	0.13	54.37	1.39	0.15	101.41	0.55	0.12	98.34	b.d.	-	-
Ni	179	165.35	1.24	68.73	18.60	32.42	93.30	20.15	50.75	b.d.	-	-	41.91	15.56	-
Cu	121	126.77	1.95	5.58	1.57	22.15	3.56	1.63	12.36	3.00	1.47	-	11.51	1.48	72.53
Ga	14	15.77	2.37	2.15	0.34	5.22	2.06	0.38	14.44	3.46	0.45	24.96	2.12	0.39	16.08
Sr	112	101.92	1.77	163.22	7.90	2.49	157.63	8.08	3.65	183.03	10.31	1.42	159.99	10.52	2.00
Y	15.8	13.33	1.73	0.32	0.05	30.75	0.49	0.05	13.76	0.47	0.05	16.67	0.19	0.04	20.33
Zr	15.3	12.52	2.00	1.21	0.21	51.24	b.d.	-	-	1.48	0.23	36.87	0.71	0.21	-
Nb	0.564	0.499	2.007	b.d.	-	-	b.d.	-	-	0.175	0.038	40.550	b.d.	-	-
Ba	6.6	6.20	1.88	11.81	0.69	12.34	10.54	0.64	20.05	19.02	1.14	11.21	8.77	0.65	21.33
La	0.623	0.549	2.958	0.302	0.025	12.458	0.265	0.024	16.313	1.026	0.061	6.025	0.191	0.020	10.017
Ce	1.93	1.884	2.515	0.755	0.048	19.398	0.633	0.045	13.413	2.417	0.144	6.779	0.453	0.037	9.076
Pr	0.381	0.351	2.221	0.103	0.013	15.331	0.090	0.013	17.927	0.290	0.027	11.467	0.055	0.010	21.923
Nd	2.49	2.193	2.719	0.547	0.071	24.421	0.403	0.065	17.613	1.118	0.108	11.697	0.234	0.050	26.509
Sm	1.14	0.981	2.653	0.138	0.047	48.109	0.172	0.053	20.683	0.222	0.057	23.610	0.086	0.041	12.099
Eu	0.537	0.481	2.136	0.746	0.064	7.424	0.679	0.064	8.615	0.863	0.083	5.280	0.706	0.079	5.391
Gd	1.91	1.514	2.279	0.133	0.035	2.664	0.138	0.041	32.191	0.182	0.045	22.810	0.094	0.033	10.916
Tb	0.369	0.300	1.571	0.024	0.007	-	0.021	0.009	20.538	0.027	0.009	25.941	0.016	0.008	14.692
Dy	2.73	2.142	2.073	0.101	0.041	0.293	0.141	0.046	19.558	0.164	0.045	33.193	0.100	0.038	14.858
Ho	0.599	0.493	2.335	0.018	0.008	19.195	0.031	0.009	42.262	0.024	0.008	20.891	0.018	0.007	8.775
Er	1.79	1.491	2.771	b.d.	-	-	0.076	0.036	12.509	0.071	0.034	21.712	b.d.	-	15.756
Tm	0.26	0.225	2.856	0.015	0.007	8.889	b.d.	-	-	0.018	0.007	-	b.d.	-	-
Yb	1.79	1.445	1.966	b.d.	-	-	b.d.	-	-	0.076	0.033	5.873	0.059	0.031	-
Lu	0.27	0.216	3.562	b.d.	-	-	b.d.	-	-	b.d.	-	22.181	b.d.	-	-
Hf	0.609	0.472	3.075	b.d.	-	-	b.d.	-	-	0.098	0.029	35.992	0.070	0.026	29.895
Ta	0.038	0.031	6.355	0.034	0.009	-	0.024	0.009	-	0.027	0.010	12.952	b.d.	-	-
Th	0.03	0.027	3.229	b.d.	-	-	b.d.	-	-	0.034	0.012	16.826	0.020	0.009	-
U	0.016	0.015	7.102	0.032	0.007	-	0.024	0.008	-	0.017	0.008	28.717	b.d.	-	-

%RSD is the percent relative standard deviation for each element across all averaged ablations. 1-sigma error is the averaged analytical error for that particular crystal. Where more than one ablation was performed on a particular crystal or on bulk material, the %RSD across all averaged measurements is reported. When only one ablation measured a given element above the detection limit, %RSD cannot be calculated.

Table 2b, ctd

	Plag 5	1σ	%RSD	Plag 6	1σ	%RSD	Plag 7	1σ	%RSD	Plag 8	1σ	Plag 9	1σ	%RSD
Spot (μm)	30			84			84			84		84		
Ablations	3			2			2			1		2		
Co (ppm)	b.d.	-	-	0.12	0.03	1.94	0.17	0.01	34.60	0.21	0.02	0.38	0.03	3.90
Ni	b.d.	-	-	3.09	1.49	-	2.77	0.62	28.52	6.39	0.72	17.12	1.31	21.83
Cu	b.d.	-	-	0.29	0.07	54.78	0.37	0.04	49.09	0.34	0.04	0.95	0.07	5.24
Ga	2.03	0.42	21.76	1.80	0.10	32.57	1.21	0.06	26.09	1.63	0.09	2.23	0.12	9.92
Sr	154.05	10.72	0.21	111.36	5.28	29.08	89.48	4.71	29.20	104.10	5.60	138.34	7.62	3.97
Y	0.46	0.05	6.92	0.33	0.02	20.73	0.20	0.02	35.53	0.15	0.01	0.10	0.01	5.82
Zr	0.67	0.23	0.00	0.87	0.08	34.77	0.40	0.05	16.68	b.d.	-	0.37	0.07	41.45
Nb	b.d.	-	-	0.104	0.007	41.120	0.047	0.004	36.130	0.026	0.003	0.012	0.003	16.398
Ba	8.19	0.64	5.54	12.51	0.56	31.31	6.18	0.26	44.88	8.38	0.35	21.17	0.90	17.04
La	0.212	0.021	0.964	0.588	0.026	30.943	0.222	0.014	47.209	0.189	0.013	0.082	0.007	4.481
Ce	0.526	0.044	5.319	1.401	0.056	30.682	0.523	0.032	45.182	0.382	0.024	0.193	0.014	12.333
Pr	0.079	0.012	7.966	0.181	0.009	30.657	0.064	0.004	40.054	0.050	0.004	0.029	0.003	5.973
Nd	0.349	0.059	4.940	0.770	0.044	28.702	0.298	0.019	38.567	0.232	0.016	0.093	0.011	3.813
Sm	0.143	0.048	7.402	0.135	0.015	24.677	0.070	0.007	43.019	0.040	0.006	0.030	0.006	-
Eu	0.674	0.081	6.809	0.513	0.028	28.798	0.428	0.022	29.387	0.521	0.027	0.630	0.034	4.438
Gd	0.100	0.037	10.448	0.106	0.012	25.824	0.062	0.006	46.770	0.037	0.005	0.036	0.006	30.243
Tb	b.d.	-	-	0.014	0.002	35.590	0.009	0.001	34.935	0.005	0.001	0.004	0.001	-
Dy	0.273	0.046	-	0.056	0.009	23.290	0.045	0.005	45.924	0.033	0.005	0.028	0.005	-
Ho	0.027	0.008	8.700	0.012	0.002	25.435	0.008	0.001	25.452	0.005	0.001	0.005	0.001	17.131
Er	0.072	0.035	-	0.029	0.006	2.215	0.014	0.003	34.834	0.016	0.003	b.d.	-	-
Tm	b.d.	-	-	0.003	0.001	-	0.002	0.001	6.110	b.d.	-	b.d.	-	-
Yb	b.d.	-	-	0.029	0.006	23.926	0.018	0.003	40.365	0.019	0.003	0.022	0.004	-
Lu	b.d.	-	-	0.002	0.001	-	0.002	0.001	48.773	0.002	0.001	b.d.	-	-
Hf	b.d.	-	-	0.018	0.004	11.450	0.007	0.002	-	b.d.	-	0.032	0.005	65.692
Ta	b.d.	-	-	0.005	0.002	8.609	0.002	0.001	41.120	b.d.	-	b.d.	-	-
Th	b.d.	-	-	0.016	0.002	38.554	0.007	0.001	2.942	0.003	0.001	0.004	0.001	17.573
U	0.013	0.007	-	0.003	0.001	19.531	0.002	0.000	2.236	0.001	0.000	0.003	0.001	8.535

1-sigma error for plagioclase is the averaged analytical error for that particular crystal. Where more than one ablation was performed on a particular crystal or on bulk material, the %RSD across all averaged measurements is reported. When only one ablation measured a given element above the detection limit, %RSD cannot be calculated.

2.2.1. Plagioclase

Maskelynite throughout the matrix of NWA 5744 is relatively homogeneous in composition (Figs. 3-5)(Table 2a). The An values (percent anorthite content, measured as molar Ca/[Ca + Na + K]) range from 93.6 to 97.4 with a mean of 96.0 ± 1.3 (2σ error; all further errors listed are 2σ unless otherwise noted). Maskelynite within ~5 μm of pyroxene tends to have lower An content than maskelynite more distant from pyroxene (Table 3). While the An averages of maskelynite near and removed from pyroxene fall within the limits of each other's error bars, the averages appear to be consistent with this compositional dichotomy.

Table 3: Anorthite in maskelynite with proximity to pyroxene

	# of Pts.	Avg. An	Min. An	Max. An	2σ
< 5μm	18	95.7	93.6	96.9	1.5
> 5μm	9	96.6	95.7	97.4	1.0

Large (≥120 μm) relict plagioclase crystals that have not been transformed to maskelynite are present with visible twinning and birefringence, most of which have completely rounded edges as though they have been physically abraded (Fig. 5). Many of these large relict plagioclase grains are poikilitic and enclose <5 μm olivines that tend to be located near the plagioclase grain rims. Some of these large plagioclase crystals exhibit compositional zoning from core to rim. The rims of all relict plagioclase grains analyzed (Fig. 5) tend to be enriched in FeO (>0.3 wt % at the edge, compared to 0.10-0.15 wt. % several tens of microns from the rim). MgO and Na_2O exhibit zoning to a

lesser extent and only within a maximum of 10 μm of the rim where present (Fig. 5). Phinney (1994) showed that MgO and FeO both equilibrate in the plagioclase of lunar anorthosites during metamorphism, so this zoning may indicate that compositional equilibration was incomplete when metamorphism ended. However, the degree of higher FeO concentrations in the rim is variable both in concentration and distance from the grain boundary, and not all grains also exhibit MgO or Na_2O zoning (Fig. 5D).

Trace element content of the relict plagioclase (Table 2b) exhibit high Light Rare Earth Elements (LREEs) relative to heavy rare earth elements (HREEs). There is also a characteristic plagioclase positive europium anomaly caused by Eu^{2+} substituting easily for Ca in plagioclase.

2.2.2. Olivine

Most of the olivine grains within NWA 5744 are under 20 μm in width and length. Olivine is distributed relatively evenly as amoeboid anhedral rounded grains ranging in size from 5 to 15 μm with relatively rare schlieren also present (Fig. 3A). A number of larger subhedral 80-400 μm relict olivine grains are also present (Fig. 3B). Most olivine have post-crystallization fractures, with the larger grains generally being more heavily fractured (Fig. 3B). No fractures in any olivine are observed to have any maskelynite infill, so any indigenous fracturing must have occurred after maskelynite formation. Poikiloblastic olivine enclosing <5 μm are present but rare (Fig. 3C). There are small differences in Mg# (molar Fe / [Fe + Mg]) for the large olivine versus those of

Table 4a: Olivine major element data

Element	olv 1	1σ	olv 2	1σ	olv 3	1σ	olv 4	1σ	olv 5	1σ	olv 6	1σ	olv 7	1σ
SiO_2 (wt. %)	39.13	0.20	39.32	0.20	39.16	0.20	39.11	0.20	38.74	0.22	38.66	0.19	38.71	0.20
TiO_2	0.02	0.02	0.05	0.02	0.17	0.02	0.02	0.02	0.04	0.02	0.06	0.02	0.02	0.02
Al_2O_3	0.04	0.02	0.02	0.02	0.05	0.02	0.01	0.02	0.04	0.01	0.03	0.02	0.07	0.02
FeO	19.93	0.32	19.70	0.32	19.65	0.32	20.19	0.32	20.30	0.34	19.24	0.32	20.21	0.32
MgO	41.16	0.32	41.54	0.32	41.31	0.32	41.14	0.32	41.62	0.21	41.24	0.32	40.13	0.31
CaO	0.10	0.02	0.08	0.02	0.09	0.02	0.09	0.02	0.07	0.02	0.12	0.02	0.12	0.02
MnO	0.26	0.05	0.25	0.05	0.27	0.05	0.24	0.05	0.26	0.06	0.23	0.05	0.25	0.05
NiO	0.03	0.06	0.02	0.06	0.04	0.06	0.03	0.06	0.03	0.06	0.02	0.06	0.03	0.06
Cr_2O_3	0.03	0.03	0.05	0.03	0.08	0.03	0.02	0.03	0.03	0.03	0.03	0.03	0.03	0.03
Total	100.70		101.03		100.82		100.86		101.13		99.64		99.57	
Mg'	78.63		78.99		78.94		78.41		78.51		79.25		77.97	

Errors reported are the averaged 1-sigma analytical errors for all EMP measurements on the specific crystal.

Table 4b: Olivine trace element data.

	Olv 1	1σ	Olv 2	1σ	Olv 3	1σ	Olv 4	1σ	Olv 5	1σ	%RSD	Olv 6	1σ	Olv 7	1σ
Spot (μm)	84		84		84		84		176			84		84	
Ablations	1		1		1		1		2			1		1	
Co (ppm)	80.18	3.01	75.34	2.84	71.95	2.72	77.23	2.94	52.84	3.82	0.30	70.36	2.55	76.65	2.66
Ni	204.34	8.11	125.54	5.11	160.90	6.61	140.65	5.79	112.66	6.28	1.58	123.26	6.00	129.35	9.84
Cu	8.61	0.38	6.30	0.28	8.78	0.40	6.41	0.29	5.10	0.36	1.01	5.77	0.28	6.59	0.53
Ga	0.18	0.01	0.70	0.04	2.02	0.10	0.24	0.02	0.30	0.04	117.66	26.54	1.18	0.13	0.07
Sr	6.37	0.27	5.10	0.22	b.d.	-	2.97	0.13	3.91	0.28	43.90	9.05	0.38	14.18	2.20
Y	0.51	0.03	0.42	0.03	0.72	0.04	0.25	0.02	0.32	0.10	10.45	0.97	0.05	0.54	0.14
Zr	2.14	0.12	2.44	0.15	2.69	0.17	0.79	0.07	1.57	0.30	17.17	4.17	0.19	0.95	0.35
Nb	0.427	0.021	0.224	0.013	0.326	0.019	0.029	0.003	0.224	0.026	11.821	0.254	0.015	0.147	0.025
Ba	b.d.	-	b.d.	-	13.94	0.52	7.91	0.30	b.d.	-	-	11.64	0.48	b.d.	-
La	0.055	0.004	0.016	0.002	0.174	0.012	0.028	0.003	0.025	0.007	19.051	0.085	0.007	0.113	0.015
Ce	0.209	0.012	0.142	0.009	0.442	0.025	0.091	0.006	0.121	0.015	8.936	0.357	0.016	0.397	0.042
Pr	0.024	0.002	0.010	0.001	0.054	0.004	0.008	0.001	0.012	0.002	1.732	0.041	0.004	0.039	0.007
Nd	0.099	0.009	0.031	0.006	0.181	0.017	0.039	0.005	0.046	0.014	10.241	0.246	0.023	0.308	0.040
Sm	0.028	0.006	b.d.	-	0.051	0.009	0.022	0.004	0.017	0.005	10.001	0.093	0.015	0.050	0.021
Eu	0.006	0.001	0.007	0.002	b.d.	-	0.003	0.001	0.005	0.001	38.442	0.011	0.003	0.007	0.013
Gd	0.051	0.006	0.018	0.004	0.058	0.008	0.016	0.004	0.025	0.008	10.602	0.089	0.014	0.068	0.027
Tb	0.009	0.001	0.002	0.001	0.009	0.002	0.001	0.001	0.004	0.002	50.943	0.021	0.003	0.007	0.005
Dy	0.067	0.007	0.037	0.006	0.101	0.011	0.028	0.005	0.037	0.012	35.224	0.133	0.018	0.036	0.038
Ho	0.016	0.002	0.014	0.002	0.021	0.003	0.009	0.001	0.011	0.004	17.184	0.036	0.004	0.016	0.008
Er	0.067	0.007	0.053	0.007	0.116	0.012	0.038	0.005	0.042	0.014	18.215	0.109	0.015	0.067	0.028
Tm	0.015	0.002	0.014	0.002	0.027	0.003	0.012	0.001	0.010	0.003	10.142	0.021	0.003	0.015	0.005
Yb	0.147	0.010	0.154	0.011	b.d.	-	0.122	0.009	b.d.	-	-	0.199	0.020	0.107	0.030
Lu	0.029	0.003	0.041	0.003	0.062	0.005	0.029	0.002	0.024	0.005	5.685	0.039	0.005	0.035	0.007
Hf	0.076	0.007	0.041	0.006	0.052	0.007	0.022	0.004	0.041	0.009	4.995	0.109	0.013	0.017	0.016
Ta	0.041	0.003	0.014	0.002	0.017	0.003	b.d.	-	0.020	0.002	8.821	0.016	0.003	0.008	0.003
Th	0.048	0.004	0.015	0.002	0.025	0.003	0.008	0.001	0.022	0.006	89.735	0.024	0.004	0.030	0.004
U	0.015	0.001	0.011	0.001	0.008	0.001	0.020	0.001	0.009	0.001	12.576	0.019	0.002	0.027	0.001

1-sigma error for olivine is the averaged analytical error for that particular crystal. Where more than one ablation was performed on a particular crystal or on bulk material, the %RSD across all averaged measurements is reported.

the very fine-grained olivine. For the large olivine >100 µm, Mg# ranges from 78.0 to 79.3 and averages 78.7 ± 0.8 (2σ)(Table 4a). By contrast, the small matrix olivines between 5 and 50 µm are more magnesian, ranging in Mg# from 79.2 to 82.1 and averaging 80.3 ± 0.8. Because of the heavy fracturing, rim to rim profiles could not be obtained for olivine crystals. However, individual points do not exhibit any heterogeneity of major elements within a given olivine crystal. Olivine trace element concentrations are presented in Table 4b.

2.2.3. Pyroxene

In addition to the common ~5 µm schlieren pyroxene grains (Figs. 3A-C), rare larger ~80 µm relict grains sometimes exhibit distorted nanometer scale exsolution lamellae. Figure 3D shows an example of such lamellae in a 250 µm pyroxene, and is one of three grains found that were large enough to be ablated for trace element analysis. 95% of the pyroxene present is low-Ca clinoenstatite, relatively homogeneous but in one instance an increase in CaO in the rim (1.71 to 3.80 wt%) was observed ($En_{77.8-81.2}$, $Fs_{14.7-17.6}$, $Wo_{2.0-6.0}$:(Table 5a, Fig. 6). High-Ca augite ($En_{48.1-52.4}$, $Fs_{8.1-10.2}$, $Wo_{37.4-43.8}$), both from lamellae and as distinct schlieren within the matrix, accounts for the remaining 5% of the pyroxenes (Fig. 6). Clinoenstatite Mg# ranges from 80.9 to 84.3 with an average of 82.4 ± 1.3, and augite Mg# ranges from 83.4 to 86.2 with an average of 84.7 ± 2.3.

Table 5a: Pyroxene, average shock vein, and titanium chromite major element data

	Pyroxene 1						Pyroxene 2				Pyroxene 3				Avg. Shock Vein		Ti-Chromite	
	C-En Core	1σ	C-En Rim	1σ	Aug	1σ	C-En	1σ	Aug	1σ	C-En Core	1σ	C-En Rim	1σ		1σ		1σ
SiO_2 (wt %)	55.48	0.24	55.39	0.24	51.88	0.23	53.48	0.46	50.62	0.43	54.48	0.32	54.63	0.33	43.84	0.37	0.25	0.02
TiO_2	0.30	0.02	0.40	0.03	1.19	0.04	0.69	0.06	1.27	0.07	0.44	0.04	0.51	0.04	0.10	0.03	6.88	0.10
Al_2O_3	0.78	0.02	0.87	0.02	2.29	0.04	1.07	0.04	2.06	0.06	1.29	0.03	0.88	0.03	28.56	0.21	12.86	0.18
FeO	12.30	0.27	11.20	0.25	6.34	0.18	12.29	0.40	6.24	0.27	11.69	0.51	11.81	0.52	3.42	0.19	27.43	0.52
MgO	29.32	0.33	28.22	0.32	17.91	0.21	29.27	0.41	17.77	0.27	28.83	0.38	28.97	0.38	7.33	0.12	8.27	0.16
CaO	1.71	0.07	3.80	0.11	19.17	0.30	2.49	0.13	20.17	0.44	2.77	0.09	2.47	0.09	15.95	0.33	0.39	0.04
Na_2O	b.d.		b.d.		b.d.		b.d.		b.d.		b.d.		b.d.		0.33	0.05	b.d.	
MnO	0.24	0.04	0.23	0.04	0.19	0.04	0.26	0.08	0.17	0.08	0.28	0.06	0.26	0.06	0.07	0.07	0.30	0.07
Cr_2O_3	b.d.		b.d.		b.d.		0.45	0.06	0.76	0.07	0.59	0.05	0.37	0.04	0.08	0.06	41.57	0.56
SO_2	b.d.		b.d.		b.d.		b.d.		b.d.		b.d.		b.d.		0.08	0.03	b.d.	
Total	100.14		100.10		98.97		100.00		99.06		100.35		99.89		99.77		97.96	
Mg#	77.38		78.34		80.21		77.37		80.35		77.97		77.88		75.45		30.20	
En	75.83		75.83		50.82		77.12		49.69		77.25		75.83					
Fs	17.02		17.02		10.09		18.17		9.79		17.61		17.02					
Wo	7.15		7.15		39.09		4.71		40.53		5.14		7.15					

Errors reported are the averaged 1-sigma analytical errors for all EMP measurements on the specific crystal or across all shock vein measurements.

Table 5b: Pyroxene and calculated bulk trace element compositions.

	Pyx 1	1σ error	%RSD	Pyx 2	1σ error	%RSD	Pyx 3	1σ error	Bulk	1σ error	%RSD
Spot (μm)	84			84			84		176		
Ablations	2			2			1		8		
Co (ppm)	32.99	1.18	0.56	36.49	1.44	8.97	32.63	1.31	22.50	1.21	11.08
Ni	70.28	3.32	22.33	102.08	4.58	63.45	35.13	1.83	78.99	4.90	32.75
Cu	9.50	0.40	13.14	7.18	0.34	21.73	8.22	0.40	5.91	0.37	16.08
Ga	0.72	0.04	2.87	1.76	0.09	29.17	1.33	0.07	2.06	0.14	20.47
Sr	18.17	0.74	24.32	8.62	0.41	9.05	16.72	0.82	90.88	5.21	18.88
Y	17.00	0.68	0.59	20.50	1.22	13.77	13.81	0.85	5.56	0.48	28.57
Zr	50.48	1.85	10.83	47.53	2.67	17.55	27.19	1.58	13.76	1.21	27.59
Nb	0.889	0.032	13.492	0.758	0.039	14.738	0.527	0.029	0.790	0.048	25.542
Ba	25.92	1.00	8.33	11.23	0.44	15.05	19.31	0.76	25.04	1.69	14.35
La	0.369	0.015	12.897	0.535	0.032	0.569	0.309	0.019	0.601	0.051	17.000
Ce	1.806	0.064	9.543	2.467	0.140	13.635	1.198	0.070	1.884	0.093	25.570
Pr	0.344	0.014	8.562	0.471	0.026	14.922	0.215	0.013	0.283	0.018	30.028
Nd	2.127	0.091	8.305	2.780	0.140	20.344	1.193	0.067	1.438	0.100	36.018
Sm	1.015	0.054	5.065	1.276	0.073	26.896	0.527	0.035	0.504	0.040	40.175
Eu	0.075	0.005	33.955	0.046	0.004	18.393	0.065	0.005	0.454	0.033	19.653
Gd	1.640	0.079	0.599	2.106	0.108	19.518	0.993	0.055	0.705	0.060	38.545
Tb	0.334	0.016	1.799	0.423	0.022	18.567	0.226	0.013	0.639	0.012	35.815
Dy	2.600	0.135	2.558	3.258	0.175	13.915	1.990	0.120	0.685	0.083	31.679
Ho	0.628	0.032	0.414	0.731	0.048	14.141	0.492	0.034	0.129	0.019	26.893
Er	2.022	0.110	1.726	2.326	0.140	14.507	1.715	0.110	0.919	0.058	26.255
Tm	0.300	0.016	0.317	0.360	0.028	7.062	0.252	0.021	0.202	0.010	23.180
Yb	2.100	0.093	3.257	2.403	0.130	6.610	1.834	0.100	0.629	0.051	23.923
Lu	0.316	0.019	3.126	0.376	0.023	2.946	0.307	0.020	0.091	0.009	23.921
Hf	1.496	0.067	11.020	1.583	0.082	22.661	0.646	0.038	0.633	0.039	29.462
Ta	0.060	0.004	11.688	0.049	0.004	16.526	0.045	0.004	0.094	0.004	34.222
Th	0.265	0.015	4.565	0.284	0.021	20.550	0.191	0.015	0.371	0.010	28.120
U	0.065	0.004	11.739	0.067	0.004	21.176	0.044	0.003	0.044	0.002	61.129

1-sigma error is the averaged analytical error for that particular crystal, and for bulk is the averaged analytical error across all bulk ablations. Where more than one ablation was performed on a particular crystal or on bulk material, the %RSD across all averaged measurements is reported.

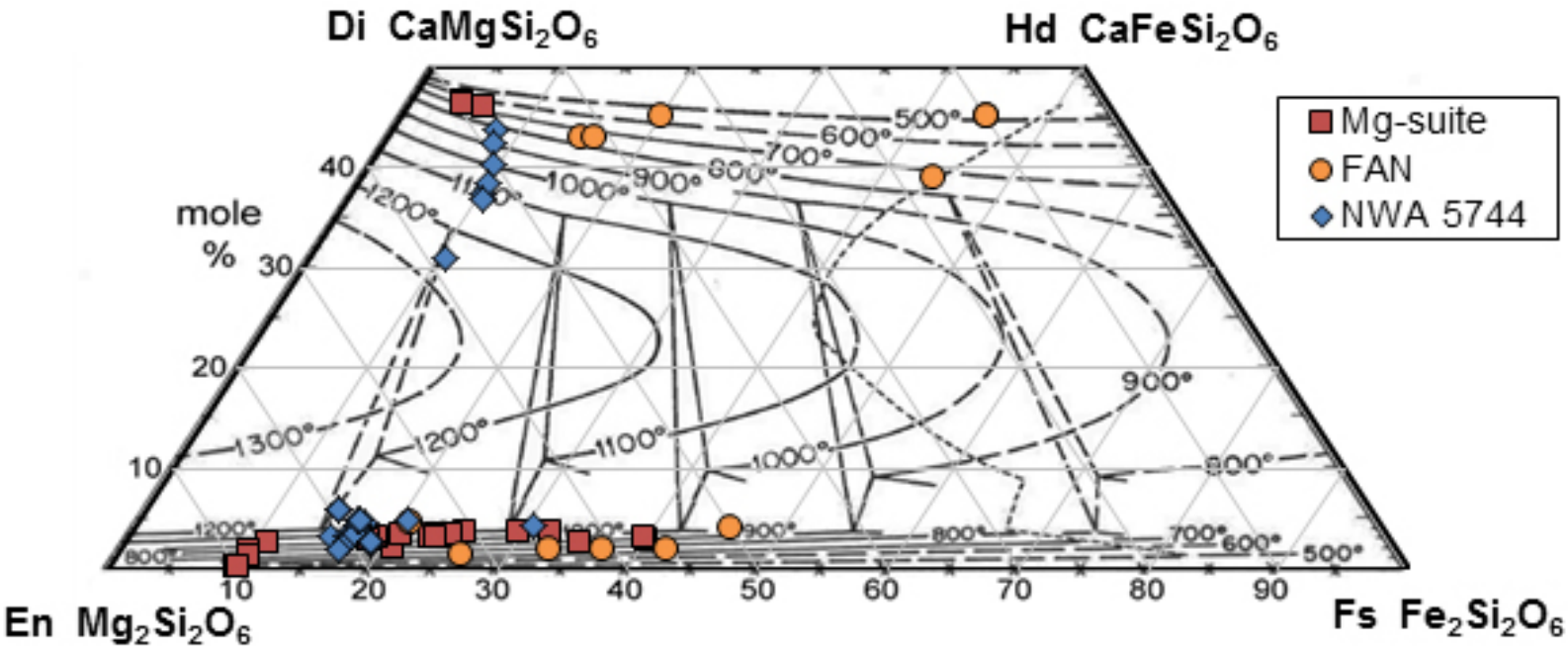

Figure 6: Pyroxene EMPA measurements in NWA 5744, compared with pyroxene from FAN and Mg-suites (Papike *et al.,* 1994; Floss *et al.,* 1998; Shervais and McGee, 1999), plotted on the graphical pyroxene thermometer of Lindsley (1983) which has been used for lunar rocks (e.g. Hudgins *et al.,* 2011). Temperatures for pyroxene pairs range from about 800 to 1120 ^{o}C with one outlier at 1270 ^{o}C on this thermometer. High calcium pyroxene in NWA 5744 is rare (<5% of observed pyroxene) and classified as augite. Low calcium pyroxene is common (>95% of all pyroxene) and low enough in Ca that it should be classified as clinoenstatite rather than pigeonite. Lunar FAN and Mg-suite data are not from metamorphosed rocks, and are only shown for direct compositional comparison.

The augite compositions in Figure 6 plot in a line, and are therefore suspected of being measurements of some mixture between the true augite composition and that of the clinoenstatite. All augite analyzed by EMP was in direct contact with clinoenstatite, and the resulting measurements may all have been influenced to some degree by the clinoenstatite.

Pyroxenes contain low chondrite normalized LREE compared to HREE (Table 5b), and a negative europium anomaly, due to europium being incompatible in the pyroxene crystal structure.

2.2.4. Accessory Phases

Ti-chromite is present in the sample matrix as an accessory phase, with typical grain size of ~1 μm. Three ~3 μm Ti-chromites were analyzed by electron microprobe (Table 5a) but were not large enough for laser ablation analysis. These chromites are usually present near <20 μm olivine (Fig. 4).

All other accessory phases identified were too small and/or had surfaces that were too irregular to get acceptable major element compositions using a microprobe. Troilite has been reported to be present in NWA 5744 (Weisberg *et al.,* 2009; Kuehner *et al.,* 2010). Only one instance of a phase with significant sulfur and nickel content detected by energy dispersive X-ray spectroscopy (EDS) is likely a grain of troilite. It is present as an inclusion within a large relict plagioclase grain. Two other instances of an

iron-bearing, sulfur-poor phase with nickel and cobalt levels apparently in excess of 5 and 3 wt% respectively were also observed, both within fractures of large olivine.

Calcite is present in most of the largest cracks (Fig. 4), which presumably precipitated from alteration fluids on Earth. This terrestrial contamination does not appear to be present in any of the smaller fractures in the rock, or within any of the previously described phases.

2.2.5. Shock Features

Based on the combination of optical examination, electron backscatter images, and EMP analyses, NWA 5744 has similar shock features to other lunar granulites such as NWA 3163 (Hudgins *et al.,* 2011), including fine-grained pyroxene and olivine within a matrix composed largely of maskelynite. Almost all pyroxene is present as 5 μm schlieren, which suggests these phases were once in a near-fluid state (Warren and Rubin, 2010). A single 5 μm olivine schlieren was also observed. Open fractures cut through nearly all of the olivine and all of the large pyroxene. Large plagioclase crystals show little or no fracturing, and those fractures present tend only to be very fine cracks. Matrix plagioclase has been fully maskelynized.

Shock-induced melt veins are present in NWA 5744, running roughly linear across the sample in random orientations for hundreds to thousands of microns in length. Thicknesses of the veins vary along their lengths, from as much as 15 μm to less than 1 μm (Fig. 3C). Average shock vein major element composition is also given in Table

5a, but the composition does vary with location across NWA 5744. The shock veins cut through relict plagioclase, maskelynite, and pyroxene, and tend to skirt around the edges of olivine with some smearing of the olivine into the veins. Some fractures cut the shock veins, and are, thus, more recent features than the shock veins or any of the phases the veins cut across. That some or all of these late-stage fractures may have been created by the process of cutting the slab or making the thin section cannot be ruled out.

2.2.6. Bulk Composition

A major element bulk composition was estimated using average plagioclase, olivine, and pyroxene compositions and the mineral mode (Table 1). All other minerals were neglected in this bulk estimate due to their extremely low abundance. Although shock veins typically represent localized and preferential melting of the material they cut through, their major element compositions may still approximate that of the bulk rock (Walton and Spray, 2003; Walton and Herd, 2007) (Table 5a). Comparing the calculated bulk composition using the mineral compositions and their modes, the average for the shock vein composition (Table 5a) is about 8% and 4% lower for MgO and FeO respectively, and about 8% and 4% in excess for Al_2O_3 and CaO respectively. This is consistent with the shock veins probably containing too little olivine material to represent an accurate bulk rock composition, given that the shock veins tend to skirt the edges of olivine rather than cut directly through them. It is unlikely the difference in shock vein composition can be explained by an unaccounted for glass component within

the matrix because such a component would necessarily contain significant MgO and FeO concentrations, and would appear distinct from the maskelynite in BSE and elemental map images. Hence, we propose that the bulk composition using the mineral compositions and modes is likely more realistic for this sample.

The bulk trace element composition of NWA 5744 was derived by analysis of 176 µm spot ablations in 8 different matrix locations containing no major cracks (to avoid terrestrial contamination) or large relict grains (to avoid biasing the results toward the composition of these grains). Calcium was used as the external element standard for each analysis. These results were then averaged together to approximate a possible bulk rock trace element composition (Table 5b).

The Ni and Co abundances from each bulk ablation point are compared with pristine lunar sample data in Figure 7. Both Ni and Co concentrations are in NWA 5744 are low compared to chondrites, plotting well within the range of pristine Apollo highlands rocks and soils. In materials with Ni and Co dominantly obtained through impactor contamination the Ni/Co ratio should approach 20 (Wasson and Kallemeyn, 1988), but in bulk NWA 5744 ablations the ratios are all less than 5. Thus, although the sample is granulitic in nature, there is no indication of any significant impactor contamination in NWA 5744.

There is a discrepancy between the expected bulk composition (calculated from the average rare earth element content of each ablated type of mineral multiplied by modal bulk content of that mineral) and the average measured bulk composition. The

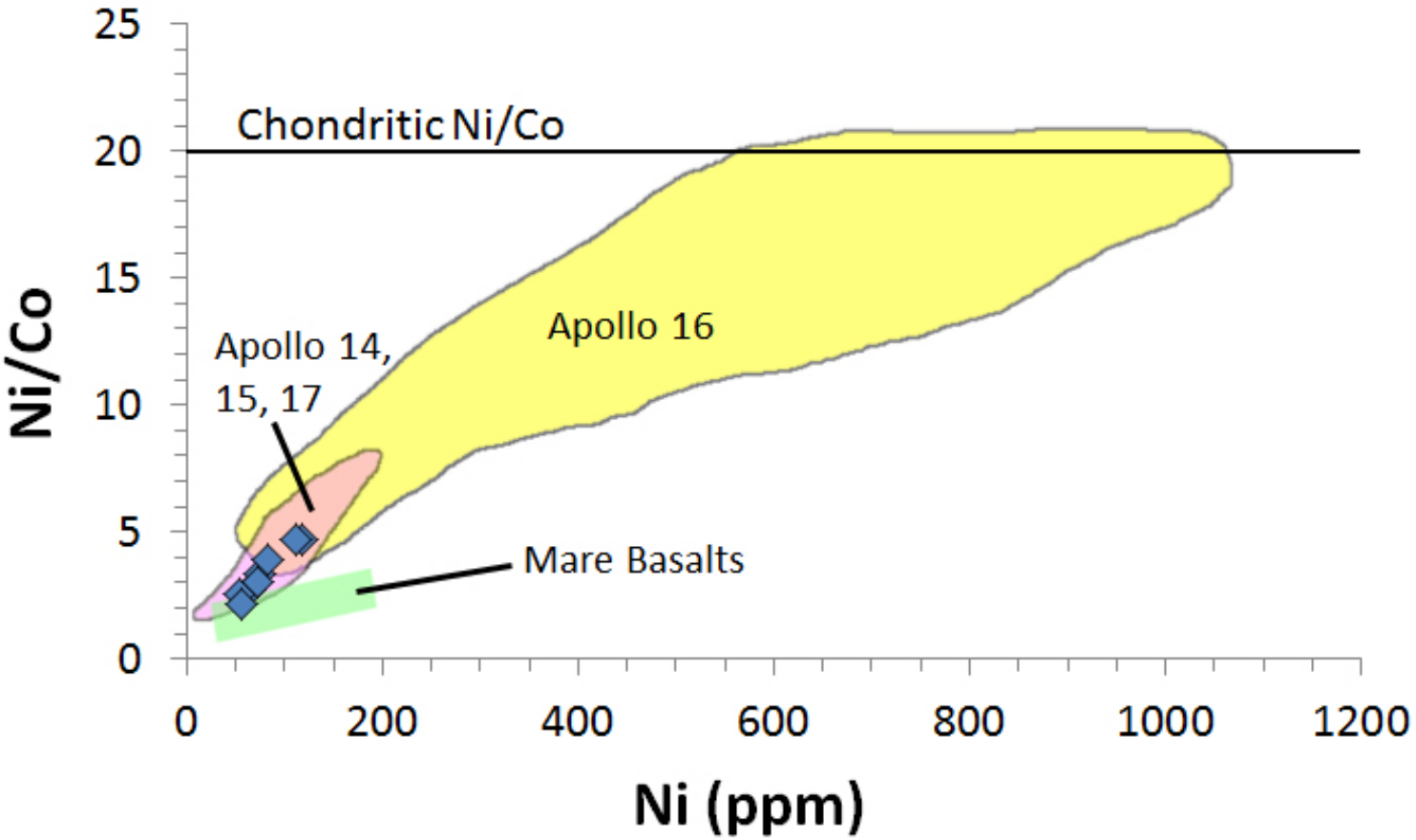

Figure 7: Individual bulk ablation points of NWA 5744 Ni concentration versus Ni and Co relative abundance plotted in blue diamonds, compared to non-meteoritic Apollo 16 highlands samples (yellow), Apollo 14, 15, 17 highlands samples (pink), mare basalts (green) and Ni/Co ratio of chondrites (fields reproduced from Ringwood and Seifert, 1986). Individual chondrite groups average 10.2 to 17.5 parts per thousand Ni (far off the scale of the chart) but have Ni/Co ratios ranging from 19.4 to 21.1 (Wasson and Kallemeyn, 1988). All NWA 5744 points plot among the pristine highlands compositions and show no indication of significant impactor contamination.

average for the measured bulk rare earth element (REE) content is about 2-4 times greater than the expected bulk composition calculated in this manner, except for La and Eu (Fig. 8). Low average bulk lanthanum is explained by the fact that two ablation spot measurements had high background readings for La, making it impossible to resolve the signal and therefore unable to be averaged in. For europium, while it is possible that the bulk ablation locations selected were not truly representative of the rock and contain an overabundance of relatively REE-rich pyroxene, that alone cannot explain the difference. The average of the measured bulk compositions for La and Ce are 2.73 and 3.36 ×CI chondrite respectively, which are both greater than the average of any of the three principle phases ablated, and greater than all but two of the individual plagioclase *in situ* ablations. And again, average La appears to be artificially depressed in the average due to two measurement attempts which could not be resolved. Instead of analytical error or biased measurements, the difference most likely stems from the fact that two different materials are being measured and compared. All of the *in situ* mineral ablations were conducted on large relict grains, but most of the materials measured in the bulk ablations (and indeed, most of the materials that comprise NWA 5744) are matrix maskelynite and recrystallized olivines and pyroxenes which are all too small to measure *in situ* via LA-ICP-MS. Bulk REE content would be greater than expected if the REE content of these metamorphic phases is greater than that of the larger relict mineral grains. Considering major element composition of maskelynite exhibits some localized variation (Table 3), it is probably reasonable to suggest that

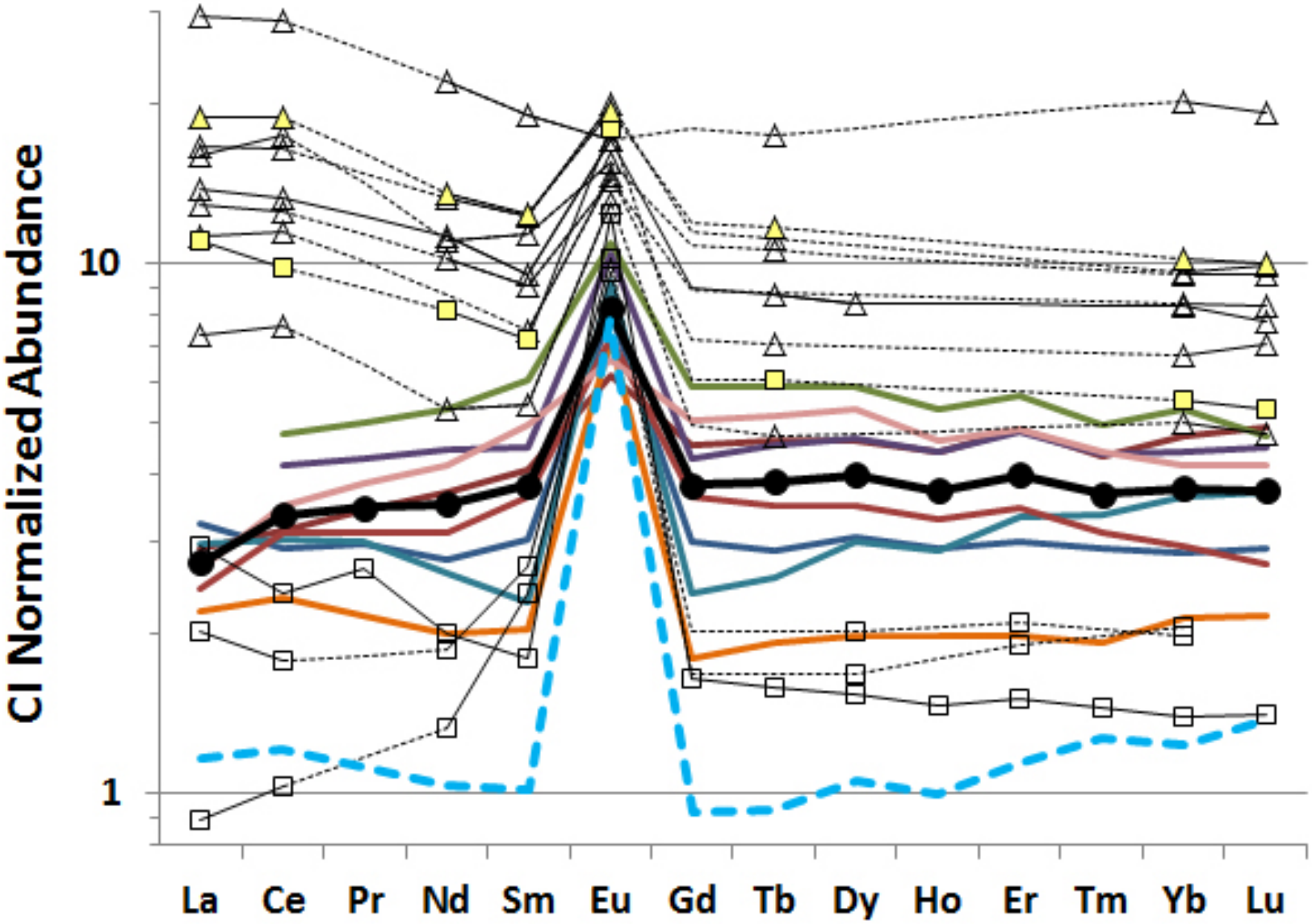
CI Normalized Abundance
10
1
La
Ce
Pr
Nd
Sm
Eu
Gd
Tb
Dy
Ho
Er
Tm
Yb
Lu

Figure 8: CI chondride normalized (Anders and Grevesse, 1989) bulk REE content. Colored lines represent REE concentrations of 8 individual 176 µm LA-ICP-MS bulk ablations of NWA 5744 (Appendix A). Black line with filled circles represents the average of those 8 ablations (Table 4b). Heavy blue dashed line represents the expected bulk REE content of average using average ablated relict mineral compositions in proportion to modal bulk rock abundance. Squares represent the following magnesian granulite meteorites: average Dhofar 489; average ALH 81005; average Dhofar 309; MAC 88105,W3 (in yellow)(Warren and Kallemeyn, 1991; Takeda *et al.,* 2006; Treiman *et al.,* 2010). Triangles represent the following Apollo magnesian granulites: 67415 (in yellow); 60035 (average of 27, 30, 59A, and 59B); 67415 (average of 33A and 33B); 67955 (average of 74A and 74B); 76230; average 79215; 72275,439/495; 76503,7021; and 76503,7052 (Ma and Schmitt, 1982; Salpas *et al.,* 1988; Lindstrom *et al.,*1991; Jolliff *et al.,* 1996; Hudgins *et al.,* 2008). Dashed lines indicate where data was interpolated.

trace element content is also similarly variable and not necessarily the same as in relict grains. If this is the case, then the average measured bulk composition should be more accurate than the expected bulk composition based on modal mineral abundance. However, the broad range in trace element content between about 2 and 6 times chondritic concentrations among these 8 ablations indicates their number may be too small for their average to represent a truly accurate bulk rock composition.

2.3. Discussion

2.3.1 Comparison of NWA 5744 with Known Lunar Highland Lithologies

2.3.1.1 Major Elements

Ferroan anorthosites and Mg-suites of pristine lunar crustal rocks define separate fields within the anorthite-forsterite space (e.g., Hollister, 1973; Goodrich *et al.,* 1984; Warren, 1993; Treiman *et al.,* 2010). Minerals within NWA 5744 plot in the Mg-suite field in this diagram, with olivine Mg#'s ranging from 76.8 to 82.3 (average 78.8 ±1.8) and plagioclase An content ranging from 93.2 to 98.5 (average 96.5 ±1.3) (Fig. 9). Plagioclase An content has considerably more variance within the diagram than Mg#'s of olivine. The range of An content appears to be centered on the field of expected FAN compositions, which also seems to be true for most if not all other magnesian granulites from the literature (Fig. 9), so NWA 5744 plagioclase appears to be representative of most other lunar magnesian granulites. Olivine in NWA 5744 and other magnesian granulites have Mg# placing them in or near the field of expected Mg-suite

compositions, but the range of values seen in NWA 5744 are too narrow to contain those values seen in most of the other lunar magnesian granulites. Pyroxene major element compositions (Table 5a) are somewhat more closely affiliated with pyroxene in the Mg-suite than the FAN suite (Fig. 6).

2.3.1.2 Plagioclase Trace Elements

Any terrestrial contamination of the plagioclase would be expected to increase Ba and Sr concentration. In NWA 5744, the Ba and Sr content of plagioclases is similar to that of Apollo FAN (Fig. 10), a strong indication that terrestrial contamination is negligible. The REE CI-normalized patterns of NWA 5744 (Fig. 11) overlap with those of FAN plagioclase composition (Papike *et al.,* 1997; Floss *et al.,* 1998), and have lower REE concentrations relative to the plagioclases from Mg-suite samples (Papike *et al.,* 1996; Shervais and McGee, 1998). There is also large spread in REE abundance between individual NWA 5744 crystals, spanning about one order of magnitude. Although Eu abundances also overlap with those of FAN, the Eu/Sm ratios of NWA 5744 plagioclase, which are a function of the size of the positive Europium anomalies, are higher than those for the FAN suite and overlap instead the lower Eu/Sm ratios in Mg-Suite plagioclases with the same An# contents (Fig. 12). The Mg-suite plagioclase displays a broad range of An and trace element content, but generally has much higher concentrations of incompatible trace elements than either FAN or NWA 5744 plagioclases (see CI-normalized La/Yb in Fig. 12). The NWA 5744 data tends to plot on the periphery of the Mg-suite in each case, rather than distinctly within the suite.

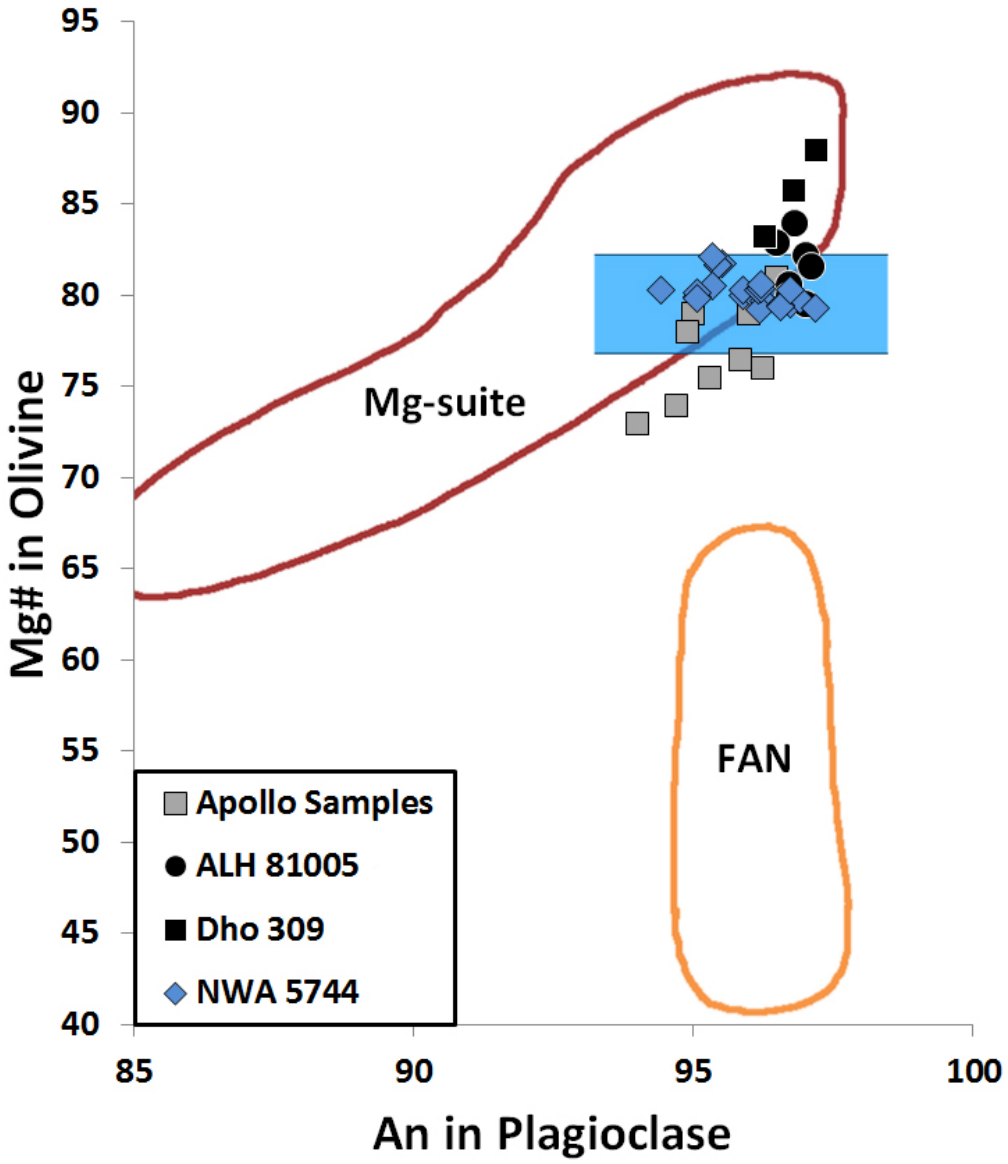

Figure 9: Blue shaded region represents the full EMPA-measured range of Mg# in olivines and An content of plagioclase in NWA 5744. Blue diamonds represent individual EPMA measurements of NWA 5744 olivine crystals vs. plagioclase matrix, physically located within 25 µm of each other. Black circles and squares are magnesian granulites within ALH 81005 and Dhofar (Dho) 309 respectively (Goodrich *et al.,* 1984; Treiman *et al.,* 2010). Gray squares are Apollo magnesian granulites from samples 60035, 67415, 67955, 72275, 76230, and 79215 (Ma and Schmitt, 1982; Lindstrom and Lindstrom, 1986; Salpas *et al.,* 1988). Mg# = molar [Mg/(Mg + Fe)]; An in this figure = molar [Ca/(Ca + Na)]. NWA 5744 points fall within the magnesian suite (Mg-suite) with little variation in olivine Mg', while plagioclase An is more variable but falls entirely within the full range of ferroan anorthosite (FAN) plagioclase. Fields reproduced from Goodrich *et al.,* (1984) and Treiman *et al.,* (2010).

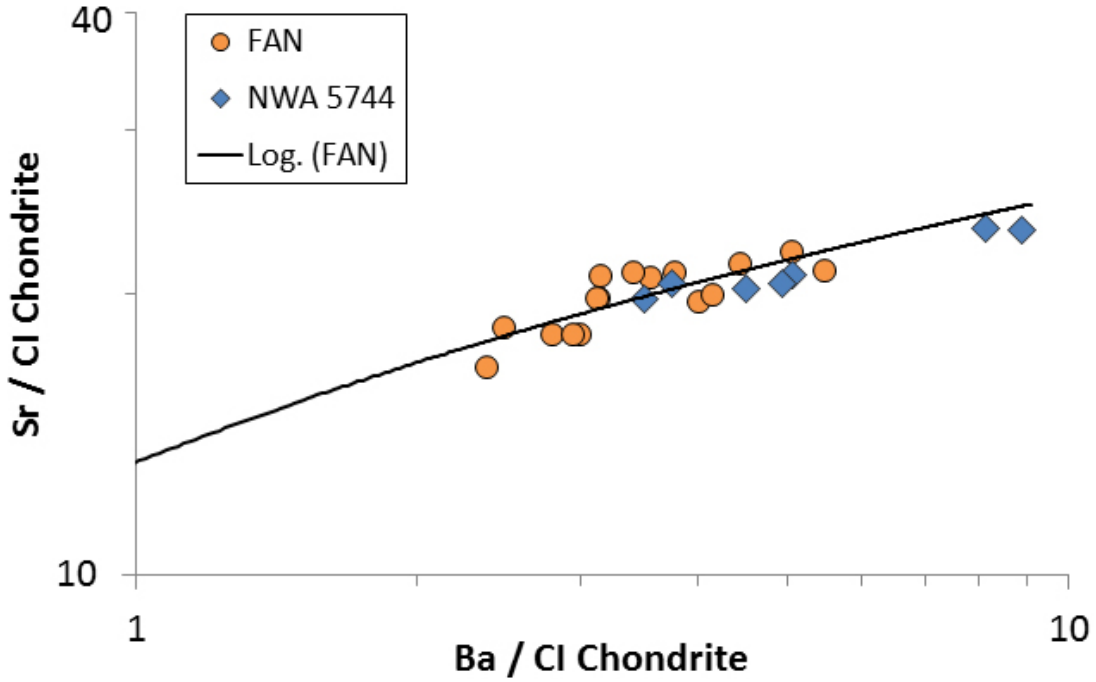

Figure 10: Ba-Sr plot of FAN (Papike *et al.,* 1997; Floss *et al.,* 1998) and NWA 5744 plagioclase. Log curve fit to FAN data closely matches NWA 5744 points. Significant terrestrial contamination would be reflected with anomalously high Sr and Ba which is not seen, and a relationship seems to be present between the Ba/Sr ratio of FAN and NWA 5744 plagioclase.

While NWA 5744 plagioclase do not perfectly overlap in all diagrams with FAN suite material, in each case they either overlap strongly or plot as an extension of the FAN suite (Figs. 9-12). NWA 5744 seems only peripherally related to the Mg-suite if at all, and bears little to no resemblance to plagioclase from any other highlands suite (i.e., the evolved High-Alkali Suite, Wieczorek *et al.,* 2006). Major elements in magnesian granulites from Apollo samples 60035, 67415, 72275, 76230, and 79215 (Ma and Schmitt, 1982; Lindstrom and Lindstrom, 1986; Salpas *et al.,* 1988), as well as both major and trace elements from Mg-rich granulite clasts in lunar meteorites ALH 81005 and Dho 309 (Treiman *et al.,* 2010) all strongly resemble NWA 5744 (Figs. 9, 11, and

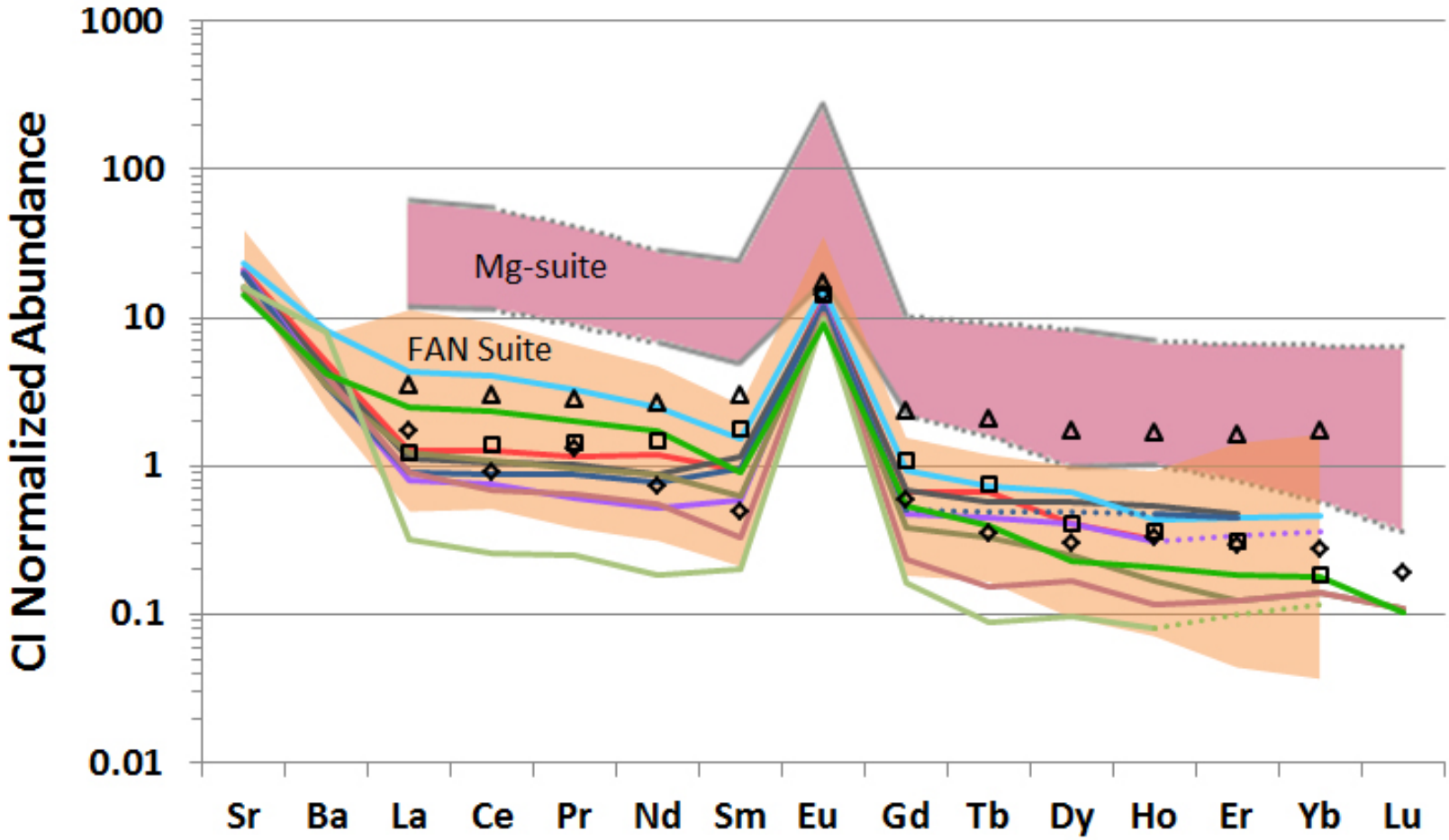
1000
100
10
1
0.1
0.01
CI Normalized Abundance
Mg-suite
FAN Suite
Sr
Ba
La
Ce
Pr
Nd
Sm
Eu
Gd
Tb
Dy
Ho
Er
Yb
Lu

Figure 11: Chondrite-normalized trace element contents of NWA 5744 plagioclase compared to those of ferroan anothosites (FAN) and magnesium suites (Mg-suite). All normalizations are to CI chondrite data from Anders and Grevesse, 1989.Solid colored lines represent ablation measurements of individual NWA 5744 plagioclase crystals. Red upper shaded region represents the range of values seen in plagioclase crystals from Apollo Mg-suite samples. Dotted lines represent regions where concentrations were interpolated. (Papike *et al.,* 1996; Shervais and McGee, 1998). Orange lower shaded region represents the range of values seen in plagioclase crystals from Apollo FAN samples (Papike *et al.,* 1997; Floss *et al.,* 1998). Three other magnesian lunar granulites are plotted in open black symbols: diamonds are data for an anorthosite clast within Dho 489 (Takeda *et al.,* 2006); triangles are plagioclase data for Dho 309; squares are plagioclase data for ALH 81005 (Treiman *et al.,* 2010).

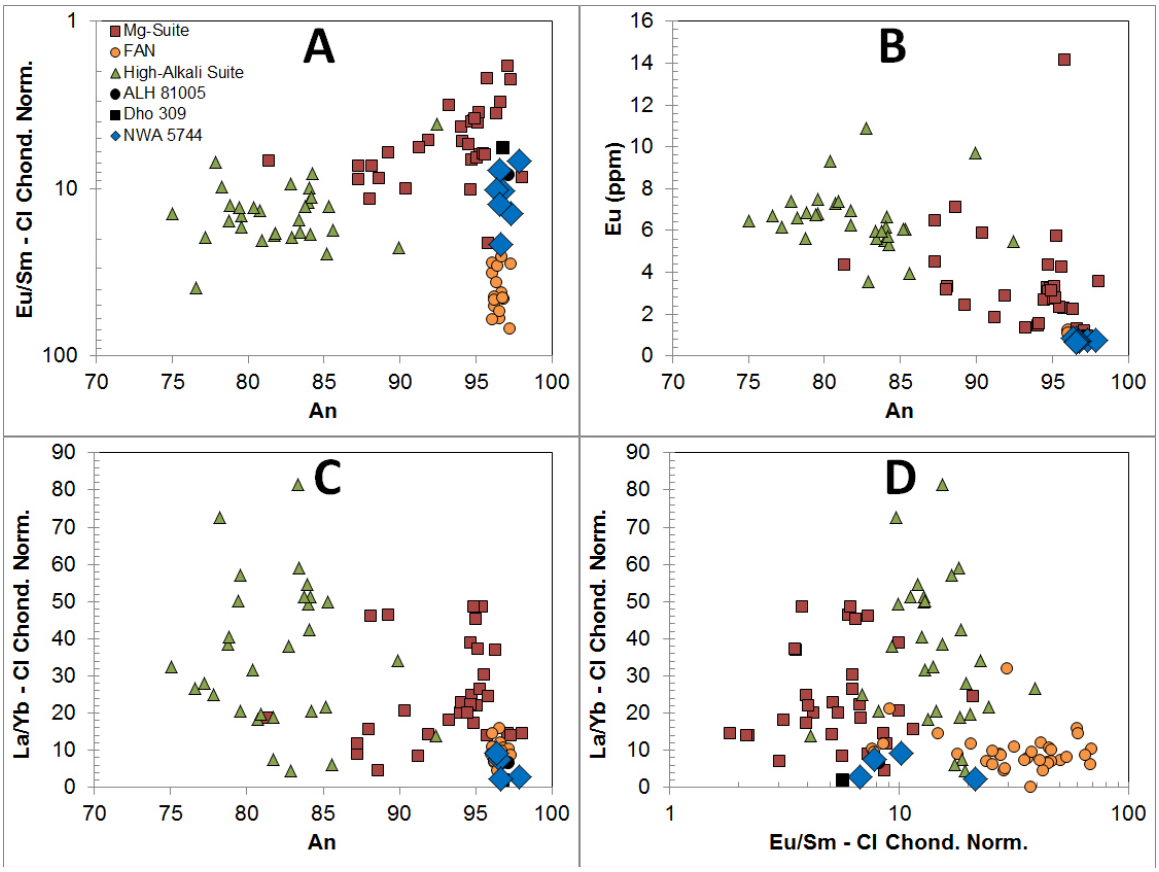

Figure 12: Comparison of plagioclase compositions in NWA 5744 (blue diamonds) and in magnesian granulites ALH 81005 and Dho 309 (Treiman *et al.,* 2010) and the three major highlands suites seen in Apollo samples (Papike *et al.,* 1997; Floss *et al.,* 1998; Papike *et al.,* 1996; Shervais and McGee, 1998; Shervais and McGee, 1999; Joy *et al.,* 2006; 2008; Schnare *et al.,* 2008; Joy, 2013). Brackets denote the use of molar values, which are then normalized to CI chondrite concentrations. **A:** Eu/Sm vs. An; **B:** Eu vs. An; **C:** La/Yb vs. An; **D:** La/Yb vs. Eu/Sm.

12). In terms of major elements NWA 5744 resembles Mg suite rocks, while the trace elements are more akin to those of the FAN, tentatively placing Mg granulites in a category of highland lunar crust lithology of their own.

2.3.1.3 Olivine and Pyroxene Trace Elements

Olivine have low LREE concentrations near the LA-ICP-MS detection limit (Appendix A), but have comparatively higher concentrations of HREEs. Olivine light rare

earth element (LREE) concentrations are relatively flat (La/Lu ratio of 0.39 to 5.53, averaging 2.20; Fig. 13). The HREE in the olivine show a strong positive slope (CI-normalized La/Lu ratio of 0.04 to 0.56, averaging 0.22), and a small negative Eu-anomaly is present (CI-normalized Eu/Eu* of 0.28 to 2.71 and averaging 1.10, where Eu* is the interpolated value between Sm and Gd measured for a given crystal).

The pyroxene each show a bulk (e.g., mix of high and low-Ca exsolutions, Fig. 2D) smooth pattern with a gradual increase in CI-normalized concentration from the light rare earth element (LREE) to the HREEs (CI-normalized La/Lu ratio of 0.12 to 0.15, averaging 0.13), with negative Eu/Eu* anomalies (0.027 to 0.086) (Fig. 14). Negative Eu-anomalies in the olivine and pyroxene are consistent with either: 1) mafic phase crystallization from a melt during or after significant plagioclase crystallization (Wood, 1975; Brophy and Basu, 1990); or 2) subsolidus equilibration between plagioclase, pyroxene, and olivine, i.e. metamorphism (Brey and Köhler, 1990; Liang *et al.,* 2013).The lamellae in the NWA 5744 pyroxene vary slightly in thickness along their length and are somewhat wavy rather than strictly straight and parallel (Fig. 3D). This may be indicative of a brief reheating event post lamellae formation. Calculations for the duration of metamorphism can be made using average grain size of the granulite, but are highly and inversely dependent on the metamorphic temperature (Cushing *et al.,* 1993). However, if metamorphism occurred at 1000 ^{o}C, which is the minimum expected temperature for lunar granulites (Cushing *et al.,* 1993), and a conservatively large average metamorphic olivine grain size of 15 µm is used, then an approximation for a

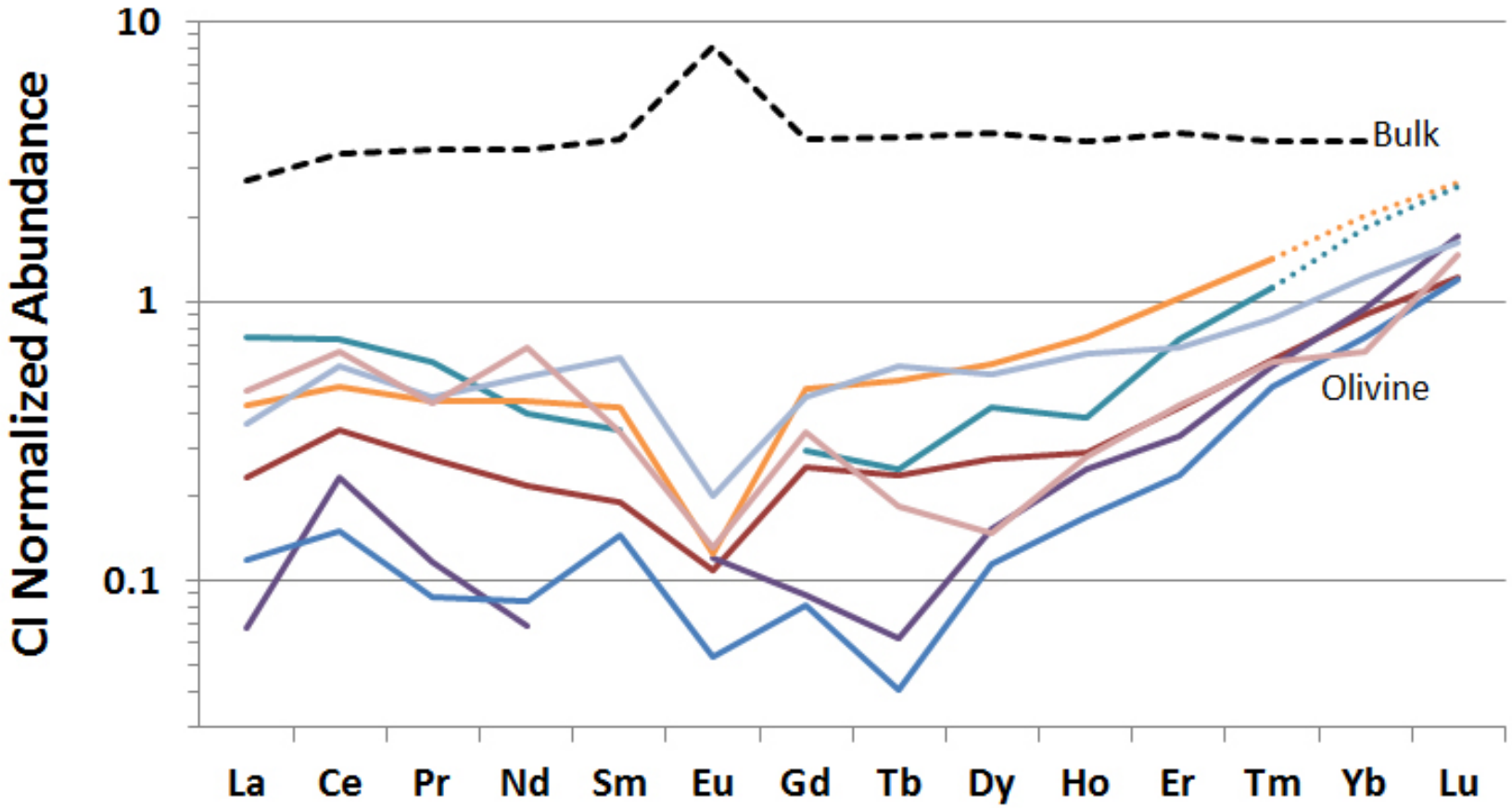

Figure 13: Trace element diagram for olivine and recalculated bulk-rock of NWA 5744. Each line is one 84 µm *in situ* LA-ICP-MS measurement of elemental abundances of separate olivine crystals except for the orange line, which is the average of two 176 µm *in situ* LA-ICP-MS measurementscrystals. For the orange and teal lines, Yb contents were below detection limits so the values were interpolated between Tm and Lu concentrations, as indicated by dotted lines. Black dashed line is the average of 8 bulk NWA 5744 analyses, using 176 µm ablation spots on regions visually judged to be typical in composition.

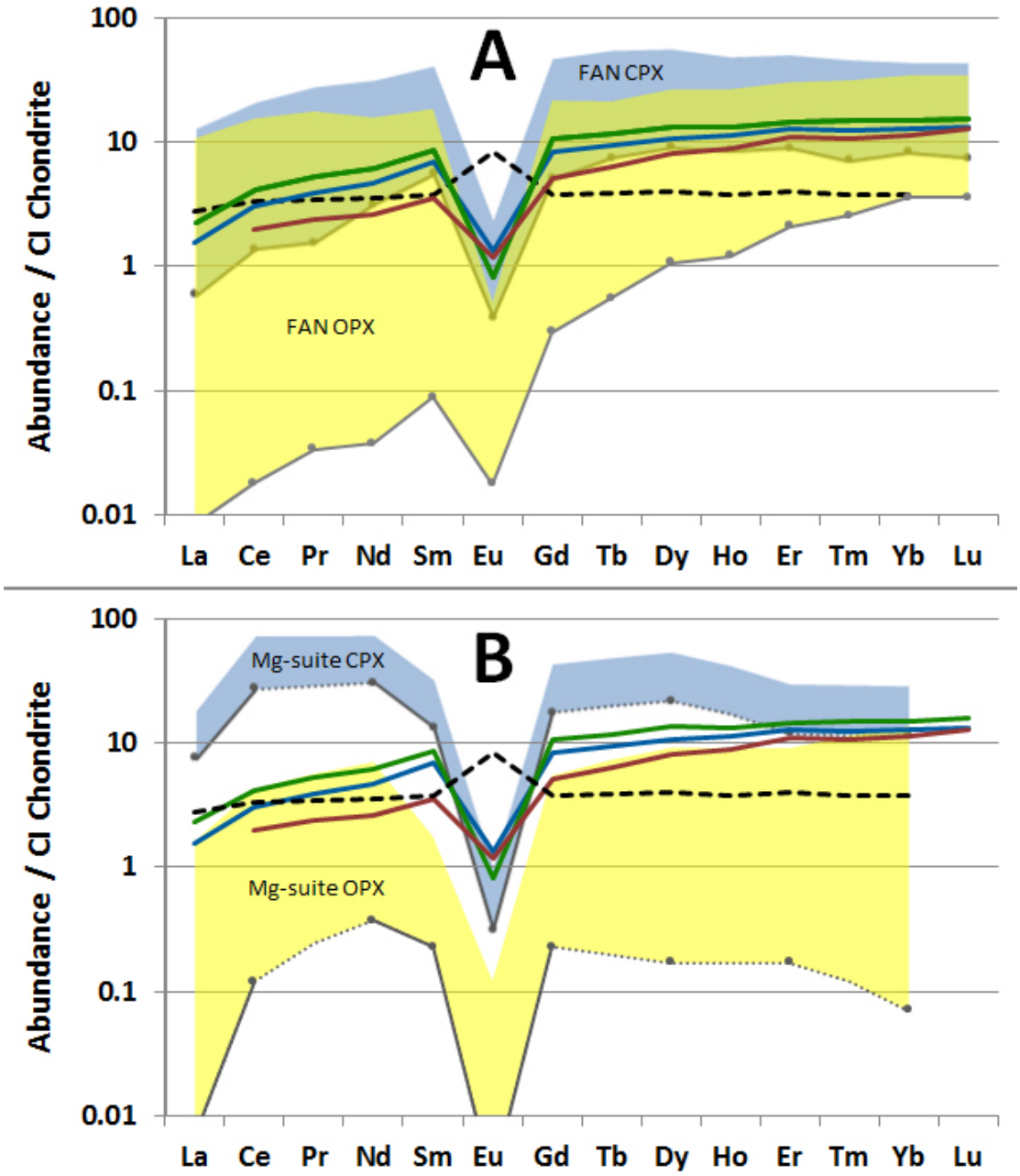

Figure 14: Colored lines represent *in situ* ablation analyses of pyroxenes within NWA 5744. The green and blue pyroxene lines are each the average of two 84 µm *in situ* ablations on crystals, and the red pyroxene line is a single 84 µm *in situ* ablation on a third pyroxene. Black dashed line is the average of 8 bulk NWA 5744 analyses, using 176 µm ablation spots on regions visually judged to be typical in composition. **A.** Shaded regions cover the range of compositions for FAN pyroxenes: Ca-rich in blue, Ca-poor in yellow (Floss *et al.,* 1998). NWA 5744 pyroxene REE data could be easily interpreted as OPX with a small amount of CPX from the FAN suite. **B.** Shaded regions cover the range of compositions for Mg-suite pyroxenes: Ca-rich in blue, Ca-poor in yellow (Papike *et al.,* 1994; Shervais and McGee, 1999). Dotted lines indicate compositions where these fields were interpolated. NWA 5744 pyroxene REE data are not a strong fit among the Mg-suite pyroxene compositional fields.

maximum metamorphic duration of no more than 1000 years is calculated (Cushing *et al.,* 1993). Using average pyroxene grain sizes of < 10 µm would make the maximum duration even shorter, on the order of 100's of years at most. The ~5 µm average width of pyroxene matrix schlieren would indicate rapid cooling during metamorphism, perhaps over a duration as brief as 15 to 1500 years (Cushing *et al.,* 1993; 1999), so it is likely that NWA 5744 did not metamorphose while deep within the crust where cooling would have been slower. With a reliable temperature of metamorphism plagioclase zoning might be used to better calculate the length of the cooling period (Grove *et al.,* 1984). However, no reliable temperature could been calculated due to apparent disequilibrium between clinoenstatite and augite.

In contrast to the major element pyroxene comparisons, the carbonaceous chondrite Ivuna (CI) -normalized REE concentrations of NWA 5744 fall completely with the range for FAN pyroxene and exhibit a similar shape to that of the FAN fields, rather than Mg-Suite pyroxene REE (Fig. 14). While the highest Eu/Sm ratio measured in NWA 5744 pyroxenes is greater than those observed in FAN pyroxene , Eu/Sm of the two other pyroxenes analyzed are similar to those of FAN pyroxene but unlike those of Mg-suite pyroxene (Fig. 14) (Papike *et al.,* 1994; Floss *et al.,* 1998; Shervais and McGee, 1999).

In summary, the pyroxene and plagioclase trace element compositions of NWA 5744 are most similar to the FAN suite counterparts. However, in some cases,

compositional data for NWA 5744 overlaps with Mg-Suite data or is transitional between FAN and Mg-Suite data.

2.3.2. Pyroxene Thermometry

Four distinct examples of coexisting low and high calcium pyroxene were identified for thermometry, and only low-Ca pyroxene (clinoenstatite) and high-Ca pyroxene (augite) in direct contact were used as thermometers. The Lindsley (1983) Ca-Mg graphical thermometer gives a very broad range of temperatures from 800^{o}C to 1270^{o}C at 1 atm (Fig. 6). The Ca-Mg two pyroxene thermometer of Brey and Köhler (1990) also shows a wide range in temperatures at 1 atm, from 835 to 1379^{o}C. This range of temperatures derived from both Ca-Mg thermometers may indicate that many of the high-Ca and low-Ca pyroxene pairs were not in equilibrium because the metamorphism event was too brief. Pyroxene major element compositions for NWA 5744 are shown in Figure 6 and compared with pyroxenes from the FAN and Mg-suites. The data for NWA 5744 plot on the magnesian side of the quadrilateral. Clinoenstatite is uniform in composition other than one outlier point, but augite present in NWA 5744 has considerable variation in Ca content. This may indicate that Ca did not reach equilibrium in the augite during metamorphism. However, it may instead be due to mixed EMP measurements when attempting to measure only augite composition.

2.3.3. Bulk Rare Earth Element Composition

The calculated average bulk sample REEs and most of the individual bulk ablation spots of NWA 5744 have higher REE concentrations than magnesian granulite clasts in lunar meteorites Dho 489 (Takeda *et al.,* 2006), ALH 81005, or Dho 309 (Treiman *et al.,* 2010) (Fig. 8). Bulk REE pattern of magnesian granulite clasts from MAC 88105 (Warren and Kellemeyn, 1991) and Apollo 16 sample 67415 (Lindstrom *et al.,* 1991) do not resemble those of NWA 5744 (Fig. 8, yellow symbols), which may indicate a different igneous and metamorphic history. The bulk rock NWA 5744 average (Table 5a) has higher concentrations of REEs than those two other magnesian granulites except for La and Eu (Fig. 8), and none of the other granulite REE patterns fall entirely within two standard deviations of the NWA 5744 average. Therefore, if this NWA 5744 average is accurate, it may represent a different crustal terrane source. Average bulk Eu may be lower than all the other magnesian granulites due to differing parental magmas, although it is also possible that plagioclase is merely underrepresented in the bulk ablation sites selected for NWA 5744.

Overall, the averages for the bulk REE concentrations in NWA 5744 are higher than those of most other magnesian granulite meteorites, but lower than those of all Apollo magnesian suites (Fig. 8). Assuming that the averaged NWA 5744 bulk composition calculated in this study is representative of the parent rock, NWA 5744, like many lunar meteorites, is sampling areas of the lunar crust that are far removed from the Apollo sample sites.

Additionally, if the compositions of the relict plagioclase, pyroxene, and olivine grains represent that of the parent rock, then the calculated bulk REE content based on modal abundance using the REE content of these relict grains indicates that aside from a Eu anomaly, the bulk REE content of the parent rock would have been approximately chondritic (Fig. 8).

2.4. Origin of NWA 5744

2.4.1 Igneous History of NWA 5744

2.4.1.1 Is the NWA 5744 Parent Rock a Ferroan Anorthosite?

Northwest Africa 5744 formed from a feldspar-rich parent rock that was likely part of the lunar feldspathic crust. During the crystallization of an LMO that initially formed this crust, plagioclase flotation depends on the Mg# in the melt. Floatation could not have occurred until the LMO became more Fe-rich (and therefore more dense) than plagioclase (2.74 g · cm^{-3}; Campbell *et al.,* 1978) after substantial crystallization of early mafic silicates (Warren 1985; 1990). Anorthosite with bulk Mg# >70 such as NWA 5744 (Bulk Mg# of 79) would still be too dense to float in an LMO (Warren, 1990; Gross *et al.,* 2012a; 2012b). The parent rock of NWA 5744 was therefore not likely a ferroan (Mg# <70) floatation cumulate. If LMO models such as summarized by Shearer *et al.* (2006) are accurate, and the Mg#-rich nature of NWA 5744 represents that of the crust where it formed, then the parent rock likely originated from the lower half of the lunar crust where compositions could have been more magnesian. This would require one or more

exceptionally large impacts to excavate the material from the lower crust. Arai *et al.* (2008) proposed a model for the lunar crust to explain remote sensing data that indicate variations in the Moon's surface composition and crustal thickness. They noted that the nearside crust is thinner and more noritic while the farside crust is thicker (except for the South Pole Aitken Basin) and more troctolitic. They proposed an asymmetric crystallization of the LMO where the nearside and farside portions developed different compositions, with the farside having cooled faster, and been more magnesian. The South Pole Aitken (SPA) Basin-forming impact ejected most of the crust from the southern hemisphere on the lunar farside, which blanketed the farside northern hemisphere in Mg-rich material from the deep crust. The NWA 5744 protolith could potentially have been some of that ejected deep-crustal material. Such a deep protolith origin may also be supported by the lack of impactor material as deduced from the Ni and Co abundances for this rock (Fig. 7). The parent rock formation (and subsequent metamorphism) may have occurred deep enough to shield the material from significant impactor contamination (i.e., the parent rock was not likely impact melt or surficial regolith material). This would also mean NWA 5744 represents an altogether different crustal lithology than those observed at the Apollo and Luna sites, and may not be directly related to either the primary crust FAN or secondary crust Mg-suite. However, greater metamorphic depth may make it more difficult to explain the apparent short metamorphic duration, because cooling rates would be inversely proportional to depth. This discrepancy may be explained if the metamorphism was primarily shock induced.

Another possibility is simply that NWA 5744 and other similar magnesian granulites originate from primary crustal FAN suite parent rock, and the FAN field in Figure 9 should be extended up to partially overlap with the Mg-suite. This would imply that the upper flotation crust on the LMO may not have been as ferroan as previously believed, or at least not as uniformly so (see also Takeda *et al.,* 2006; Arai *et al.,* 2008; Gross *et al.,* 2012a and 2012b). Models for LMO composition and crystallization would need to be adjusted to make the magma more magnesian, yet still allow for plagioclase floatation. In this scenario, NWA 5744 would represent an early batch of floatation cumulate crystallization from the LMO when the liquid had just become dense enough, and before compositions had progressed to becoming more ferroan. It may be possible to float magnesian anorthosite in a magma ocean, but it would probably require more vigorous convection and a greater proportion of liquid to solid during the late stages of magma ocean crystallization than most models currently predict (Arai, 2008). However, it is probably not enough to float most magnesian anorthosites, including a rock as highly magnesian as NWA 5744, and even if there was a small window in the stages of LMO development where magnesian magma could float plagioclase, it was probably too brief to account for the number of magnesian granulites seen in meteorites and Apollo samples.

2.4.1.2. Is the NWA 5744 Parent Rock a Magnesian Anorthosite?

Alternatively, if the parent rock originated in the upper crust, it was probably a magnesian anorthosite, a rock type lacking KREEP content and believed to

predominantly originate from the farside feldspathic highlands terrane (Takeda *et al.,* 2006; Arai *et al.,* 2008; Gross *et al.,* 2012a and 2012b). Upper crustal magnesian anorthosite has several postulated origins. For example, Longhi and Ashwall (1985) and Longhi (2003) suggested this lithology formed via serial magmatism rather than as primary floatation cumulates in a magma ocean, and this may explain the origin of the igneous precursor to NWA 5744. However, these types of magma bodies and any crystals entrained within them should be well-equilibrated, and the broad range of REE contents in NWA 5744 between relict grains of major phases fails to reflect that expected equilibration (Figs. 11, 13, 14).

2.4.1.3 Is the NWA 5744 Parent Rock a Mix of Ferroan and Magnesian Anorthosites?

Given the similarities NWA 5744 has to both the FAN and Mg-suites, perhaps it represents either a magnesian suite parent that got metasomatized by FAN-sourced melts, or a hybridized magma composition that was a partial melt of mixed FAN and Mg-suite source materials, or brecciated products of the FAN suite and Mg-Suite materials mixed together in the deep lunar megaregolith. However, these last two scenarios seem unlikely, as both would predict major and trace element compositions to be intermediate between the FAN and Mg-suites, which is not what is observed in NWA 5744 plagioclase and pyroxene (Figs. 9, 11, 14). The latter would also make NWA 5744 distinctly polymict, and there is no indication of any clasts of differing rock type within NWA 5744, ferroan or otherwise.

The latter two scenarios may or may not require significant excavation, depending on depth of formation. Using a formula published by Cintala and Grieve (1998), an impact that produces a 110 km diameter crater would be necessary to fully excavate material from a depth of 20 km. For material from 50 km deep, an impact producing a 206 km diameter crater would be required. If the NWA 5744 parent rock lithology was originally emplaced in the lower crust, it must have come from beneath a crater of at least 110 km in diameter.

2.4.2. Metamorphic History of NWA 5744

2.4.2.1. Characteristics of the Metamorphism of NWA 5744

The possibility that NWA 5744 major element characteristics come from a magnesian suite-like parent and that its trace element characteristics were later modified by metasomatism or metamorphism by FAN-sourced melts is explored here. Trace element content appears to be greater in the fine-grained metamorphic matrix of NWA 5744 than in larger relict grains (Figs. 8, 10, 13-14), which may indicate metamorphism occurred in different surroundings than when the parent rock originally formed. Following the formation of the parent rock, NWA 5744 was subjected to one or more metamorphic events. This metamorphism would have initiated equilibration with surrounding material of different composition, which may explain the FAN-like signature of the trace element content in plagioclase and pyroxene. For REE diffusion through the minerals of the rock, long equilibration times would be required. However,

equilibration appears to have been incomplete as indicated by the spread in REE abundance between individual plagioclase and olivine crystals (Figs. 11, 13). Incomplete plagioclase equilibration and small average pyroxene grain size indicate the duration of metamorphism was brief, probably occurring near the surface where cooling would have been more rapid (Cushing *et al.,* 1999; Hudgins *et al.,* 2011), yet still deep enough to be shielded from addition of impactor material.

As has already been discussed, none of the attempts at thermometry proved to be consistent due to the minerals in NWA 5744 apparently never equilibrating during metamorphism, but using a minimum estimate along with the metamorphic grain size indicated the duration of metamorphism was likely to be <1000 years (Section 4.1.3). Given this short duration, metamorphism almost certainly occurred in the shallow crust where cooling would have been rapid, and equilibration with any surrounding material of different composition probably wasn't significant.

2.4.2.2. Heat Source for Metamorphism: Impact or Igneous Intrusive?

One plausible metamorphic heat source would be an impact melt sheet on the lunar surface or pile. Alternatively, the metamorphism could be primarily shock-induced with a lesser duration of heating involved. In anorthosite, plagioclase begins to transform into maskelynite in small patches at pressures of 25-27 GPa, with near-complete maskelynization at pressures >30 GPa (Johnson and Hörz, 2003). Because the matrix was near fully maskelynized but the relict plagioclase was not, it seems unlikely

that shock pressures exceeded 30 GPa. Typical shock pressures of 10-60 GPa in rock surrounding an impact typically generate temperatures from 500 ^{o}C to 3000 ^{o}C (French, 1998), which would be more than sufficient to produce the range of temperatures seen in the pyroxene thermometry modeling attempted. Basin-forming and cratering impact processes dominated the early history of the Moon prior to 3.7 Ga (Stöffler and Ryder, 2001), excavating, remelting and mixing the lunar crust. According to Stöffler and Ryder (2001), at 4.1-4.2 Ga, as many as one crater of diameter > 1 km was being created per 2 km^2 of the lunar surface, and this rate slowed down to one crater of diameter > 1 km per 330 km^2 by the end of the basin-forming epoch. It is notable though that craters 10 times smaller were about 100 times more common per unit area of the lunar surface (Barlow, 1990). Recent work by Bottke *et al.* (2012) indicates that large scale inner Solar System bombardment may have lasted even longer, with about 15 basin-forming impacts striking Earth between 2.5 and 3.7 billion years ago, some of which may have been as large as the Nectaris Basin on the Moon (860 km diameter; Stöffler *et al.,* 2006). Since impacts have, therefore, occurred over the Moon's history, one such event, or a closely timed cluster of events, may well have provided the heat to metamorphose the source rock that produced NWA 5744. If NWA 5744 was excavated close to the surface prior to metamorphism, it seems logical that the same impact or impacts could have generated a melt sheet that served as the metamorphic heat source. Metamorphic textures (rounded relict grain boundaries, maskelynization of plagioclase, amoeboid olivines, olivine and pyroxene schlieren), plagioclase zoning (Figs. 3-5), a wide range of

bulk (Fig. 8), plagioclase (Fig. 11), and olivine (Fig. 13) REE profiles, and wavy pyroxene lamellae (Fig. 3D) all support a hypothesis that the metamorphic event was intense but short in duration, as there was not enough time to completely equilibrate the rock and thus homogenize the textures or elemental concentrations. Hudgins *et al.,* (2011) proposed that lunar granulites containing olivine crystals with zoning in the major elements may have been metamorphosed by melt sheets over time scales of less than 13,000 years that were: (i) <1 km thick; (ii) of lower initial temperature than the modeled ~2000 ^{o}C; and/or (iii) buried deeper than 110 m or 350 m below modeled melt sheets of 1000 m and 5000 m thickness, respectively. A similar metamorphic history for NWA 5744 may explain the zoning in its plagioclase, although Mg closure temperature is lower in plagioclase than in olivine (Onorato and Uhlmann, 1978; Van Orman *et al.,* 2012), so metamorphism of NWA 5744 was probably of somewhat with a shorter duration and/or cooler than those models presented by Hudgins *et al.* (2011).

If metamorphism was caused by an impact melt sheet, the impactor must have been small enough for the heat to dissipate before the minerals could fully equilibrate. If the parent rock did originate from the deep crust, then the impact(s) which excavated it must have been very large and either the shock from the excavation was sufficient to cause the observed metamorphism by itself, or the excavation preceded a later, smaller impact which caused the metamorphism by either shock or an impact melt sheet.

If the heat source was an igneous intrusion, it probably occurred close enough to the lunar surface to cool rapidly. Due to the short duration of metamorphism it is

possible that metamorphism is largely shock-induced, but this is questionable because of the lack of impactor content. If true, it must have been deep enough to be shielded from impactor contamination, yet shallow enough to experience significant shock.

2.5. Conclusions

The lunar meteorite NWA 5744 has compositional features similar to a number of other magnesian granulites and its geochemistry does not allow it to be clearly classified into any major suite of lunar crustal rocks. This meteorite bears strong geochemical correlations and discrepancies with both the lunar crustal FAN (i.e., primary crust) and Mg-suites (i.e., secondary crust intrusive magmatics). The meteorite is monomict, and records a complex history of crustal formation and subsequent impacts and metamorphism on the Moon.

Its parent rock crystallization would have occurred in the lower half of the lunar crust according to classical models (e.g. Warren 1985), but could possibly have occurred nearer the surface under certain conditions (e.g. Arai *et al.,* 2008). If the latter did happen, then serial magmatism may explain the origin of magnesian anorthosite.

The data obtained in this study indicate that NWA 5744 likely originated in some other portion of the Moon than the region sampled by the Apollo and Luna landing sites as compositionally, it is distinct from samples obtained from these locales. The data are also consistent with a deep crustal origin for the igneous protolith of NWA 5744, and if that is the case then there is a strong likelihood that it was excavated by the SPA Basin

impact event or another major impact event away from the Apollo and Luna sites. However, an upper crustal origin through serial magmatic action cannot be ruled out, and would imply the Apollo and Luna landing sites are not representative of the average lunar crustal composition.

Metamorphism appears to have been intense but short-lived with a maximum time of 1000 years, almost certainly occurring near the lunar surface. Contact metamorphism from an igneous intrusion cannot be ruled out for the source of the heat that triggered NWA 5744 metamorphism. However, our observations are more consistent with a series of impacts beginning with one or more very large impacts to excavate the parent rock of NWA 5744 followed by relatively rapid dissipation of the heat away from the impact site that affected this stone. A relatively small impact melt sheet could have followed and serve as a heat source for the metamorphism, because a small volume of melt would have a low thermal inertia and cool quickly on the lunar surface.

The lunar meteorite NWA 5744 is a unique sample of lunar crust that may have been monomict prior to one or more brief metamorphic episodes, and we expect the complex history it records will continue to provide insight into the nature of the Moon and its processes through numerous and varied future studies.

2.6. Acknowledgements

We thank Dr. Tony Irving, curator of the meteorite type specimens archived at the University of Washington, Seattle, for providing the NWA 5744 sample. This research was supported by NASA grants NNX12AD06G, NNX10AB37G, and the Lunar Science Institute to AB, and The Leverhulme Trust grant 2011-569 to KHJ. We acknowledge the excellent resources of Randy Korotev's Lunar Meteorite List website and NASA's Lunar Meteorite Compendium. We are grateful to Kent Ross for help on the SEM.

Chapter 3: The Geochemistry and Implications of Lunar Granulites from Queen Alexandra Range 93069 and MacAlpine Hills 88105

3.1. Introduction

3.1.1. MacAlpine Hills 88104/5

MacAlpine Hills (MAC) 88105 is an anorthositic lunar meteorite that was recovered from Antarctica in 1989 along with paired stone MAC 88104 (Score and Mason, 1989; Lindstrom *et al.,* 1991a; Lindstrom *et al.,* 1991b). They are a polymict breccia with a mineralogical composition of mostly plagioclase along with some glass, olivine, pyroxene, and metallic grains (Lindstrom *et al,* 1991a), contained within anorthositic, granulitic, and impact melt clasts (Lindstrom *et al.,* 1991b). MAC 88105 has a bulk Mg# = 62.6 classifying it as ferroan, it is aluminous with 28.1% bulk Al_2O_3, and bulk siderophile element concentrations (14.6 and 148 ppm Co and Ni respectively) indicate the presence of impactor contamination (Lindstrom *et al.,* 1991b). Trace element content was originally found to lack a KREEP signature, suggesting MAC 88105 formed far away from the Apollo landing sites (Jolliff *et al.,* 1991; Neal *et al.,* 1991), but further study has shown that some portions of the meteorite do contain a KREEP component (Joy *et al.,* 2010) so a lunar nearside origin is likely. Most of the clasts that make up the breccia are of noritic anorthosite composition and have an affinity to the ferroan anorthosite suite (Jolliff *et al.,* 1991). Anorthositic and granulitic breccia clasts are present but much less common than impact melt clasts, and clasts of mare basalt

and regolith glasses are rarely present (Lindstrom *et al.,* 1991b). Granulite clasts account for 15.1% of the meteorite volume (Palme *et al.,* 1991). Impact melt clasts from a different section of MAC 88105 than that studied here dated impact events via ^{40}Ar-^{39}Ar which occurred at 3.35 ±0.37 Ga and 3.92 ±0.14 Ga (Cohen *et al.,* 2000).

There was debate regarding the place of origin for MAC 88105 following its original examinations. On one hand it was suggested to be a regolith breccia from near the lunar surface due to high Al_2O_3 content, presence of impact glass spherules and metal grains, and compositional similarity to Apollo 16 regolith breccias (Koeberl *et al.,* 1991; Jolliff *et al.,* 1991; Warren and Kallemeyn, 1991). On the other hand, MAC 88105 was deemed a fragmental breccia from deeper in the megaregolith because it contains abundant impact melt breccia clasts but very few regolith glass spherules, and did not find evidence that it was exposed to cosmic rays on the lunar surface (Lindstrom *et al.,* 1991b; Palme *et al.,* 1991). The matter was settled when the presence of solar wind noble gases was shown to indicate components of MAC 88104/5 must have spent several hundred million years in the upper few meters of the lunar regolith prior to brecciation (Eugster *et al.,* 1991), and therefore the meteorite is a regolith breccia.

Although most research on this meteorite has been focused on other components, some prior work has been done with granulite clasts. Neal *et al.,* (1991) and Warren and Kallemeyn (1991) each analyzed granulite clasts within MAC 88104/5 for major element content, and all clasts analyzed were noritic anorthosites. Warren

and Kallemeyn (1991) also measured the bulk trace element content of one granulite clast in MAC 88105.

3.1.2. Queen Alexandra Range 93069

Queen Alexandra Range (QUE) 93069 is a lunar meteorite that was recovered from Antarctica in 1994 (Satterwhite *et al.,* 1994). It is a polymict regolith breccia containing plagioclase grains, impact glass spherules and fragments, metallic iron, and granulite clasts, and in bulk is petrographically and chemically similar to MAC 88105 (Satterwhite *et al.,* 1994; Kring *et al.,* 1995; Lindstrom *et al.,* 1995; Bischoff 1996; Koeberl *et al.,* 1996). QUE 93069 has a bulk Mg# = ~70.0 which classifies the whole rock on the boundary between FAN and Mg-suite compositions (Kring *et al.,* 1995), and all plagioclase is anorthositic, falling with a narrow range of An 96-98 (Koeberl *et al.,* 1996). Pyroxene is the most common mafic mineral, followed by olivine (Koeberl *et al.,* 1996). Clasts of granulite and impact melt are much more common than igneous clasts (Lindstrom *et al.,* 1995; Bischoff, 1996). Granulites are common, representing 10.4% of the meteorite volume (Bischoff, 1996). Koeberl *et al.,* (1996) found QUE 93069 bulk REE abundance patterns to be similar to MAC 88105 and little or no KREEP signature (they found only one clast which bore an REE signature resembling Apollo 16 soils). Impact melt clasts from the same section of QUE 93069 studied here dated two impact events via ^{40}Ar-^{39}Ar which occurred at 3.00 ±0.47 Ga and 3.87 ±0.23 Ga (Cohen *et al.,* 2000).

QUE 93069 is strongly believed to be a mature regolith breccia from the lunar surface because it is composed mostly of fine melt rock fragments (Koeberl *et al.,* 1996), is has a strong ferromagnetic resonance (Lindstrom *et al.,* 1995), and is rich in glass fragments (3.5% by volume), most of which appear to be impact-related (Bischoff, 1996). The bulk rock also contains double the concentration of siderophile elements compared to MAC 88105 (Lindstrom *et al.,* 1995). Additionally, the abundance of cosmic ray-produced radionuclides and noble gases indicate QUE 93069 was exposed to cosmic rays at or near the lunar surface for at least several hundred million years prior to ejection (Nishiizumi *et al.,* 1996; Thalmann *et al.,* 1996).

3.2. Methods

For this study, we have focused on granulite clasts within thick sections MAC 88104,48 (Fig. 15), MAC 88105,158 (Fig. 16) and QUE 93069,52 (Fig. 17). Some impact melt clasts from MAC 88105,158 were extracted in a previous study by Cohen *et al.,* (2000) to perform ^{49}Ar-^{39}Ar age dating. Major element compositions of the different mineral phases within each granulite were acquired via i*n situ* EMP measurements for each granulite clast identified in each thick section, and LA-ICP-MS ablations were then performed on the granulites in the two thick sections. All analyses were performed according to the methods described in Chapter 1. One granulite clast in MAC 88104, two granulite clasts in MAC 88105, and 13 granulite clasts in QUE 93069 were analyzed. None of the granulite clasts analyzed in either meteorite were large enough to characterize optically.

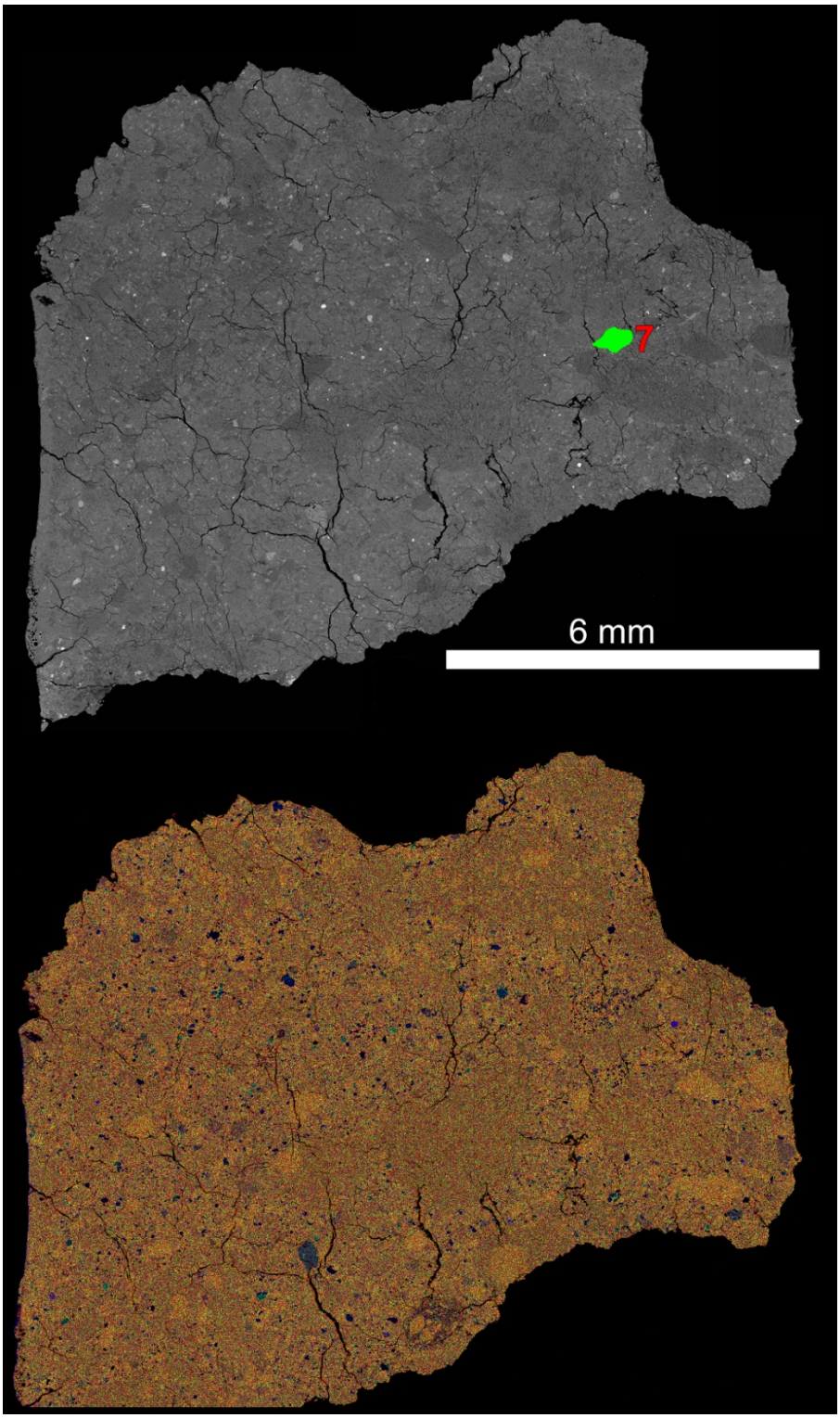

Figure 15: Top: BSE image of thick section MAC 88104,48 with the location of granulite Clast 7 shown in green. Bottom: EDS elemental map of MAC 88104,48 with aluminum in red, calcium in green, and silicon in blue.

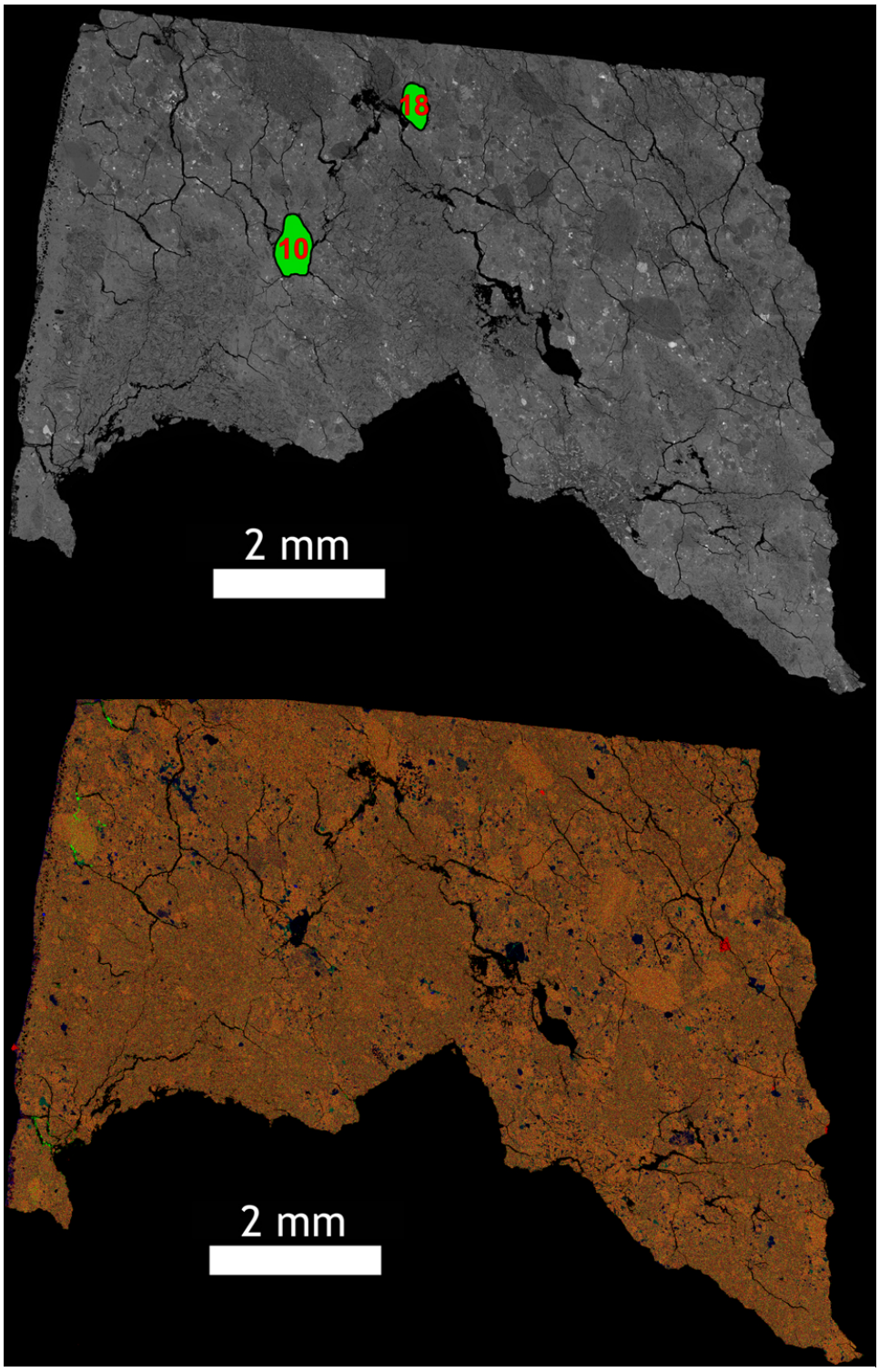

Figure 16: Top: BSE image of thick section MAC 88105,158. Bottom: Elemental map of thick section MAC 88105,158 where aluminum is shown in red, calcium is shown in green, and silicon is shown in blue.

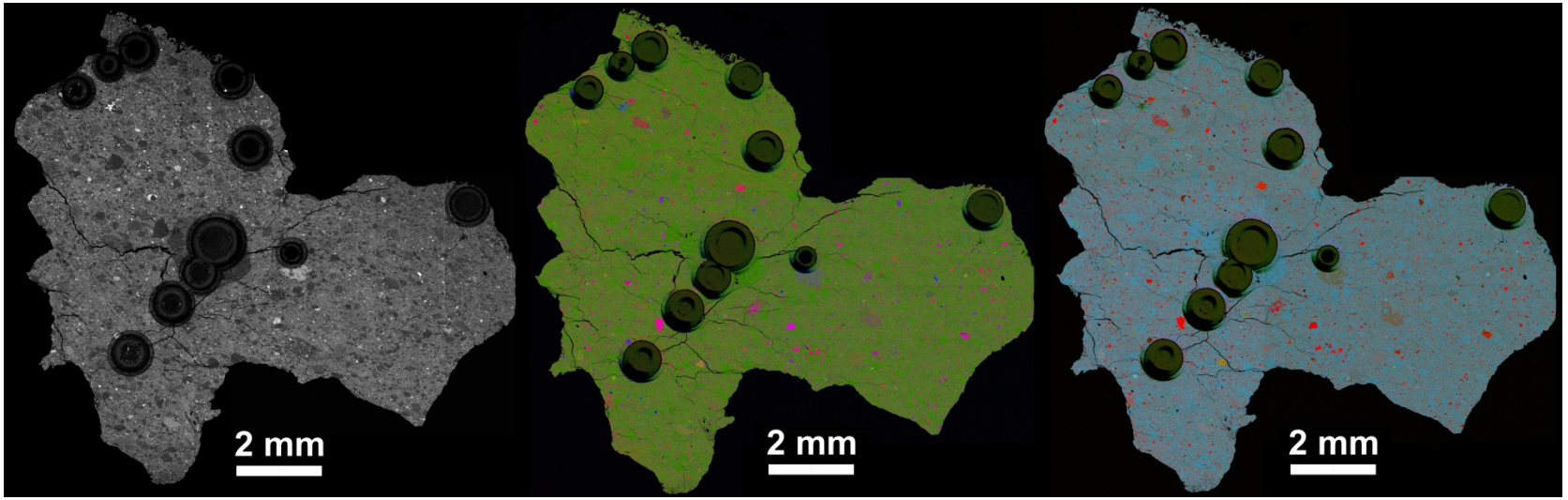

Figure 17: Left: BSE image of thick section QUE 93069,52. Center: Elemental map of QUE 93069,52 where magnesium, calcium, and iron are respectively shown in red, green, and blue. Right: Elemental map of QUE 93069,52 where magnesium, calcium, and aluminum are respectively shown in red, green, and blue.

3.3. Results

3.3.1. MAC 88104/5

Plagioclase An content vs. olivine Mg# for each clast is plotted in Figure 18, and pyroxene compositions are plotted in Figure 19.

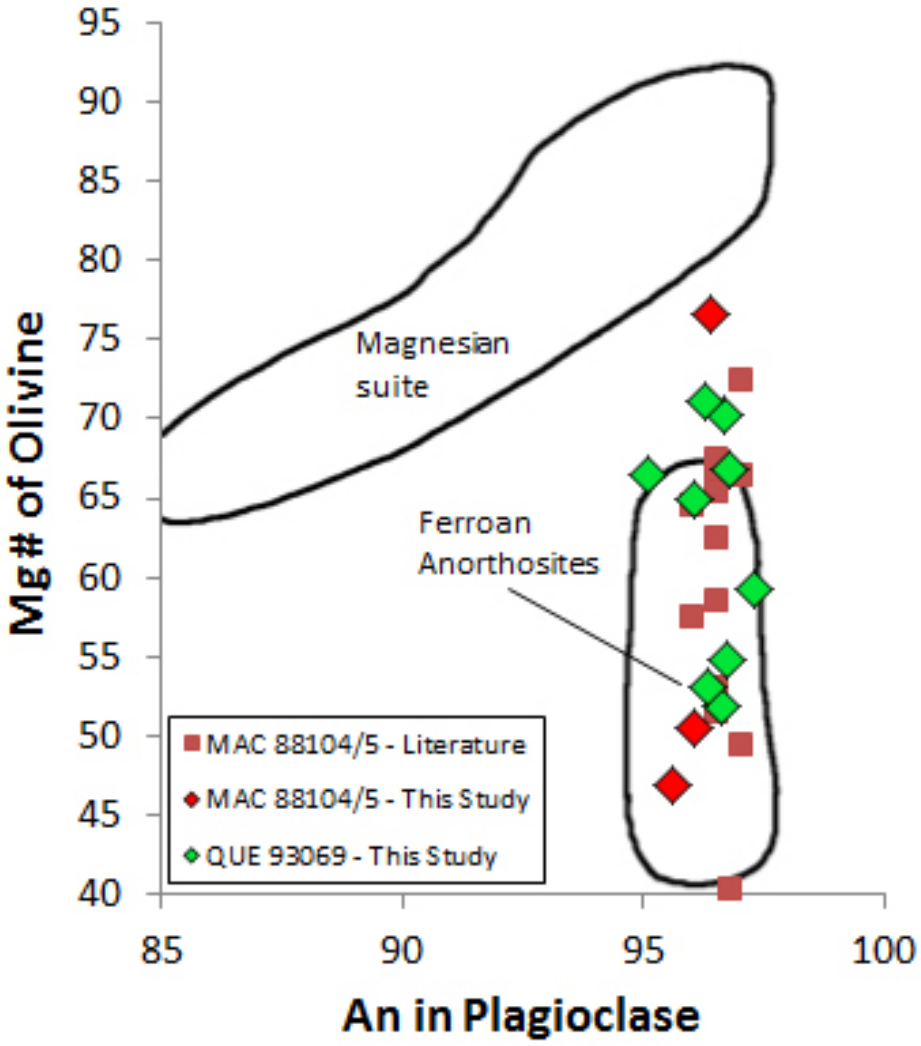

Figure 18: Plot of plagioclase anorthite content against Mg# of olivine for each granulite clast analyzed. MAC88104 and 88105 granulite clasts are shown in red diamonds, compared to other granulite clasts from 88104/5 analyzed in the literature in red squares (Neal *et al.,* 1991; Warren and Kallemeyn, 1991). QUE 93069 granulite clasts are plotted as green diamonds. Fields reproduced from Goodrich *et al.,* (1984) and Treiman *et al.,* (2010).

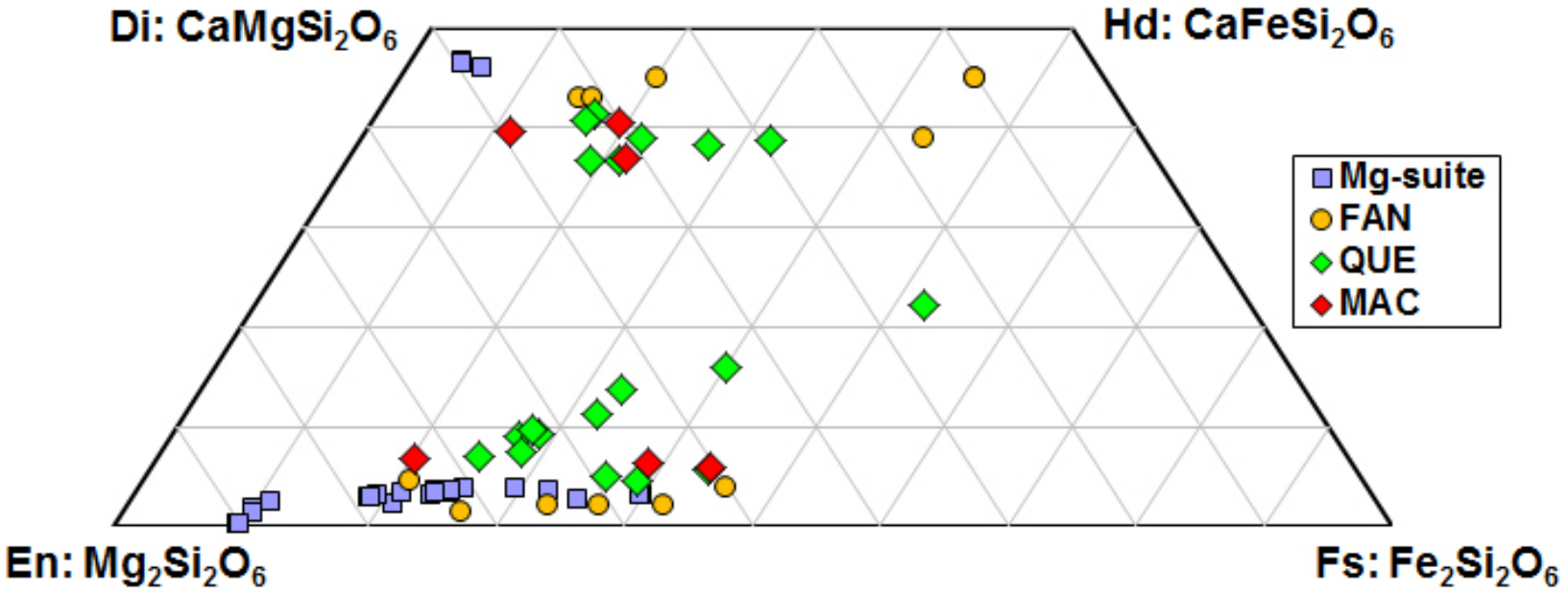

Figure 19: Plot of the composition of pyroxenes found in MAC 88104/5 granulite clasts in red, and QUE 93069,52 granulite clasts in green, compared with pyroxene from FAN and Mg-suites (Papike *et al.,* 1994; Floss *et al.,* 1998; Shervais and McGee, 1999).

3.3.1.1. MAC 88104 Clast 7

Clast 7 (Fig. 20) is a rounded noritic granoblastic granulite clast (0.4 x 0.55 mm) composed of a fractured plagioclase matrix ($An_{95.5-96.4}$, five analyses) encompassing grains of pigeonite (Mg# 58.2-59.4, $En_{54.1-55.9}Fs_{37.2-39.8}Wo_{4.2-8.4}$, four analyses), augite (Mg# 65.2-66.3, $En_{41.4-41.5}Fs_{22.1}Wo_{36.5-37.4}$, two analyses) and olivine ($Fo_{50.0-50.9}$, four analyses). No other minerals were identified in the clast. Major element compositions are given in Table 6.

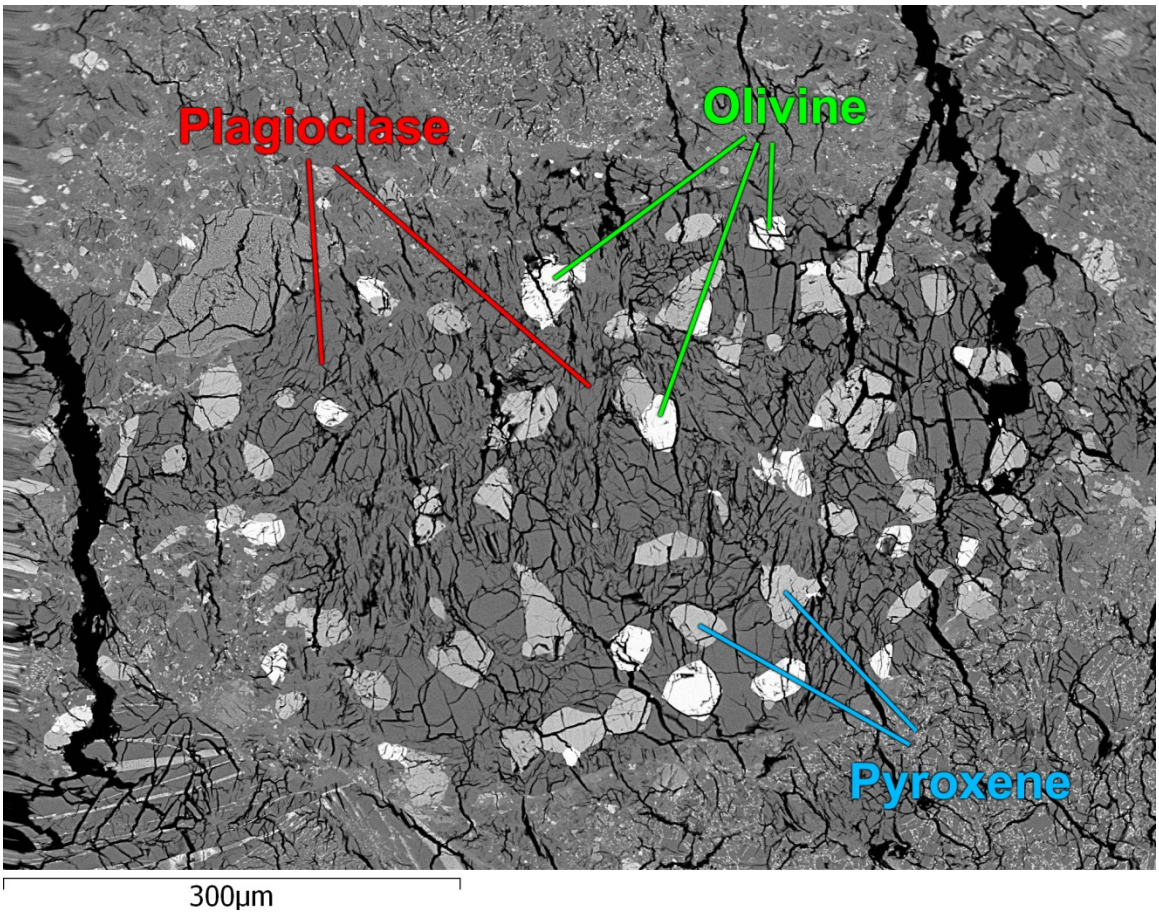

Figure 20: BSE image of granulite Clast 7 in MAC 88104,48 containing plagioclase, pyroxene, and olivine.

Table 6: Major element composition of minerals in MAC 88104,48 Clast 7

	OPX	1σ	CPX	1σ	Plag	1σ	Olv	1σ
Analyses	4		2		5		4	
SiO_2 (wt %)	50.85	0.24	50.33	0.25	43.13	0.23	34.35	0.24
Al_2O_3	0.51	0.04	1.64	0.06	34.73	0.31	0.03	0.02
FeO	23.85	0.62	13.16	0.45	0.25	0.07	40.89	0.71
MgO	19.03	0.22	14.17	0.19	0.05	0.02	23.38	0.27
CaO	3.00	0.13	17.58	0.34	19.32	0.28	0.19	0.03
Na_2O	b.d.	-	0.04	0.04	0.43	0.06	b.d.	-
TiO_2	0.41	0.05	1.09	0.07	b.d.	-	0.05	0.03
Cr_2O_3	0.17	0.05	0.46	0.08	b.d.	-	b.d.	-
MnO	0.43	0.07	0.29	0.07	b.d.	-	0.42	0.07
Total	98.25		98.77		97.91		99.31	
An					96.0			
Mg#	58.7		65.8		26.5		50.5	
En	55.0		41.4					
Fs	38.7		21.6					
Wo	6.2		37.0					

3.3.1.2. MAC 88105 Clast 10

Clast 10 (Fig. 21) is an elongate rounded troctolitic clast (0.5 x 0.9 mm) dominated by plagioclase ($An_{95.0\text{-}96.0,}$ nine analyses) and a single coarse olivine grain ($Fo_{46.8\text{-}47.1}$, three analyses) which accounts for approximately one third of the clast volume. Also present are pyroxenes composed of augite (Mg# 66.5-68.3, $_{En40.0\text{-}40.3}Fs_{18.6\text{-}20.4}Wo_{39.3\text{-}41.4}$, three analyses) with pigeonite lamellae (Mg# 52.8, $En_{51.5}Fs_{46.2}Wo_{2.4}$, one analysis) (Fig. 22). Two grains of iron-nickel metal were present, but I was unable to acquire an EMP measurement on either of them where weight percents totaled 100 ±2.5%. The clast is heavily fractured. Major element compositions are given in Table 7.

Due to the coarse-grained texture of Clast 10 with well-developed pyroxene exsolution lamellae, which differ from the other granulites studied, it may actually be a

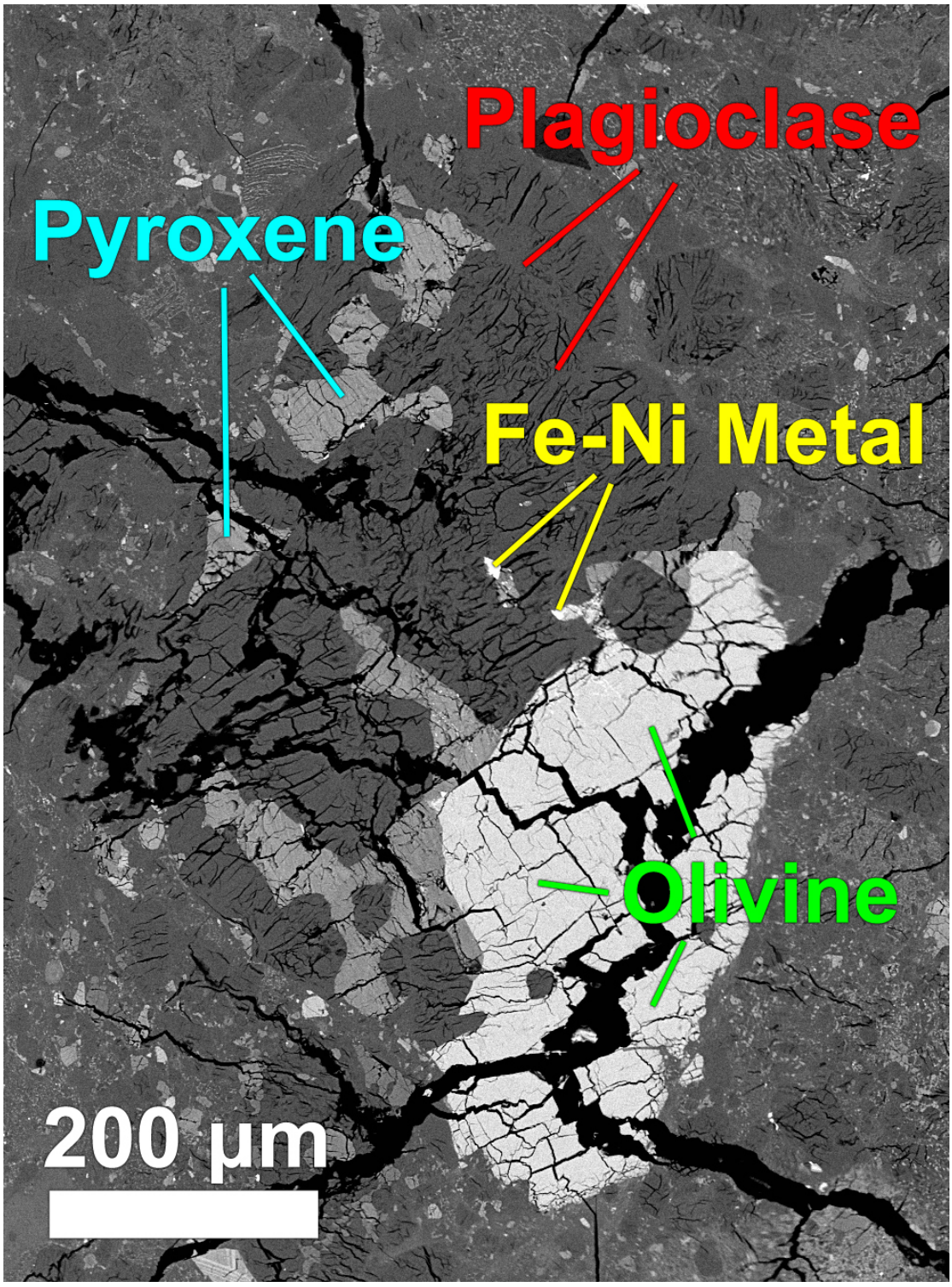

Figure 21: BSE image of granulite clast 10 in MAC 88105,158, containing plagioclase, pyroxene, olivine, and traces of iron-nickel metal.

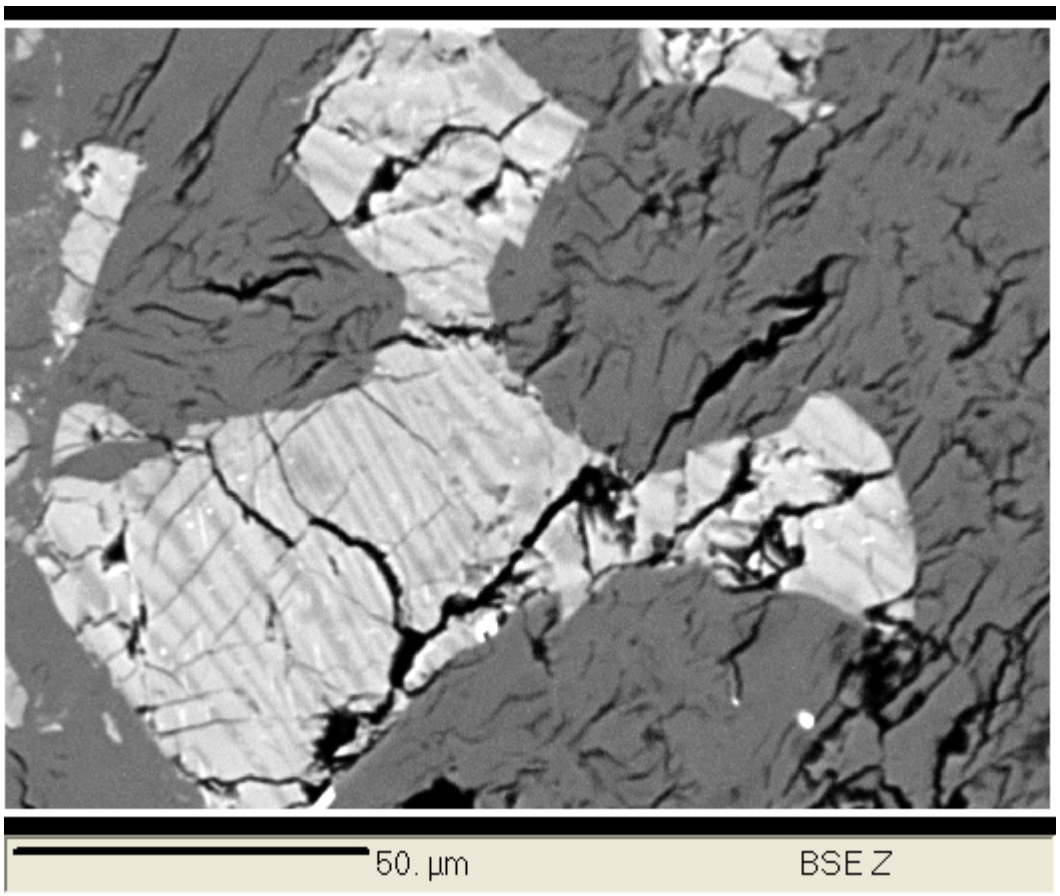

Figure 22: BSE image of a pyroxene grain in Clast 10 of MAC 88105,158, surrounded by plagioclase. The pyroxene is primarily composed of light-colored augite with darker semi-parallel lamellae of pigeonite.

Table 7a: Major element composition of MAC 88105,158 Clast 10 minerals

	OPX	1σ	CPX	1σ	Plag	1σ	Olv	1σ
Points	3		3		9		15	
SiO_2 (wt %)	49.65	0.36	49.79	0.36	43.69	0.21	32.32	0.24
Al_2O_3	0.50	0.02	1.81	0.04	34.97	0.28	0.03	0.01
FeO	27.22	0.65	11.95	0.34	0.55	0.07	44.01	0.62
MgO	17.60	0.27	13.83	0.21	0.04	0.01	21.85	0.16
CaO	2.84	0.09	19.41	0.27	19.09	0.32	0.05	0.02
Na_2O	b.d.	-	0.03	0.03	0.49	0.04	b.d.	-
TiO_2	0.39	0.04	0.97	0.05	0.03	0.02	0.04	0.02
Cr_2O_3	0.12	0.04	0.35	0.04	b.d.	-	b.d.	-
MnO	0.47	0.06	0.24	0.06	b.d.	-	0.49	0.07
SO_2	0.08	0.03	b.d.	-	b.d.	-	0.03	0.02
Total	98.89		98.38		98.85		98.82	
An					95.6			
Mg#	53.6		67.4		10.7		46.9	
En	50.4		40.1					
Fs	43.7		19.4					
Wo	5.8		40.5					

Table 7b: Trace element composition of individual minerals and bulk granulite Clast 10 in MAC 88105,158

	BIR Ref	BIR Avg	%RSD	Plag 1	1σ error	Plag 2	1σ error	Plag 3	1σ error	Plag 4	1σ error	Plag 5	1σ error
Spot (μm)				30		30		84		84		84	
Co (ppm)	52.5	55.62	2.37	b.d.	-	1.77	0.41	0.30	0.07	0.75	0.17	1.09	0.25
Ni	179	166.90	5.73	b.d.	-	b.d.	-	b.d.	-	10.50	3.63	b.d.	-
Cu	121	125.57	3.20	b.d.	-	b.d.	-	b.d.	-	0.52	0.20	0.47	0.19
Ga	14	16.28	3.59	2.41	0.95	2.16	0.88	3.46	1.16	3.99	1.34	3.53	1.18
Sr	112	112.44	3.06	214.19	34.29	209.22	33.41	214.32	34.60	207.70	33.68	203.81	33.20
Y	15.8	14.99	5.11	0.54	0.10	0.85	0.14	0.68	0.08	2.04	0.23	2.39	0.28
Zr	15.3	14.76	4.71	0.72	0.26	2.45	0.43	0.48	0.07	4.26	0.52	4.10	0.51
Nb	0.564	0.547	8.301	b.d.	-	0.224	0.087	b.d.	-	0.105	0.021	0.040	0.014
Ba	6.6	7.00	10.72	31.02	6.01	29.75	5.74	31.49	6.06	28.08	5.39	30.66	5.86
La	0.623	0.591	6.203	1.144	0.200	1.187	0.210	1.077	0.180	1.164	0.200	1.165	0.200
Ce	1.93	1.977	6.213	2.147	0.330	2.462	0.380	2.264	0.370	2.415	0.400	2.405	0.400
Pr	0.381	0.375	4.280	0.276	0.056	0.303	0.062	0.290	0.053	0.298	0.055	0.329	0.061
Nd	2.49	2.363	5.411	0.961	0.160	1.228	0.200	1.172	0.160	1.223	0.170	1.415	0.190
Sm	1.14	1.121	11.988	b.d.	-	b.d.	-	0.219	0.036	0.294	0.045	0.340	0.051
Eu	0.537	0.521	5.484	1.132	0.180	1.094	0.180	1.142	0.180	1.134	0.180	1.115	0.170
Gd	1.91	1.753	5.445	b.d.	-	b.d.	-	0.226	0.032	0.343	0.044	0.404	0.051
Tb	0.369	0.341	4.442	b.d.	-	0.027	0.013	0.027	0.005	0.052	0.008	0.059	0.009
Dy	2.73	2.481	6.338	b.d.	-	0.199	0.073	0.079	0.019	0.343	0.051	0.517	0.073
Ho	0.599	0.554	4.675	0.040	0.014	0.044	0.014	0.024	0.004	0.077	0.011	0.084	0.011
Er	1.79	1.632	7.473	0.162	0.064	b.d.	-	0.058	0.014	0.198	0.030	0.269	0.038
Tm	0.26	0.253	8.587	b.d.	-	b.d.	-	0.010	0.003	0.029	0.006	0.037	0.007
Yb	1.79	1.671	6.968	b.d.	-	b.d.	-	0.040	0.013	0.181	0.032	0.246	0.039
Lu	0.27	0.245	7.292	b.d.	-	b.d.	-	0.005	0.002	0.018	0.004	0.025	0.005
Hf	0.609	0.561	5.558	b.d.	-	b.d.	-	0.015	0.007	0.093	0.017	0.140	0.022
Ta	0.038	0.035	21.471	b.d.	-	b.d.	-	b.d.	-	b.d.	-	b.d.	-
Th	0.03	0.029	15.826	b.d.	-	b.d.	-	0.004	0.002	0.042	0.008	0.017	0.004
U	0.016	0.016	11.726	b.d.	-	0.031	0.014	0.002	0.001	0.013	0.004	0.004	0.002

Table 7b, ctd

	Pyx 1	1σ error	Pyx 2	1σ error	Pyx 3	1σ error	Olv 1	1σ error	Olv 2	1σ error	Bulk	1σ error
Spot (μm)	30		30		30		84		84		176 x5	
Co (ppm)	26.78	2.38	27.48	2.43	26.42	2.33	88.92	8.56	81.75	7.94	46.52	12.82
Ni	b.d.	-	36.68	10.36	24.99	9.97	74.06	9.35	64.63	8.24	270.55	89.73
Cu	3.50	0.65	5.05	0.79	5.74	0.85	9.60	1.16	5.25	0.65	18.04	5.80
Ga	0.90	0.26	1.24	0.30	0.87	0.27	b.d.	-	0.35	0.07	2.91	1.19
Sr	2.67	0.31	5.33	0.60	4.15	0.47	1.73	0.19	2.53	0.29	138.80	27.36
Y	45.59	6.83	39.54	5.95	42.46	6.41	2.25	0.33	2.21	0.32	10.06	1.38
Zr	84.89	14.13	63.39	10.63	68.01	11.48	0.56	0.09	0.35	0.06	17.76	2.58
Nb	0.259	0.046	0.345	0.057	0.191	0.046	b.d.	-	b.d.	-	0.363	0.075
Ba	0.18	0.09	0.75	0.14	0.99	0.15	0.36	0.04	0.44	0.05	22.66	5.65
La	1.286	0.120	1.325	0.120	1.343	0.130	0.356	0.033	0.286	0.027	1.780	0.374
Ce	5.400	0.530	4.350	0.420	4.633	0.450	0.093	0.010	0.136	0.015	3.960	0.801
Pr	1.111	0.093	1.020	0.087	0.949	0.081	0.118	0.010	0.101	0.009	0.718	0.164
Nd	6.903	0.720	6.113	0.640	6.359	0.660	0.527	0.057	0.408	0.045	3.479	0.553
Sm	3.019	0.390	2.461	0.330	2.411	0.320	0.117	0.017	0.106	0.016	1.068	0.171
Eu	0.048	0.013	0.067	0.017	0.087	0.019	0.030	0.004	0.035	0.005	0.768	0.150
Gd	4.733	0.66	4.156	0.58	4.495	0.62	0.157	0.024	0.136	0.022	1.443	0.196
Tb	0.990	0.13	0.901	0.12	0.967	0.13	0.024	0.004	0.022	0.004	0.251	0.038
Dy	7.438	1.07	6.143	0.90	7.064	1.03	0.252	0.039	0.202	0.032	1.763	0.270
Ho	1.801	0.24	1.442	0.19	1.729	0.23	0.070	0.010	0.075	0.011	0.376	0.053
Er	5.150	0.72	4.459	0.64	5.091	0.73	0.334	0.047	0.378	0.053	1.113	0.153
Tm	0.812	0.130	0.731	0.120	0.787	0.120	0.081	0.013	0.093	0.015	0.164	0.029
Yb	4.656	0.720	4.645	0.720	4.808	0.730	0.709	0.100	0.798	0.120	1.187	0.198
Lu	0.829	0.13	0.754	0.12	0.783	0.12	0.183	0.029	0.172	0.027	0.167	0.031
Hf	2.927	0.41	2.425	0.34	2.598	0.37	0.022	0.007	0.010	0.005	0.573	0.082
Ta	b.d.	-	b.d.	-	b.d.	-	b.d.	-	b.d.	-	0.013	0.003
Th	0.052	0.01	0.125	0.02	0.096	0.02	b.d.	-	b.d.	-	0.084	0.015
U	0.029	0.01	0.039	0.01	0.033	0.01	0.007	0.002	0.004	0.001	0.023	0.008

clast of an igneous lithology rather than a granulite. However, the shape of the pyroxene grains and the plagioclase around them resemble that of other granoblastic granulites analyzed, and the grain sizes within the clast were large enough for *in situ* laser ablation, so the clast was included in the study. If it is a granulite, the grain sizes might indicate the source material prior to metamorphism was coarser grained than that of the other granulites analyzed here.

Trace element content was measured *in situ* for plagioclase, olivine, and pyroxene via laser ablation on each mineral type (Fig. 23). Plagioclase has a characteristic positive Eu anomaly, and pyroxene has a similar negative anomaly. Olivine has a small negative Eu anomaly but a very large negative Ce anomaly. Cerium can occur in both 3+ and 4+ valence states, and Ce^{4+} is compatible in zircon (Thomas *et al.,* 2003). Therefore, the negative Ce anomaly could be explained if Clast 10 represents a source lithology that is relatively rich in zircon. After the *in situ* measurements, bulk trace element content was measured (Fig. 23) by fully ablating as much of the entire clast as possible. Bulk REE content is roughly 10x chondritic. All trace element data is presented in Table 8.

Plagioclase LREE content falls within the FAN suite range, although the concentrations of HREE elements are at the upper end seen in FAN material and becoming a better fit with the Mg-suite. However, pyroxene REE content is clearly a good fit within the range of compositions seen in FAN clinopyroxene. Overall the REE content of Clast 10 minerals appears to fit the FAN suite better than the Mg-suite.

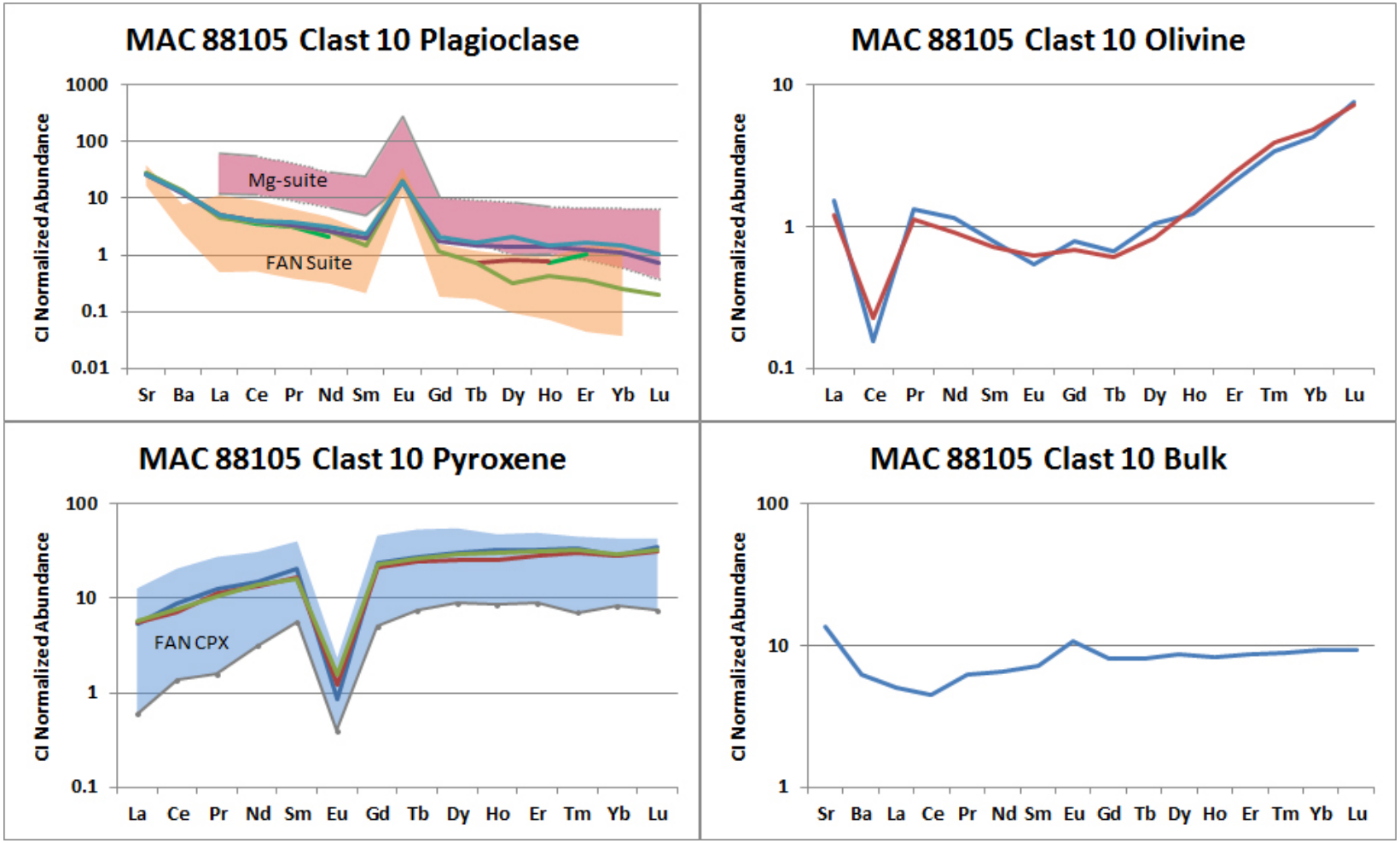

Figure 23: Trace element diagrams for MAC 88105,158 Clast 10 plagioclase (five analyses), olivine (two analyses), pyroxene (three analyses), and bulk (average of five ablations, together covering the entire clast).

3.3.1.3. Clast 18

Clast 18 (Fig. 24) is a granoblastic troctolitic granulite clast (0.4 x 0.6 mm) dominated by a plagioclase matrix ($An_{95.6\text{-}97.1,}$ twelve analyses) and rounded amoeboid olivine grains ($Fo_{46.8\text{-}47.1}$, three analyses). Two pigeonite grains were also present (Mg# 76.2-79.4, $En_{69.7\text{-}75.6}Fs_{18.9\text{-}21.9}Wo_{4.6\text{-}9.6}$, nine analyses), and one pyroxene grain (Fig. 25) also contained both pigeonite and augite (Mg# 80.9-81.9, $En_{48.5\text{-}50.1}Fs_{10.8\text{-}11.9}Wo_{38.0\text{-}40.6}$, three analyses). Major element composition of the plagioclase, olivine, and pyroxene is given in Table 8a.

Table 8a: Major element compositions of principle minerals in Clast 18 of MAC 88105,158

	Plag	1σ	Olv	1σ	CPX	1σ	OPX	1σ
Points	12		17		9		12	
SiO_2 (wt %)	43.64	0.21	37.34	0.37	49.63	0.29	52.63	0.27
Al_2O_3	34.82	0.28	0.06	0.01	2.71	0.05	1.38	0.03
FeO	0.35	0.06	21.61	0.36	7.00	0.23	13.17	0.36
MgO	0.14	0.02	39.67	0.25	17.01	0.26	26.55	0.39
CaO	19.30	0.33	0.18	0.03	19.06	0.27	3.43	0.10
Na_2O	0.38	0.04	b.d.	-	0.06	0.03	b.d.	-
K_2O	0.03	0.02	b.d.	-	b.d.	-	b.d.	-
TiO_2	0.04	0.02	0.05	0.02	2.13	0.07	0.85	0.05
Cr_2O_3	b.d.	-	0.09	0.03	0.82	0.05	0.50	0.05
MnO	b.d.	-	0.27	0.06	0.18	0.05	0.29	0.06
SO_2	b.d.	-	0.02	0.02	0.04	0.03	0.25	0.04
CoO	b.d.	-	0.01	0.001	b.d.	-	b.d.	-
Total	98.71		99.31		98.64		99.05	
An	96.4							
Mg#	41.8		76.6		81.3		78.2	
En					49.1		72.9	
Fs					11.3		20.3	
Wo					39.6		6.8	

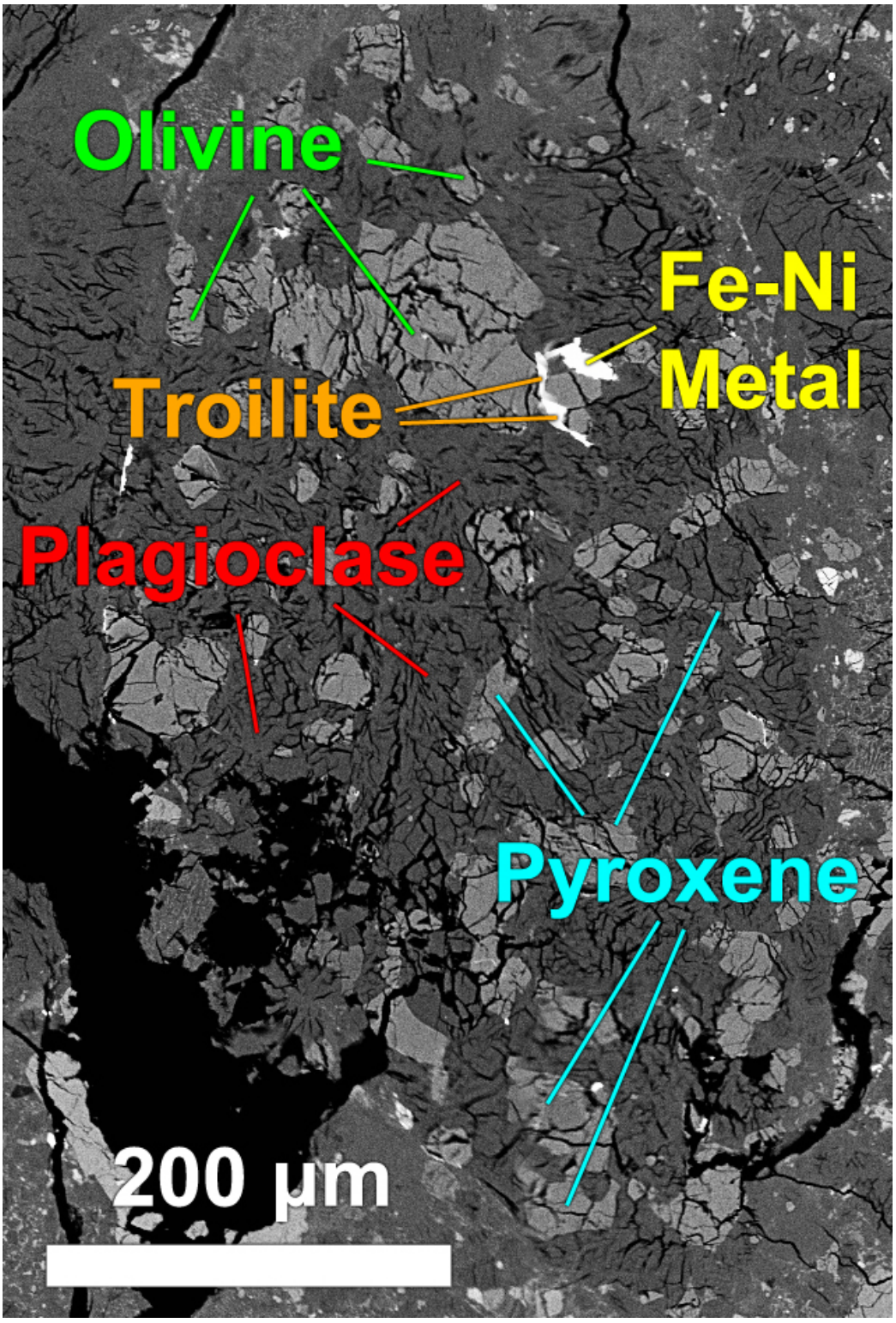

Figure 24: BSE image of granulite Clast 18 in MAC 88105,158 containing plagioclase, olivine, pyroxene, and traces of troilite and iron-nickel metal.

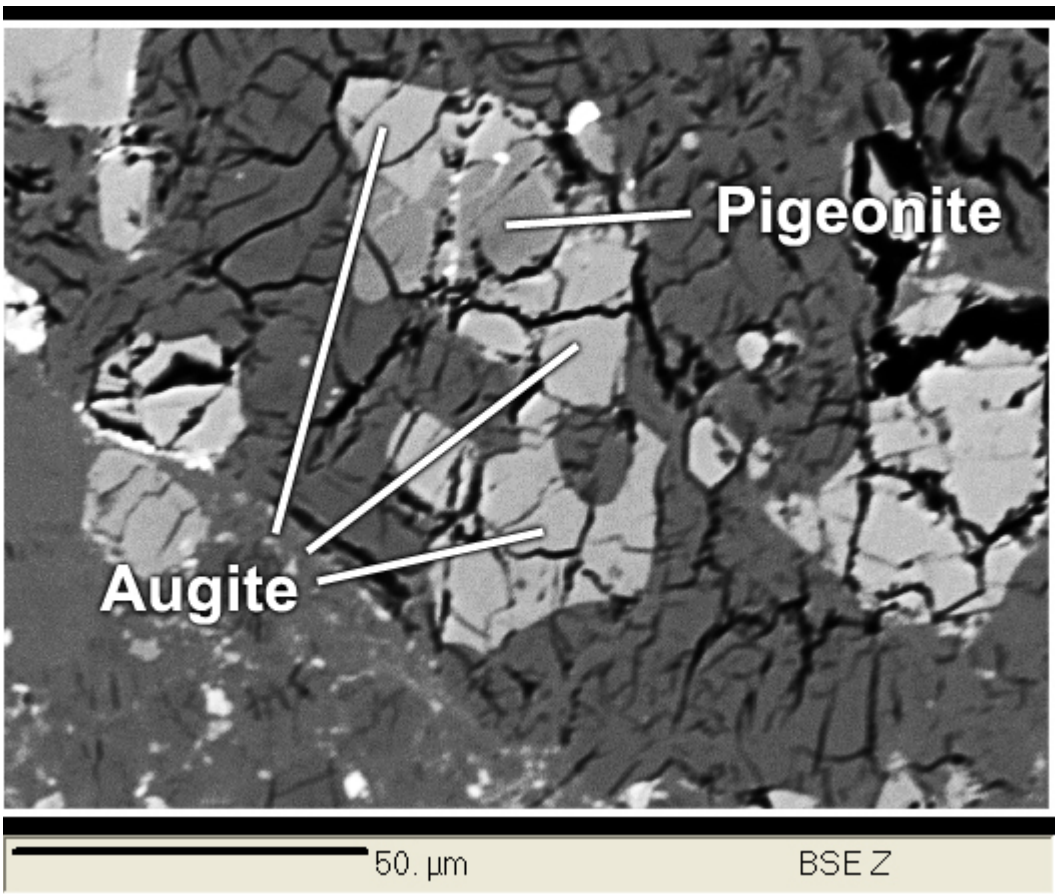

Figure 25: BSE image of dual pyroxene grain in MAC 88105,158 Clast 18 containing both augite and pigeonite, but no lamellae.

Single grains of troilite and nickel-iron metal were also present in Clast 18. Major element composition of the troilite is given in Table 8b, but we were unable to acquire an EMP measurement on the Fe-Ni metal with weight percent = 100 ±2.5.

Table 8b: Major element composition of troilite in Clast 18, MAC 88105,158, one EMP analysis

	Si	Fe	Mg	Ca	Ni	Co	S	Total
wt %	0.10	62.11	0.03	0.17	0.47	0.22	36.32	99.42
1σ	0.02	1.97	0.02	0.03	0.09	0.07	0.68	

The mafic grains in Clast 18 were too small to target *in situ* via LA-ICP-MS, and were too evenly distributed throughout the plagioclase matrix to *in situ* target the plagioclase. Bulk trace element content was measured by ablating as much of the clast as possible and averaging the results together, however the result has erroneous-looking swings in concentration between elements for multiple orders of magnitude, possibly due to ablating some of the mounting epoxy or other material from beyond the edge of the clast. Regardless, the trace element data for this clast was assumed to be contaminated and was therefore not used in this study.

3.3.2. QUE 93069

All major and trace element data for each granulite clast analyzed in QUE 93069,58 is presented in Appendix B. Plagioclase An content vs. olivine Mg# for each clast is plotted in Figure 18, and pyroxene compositions are plotted in Figure 19. Bulk REE content for all QUE 93069 granulite clasts analyzed here is plotted in Figure 26.

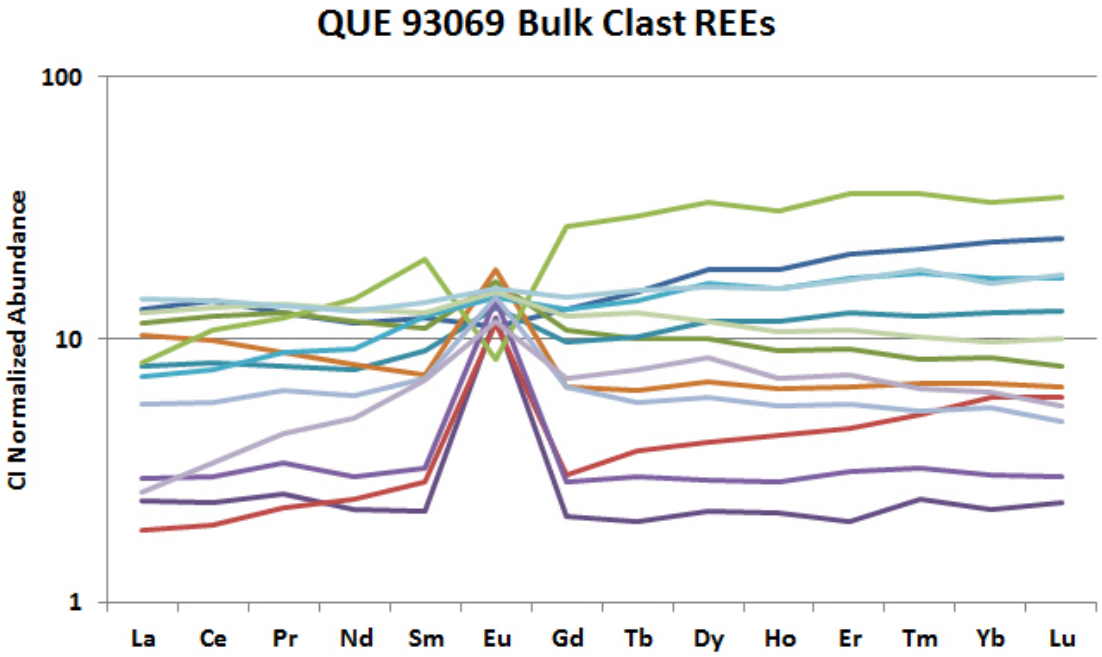

Figure 26: Diagram of the REE profiles of all 13 clasts analyzed via LA-ICP-MS in QUE 93069,52. These clasts exhibit a wide variety of bulk REE concentrations.

3.3.2.1. Clast 1

Clast 1 (Fig. 27) is an elongated granoblastic granulite clast (0.2 x 0.6 mm) composed of plagioclase (An96.5-97.1, three analyses), olivine (Fo66.7-67.2, three analyses), and pyroxene (Mg# 69.0-69.2, $En_{62.2-62.5}Fs_{27.7-28.1}Wo_{9.3-10.0}$, two analyses). One grain each of ilmenite and Ti-chromite were present in Clast 1. All olivine grains is

concentrated near the center of the clast and is the matrix surrounding rounded plagioclase grains. All pyroxene grains are located at the two ends of the clast, occur with rounded to elongated amoeboid texture, and are surrounded by a plagioclase matrix. The clast has several fractures running through it that tend to follow grain boundaries within the clast.

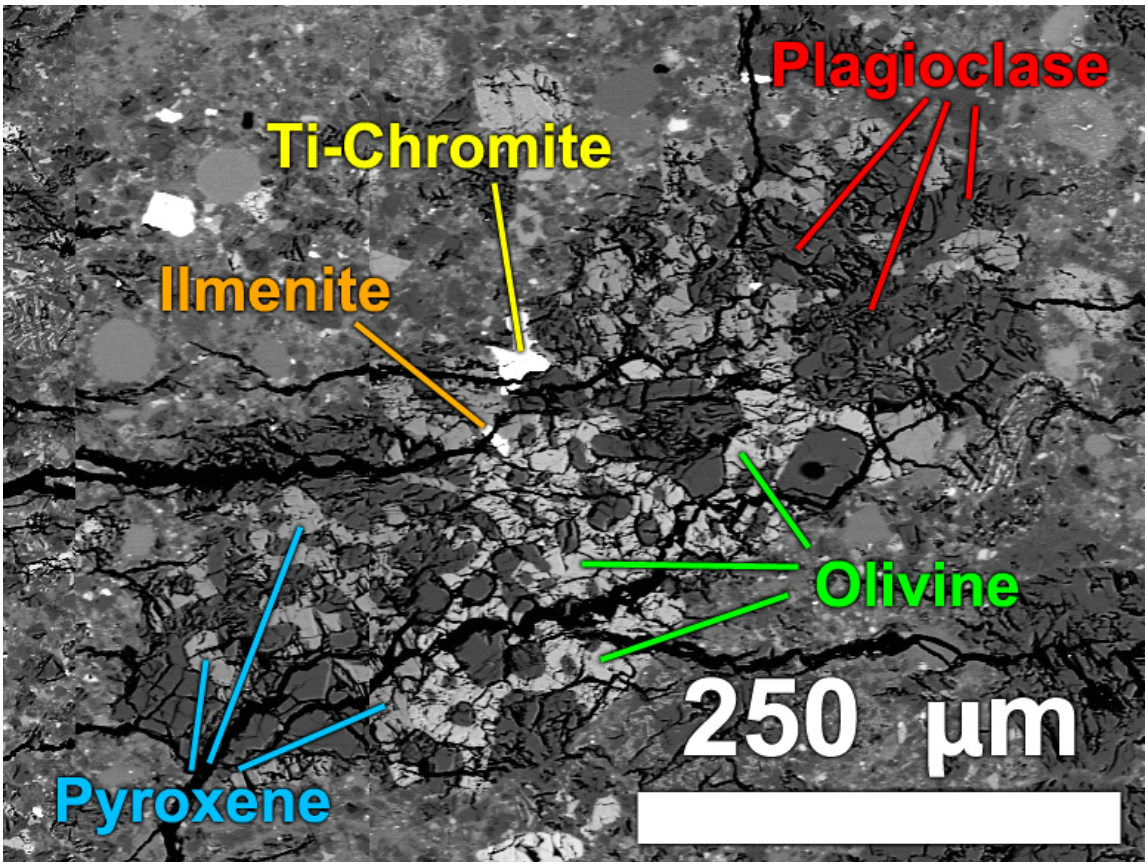

Figure 27: BSE image of granulite Clast 1 in QUE 93069,58 containing plagioclase, olivine, pyroxene, ilmenite, and titanium chromite.

3.3.2.2. Clast 2

Clast 2 (Fig. 28) is a rounded noritic granulite clast (0.15 x 0.2 mm) dominated by pigeonite (Mg# 68.0-68.8, $En_{62.0-62.1}Fs_{28.2-29.3}Wo_{8.7-9.7}$, two analyses) in a plagioclase matrix ($An_{95.5-96.5}$, three analyses). Some olivine is also present ($Fo_{64.7-65.1}$, four analyses), as well as several grains of ilmenite and nickel-iron metal, and one grain each of troilite and chromite. The amounts of olivine and pyroxene in the clast are similar.

On one end of Clast 2 is a large pyroxene (Fig. 29) composed of pigeonite with augite lamellae (Mg# 46.7-48.4, $En_{29.0-29.5}Fs_{31.0-33.7}Wo_{36.8-40.0}$, three analyses). The pigeonite had a different composition than that is the rest of the clast, but all EMP measurements of this pigeonite resulted in unacceptable cation sums after stoichiometric analysis.

Ni-Fe metal, troilite, and chromite in Clast 2 were identified by EDS spectral analysis, but acceptable weight percent totals and/or cation totals were unable to be acquired, presumably due to the size and/or shape of the grains.

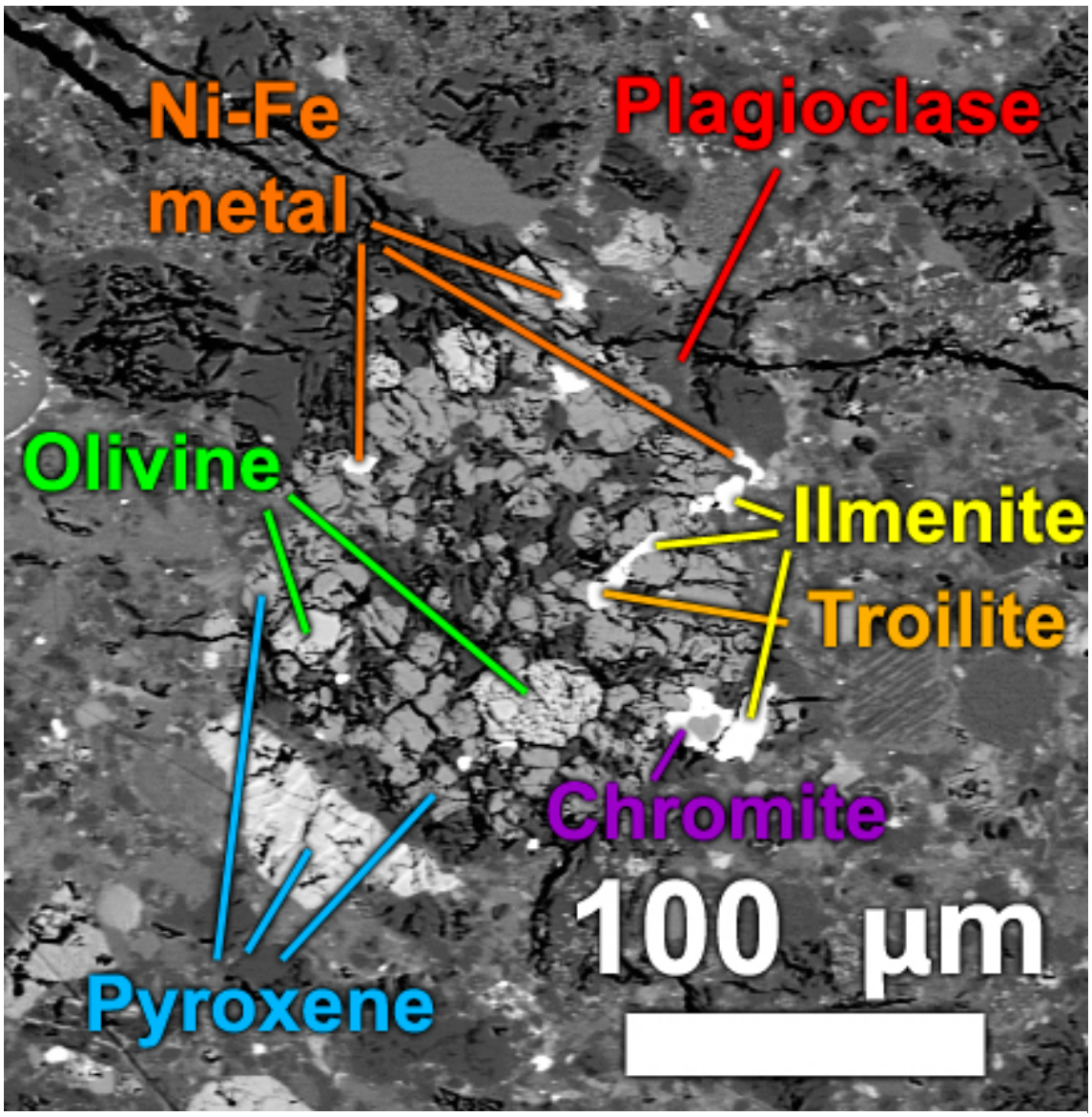

Figure 28: BSE image of Granulite Clast 2 in QUE 93069,58 containing pyroxene, plagioclase, olivine, ilmenite, nickel-iron metal, troilite, and chromite.

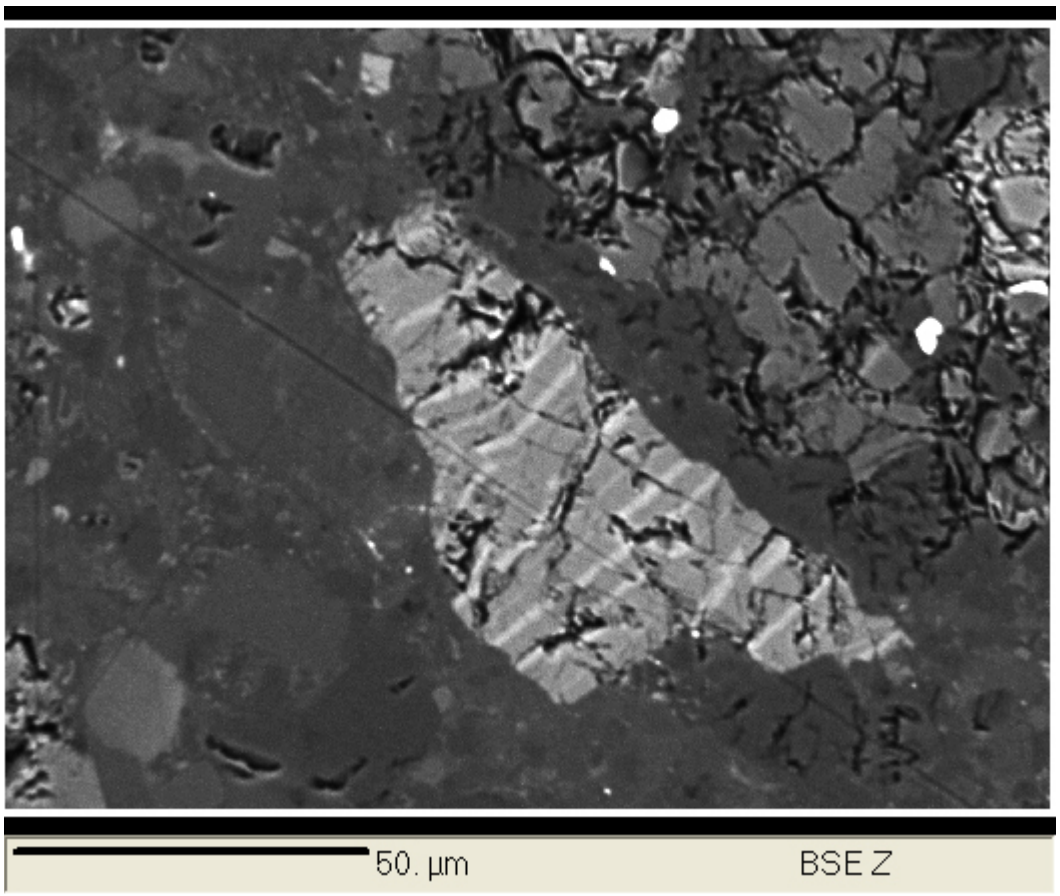

Figure 29: BSE image of the dual pyroxene attached to the end of Clast 2, composed of pigeonite with augite lamellae.

3.3.2.3. Clast 3

Clast 3 (Fig. 30) is an irregularly-shaped noritic granoblastic granulite clast (0.1 x 0.25 mm) dominated by highly fractured plagioclase ($An_{96.4-97.0}$, three analyses) with rounded amoeboidal olivine ($Fo_{50.6-53.0}$, two analyses) and augite (Mg# 70.9, $En_{41.5}Fs_{17.1}Wo_{41.4}$, one analysis) dispersed evenly throughout the plagioclase matrix.

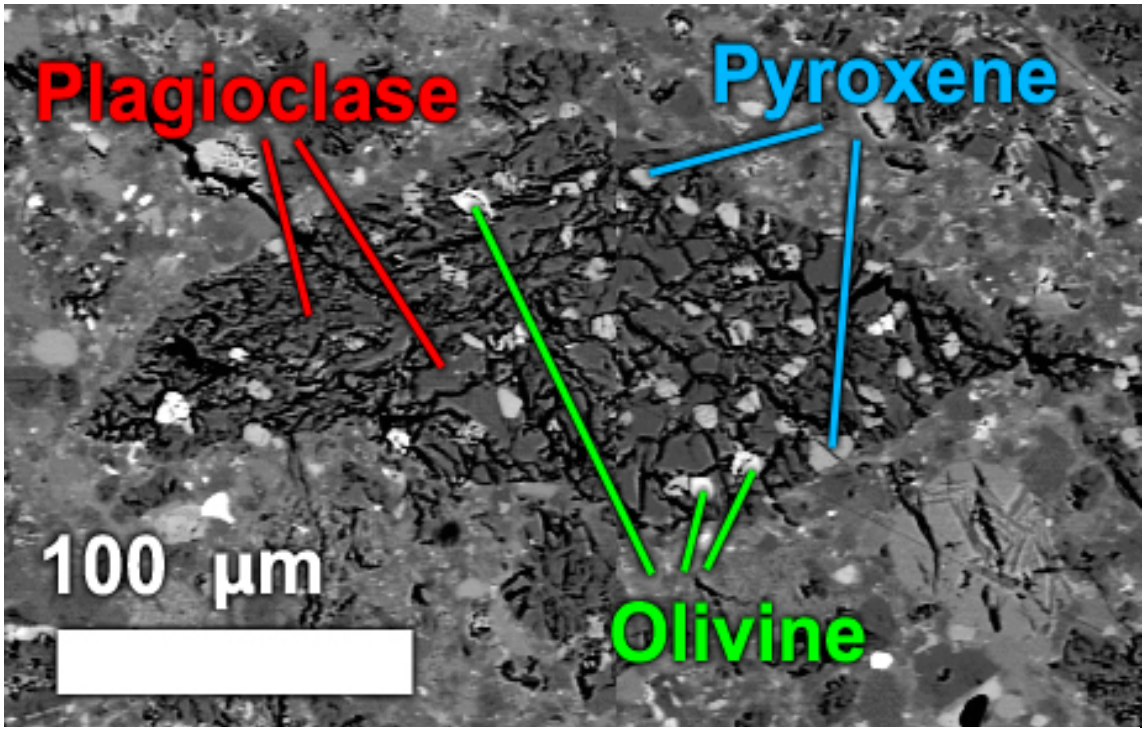

Figure 30: BSE image of granulite Clast 3 in QUE 93069,58 composed of plagioclase with olivine and pyroxene.

3.3.2.4. Clast 3b

Clast 3b (Fig. 31) is a tabular-shaped noritic granulite grain (0.08 x 0.35 mm) composed primarily of fractured plagioclase ($An_{96.1-96.9}$, four analyses) with rounded grains of pigeonite (Mg# 61.6-62.5, $En_{58.1-59.8}Fs_{35.9-36.2}Wo_{4.4-5.7}$, two analyses) and augite (Mg# 71.7-71.9, $En_{42.0-43.2}Fs_{16.4-17.1}Wo_{39.7-41.6}$, two analyses).

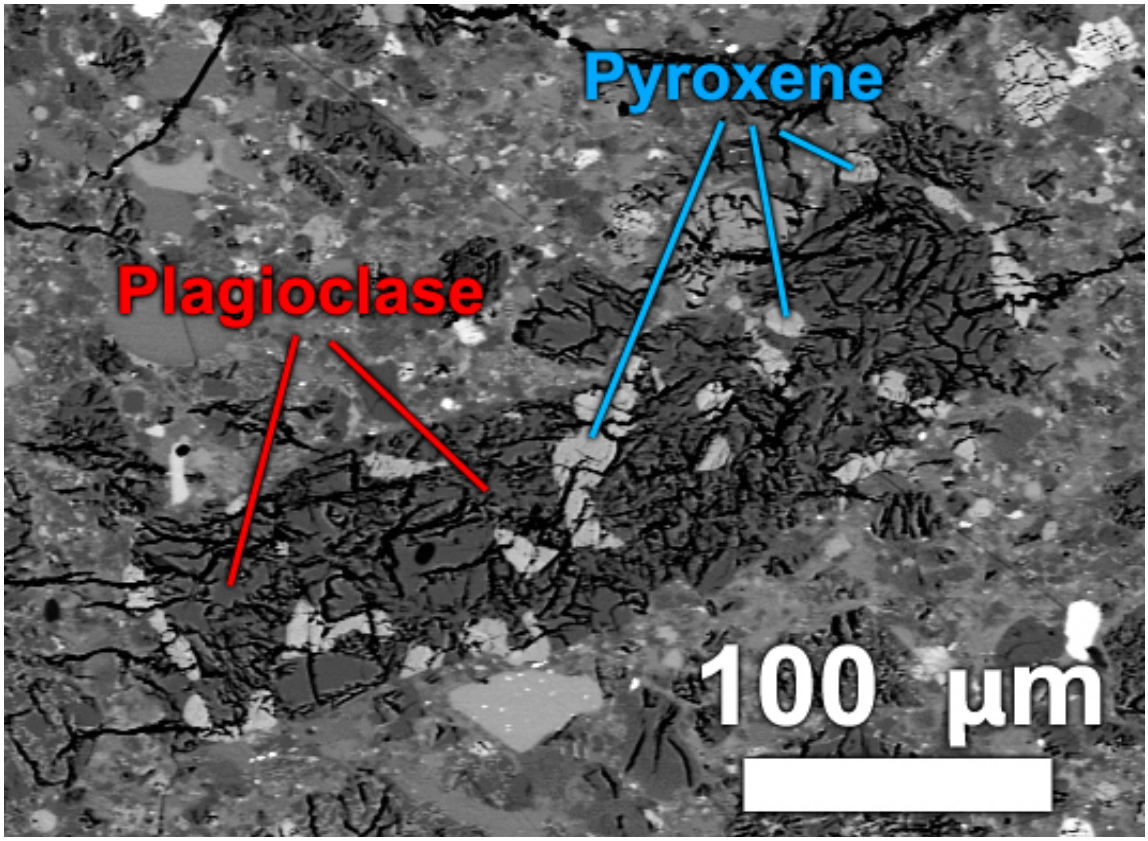

Figure 31: BSE image of granulite Clast 3b in QUE 93069,58 composed of plagioclase and pyroxene.

3.3.2.5. Clast 5a

Clast 5a (Fig. 32) is a rounded clast of noritic granulite (0.15 x 0.2 mm) composed of a plagioclase matrix ($An_{95.1}$, one analysis) with grains of pigeonite (Mg# 69.2, $En_{57.9}Fs_{25.8}Wo_{16.3}$, one analysis) and one olivine ($Fo_{66.4}$, one analysis). Most of the pigeonite is clustered near the edges of the clast rather than distributed evenly within the matrix.

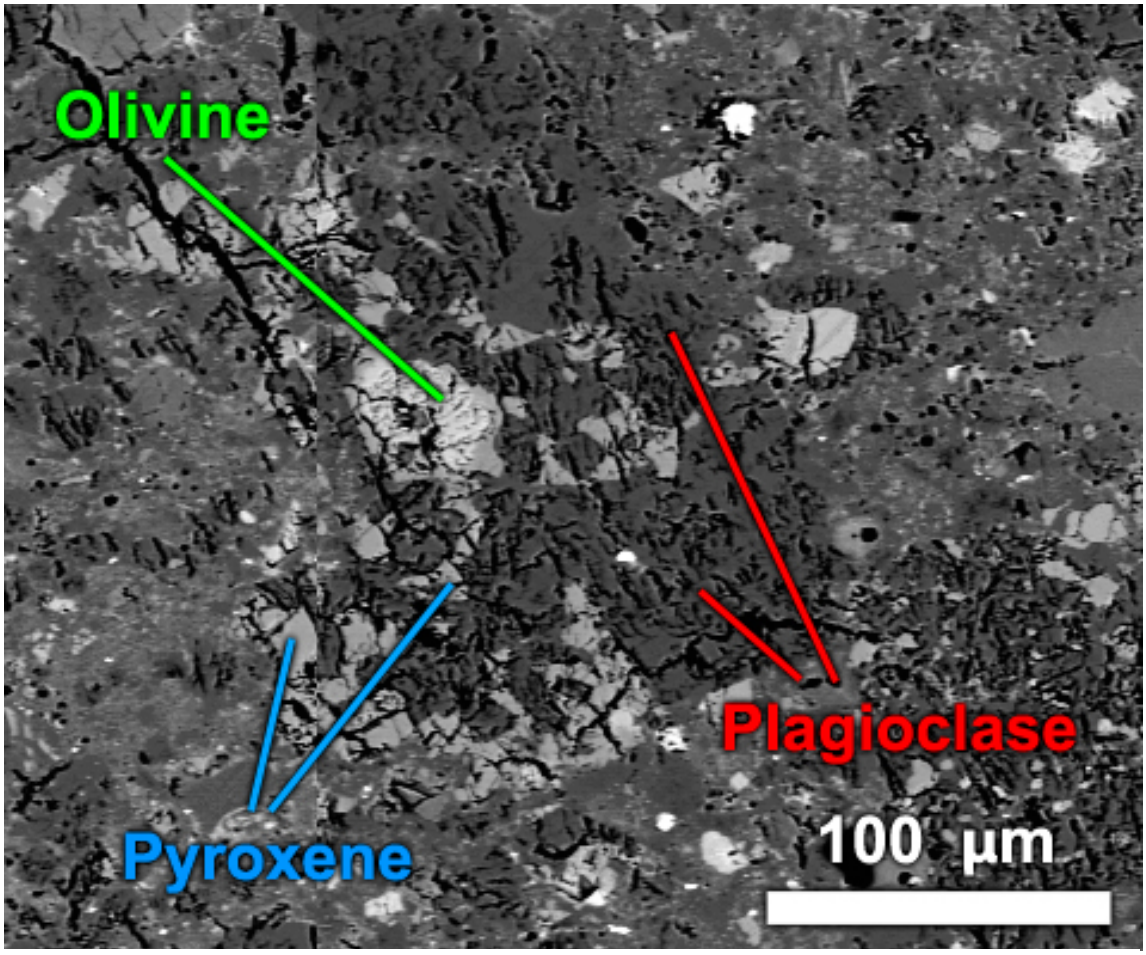

Figure 32: BSE image of granulite Clasts 5a and 5b in QUE 93069,58. Both noritic granulites contain a plagioclase matrix surrounding pyroxene and olivine. Clast 5b also contains a grain of nickel-iron metal and has some cracks filled with material rich in iron and chlorine.

3.3.2.6. Clast B

Clast B (Fig. 33) is a rounded noritic granoblastic granulite clast (0.15 x 0.2 mm) composed of a heavily fractured plagioclase matrix ($An_{96.1-97.7}$, six analyses) enclosing pigeonite (Mg# 58.7-60.4, $En_{56.0-57.7}Fs_{37.8-39.4}Wo_{4.4-5.1}$, five analyses) and olivine ($Fo_{53.4-54.8}$, two analyses). The pigeonite occurs exclusively in 2/3 of the clast and the olivine exclusively in the remaining 1/3, but pyroxene and olivine do come in contact at that boundary.

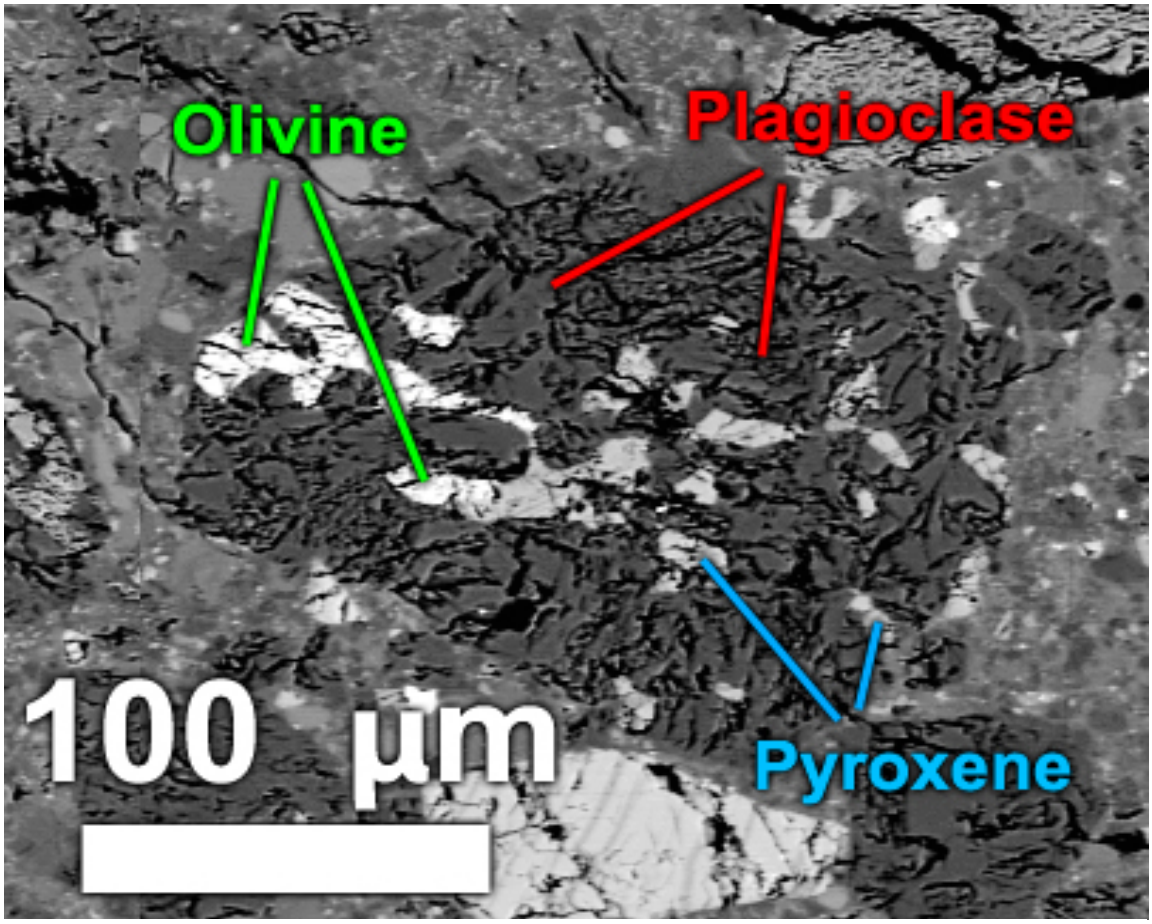

Figure 33: BSE image of noritic granulite Clast B in QUE 93069,58 composed of plagioclase, pyroxene, and olivine.

3.3.2.7. Clast C

Clast C (Fig. 34) is a rounded granoblastic noritic granulite clast (0.15 x 0.15 mm) composed of a fractured plagioclase matrix ($An_{96.1-96.7}$, two analyses) enclosing pigeonite (Mg# 60.6-63.1, $En_{49.2-55.6}Fs_{32.0-33.0}Wo_{10.6-18.8}$, four analyses), augite (Mg# 66.5, $En_{42.1}Fs_{21.3}Wo_{36.6}$, one analysis), olivine ($Fo_{52.7}$, one analysis), and ilmenite.

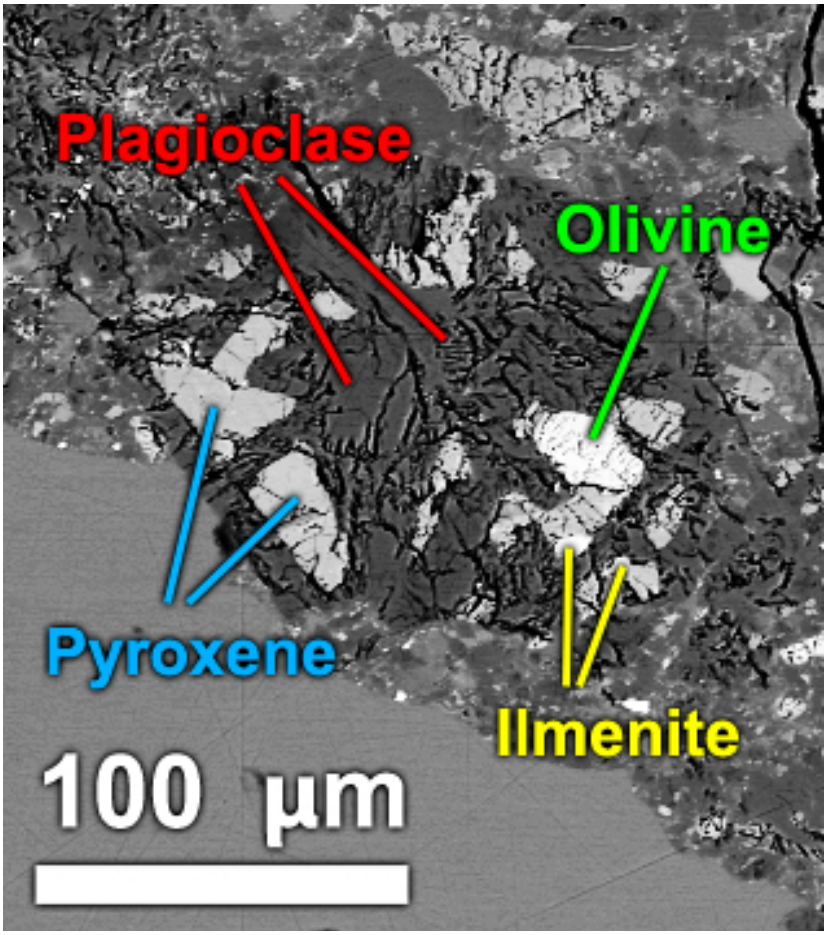

Figure 34: BSE image of noritic granulite Clast C in QUE 93069,58 composed of plagioclase, pyroxene, olivine, and ilmentie.

3.3.2.8. Clast D

Clast D (Fig. 35) is an irregularly-shaped noritic granoblastic granulite clast (0.2 x 0.45 mm) composed of a fractured plagioclase matrix ($An_{95.0-95.7}$, two analyses) encompassing pigeonite (Mg# 53.6, $En_{50.5}Fs_{43.8}Wo_{5.7}$, one analysis), augite (Mg# 64.2, $En_{39.2}Fs_{21.9}Wo_{38.9}$, one analysis), troilite, and ilmenite. The grain of troilite in this clast is the largest grain seen in any of the granulites analyzed here. There is no olivine present in Clast D.

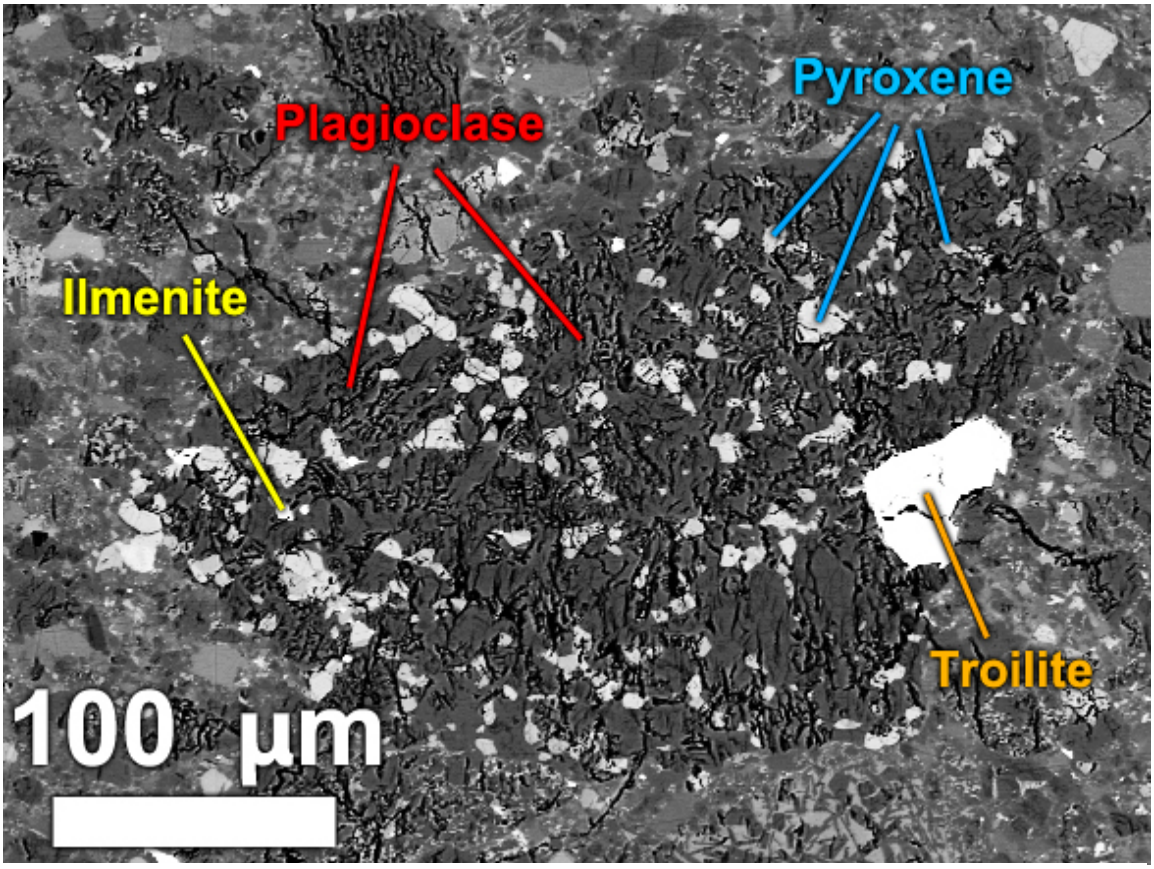

Figure 35: BSE image of noritic granulite Clast D in QUE 93069,58 composed of plagioclase, pyroxene, ilmenite, and troilite.

3.3.2.9. Clast E

Clast E (Fig. 36) is a rounded noritic granoblastic granulite (0.35 x 0.25 mm) composed of fractured plagioclase matrix ($An_{97.1-97.5}$, two analyses) encompassing elongated grains of pigeonite (Mg# 63.6, $En_{56.4}Fs_{32.3}Wo_{11.3}$, one analysis) and augite (Mg# 69.9, $En_{44.3}Fs_{19.1}Wo_{36.6}$, one analysis) along with two rounded olivine grains ($Fo_{58.2-60.2}$, three analyses) and a single ilmenite grain at the edge of the clast. A melt vein appears to cut through the clast near one edge. This was avoided during ablation because it may contain some material from external to Clast E.

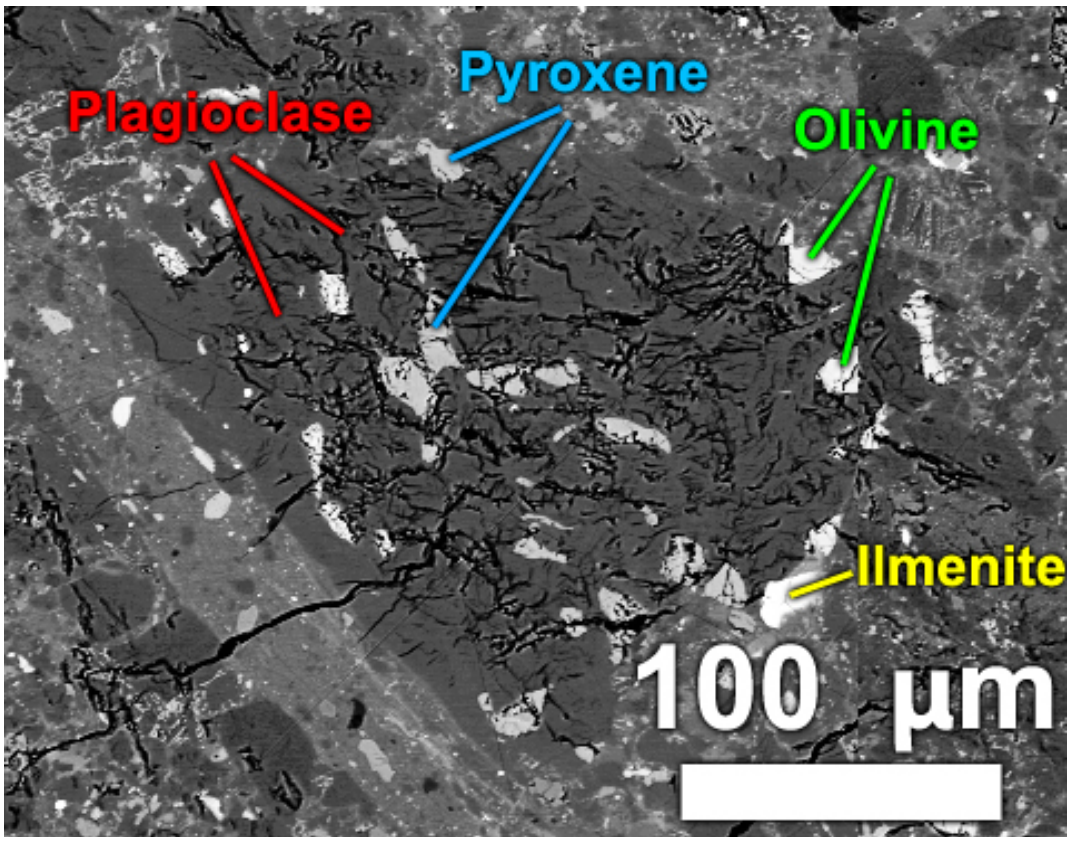

Figure 36: BSE image of noritic granulite Clast E in QUE 93069,58 composed of plagioclase, pyroxene, olivine, and ilmenite. A melt vein cuts through the left side of the clast.

3.3.2.10. Clast F

Clast F (Fig. 37) is a small rounded noritic granoblastic granulite clast (0.07 x 0.08 mm) composed of fractured plagioclase matrix ($An_{96.3}$, one analysis) encompassing pigeonite (Mg# 71.8, $En_{65.1}Fs_{25.6}Wo_{9.4}$, one analysis), olivine ($Fo_{71.2}$, one analysis), and one grain of ilmenite.

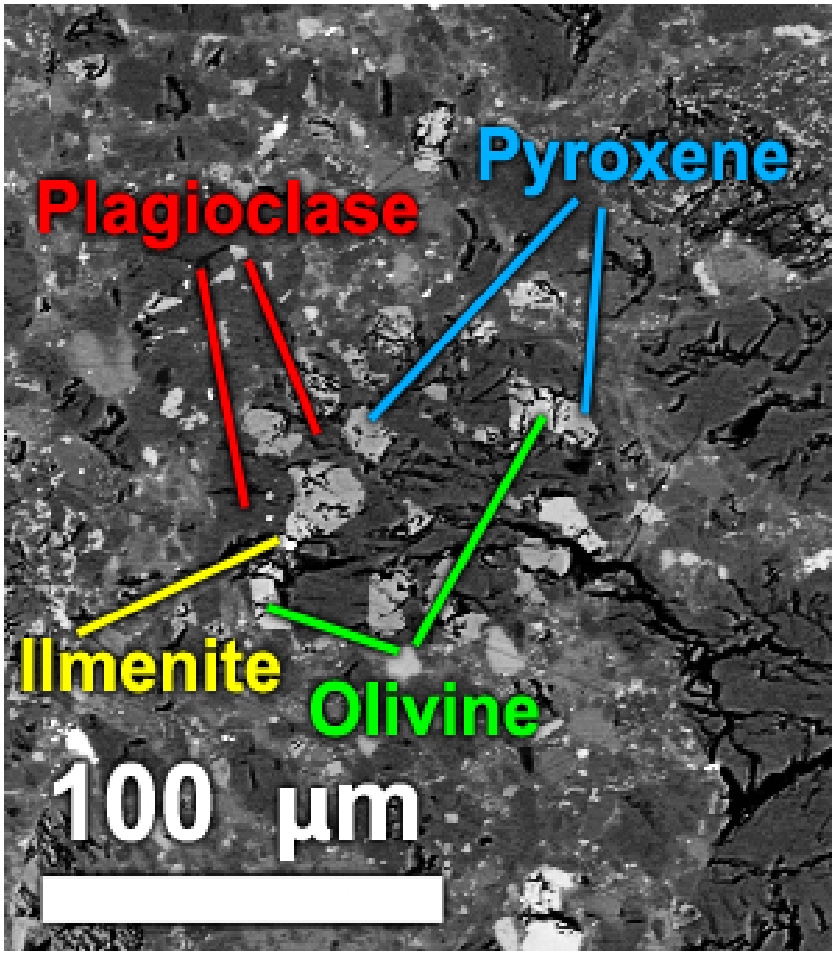

Figure 37: BSE image of noritic granulite Clast F in QUE 93069,58 composed of plagioclase, pyroxene, olivine, and ilmenite.

3.3.2.11. Clast G

Clast G (Fig. 38) is a rounded noritic granoblastic granulite composed of fractured plagioclase matrix ($An_{96.5-97.1}$, three analyses) encompassing rounded grains of pigeonite (Mg# 69.2-69.2, $En_{62.3-62.5}Fs_{27.7-28.1}Wo_{9.3-10.0}$, two analyses) and olivine ($Fo_{66.7-67.2}$, two analyses).

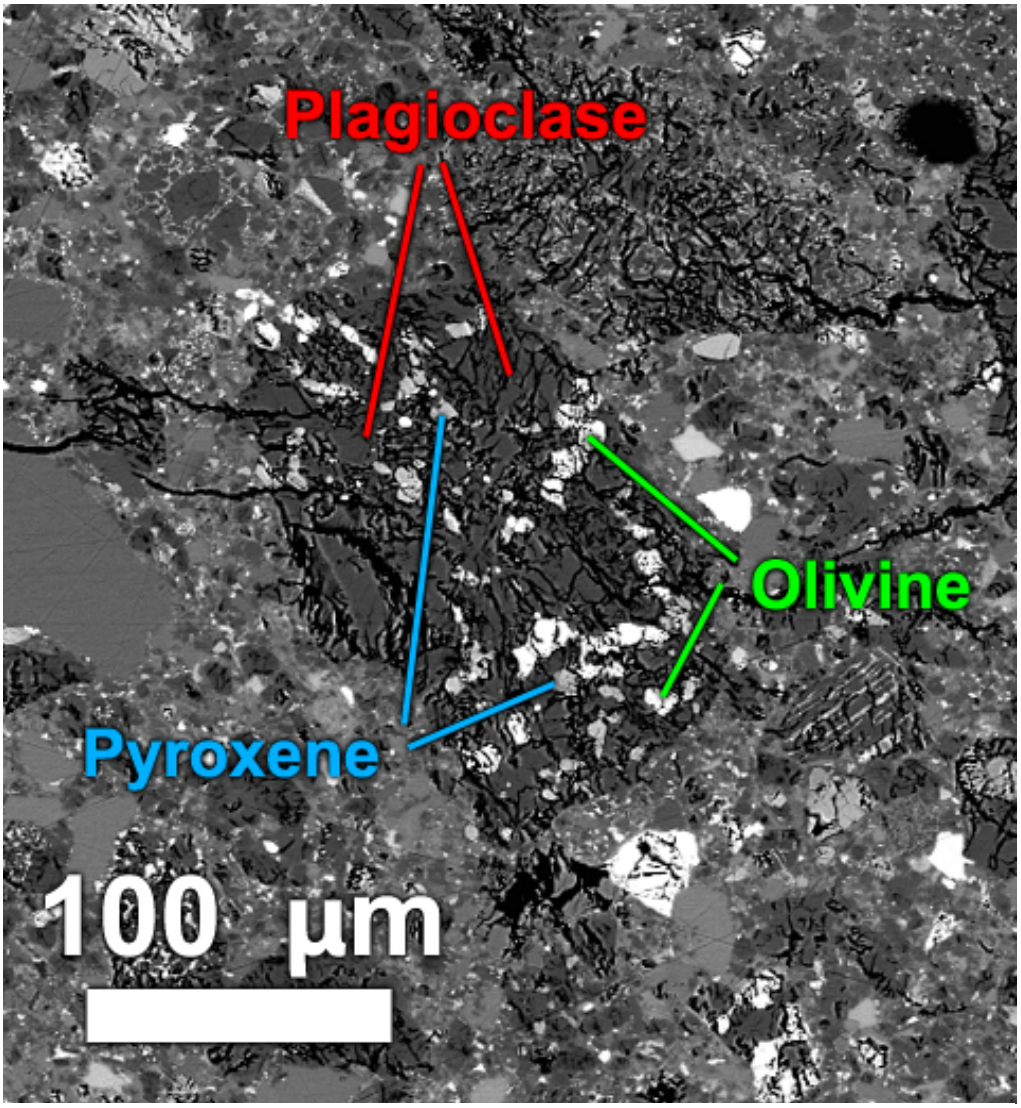

Figure 38: BSE image of noritic granulite Clast G in QUE 93069,58 composed of plagioclase, pyroxene, and olivine.

3.3.2.12. Clast T1

Clast T1 (Fig. 39) is a rounded noritic granoblastic granulite clast (0.2 x 0.23 mm) composed of fractured plagioclase matrix ($An_{95.7}$, one analysis) surrounding pigeonite (Mg# 70.1, $En_{63.8}Fs_{27.2}Wo_{9.0}$, one analysis).

3.3.2.13. Clast T3

Clast T3 (Fig. 39) is a rounded noritic granulite clast (0.2 x 0.3 mm) composed of fractured plagioclase ($An_{94.7\text{-}96.2}$, three analyses) encompassing pigeonite (Mg# 52.5, $En_{44.1}Fs_{40.0}Wo_{16.0}$, one analysis), augite (Mg# 55.4-55.9, $En_{33.9\text{-}34.9}Fs_{27.3\text{-}27.5}Wo_{37.5\text{-}38.9}$, two analyses), and olivine ($Fo_{49.2\text{-}49.3}$, two analyses).

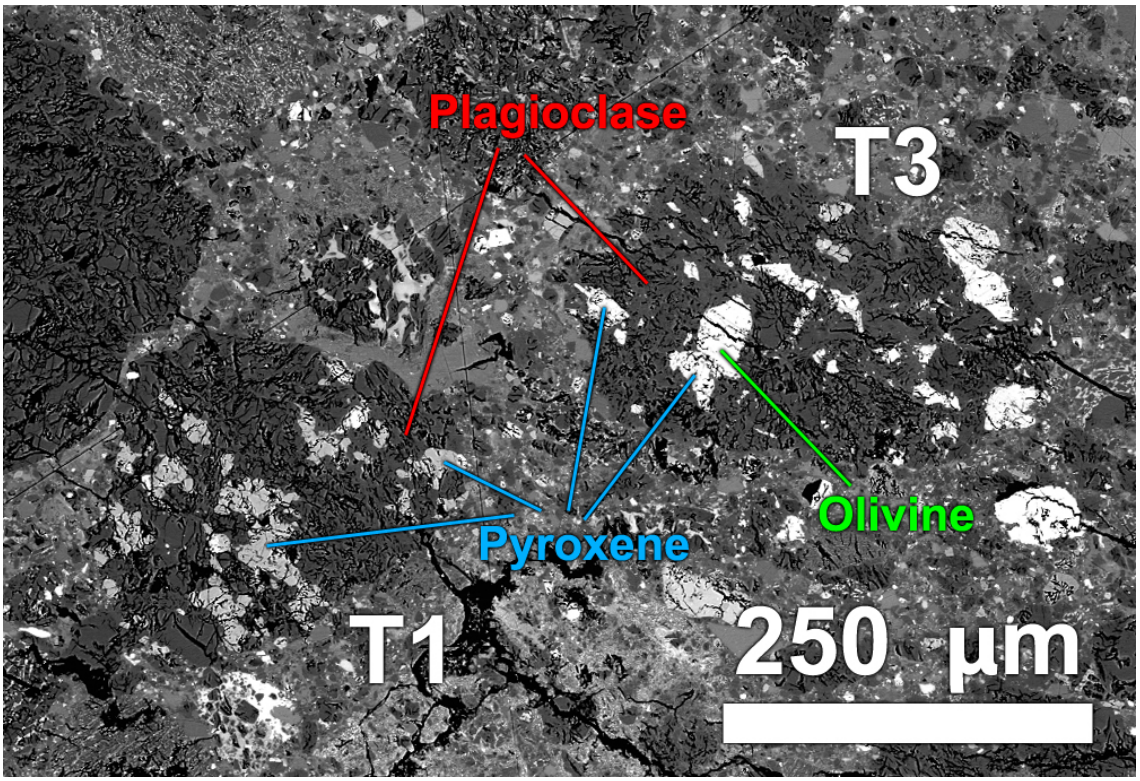

Figure 39: BSE image of noritic granulite Clast T1 composed of plagioclase and pyroxene, and granulite Clast T3 composed of plagioclase, pyroxene, and olivine.

3.4. Discussion

3.4.1. Major Elements

Taking the same approach as with NWA 5744 in Chapter 2, MAC 88104/5 and QUE 93069 can be compared to the two major lunar highlands lithologies: the FAN and Mg-suites (Warren, 1985). In Figure 18, most of the granulite clasts plot clearly within the FAN suite, with olivine Mg#'s as low as 46. However, several granulite clasts from QUE 93069 (Clasts 1, 5b, A, and F) as well as Clast 18 and one of the literature points from MAC 88105, plot distinctly above the FAN suite zone in the region between the

FAN and Mg-suites. None of the granulites for either meteorite has plagioclase that falls outside the range of anorthite content expected for the FAN suite. As was suggested in Chapter 2, perhaps the FAN suite boundary should be extended to include materials with olivine that has an Mg# of 70+.

Combined with literature data, MAC 88104/5 granulite olivines appear to evenly span the entire range of Mg#'s, with the magnesian Clast 18 (Mg# = 76.6) further extending that range toward the Mg-suite. Since the granulites in MAC 88104/5 exhibit a widely varying major element composition, it seems reasonable to presume that this meteorite is sampling lunar material from a wide variety of source compositions, and likely a wide variety of source locations, with all source locations being sampled relatively equally.

Conversely, the QUE 93069 granulites appear to fall into two clusters, with Mg#'s either above or below 60. The four clasts that are more ferroan than Mg# = 60 are Clasts 3, B, C, and E, and the eight clasts more magnesian than Mg# = 60 are 1, 2, 4, A, 5a, 5b, F, and G. The other QUE clasts lacked measurable olivine data to plot. The more-magnesian cluster appears to be about twice as prevalent within QUE 93069 as the more-ferroan cluster. If this meteorite is sampling granulitic material from two chemically/locationally distinct sources, then it may have formed closer to the source with the more magnesian of the two compositions.

Pyroxene compositions in the analyzed MAC 88104/5 granulite clasts (Fig. 19) show a significant amount of variation in Fe vs. Mg content in both pigeonite and augite,

but very little variation in Ca content between the different granulite clasts. QUE 93069 granulite pyroxenes exhibit much wider compositional variation. Because most of the granulite pyroxenes from both meteorites have Mg#'s < 70, they resemble FAN pyroxenes more closely than they do those of the Mg-suite.

3.4.2. Trace Elements

In situ trace element analysis was able to be done on MAC 88105 Clast 10 (Fig. 23). Plagioclase REE patterns diverge at the HREE end of the spectrum, but this may simply be an artifact of using two different laser spot sizes among the five *in situ* ablations. The three patterns with the lowest HREE abundance were measured using a 30 µm spot size, while the two measurements with the highest abundance used an 84 µm spot size. Since the larger spot sizes ablate more material to measure and also gave more complete results without any gaps, they are probably also more accurate.

The two ablations performed on the one large olivine crystal (Fig. 21) give very similar results (Fig. 23). There is very little if any negative Eu anomaly, with most of the REE concentrations being close to chondritic from lanthanum to holmium, after which the HREEs increase rapidly in concentration due to their greater compatibility in olivine crystal structure. However there is a very unusual negative cerium anomaly, which is about a factor of ten lower in concentration than either lanthanum or praseodymium. Whether this is a natural occurrence or is reflective of some sort of contamination or procedural error is not readily apparent.

Three pyroxene trace element measurements were made on Clast 10, and they all overlap tightly (Fig. 23). The shape of the curves and the absolute concentrations are a good match for FAN pyroxene (Fig. 23). REE content of Clast 10 pyroxene is about 3-4 times that of the magnesian NWA 5744, except for europium concentrations that are about equal.

Plagioclase in Clast 10 might also be used to compare to the different highlands crustal suites (Fig. 40), as in Chapter 2. Although major element concentrations are considerably different, MAC 88105 Clast 10 plagioclase has very similar trace element content to that of NWA 5744. Both plot more closely with the FAN suite or as an extension off of it.

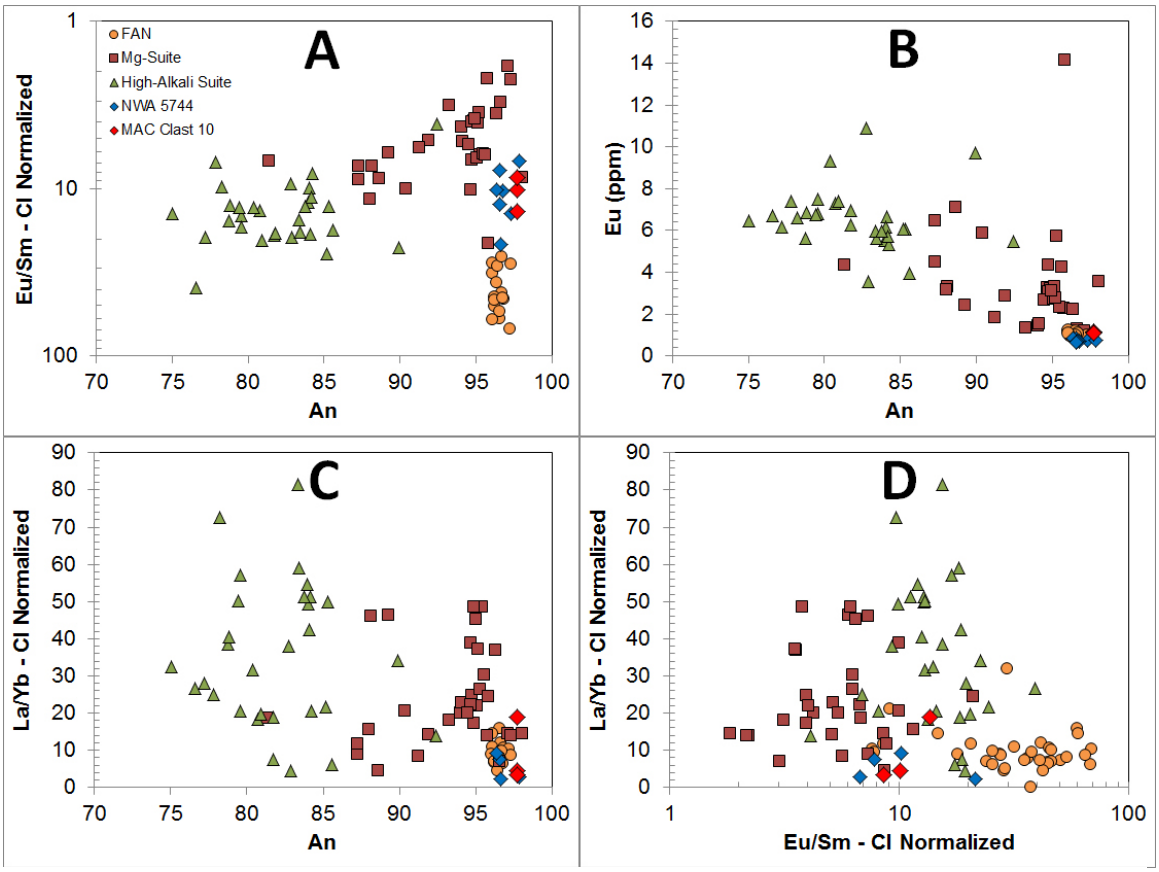

Figure 40: Comparison of plagioclase compositions in MAC 88105 ferroan Clast 10 (bright red diamonds) to magnesian NWA 5744 (blue diamonds) and the three major highlands suites seen in Apollo samples (Papike et al., 1997; Floss et al., 1998; Papike et al., 1996; Shervais and McGee, 1998; Shervais and McGee, 1999). A: Eu/Sm vs. An (after Joy, 2013); B: Eu vs. An; C: La/Yb vs. An; D: La/Yb vs. Eu/Sm.

3.4.3. Bulk Composition

MAC 88105 Clast 10 bulk trace element content (Fig. 23) is close to 10x chondritic. QUE 93069 granulites have a wide variety of REE patterns (Fig. 26), and they can be separated into different compositional groups according to these patterns, which will now be described.

3.4.3.1. Group 1

The first group (Fig. 41) contains Clasts 2 and 3b. These clasts have REE patterns similar to that of pyroxene, which makes sense because these three clasts contain large amounts of pyroxene. The clast with the weaker correlation to a pyroxene profile, Clast 3b shown in lavender, contains a lesser amount of pyroxene and is dominated by plagioclase, which explains the positive europium anomaly.

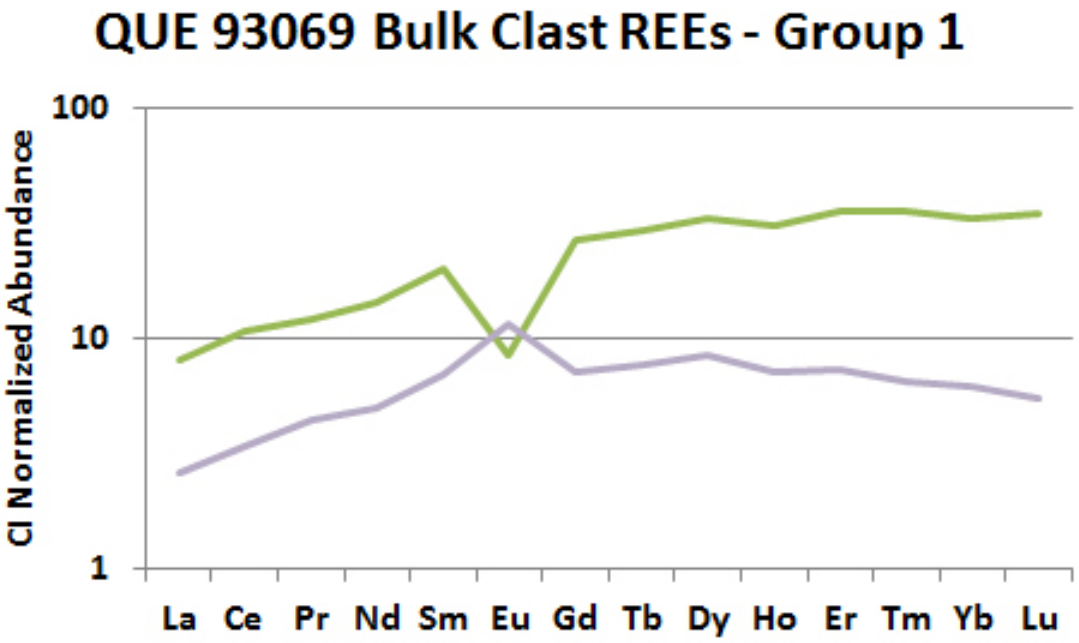

Figure 41: Bulk REE content of clasts 2 and 3b, measured via LA-ICP-MS by ablating as much of the clast as possible. These profiles are heavily influenced by the high pyroxene content of the clasts.

3.4.3.2. Group 2

Group two (Fig. 42) is given by Clasts 3, B, and E. They have the lowest concentration of REEs among the clasts of QUE 93069 analyzed. Clasts B and E (purple and lavender) have very flat profiles at about 2-3 times chondritic. Clast 2 has a slight upward slope indicating greater concentrations of HREEs than LREEs. This clast had a cluster of olivine grains in it, and they are probably causing that pattern. All three clasts have a positive Eu anomaly up to 10-11 times chondritic, which makes sense given that these clasts have more plagioclase than any other mineral.

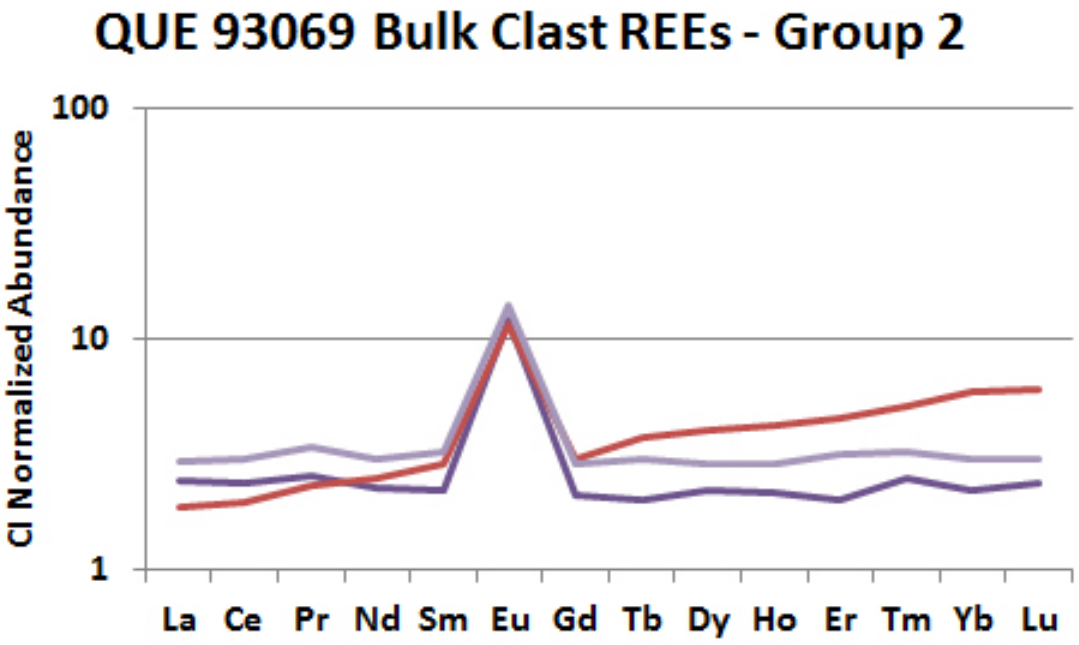

Figure 42: Bulk REE content of clasts 3, B, and E, measured via LA-ICP-MS by ablating as much of the clast as possible. They contain the lowest REE concentration among the clasts analyzed here.

3.4.3.3. Group 3

Group three (Fig. 43) is richer in REEs than group two, but also has a very flat REE profile aside from a positive Eu anomaly. The difference is that abundance here varies from 7-11 times chondritic, but the Eu peak is at the same concentration in both groups. Group four is more common than the previous groups, with four constituent clasts analyzed from QUE 93069.

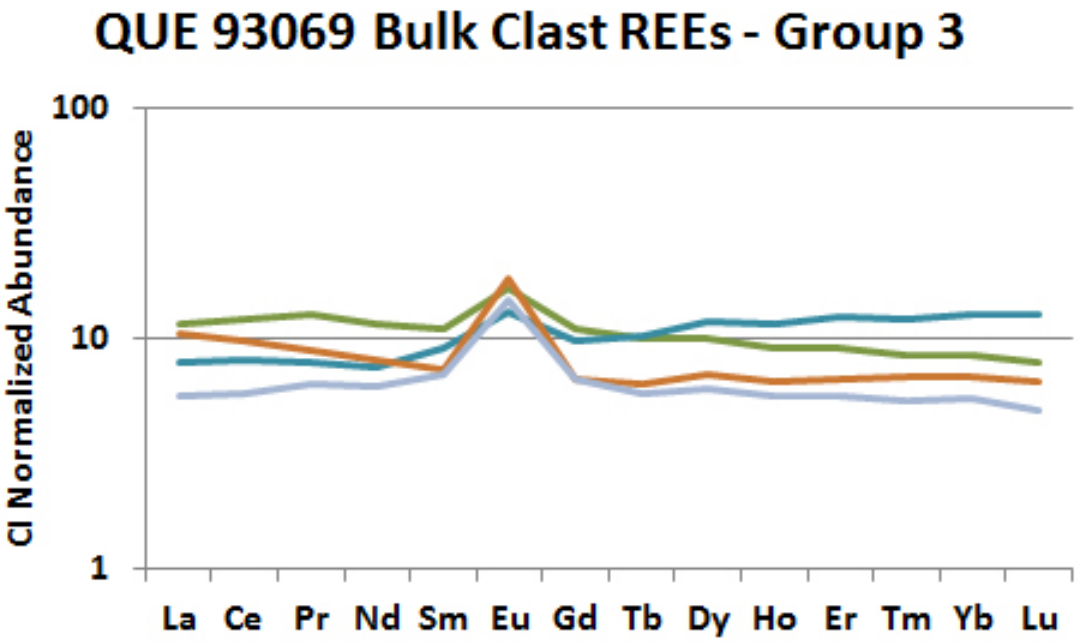

Figure 43: Bulk REE content of clasts C, D, T1, and T3, measured via LA-ICP-MS by ablating as much of the clast as possible. They contain flat REE profiles other than a positive Eu anomaly.

3.4.3.4. Group 4

Group four (Fig. 44) is the final grouping for QUE 93069 granulite clasts. Equally as prevalent as group four, there are four granulite clasts that fit within this trace element grouping (1, 5a, F, and G). They have REE concentrations just above 10 times chondritic, have nearly flat REE profiles, and exhibit little or no Eu anomaly at all.

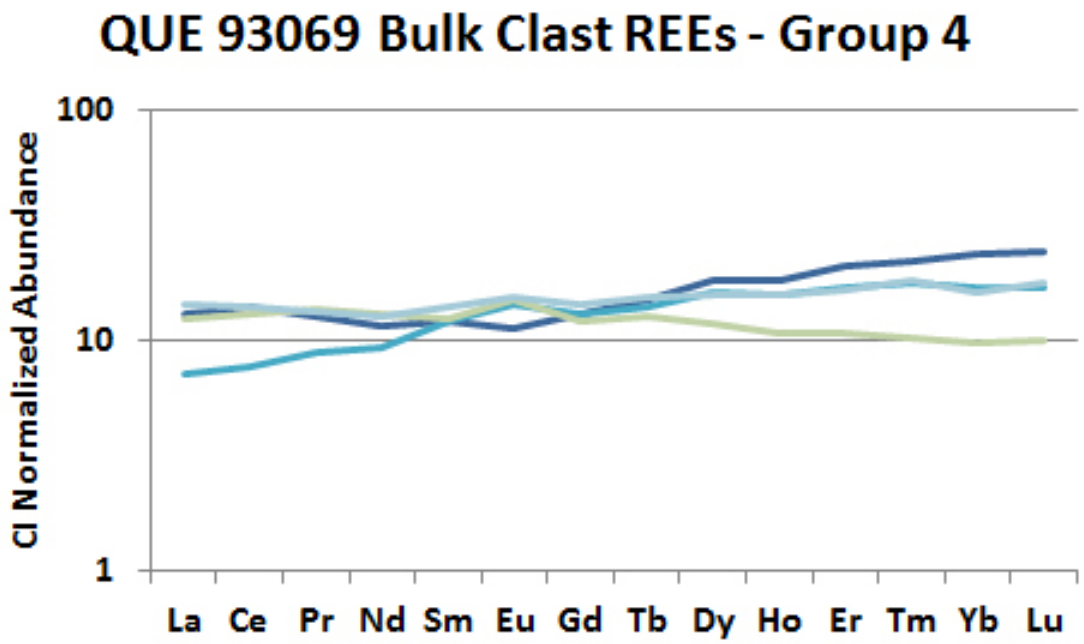

Figure 44: Bulk REE content of clasts 1, 5a, F, and G, measured via LA-ICP-MS by ablating as much of the clast as possible. They contain flat REE profiles above 10 times chondritic, and have little or no Eu anomaly.

3.4.4. Origins and History

Based on the wide range of compositions and textures observed, MAC 88104/5 granulites have a range of different histories. Figures 18 and 19 show the major elements of these clasts classify it into the FAN suite. The FAN suite includes a broad

range of lithologies thought to account for about half of all of the lunar highlands crustal terrain (Warren, 1985; Wieczorek *et al.,* 2006). The range in olivine Mg# from 40 to 76 indicates that the MAC 88104/5 granulite clasts may be sampling nearly the full range of compositions within the FAN suite, and sampling them in roughly equal amounts as well. In order to contain this range of granulites, MAC 88104/5 must have formed in a place where different materials from different source locations were being concentrated together as impact ejecta. Large impact melt sheets can mix meteoritic metal into the megaregolith to a depth of at least 2-3 km (Hiesinger and Head, 2006), which means the presence of metal grains and troilite in Clasts 10 and 18 is not a good indicator for either a shallow or deep origin within the regolith. However, the broad range of granulite clast compositions and the presence of solar wind-implanted noble gases within the meteorite (Eugster *et al.,* 1991) seem to indicate it must have originated on or near the lunar surface, from within a well-mixed regolith.

QUE 93069 granulites are compositionally similar to those in MAC 88104/5, but there are some key differences. Major element content of the granulite clasts in QUE falls into two different clusters, with olivine Mg#'s of either greater than or less than 60. This indicates its source location may not be as well mixed as that of MAC 88104/5. A history of extended cosmic ray and solar wind exposure (Eugster *et al.,* 1991; Nishiizumi *et al.,* 1996; Thalmann *et al.,* 1996) and lack of KREEP content (Koeberl *et al.,* 1996) mean QUE probably originates from a location on the lunar surface among FAN suite materials far away from the Apollo landing sites.

Robinson *et al.,* (2012) used remote sensing spectral data from Clementine (a NASA-supported lunar orbiter which measured the electromagnetic spectra of the lunar surface in 1994) to compare to the compositions of basaltic clasts in both MAC 88104/5 and QUE 93069 and found that MAC 88104/5, because it contains numerous high-Ti basalt clasts, probably came from a place on the Moon near one of the few areas where high-Ti basalts outcrop. These sites are all on the lunar nearside. The noritic composition of the granulites in both meteorites also fits with the idea they may have both come from the nearside, since the nearside is more noritic and the farside is more troctolitic (Arai *et al.,* 2008).

3.5. Conclusions

MAC 88104/5 and QUE 93069 granulites belong to the ferroan anorthosite suite, and therefore the meteorites themselves probably originated from an area of the Moon rich in FAN materials. Because of the general compositional makeup of the lunar surface, it is more likely that both originated from the nearside of the Moon than the farside, and QUE 93069 probably also came from a location far away from the Apollo and Luna landing sites where KREEP material is limited to not present. The high-Ti basalt and KREEP-component clasts within MAC 88104/5 indicate it originates from a location containing ejecta of each of those lithologic types, probably in the Procellarum region.

The two meteorites probably didn't come from the same location. MAC 88104/5 probably formed at or near the lunar surface within a well-mixed regolith, while QUE 93069 formed at or near the lunar surface in a regolith that was either not as well-mixed or not as broadly sourced. At least two major element and four trace element populations appear to exist within the range of FAN suite granulites in QUE 93069, and these populations are not all equally represented.

The trace elements present in analyzed plagioclase show that there are distinct similarities between ferroan granulites in MAC 88105 and magnesian granulite NWA 5744. This could mean they both actually belong to the same crustal suite, likely the FAN suite, and if so the definitional boundaries of that suite need to be extended to allow for more magnesian compositions.

Chapter 4: Summary

4.1. Lunar Crustal Geology

According to the LMO theory, shortly after the Moon's formation its crust was largely molten, which began to crystallize in a particular sequence as it cooled. In the later stages of the crystallization process, plagioclase would have been forming and floating in the magma. Once the crust fully solidified, the upper crust would have been composed primarily of ferroan anorthosite. This composition was confirmed on the lunar nearside by samples taken during the Apollo missions.

The feldspathic highlands portion of the crust is composed of two major lithological classification suites: the ferroan anorthosite and magnesian suites. FAN suite material has Mg#'s < 70 and is believed to have originated as the upper floatation crust on the LMO, making up the upper half of the crust. The Mg-suite is richer in magnesium with Mg#'s > 70, generally more mafic than the FAN suite, and is believed to either have made up the lower half of the crust as part of the LMO crystallization process, or to have been emplaced into the crust via secondary intrusions after the LMO solidification. The lunar crust is believed to be thinner on the farside than the nearside, which means a farside source for Mg-suite material may be shallower there, and Mg-rich rocks are believed to be more prevalent on the lunar farside surface. There is also a larger amount of feldspathic highlands terrane on the lunar farside, due to the presence of basaltic maria covering significant portions of the nearside (Fig. 1).

Lunar meteorites are important for further understanding the composition and history of the lunar crust, because samples returned from the Apollo and Luna missions are probably not representative of the entire lunar crust. I am studying lunar granulites because they are present as clasts within many Apollo samples and lunar meteorites, yet they may not be related to the FAN or Mg-suites.

4.2. Methods

I studied samples of three different meteorites to analyze the composition and history of lunar granulites. I studied the granulite meteorite Northwest Africa 5744, granulite clasts from paired meteorites MacAlpine Hills 88104 and 88105, and granulite clasts from meteorite Queen Alexandra Range 93069. NWA 5744 was first scanned in an X-ray Computed Tomography machine in order to create a 3D digital density map of the interior of my slab of the rock and view the interior structure (Fig. 2). All meteorite samples were mapped on a field emission scanning electron microscope, and major element data were acquired using an electron microprobe. Finally, trace element content for each granulite sample was acquired via laser ablation inductively coupled plasma mass spectrometry.

4.3. Northwest Africa 5744

Northwest Africa 5744 is an anorthositic troctolitic lunar meteorite that is entirely granulitic and may be monomict. It was a recent find, and has not been studied in detail until now. It is magnesian in composition with a bulk Mg# = 79, and is

composed primarily of plagioclase, olivine, and clinoenstatite, with minor amounts of associated augite and Ti-chromite (Fig. 3). Impactor content is minor or not present, and terrestrial contamination is also minor and limited only to the larges cracks within the sample (Fig. 4). The matrix is composed of plagioclase shocked to maskelynite, <10 μm clinoenstatite schlieren, and <20 μm amoeboid olivine, all of which appear to be products of metamorphism. Distributed unevenly within the matrix are larger 80+ μm relict grains of plagioclase that has not been maskelynized, olivine, and rarely pyroxene. The relict grains are usually very rounded and fractured as though they have been mechanically abraded, and the relict plagioclase grains each exhibit some amount of compositional zoning (Fig. 5). All relict grains vary in both major and trace element composition and so does the bulk composition of the matrix throughout the rock (Figs. 5-6, 8-9, and 11-14). Overall, the major element composition seems to fit the Mg-suite (Fig. 9), but trace element content of the plagioclase and pyroxene fit much better within the range of compositions seen in the FAN suite (Figs. 11, 12, and 14).

By multiplying the average trace element content of each major phase by the modal abundance of that phase and taking the sum, the expected bulk trace element content of NWA 5744 is estimated to be approximately chondritic except for a positive Eu anomaly (Fig. 8). This would mean that if the parent rock to NWA 5744 had the composition of the current relict grains in the same modal proportion as the bulk NWA 5744, then the lithologic unit the parent rock originated from had a chondritic trace element signature aside from Eu. However, the measured average bulk REE content

determined by ablating several portions of matrix material is roughly 3-4 times chondritic with a similar Eu anomaly. But this difference can be explained if the matrix material has greater REE content than the relict grains, and presumably became relatively enriched during metamorphism. The measured bulk REE content is probably more reflective of the bulk NWA 5744 because the matrix accounts for a larger proportion of the total rock than the relict grains, but regardless, the REE content appears to be distinct from any other magnesian lunar granulites.

Metamorphism of NWA 5744 likely lasted fewer than 1000 years, and could have been only 100's of years or less. This means that whatever heat was applied must have dissipated quickly, and therefore probably occurred near the lunar surface. The lack of impactor content in NWA 5744, however, means it was probably still buried deep enough to be shielded from contamination, and thus would have had some insulation against rapid cooling. It is therefore most likely that metamorphism was largely shock induced.

The parent rock appears to have had a composition distinct from current classification schemes, and due to its magnesian composition is consistent with having formed in the deep crust far away from the Apollo and Luna sites, and experienced subsequent excavation by one or more major impact events prior to metamorphism.

4.4. MacAlpine Hills 88104/5

MacAlpine Hills 88104 and 88105 are paired lunar regolith breccia meteorites that contain granulite clasts. Three clasts were analyzed, one of which (Clast 10; Fig. 21)

may or may not be a granulite, but Clast 10 is also the only clast analyzed that had large enough grain sizes for *in situ* trace element analysis via laser ablation. Major element content of the three clasts plus literature data on other granulite clasts from this meteorite indicate this it contains granulites spanning the full range of FAN suite major element compositions and even contains some that are more magnesian (Fig. 18). Rare earth element content of Clast 10 pyroxene fits well within the range of FAN suite compositions, and plagioclase REE content is also a better fit in the FAN suite than the MG-suite (Fig. 23). Olivine REE content has a negative Ce anomaly, which may indicate the clast originates from a lithology containing zircon. Clast 10 plagioclase REE content also bears similarities to NWA 5744 plagioclase content (Fig. 40).

Due to the types of clasts MAC 88104/5 contains and their distinguishing chemistries, the place of origin for MAC 88104/5 is most likely on the lunar nearside, at or near the surface, in an area of well-mixed regolith containing ejecta from source regions for high-Ti basalts, KREEP basalts, and roughly equal proportions of granulites covering the full spectrum of FAN suite major element compositions.

4.5. Queen Alexandra Range 93069

Queen Alexandra Range 93069 is a polymict lunar regolith breccia containing granulite clasts, 13 of which I analyzed. They were all noritic, and of the 9 that did contain olivine, five of them cluster with Mg#'s > 60 and the other four cluster with Mg#'s < 60 (Fig. 18). Pyroxene major element compositions vary significantly from clast to clast (Fig. 19). Trace element content of QUE 93069 granulites is also highly variable

(Fig. 26), but the 13 clasts can be broken into four groups of similar REE profiles, some of which are more populous than others. If the bulk compositions of these clasts are representative of the regions from which they are sourced, then QUE 93069 granulites are likely sampling at least four different ferroan lithologies.

The place of origin for QUE 93069 is probably different from that of MAC 88105, and certainly different from NWA 5744; it is more likely to originate from the lunar surface on the nearside rather than the farside due to the ferroan composition of its granulites, but from far away from the Apollo and Luna sites due to its lack of a KREEP component. It was either formed from a regolith that is not as well-mixed as that of MAC 88105, or not as uniformly sourced due to the clustering seen in its granulite compositions.

References

Anders E. and Grevesse N. 1989. Abundances of the elements: Meteoritic and solar. Geochimica et Cosmochimica Acta 53:197-214.

Arai T. 2008. Magnesian Anorthosite: A new class of lunar crustal rock and implications for crustal genesis (abstract). Meteoritics and Planetary Science 43:A179-A192.

Arai T., Takeda H., Yamaguchi A., and Ohtake M. 2008. A new model of lunar crust: asymmetry in crustal composition and evolution. Earth Planets Space 60:433-444.

Barlow N. G. 1990. The Late Heavy Bombardment crater size-frequency distribution in the inner solar system (abstract). Proceedings, International Workshop on Meteorite Impact on the Early Earth. pp. 6-7.

Bischoff A. 1996. Lunar meteorite Queen Alexandra Range 93069: A lunar highland regolith breccia with very low abundances of mafic components. Meteoritics & Planetary Science 31:849-855.

Bottke W. F., Vokrouhlicky D., Minton D., Nesvorny D., Morbidelli A., Brasser R., Simonson B., and Levison H. F. 2012. An Archean heavy bombardment from a destabilized extension of the asteroid belt. Nature 485:78-81.

Braun S. A., Brandon A. D., Joy K. H., and Kring D. A. 2011. Did meteorite bombardment sample deep lunar crust?: Major and trace element compositions of granulite clasts in lunar regolith breccia MAC 88104 (abstract). Proceedings, 42nd Lunar and Planetary Science Conference #2762.

Brey G. P. and Kohler T. 1990. Geothermobarometry in four-phase lherzolites II. New thermobarometers, and practical assessment of existing thermometers. Journal of Petrology 31:1353-1378.

Brophy J. G. and Basu A. 1990. Europium anomalies in mare basalts as a consequence of mafic cumulate fractionation from an initial lunar magma. Proceedings, 20th Lunar and Planetary Science Conference. pp. 25-30.

Cahill J. T., Floss C., Anand M., Taylor L. A., Nazarov M. A., and Cohen B. A. 2004. Petrogenesis of lunar highlands meteorites: Dhofar 025, Dhofar 081, Dar al Gani 262, and Dar al Gani 400. Meteoritics & Planetary Science 39:503-529.

Campbell I. H., Roeder P. L., and Dixon J. M. 1978. Plagioclase buoyancy in basaltic liquids as determined with a centrifuge furnace. Contributions to Mineralogy and Petrology 67:369-377.

Cintala M. J. and Grieve R. A. F. 1998. Scaling impact melting and crater dimensions: Implications for the lunar cratering record. Meteoritics and Planetary Science 33:889-912.

Cohen B. A., Swindle T. D., and Kring D. A. 2000. Support for the lunar cataclysm hypothesis from lunar meteorite impact melt ages. Science 290:1754-1756.

Cushing J. A., Taylor G. J., Norman M. D., and Keil K. 1993. The granulite suite: Impact melts and metamorphic breccias of the early lunar crust (abstract). Proceedings, 24th Lunar and Planetary Science Conference. pp. 369C-370C.

Cushing J. A., Taylor G. J., Norman M. D., and Keil K. 1999. The granulite suite: Impact melts and metamorphic breccias of the early lunar crust. Meteoritics & Planetary Science 34:185-195.

Elardo S. M., Draper D. S., and Shearer, Jr. C. K. 2011. Lunar magma ocean crystallization revisited: Bulk composition, early cumulate mineralogy, and the source regions of the highlands Mg-suite. Geochimica et Cosmochimica Acta 75:3024-3045.

Elkins-Tanton L. T., Van Orman J. A., Hager B. H., and Grove T. L. 2002. Re-examination of the lunar magma ocean cumulate overturn hypothesis: Melting or mixing is required. Earth and Planetary Science Letters 196:239-249.

Eugster O., Beer J., Burger M., Finkel R. C., Hofmann H. J., Krähenbühl U., Michel Th., Synal H. A., and Wölfli W. 1991. History of the paired lunar meteorites MAC88104 and MAC88105 derived from noble gas isotopes, radionuclides, and some chemical abundances. Geochimica et Cosmochimica Acta 55:3139-3148.

Floss C., James O. B., McGee J. J., and Crozaz G. 1998. Lunar Ferroan Anorthosite Petrogenesis: Clues from Trace Element Distributions in FAN Subgroups. Geochimica et Cosmochimica Acta 62:1255-1283.

French B. M. 1998. Traces of catastrophe: A handbook of shock-metamorphic effects in terrestrial meteorite impact structures. LPI Contribution No. 954, Lunar and Planetary Institute, Houston. 120 pp.

Goodrich C. A., Taylor J., and Keil K. 1984. Petrology and chemistry of hyperferroan anorthosites and other clasts from lunar meteorite ALHA81005. Journal of Geophysical Research 89:C87-C94.

Gross J., Treiman A. H., and Mercer C. 2012. Lunar feldspathic meteorites: Constraints on the geology of the lunar farside highlands, and the origin of the lunar crust (abstract). 2nd Conference on the Lunar Highlands Crust #9021.

Gross J., Treiman A. H., and Mercer C. 2012. Sinking of the lunar magma ocean: New evidence from meteorites and the return of serial magmatism (abstract). Proceedings, 43rd Lunar and Planetary Science Conference #2306.

Grove T. L., Baker M. B., and Kinzler R. J. 1984. Coupled CaAl-NaSi diffusion in plagioclase feldspar: Experiments and applications to cooling rate speedometry. Geochimica et Cosmochimica Acta 48:2113-2121.

Hiesinger, H. and Head, J. 2006. New views in lunar geoscience: An introduction and overview. Reviews in Mineralogy & Geochemistry 60:1-81.

Hudgins J. A., Spray J. G., Kelley S. P., Korotev R. L., and Sherlock S. C. 2008. A laser probe $^{40}Ar/^{39}Ar$ and INAA investigation of four Apollo granulitic breccias. Geochimica et Cosmochimica Acta 72:5781-5798.

Hudgins J. A., Spray J. G., and Hawkes C. D. 2011. Element diffusion rates in lunar granulitic breccias: Evidence for contact metamorphism on the Moon. American Mineralogist 96:1673-1685.

Johnson J. R. and Hörz F. 2003. Visible/near-infrared spectra of experimentally shocked plagioclase feldspars. Journal of Geophysical Research 108(E11), 5120.

Jolliff B. L., Korotev R. L., and Haskin L. A. 1991. A ferroan region of the lunar highlands as recorded in meteorites MAC88104 and MAC88105. Geochimica et Cosmochimica Acta 55:3051-3071.

Jolliff B. L., Rockow K. M., Korotev R. L., and Haskin L. A. 1996. Lithologic distribution and geologic history of the Apollo 17 site: The record in soils and small rock particles from the highland massifs. Meteoritics & Planetary Science 31:116-145.

Joy K. H. 2013. Trace elements in lunar plagioclase as indicators of source lithology (abstract). Proceedings, 44th Lunar and Planetary Science Conference #1033.

Joy K. H., Crawford I.A., Russell S.S., and Kearsley A.T. (2010). Lunar meteorite regolith breccias: An *in situ* study of impact melt composition using LA-ICP-MS and implications for the composition of the lunar crust. Meteoritics & Planetary Science 45:917-946.

Koeberl C., Kurat G., and Brandstätter F. 1991. MAC88105 – A regolith breccia from the lunar highlands: Mineralogical, petrological, and geochemical studies. Geochimica et Cosmochimica Acta 55:3073-3087.

Koeberl C., Kurat G., and Brandstätter F. 1996. Mineralogy and geochemistry of lunar meteorite Queen Alexandra Range 93069. Meteoritics & Planetary Science 31:897-908.

Korotev R. L., Jolliff B. L., Zeigler R. A., Gillis J. J., and Haskin L. A. 2003. Feldspathic lunar meteorites and their implications for compositional remote sensing of the lunar surface and the composition of the lunar crust. Geochimica et Cosmochimica Acta 67:4895–4923.

Korotev R. L., Zeigler R. A., and Jolliff B. L. 2006. Feldspathic lunar meteorites Pecora Escarpment 02007 and Dhofar 489: Contamination of the surface of the lunar highlands by post-basin impacts. Geochimica et Cosmochimica Acta 70:5935-5956.

Kring D. A., Hill D. H., and Boynton W. V. 1995. The geochemistry of a new lunar meteorite, QUE93069, a breccia with highland affinities (abstract). Proceedings, 26th Lunar and Planetary Science Conference. pp. 801-802.

Kuehner S. M., Irving A. J., Gellissen M., and Korotev R. L. 2010. Petrology and composition of lunar granulite Northwest Africa 5744: A unique recrystallized, magnesian crustal sample (abstract). Proceedings, 41st Lunar and Planetary Science Conference #1552.

Kent J. J., Brandon A. D., Lapen T. J., Peslier A. H., Irving A. J., and Coleff D. M. 2012. In situ chemical characterization of mineral phases in lunar granulite Northwest Africa 5744 (abstract). Proceedings, 43rd Lunar and Planetary Science Conference #2559.

Liang Y., Sun C., and Yao L. 2013. A REE-in-two-pyroxene thermometer for mafic and ultramafic rocks. Geochimica et Cosmochimica Acta 102:246-260.

Lindsley D. H. 1983. Pyroxene thermometry. American Mineralogist 68:477-493.

Lindstrom M. M. and Lindstrom D. J. 1986. Lunar granulites and their precursor anorthositic norites of the early lunar crust. Journal of Geophysical Research 91, B4:D263-D276.

Lindstrom M. M., Schwarz C., Score R., and Mason B. 1991. MacAlpine Hills 88104 and 88105 lunar highland meteorites: General description and consortium overview. Geochimica et Cosmochimica Acta 55:2999-3007.

Lindstrom M. M., Wentworth S. J., Martinez R. R., Mittlefehldt D. W., McKay D. S., Wang M.-S., and Lipschutz M. E. 1991. Geochemistry and petrography of the MacAlpine Hills lunar meteorites. Geochimica et Cosmochimica Acta 55:3089-3103.

Lindstrom M. M., Mittlefehldt D. W., Morris R. V., Martinez R. R., and Wentworth S. J. 1995. QUE93069, a more mature regolith breccia for the Apollo 25th anniversary (abstract). Proceedings, 26th Lunar and Planetary Science Conference. pp. 849-850.

Longhi J. and Ashwall L. D. 1985. Two-stage models for lunar and terrestrial anorthosites: Petrogenesis without a magma ocean. Proceedings, 15th Lunar and Planetary Science Conference. pp. C571-C584.

Longhi J. 2003. A new view of lunar ferroan anorthosites: Postmagma ocean petrogenesis. Journal of Geophysical Research 108:E8 pp. 5083.

Ma M.-S. and Schmitt R. A. 1982. Chemistry of the matrix, the glass coating and an olivine clast from polymict ANT breccia 60035 (abstract). Proceedings, 13th Lunar and Planetary Science Conference. pp. 453-454.

Maloy A. K., Treiman A. H., and Shearer C. K. Jr. 2005. A magnesian granulite clast in lunar meteorite ALHA81005 (abstract). Proceedings, 68th Annual Meeting of the Meteoritical Society #5278.

McCallum I. S. and O'Brien H. E. 1996. Stratigraphy of the lunar highlands crust: Depth of burial of lunar samples from cooling rate studies. American Mineralogist 81:1166-1175.

McCallum I. S. and Schwartz J. M. 2001. Lunar Mg suite: Thermobarometry and petrogenesis of parental magmas. Journal of Geophysical Research 106:27969-27983.

Neal C. R., Taylor L. A., Lui Y.-G., and Schmitt R. A. 1991. Paired lunar meteorites MAC88104 and MAC88105: A new "FAN" of lunar petrology. Geochimica et Cosmochimica Acta 55:3037-3049.

Nishiizumi K., Caffee M. W., Jull A. J. T., and Reedy R. C. 1996. Exposure history of lunar meteorites Queen Alexandra Range 93069 and 94269. Meteoritics & Planetary Science 31:893-896.

Onorato P. I. K. and Uhlmann D. R. 1978. Olivine cooling speedometers. Proceedings, 9th Lunar and Planetary Science Conference. pp. 613-628.

Palme H., Spettel B., Jochum K. P., Dreibus G., Weber H., Weckwerth G., Wänke H., Bischoff A., and Stöffler D. 1991. Lunar highland meteorites and the composition of the lunar crust. Geochimica et Cosmochimica Acta 55:3105-3122.

Papike J. J., Fowler G. W., and Shearer C. K. 1994. Orthopyroxene as a recorder of lunar crust evolution: An ion microprobe investigation of Mg-suite norites. American Mineralogist 79:796-800.

Papike J. J., Fowler G. W., Shearer C. K., and Layne G. D. 1996. Ion microbrobe investigation of plagioclase and orthopyroxene from lunar Mg-suite norites:Implications for calculating parental melt REE concentrations and for assessing postcrystallization REE redistribution. Geochimica et Cosmochimica Acta 60:3967-3978.

Papike J. J., Fowler G. W., and Shearer C. K. 1997. Evolution of the lunar crust: SIMS study of plagioclase from ferroan anorthosites. Geochimica et Cosmochimica Acta 61:2343-2350.

Phinney W. C. 1994. FeO and MgO in plagioclase of lunar anorthosites: Igneous or metamorphic? (abstract). Proceedings, 25th Lunar and Planetary Science Conference. pp. 1081-1082.

Ringwood A. E. and Seifert S. 1986. Nickel-cobalt abundance systematics and their bearing on lunar origin. In Origin of the Moon, edited by Hartmann W. K., Phillips R. J., and Taylor G. J. Houston: Lunar and Planetary Institute. pp. 249-278.

Robinson K. L., Treiman A. H., and Joy K. H. 2012. Basaltic fragments in lunar feldspathic meteorites: Connecting sample analyses to orbital remote sensing. Meteoritics & Planetary Science 47:387-399.

Salpas P. A., Lindstrom M. M., and Taylor L. A. 1988. Highland materials at Apollo 17: Contributions from 72275. Proceedings, 18th Lunar and Planetary Science Conference. pp. 11-19.

Satterwhite C., Lindstrom M., and Mason B., edited by Score R. and Lindstrom M. 1994. Antarctic Meteorite Newsletter 17:2.

Score R. and Mason B., edited by Lindstrom M. M. 1989. Antarctic Meteorite Newsletter 12:3 amended version.

Shearer C. K., Hess P. C., Wieczorek M. A., Pritchard M. E., Parmentier E. M., Borg L. E., Longhi J., Elkins-Tanton L. T., Neal C. R., Antonenko I., Canup R. M., Halliday A. N., Grove T. L., Hager B. H., Lee D-C., and Wiechert U. 2006. Thermal and magmatic evolution of the Moon. Reviews in Mineralogy and Geochemistry 60:365-502.

Shearer C. K. and Papike J. J. 1999. Magmatic evolution of the Moon. American Mineraolgist 84:1469-1494.

Shearer C. K. and Papike J. J. 2005. Early crustal building processes on the Moon: Models for the petrogenesis of the magnesian suite. Geochimica et Cosmochimica Acta 69:3445-3461.

Shervais J. W. and McGee J. J. 1998. Ion microprobe study of troctolites, norite, and anorthosites from Apollo 14: evidence for urKREEP assimilation during petrogenesis of Apollo 14 Mg-suite rocks. Geochimica et Cosmochimica Acta 62:3009-3023.

Shervais J, and McGee J. 1999. Petrology of the Western Highland Province: Ancient crust formation at the Apollo 14 site. Journal of Geophysical Research 104, E3:5891-5920

Shervais J. W. and McGee J. J. 1999. KREEP cumulates in the western lunar highlands: Ion and electron microprobe study of alkali-suite anorthosites and norites from Apollo 12 and 14. American Mineralogist 84:806-820.

Snyder G. A., Taylor L. A., and Neal C. R. 1992. The sources of mare basalts: A model involving lunar magma ocean crystallization, plagioclase floatation and trapped instantaneous residual liquid. Geochimica et Cosmochimica Acta 56:3809-3823.

Spudis P. D. and Davis P. A. 1986. A chemical and petrological model of the lunar crust and implications for lunar crustal origin. Proceedings, 17th Lunar and Planetary Science Conference. pp. E84-E90.

Stöffler D. and Ryder G. 2001. Stratigraphy and isotope ages of lunar geologic units: chronological standard for the inner Solar System. Space Science Reviews 96:9-54.

Stöffler D., Ryder G., Ivanov B. A., Artemieva N. A., Cintala M. J., and Grieve R. A. 2006. Cratering history and lunar chronology. Reviews in Mineralogy & Geochemistry 60:519-596.

Takeda H., Yamaguchi A., Bogard D. D., Karouji Y., Ebihara M., Ohtake M., Kaiki K., and Arai T. 2006. Magnesian anorthosites and a deep crustal rock from the farside crust of the moon. Earth and Planetary Science Letters 247:171-184.

Thalmann C., Eugster O., Herzog G. F., Klein J., Krähenbühl U., Vogt S., and Xue S. 1996. History of lunar meteorites Queen Alexandra Range 93069, Asuka 881757, and Yamato 793169 based on noble gas isotopic abundances, radionuclide concentrations, and chemical composition. Meteoritics & Planetary Science 31:857-868.

Thomas J. B., Bodnar R. J., Shimizu N., and Chesner C. A. 2003. Melt inclusions in zircon. Reviews in Mineralogy and Geochemistry 53:63-87.

Toksöz M. N. 1979. Planetary seismology and interiors. Reviews of Geophysics and Space Physics 17:1641-1655.

Treiman A. H., Maloy A. K., Shearer C. K., and Gross J. 2010. Magnesian anorthositic granulites in lunar meteorites Allan Hills A81005 and Dhofar 309: Geochemistry and global significance. Meteoritics & Planetary Science 45:163-180.

Tsuchiyama A., Nakamura T., Nakano T., and Nakamura N. 2002. Three-dimensional description of the Kobe meteorite by micro X-ray CT method: Possibility of three-dimensional curation of meteorite samples. Geochemical Journal 36:369-390.

Van Orman J. A., Cherniak D. J., and Kita N. T. 2012. Magnesium diffusion in plagioclase (abstract). Proceedings, 43rd Lunar and Planetary Science Conference, #1467.

Walker D., Grove T. L., Longhi J., Stolper E. M., and Hays J. F. 1973. Origin of lunar feldspathic rocks. Earth and Planetary Science Letters 20:325-336.

Walton E. L. and Spray J. G. 2003. Mineralogy, microtexture, and composition of shock-induced melt pockets in the Los Angeles basaltic shergottite. Meteoritics & Planetary Science 38: 1865-1875.

Walton E. L. and Herd C. D. K. 2007. Localized shock melting in lherzolitic shergottite Northwest Africa 1950: Comparison with Allan Hills 77005. Meteoritics & Planetary Science 42:63-80.

Warner J. L., Simonds C. H., and Phinney W. C. 1976. Genetic distinction between anorthosites and Mg-rich plutonic rocks: new data from 76255. Proceedings, 7th Lunar Science Conference. pp. 915-917.

Warren P. H. 1985. The magma ocean concept and lunar evolution. Annual Reviews of Earth and Planetary Sciences 13:201-240.

Warren P. H., Jerde E. A., and Kallemeyn G. W. 1989. Lunar meteorites: Siderophile element contents, and implications for the composition and origin of the Moon. Earth and Planetary Science Letters 91:245-260.

Warren P. H. 1990. Lunar anorthosites and the magma-ocean plagioclase-floatation hypothesis: Importance of FeO enrichment in the parent magma. American Mineralogist 75:46-58.

Warren P. H. and Kallemeyn G. W. 1991. The MacAlpine Hills lunar meteorite and implications of the lunar meteorites collectively for the composition and origin of the moon. Geochimica et Cosmochimica Acta 55:3123-3138.

Warren P. H. 1993. A concise compilation of petrologic information on possibly pristine nonmare Moon rocks. American Mineralogist 78:360-376.

Warren P. H. and Rubin A. E. 2010. Pyroxene-selective impact smelting in ureilites. Geochimica et Cosmochimica Acta 74:5109-5133.

Wasson J. T. and Kallemeyn G. W. 1988. Compositions of chondrites. Philosophical Transactions of the Royal Societs of London, Series A, Mathematical and Physical Sciences 325:535-544.

Warren P.H., Ulff-Møller F., and Kallemeyn G.W. 2005. “New” lunar meteorites: Impact melt and regolith breccias and large-scale heterogeneities of the upper lunar crust. *Meteorit. Planet. Sci.* 40. pp. 989.

Weill D. F. and Drake M. J. 1973. Europium anomaly in plagioclase feldspar: Experimental results and semiquantatitative model. Science 180, 4090:1059-1060

Weisberg M. K., Smith C., Benedix G., Herd C. D. K., Righter K., Haack H., Yamaguchi A., Chennaoui Aoudjehane H., and Grossman J. N. 2009. The Meteoritical Bulletin. Meteoritics & Planetary Science 44:1355-1397.

Wieczorek M. A. and Zuber M. T. 2001. The composition and origin of the lunar crust: Constraints from central peaks and crustal thickness modeling. Geophysical Research Letters 28:4023-4026.

Wieczorek M. A., Jolliff B. L., Khan A., Pritchard M. E., Weiss B. P., Williams J. G., Hood L. L., Righter K., Neal C. R., Shearer C. K., McCallum I. S., Tompkins S., Hawke B. R., Peterson C., Gillis J. J., and Bussey B. 2006. The Constitution and structure of the lunar interior. Reviews in Mineralogy and Geochemistry 60:221-364.

Wieczorek M. A., Neumann G. A., Nimmo F., Kiefer W. S., Taylor G. J., Melosh H. J., Phillips R. J., Solomon S. C., Andrews-Hanna J. C., Asmar S. W., Konopliv A. S., Lemoine F. G., Smith D. E., Watkins M. M., Williams J. G., and Zuber M. T. 2013. The crust of the Moon as seen by GRAIL. Science 339:671-675.

Wood J. A. 1975. Lunar petrogenesis in a well-stirred magma ocean (abstract). Proceedings, 6th Lunar Science Conference. pp. 881-883.

Appendices:

Supplementary Files

NWA5744_Tif_Image_Stack.zip: TIF image stack of the 3D CT volume

NWA5744_Video_Color.zip: AVI video files panning through the 3D volume along the X, Y, and Z planes in false color, with warmer colors indicating greater density.

NWA 5744_Video_BW.zip: AVI video files panning through the 3D volume along the X, Y, and Z planes in black and white, with lighter color indicating greater density.

NWA5744_CT_Images.zip: JPG and PDF images of select slices through the 3D volume, indicating calculated density ranges for those slices.

Appendix A

NWA 5744 Major Element Data

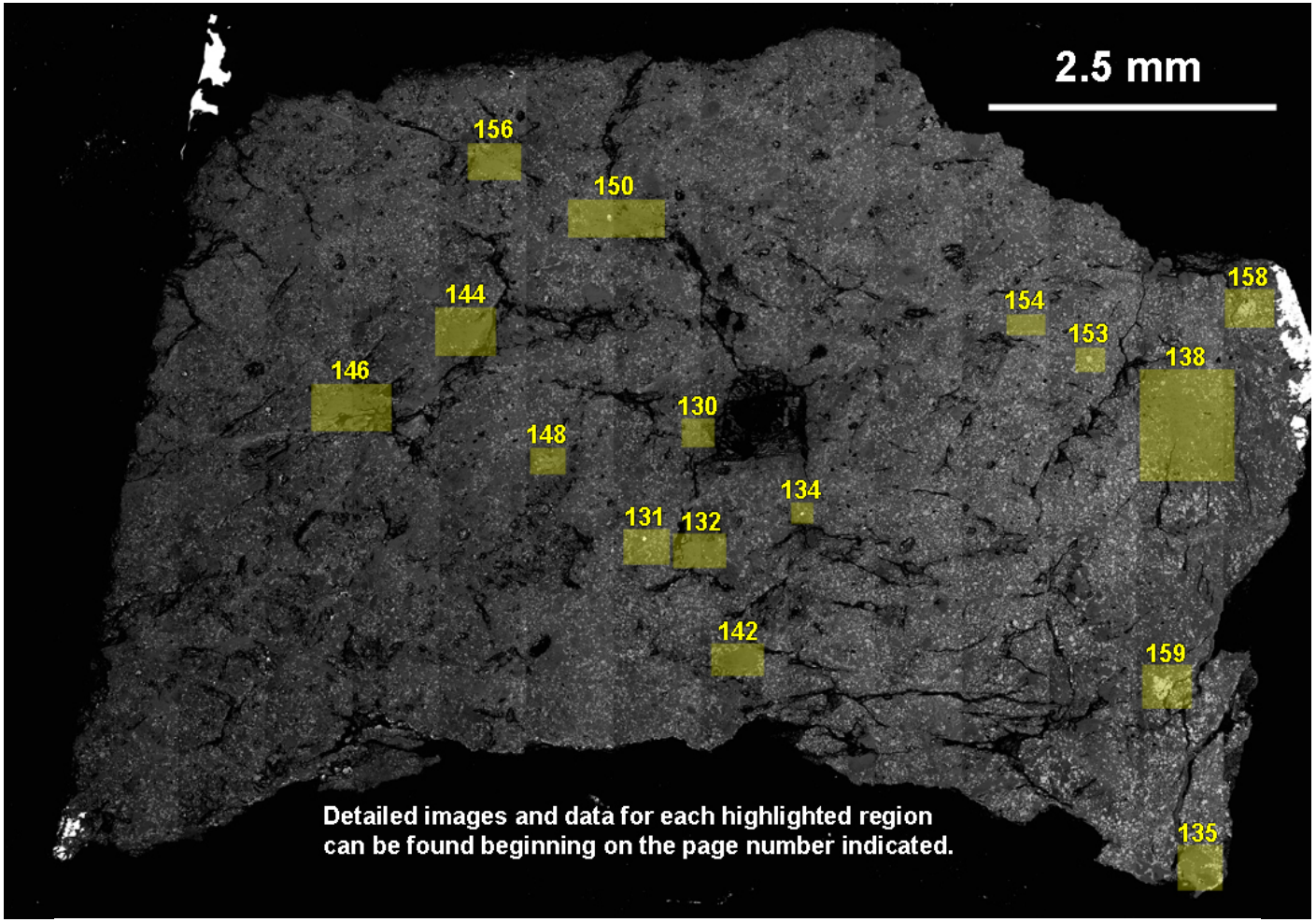

Figure A1: Map of slab piece 1 indicating the regions I obtained major element data via EMP analysis. The number beside each reagion indicates the page that data can be found on.

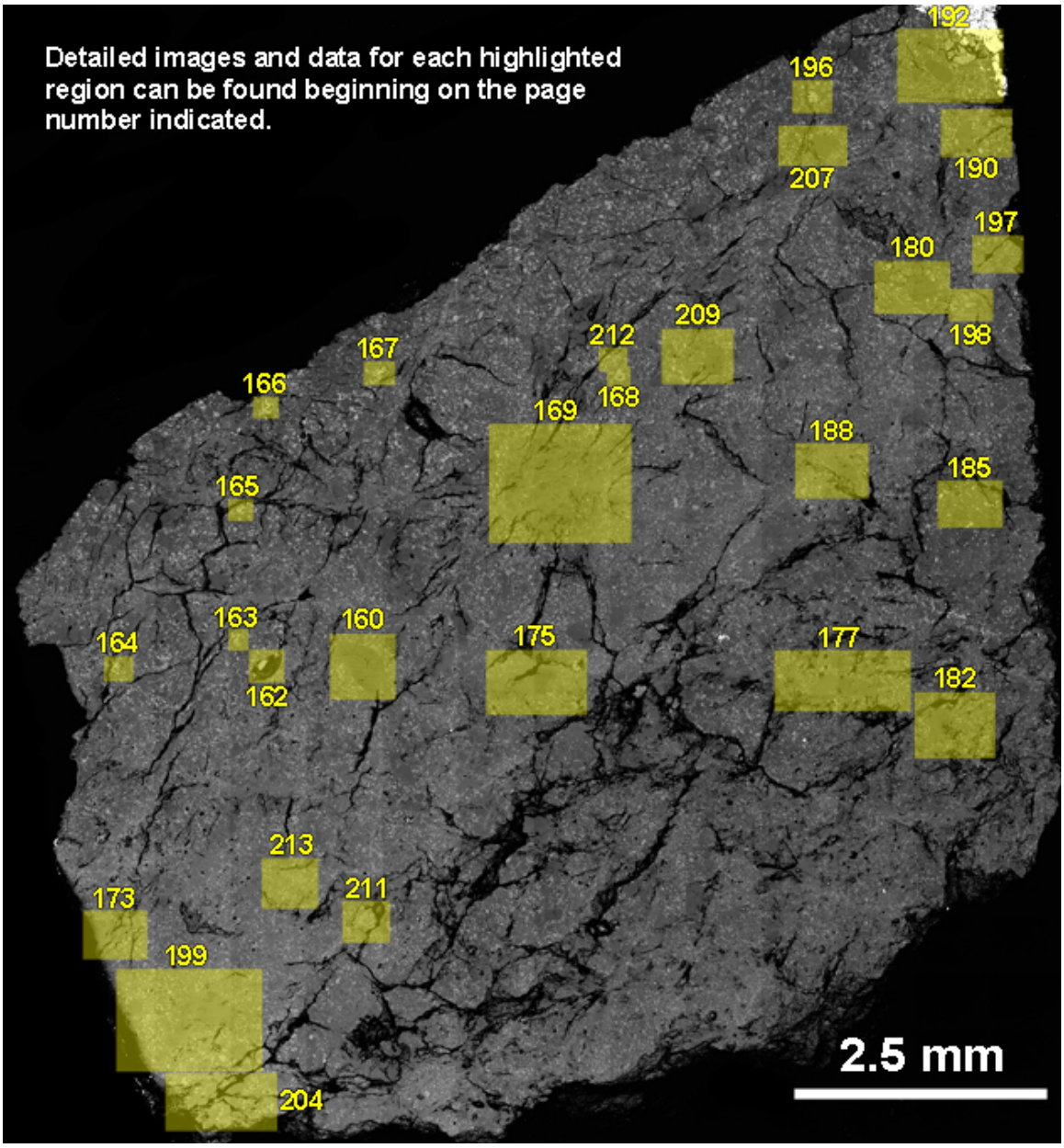

Figure A2: Map of slab piece 2 indicating the regions I obtained major element data via EMP analysis. The number beside each reagion indicates the page that data can be found on.

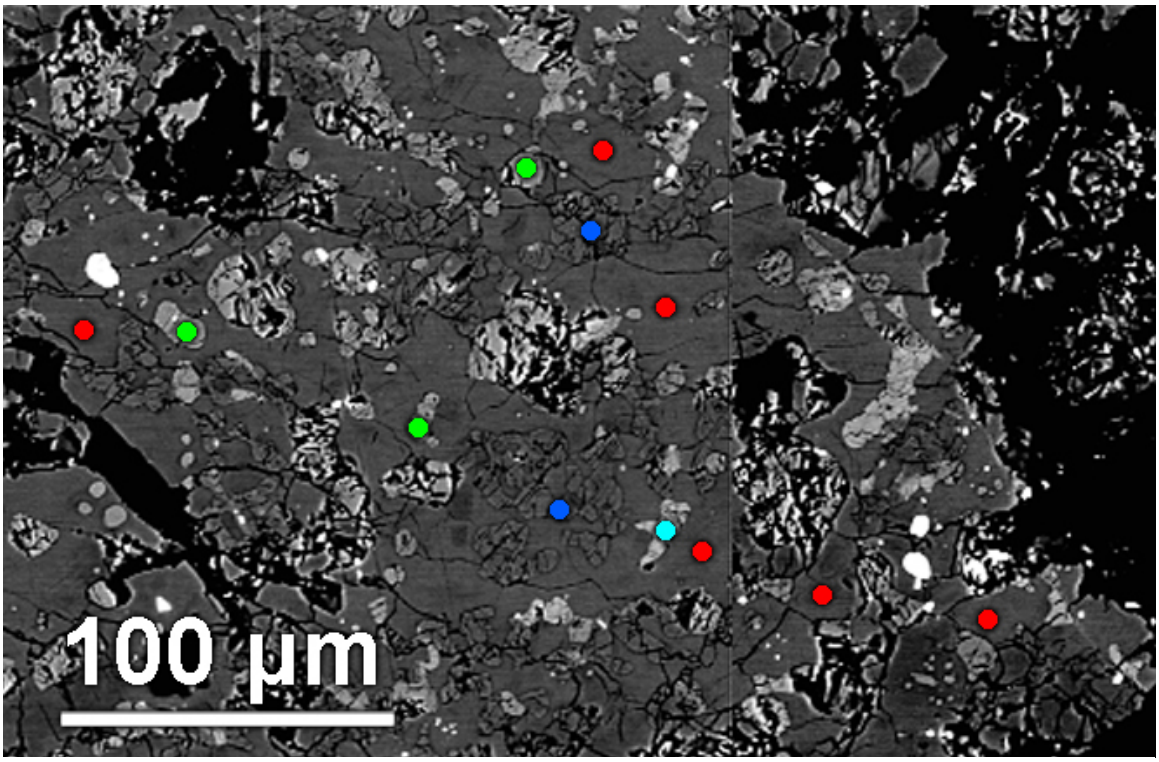

Figure A3: Map of Table A1 EMP point locations. Red, green, dark-blue, and light-blue dots respectively represent plagioclase, olivine, clinoenstatite, and augite measurement locations.

Table A1: Averaged major element content of minerals in Figure A3

	Plag	1σ	Olv	1σ	C-En	1σ	Aug	1σ
Points	6		3		2		1	
Na_2O (wt %)	0.43	0.04	0.03	0.02	b.d.	-	0.17	0.03
MgO	0.09	0.01	43.04	0.35	29.83	0.33	13.27	0.16
Al_2O_3	34.96	0.20	0.15	0.02	1.33	0.03	10.88	0.09
SiO_2	44.78	0.32	38.80	0.24	54.95	0.24	50.91	0.23
P_2O_5	b.d.	-	b.d.	-	b.d.	-	0.03	0.03
K_2O	b.d.	-	b.d.	-	b.d.	-	0.06	0.03
CaO	19.03	0.30	0.22	0.03	2.42	0.09	20.76	0.31
TiO_2	b.d.	-	0.15	0.02	0.77	0.03	1.05	0.03
MnO	0.05	0.03	0.23	0.04	0.23	0.04	0.08	0.03
FeO	0.29	0.06	17.21	0.33	10.06	0.24	3.77	0.14
Total	99.62		99.83		99.58		101.00	

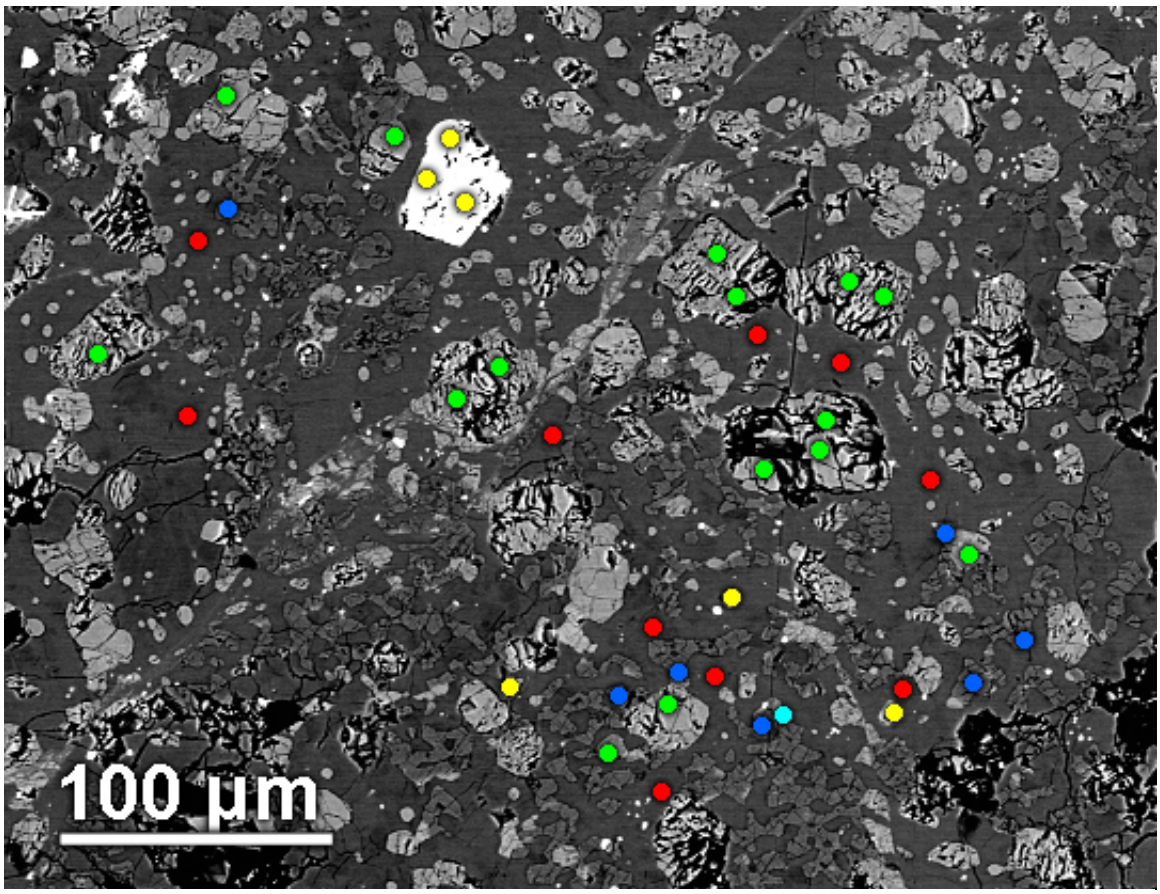

Figure A4: Map of Table A2 EMP point locations. Red, green, dark-blue, light-blue, and yellow dots respectively represent plagioclase, olivine, clinoenstatite, augite, and Ti-chromite measurement locations.

Table A2: Averaged major element content of minerals in Figure A4

	Plag	1σ	Olv	1σ	C-En	1σ	Aug	1σ	Chrm[1]	1σ	Chrm[2]	1σ
Points	10		15		7		1		3		3	
Na_2O	0.44	0.04	0.03	0.02	0.03	0.02	0.07	0.03	b.d.	-	b.d.	-
MgO	0.10	0.01	41.57	0.34	29.18	0.33	16.73	0.20	8.65	0.17	7.88	0.16
Al_2O_3	34.98	0.20	0.21	0.02	1.90	0.03	1.98	0.03	12.68	0.18	12.79	0.18
SiO_2	44.94	0.32	39.14	0.24	54.32	0.24	52.54	0.23	0.19	0.02	0.22	0.02
P_2O_5	0.03	0.03	b.d.	-	b.d.	-	b.d.	-	b.d.	-	b.d.	-
K_2O	0.02	0.02	b.d.	-	0.03	0.02	0.06	0.03	0.04	0.03	b.d.	-
SO_2	0.02	0.03	b.d.	-	b.d.	-	b.d.	-	b.d.	-	b.d.	-
CaO	19.03	0.30	0.23	0.03	1.86	0.08	21.15	0.32	0.26	0.04	0.57	0.04
TiO_2	0.02	0.02	0.18	0.02	0.65	0.03	0.99	0.03	7.33	0.10	6.30	0.10
MnO	0.01	0.03	0.24	0.04	0.23	0.04	0.13	0.04	0.31	0.07	0.31	0.07
FeO	0.36	0.06	18.94	0.35	11.23	0.25	5.02	0.16	26.85	0.51	27.98	0.53
Cr_2O_3	b.d.	-	b.d.	-	b.d.	-	b.d.	-	41.61	0.56	41.38	0.56
Total	99.94		100.52		99.45		98.67		97.91		97.43	

[1] The average of the three points on the single grain near the top of Figure A4.
[2] The average of the three smaller separate grains nearer the bottom of Figure A4.

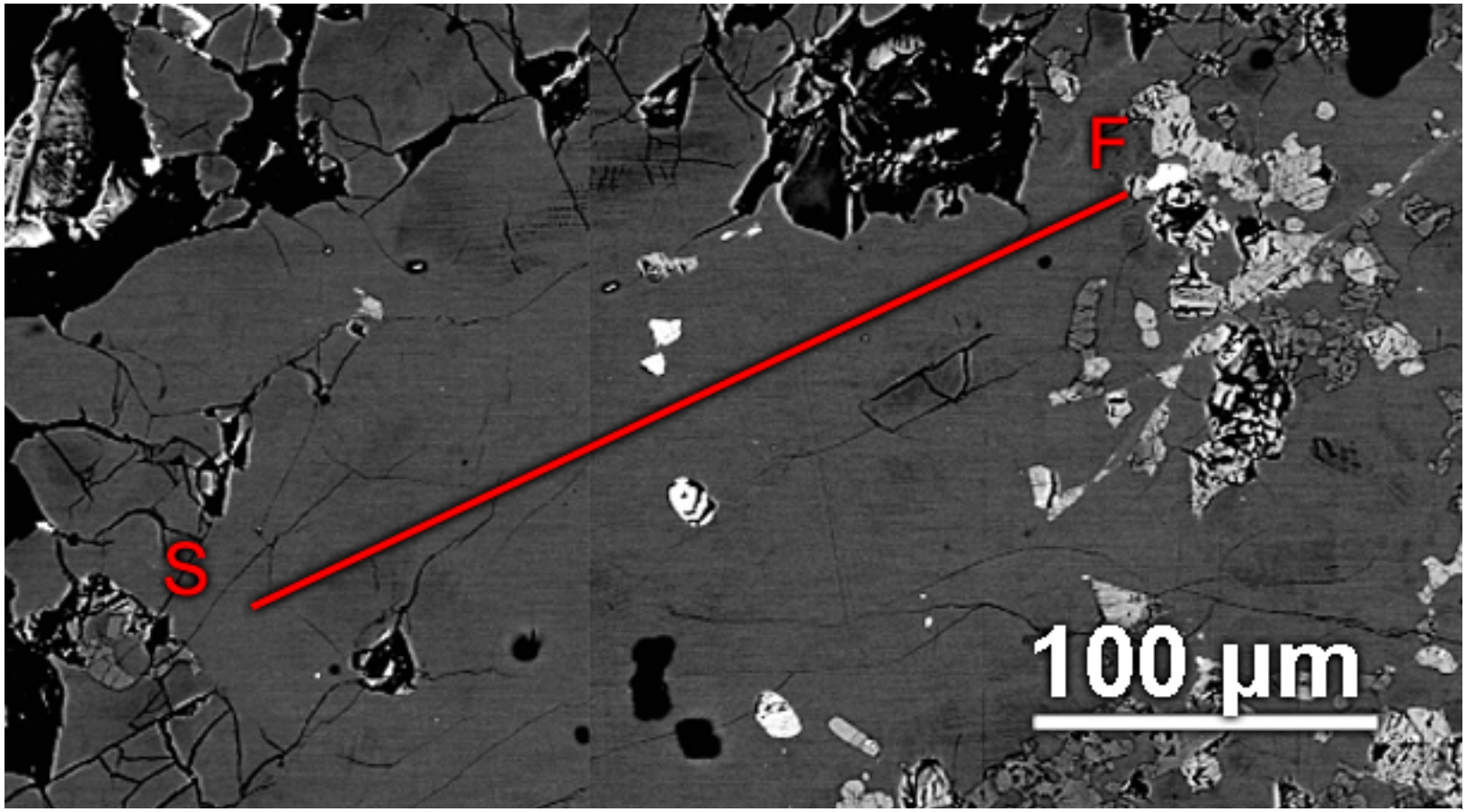

Figure A5: Map of Table A3 EMP plagioclase line scan location. Line is 310 µm in length and was configured to acquire 25 points with 12.4 µm spacing.

Table A3: Major element content of individual plagioclase points in the line scan shown in Figure A5

Point #	1σ	1	2	3	4	5	6	7	8	9	10	11	12	13	14	15	16	17
Na_2O	0.04	0.19	0.19	0.22	0.20	0.17	0.28	0.28	0.26	0.22	0.25	0.18	0.20	0.23	0.23	0.21	0.27	0.23
MgO	0.03	0.03	0.04	0.04	0.03	0.24	0.05	0.03	0.05	0.03	0.04	0.03	0.09	0.03	0.04	0.03	0.05	0.06
Al_2O_3	0.20	35.65	35.44	35.56	35.34	35.61	35.13	35.48	35.43	35.81	35.77	35.87	35.21	35.51	35.68	35.70	35.63	35.49
SiO_2	0.31	44.70	44.57	44.12	44.04	44.37	44.24	44.81	44.86	44.65	44.92	44.70	43.99	44.95	44.74	44.35	44.84	44.80
K_2O	0.02	b.d.	b.d.	b.d.	b.d.	b.d.	b.d.	b.d.	b.d.	b.d.	b.d.	b.d.	b.d.	b.d.	b.d.	b.d.	b.d.	b.d.
CaO	0.29	19.38	19.43	19.53	19.74	19.49	19.24	19.53	19.52	19.49	19.49	19.28	19.51	19.45	19.42	19.61	19.51	19.48
FeO	0.06	0.12	0.09	0.07	b.d.	0.10	b.d.	0.07	b.d.	b.d.	0.07	0.10	0.11	0.09	0.09	0.07	0.10	0.09
Total		100.07	99.78	99.54	99.35	99.98	98.94	100.21	100.12	100.19	100.53	100.16	99.10	100.25	100.20	99.97	100.40	100.15

Table A3, ctd

Point #	18	19	20	22	23	24	25
Na_2O	0.25	0.25	0.30	0.37	0.50	0.34	0.42
MgO	0.06	0.07	0.07	1.27	0.10	0.08	0.08
Al_2O_3	35.45	35.08	35.34	32.09	34.57	35.30	34.82
SiO_2	44.97	43.64	45.36	45.45	44.69	45.05	44.96
K_2O	0.03	0.09	b.d.	0.03	b.d.	b.d.	b.d.
CaO	19.40	19.36	19.30	19.17	19.00	19.17	19.09
FeO	0.08	0.14	0.23	0.49	0.27	0.22	0.22
Total	100.24	98.62	100.60	98.87	99.13	100.16	99.60

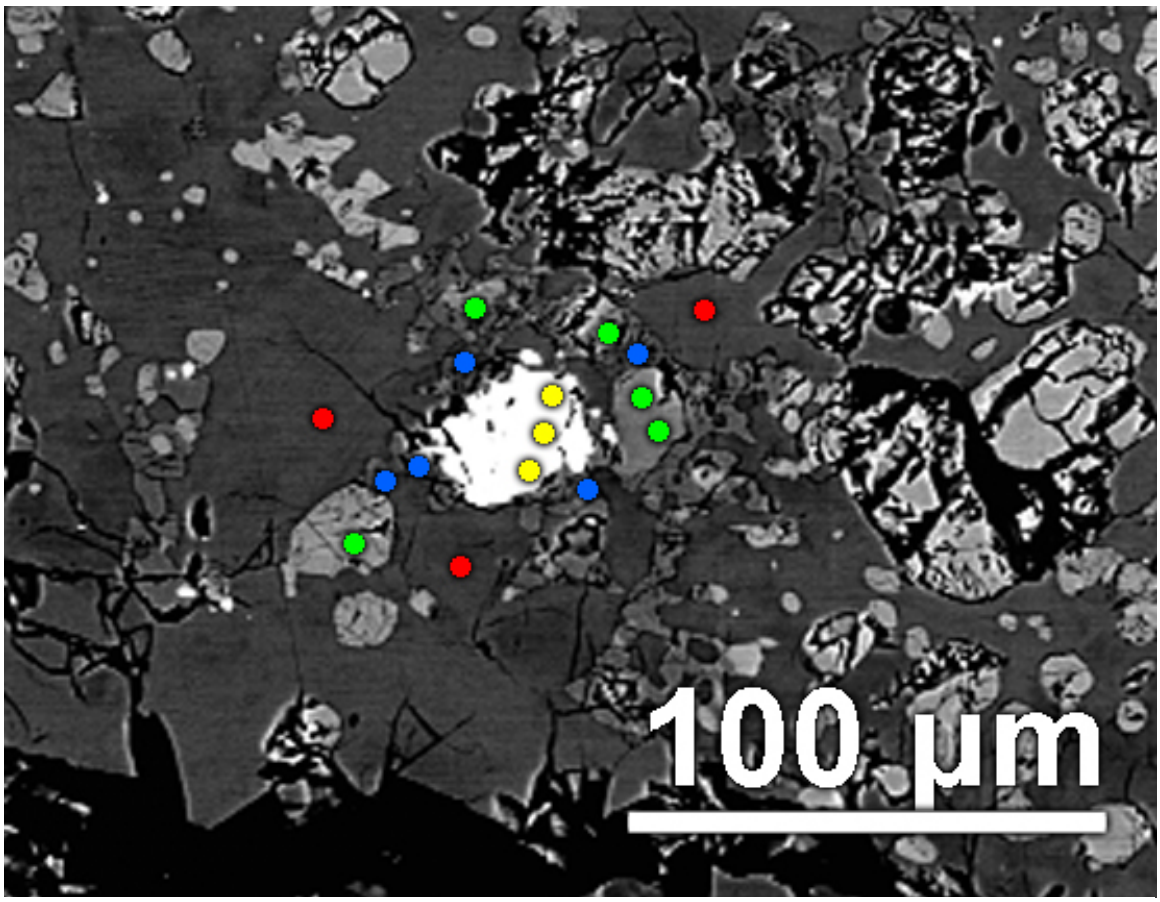

Figure A6: Map of Table A4 EMP point locations. Red, green, dark-blue, and yellow dots represent plagioclase, olivine, clinoenstatite, and Ti-chromite measurement locations, respectively.

Table A4: Averaged major element content of minerals in Figure A6

	Plag	1σ	Olv	1σ	C-En	1σ	Chrm	1σ
Points	3		5		5		3	
Na_2O	0.42	0.04	0.04	0.02	0.04	0.02	b.d.	-
MgO	0.09	0.01	42.72	0.35	29.45	0.33	8.00	0.16
Al_2O_3	35.06	0.20	0.08	0.01	1.54	0.03	13.44	0.19
SiO_2	45.13	0.32	38.88	0.24	54.64	0.24	0.03	0.02
K_2O	b.d.	-	0.05	0.02	0.03	0.02	b.d.	-
CaO	19.03	0.30	0.18	0.03	1.95	0.08	0.15	0.03
TiO_2	b.d.	-	0.13	0.02	0.68	0.03	6.17	0.10
MnO	b.d.	-	0.23	0.04	0.23	0.04	0.31	0.07
FeO	0.31	0.06	17.76	0.33	11.09	0.25	27.86	0.53
Cr_2O_3	b.d.	-	b.d.	-	b.d.	-	42.84	0.58
Total	100.05		100.07		99.64		98.80	

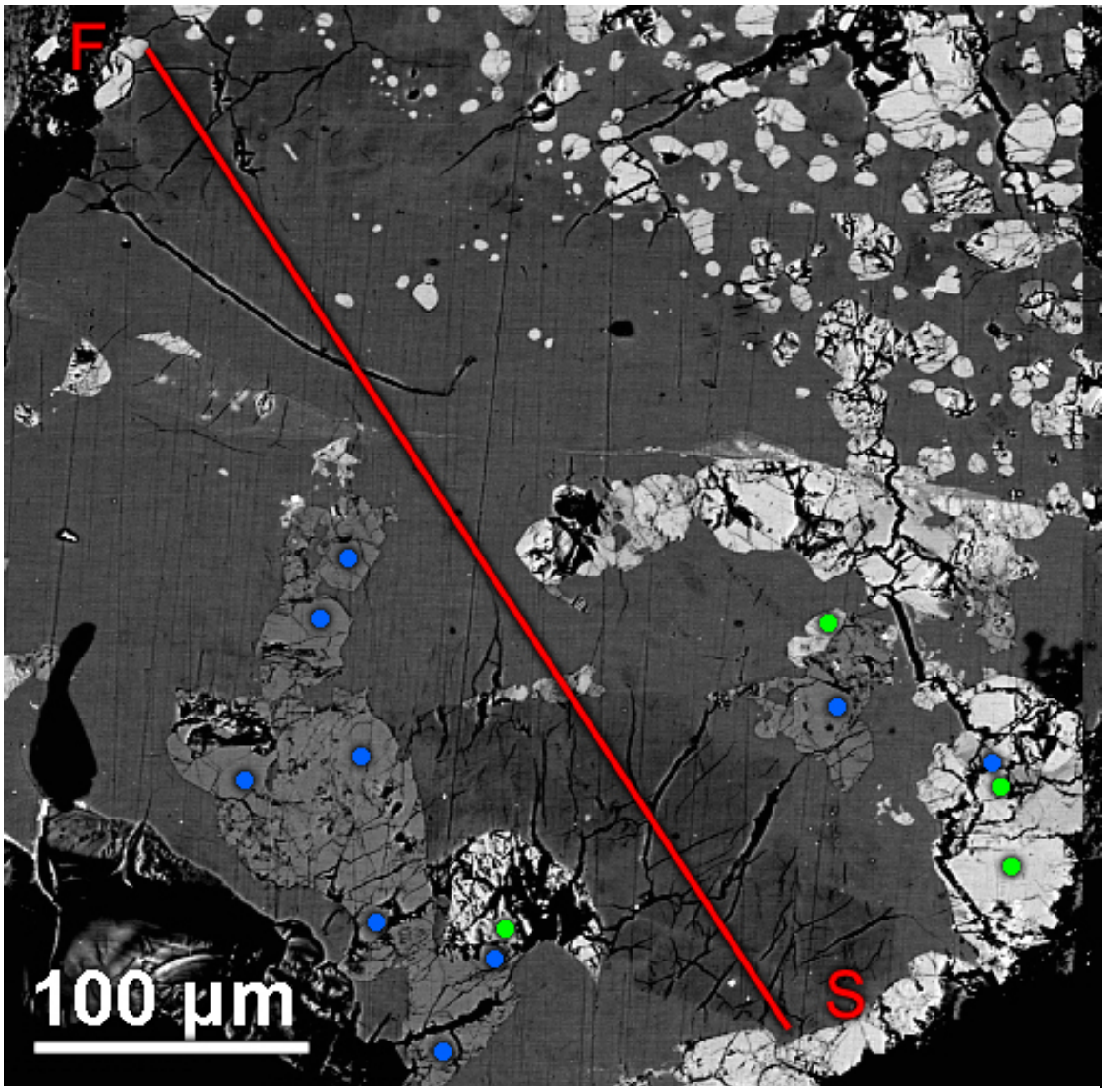

Figure A7: Map of Table A5 EMP point and Table A6 plagioclase line locations. Green and blue dots represent olivine and clinoenstatite, respectively. The line scan is 127 µm in length and was configured to acquire 35 points with 12.6 µm spacing.

Table A5: Averaged major element content of minerals in Figure A7

	Olv	1σ	C-En	1σ
Points	4		9	
Na_2O	0.09	0.02	b.d.	-
MgO	39.35	0.33	28.82	0.32
Al_2O_3	0.23	0.02	0.87	0.02
SiO_2	38.29	0.24	55.44	0.24
P_2O_5	0.05	0.03	b.d.	-
K_2O	0.07	0.03	b.d.	-
CaO	0.42	0.04	1.58	0.07
TiO_2	0.08	0.02	0.50	0.03
MnO	0.27	0.04	0.25	0.04
FeO	20.88	0.37	12.57	0.27
Total	99.73		100.01	

Table A6: Major element content of individual plagioclase points in the line scan shown in Figure A7

Point #	1σ	1	3	4	5	6	7	9	10	11	13	14	15	16	17	18	19	20
Na_2O	0.04	0.44	0.42	0.43	0.52	0.43	0.40	0.49	0.43	0.44	0.42	0.32	0.31	0.32	0.53	0.41	0.33	0.33
MgO	0.02	0.13	0.17	0.15	0.16	0.17	0.14	0.15	0.15	0.15	0.10	0.08	0.08	0.08	0.11	0.09	0.10	0.12
Al_2O_3	0.20	34.95	34.66	34.55	34.48	34.64	34.59	34.27	34.74	34.56	35.19	35.20	35.61	35.59	35.18	34.92	35.07	35.45
SiO_2	0.32	44.84	44.98	44.68	44.47	44.86	44.59	44.63	44.58	44.59	45.36	44.25	45.00	44.98	45.45	45.03	44.86	45.19
K_2O	0.02	0.03	0.03	0.03	0.07	0.05	0.03	0.05	b.d.	0.03	0.03	b.d.	0.03	b.d.	0.04	b.d.	0.03	b.d.
CaO	0.30	18.99	19.00	19.31	19.26	19.14	19.43	18.90	19.40	19.13	19.20	19.25	19.22	19.28	18.94	18.95	19.25	19.22
FeO	0.06	0.27	0.22	0.23	0.18	0.20	0.20	0.18	0.22	0.20	0.21	0.17	0.20	0.22	0.19	0.13	0.16	0.17
Total		99.65	99.49	99.37	99.14	99.49	99.38	98.68	99.52	99.09	100.50	99.25	100.46	100.47	100.44	99.53	99.80	100.47

Table A6, ctd

Point #	21	22	24	25	26	27	28	29	30	31	32	33	34	35
Na_2O	0.40	0.44	0.37	0.41	0.39	0.45	0.47	0.56	0.50	0.47	0.48	0.52	0.39	0.42
MgO	0.15	0.16	0.14	0.11	0.12	0.13	0.16	0.18	0.17	0.15	0.16	0.14	0.25	1.13
Al_2O_3	34.91	34.93	35.32	35.12	34.90	34.78	34.59	34.69	34.16	34.60	34.41	34.63	34.78	34.09
SiO_2	45.14	45.76	45.25	45.31	44.90	45.25	45.31	46.09	44.86	44.47	44.47	44.63	44.15	43.88
K_2O	0.03	b.d.	0.03	b.d.	0.03	0.03	0.04	0.05	0.04	b.d.	b.d.	0.03	b.d.	0.10
CaO	19.21	19.28	19.23	19.23	19.20	19.16	18.99	18.78	18.78	19.01	19.11	19.17	19.33	18.98
FeO	0.17	0.18	0.18	0.19	0.16	0.19	0.16	0.18	0.21	0.22	0.27	0.29	0.31	0.54
Total	100.02	100.75	100.51	100.38	99.70	99.98	99.72	100.52	98.72	98.93	98.91	99.41	99.21	99.13

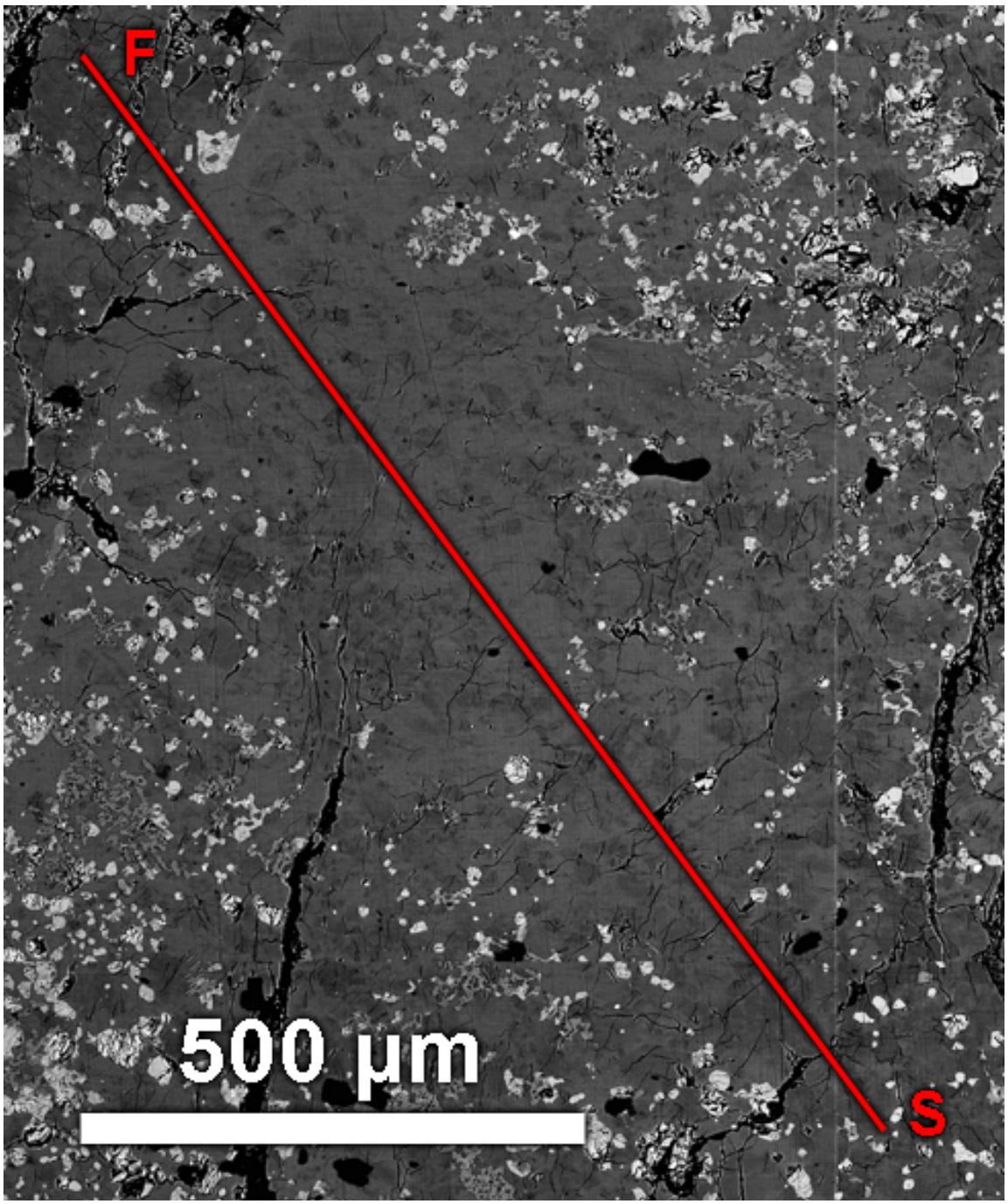

Figure A8: Map of Table A7 EMP plagioclase line location. The line scan is 1204 µm in length and was configured to acquire 100 points with 12.2 µm spacing.

Table A7: Major element content of individual plagioclase points in the line scan shown in Figure A8

Point #	1σ	1	2	3	4	5	7	8	9	10	11	12	13	14	15	16	17	18
Na_2O	0.04	0.39	0.25	0.37	0.41	0.30	0.31	0.39	0.47	0.38	0.32	0.36	0.34	0.44	0.39	0.52	0.40	0.41
MgO	0.01	0.05	0.04	0.06	0.07	0.06	0.04	0.06	0.11	0.08	0.05	0.04	0.04	0.06	0.08	0.08	0.08	0.07
Al_2O_3	0.20	35.22	35.34	35.22	34.91	35.20	35.13	34.90	35.40	35.08	35.19	35.07	35.11	34.81	34.80	34.44	35.08	34.90
SiO_2	0.31	44.75	43.76	44.23	44.16	44.06	44.15	44.56	45.47	44.78	44.63	44.08	44.06	43.95	44.10	44.68	44.42	44.91
K_2O	0.02	b.d.	b.d.	0.03	0.03	b.d.	b.d.	0.03	0.10	0.03	b.d.	b.d.	b.d.	b.d.	0.08	0.06	b.d.	0.03
CaO	0.30	19.27	19.55	19.31	19.26	19.58	19.47	19.19	18.58	19.04	19.44	19.09	19.34	19.36	19.29	19.31	19.19	19.40
FeO	0.05	0.16	0.14	0.14	0.12	0.13	0.07	0.13	0.14	0.15	0.12	0.10	0.14	0.10	0.13	0.14	0.13	0.12
Total		99.85	99.08	99.36	98.96	99.34	99.17	99.26	100.27	99.54	99.75	98.74	99.03	98.71	98.88	99.23	99.31	99.83

Table A7, ctd

Point #	21	22	23	24	25	26	27	28	29	30	32	33	34	35	36	38	39	41
Na_2O	0.37	0.42	0.48	0.22	0.29	0.29	0.31	0.44	0.37	0.43	0.33	0.17	0.17	0.18	0.20	0.40	0.39	0.40
MgO	0.09	0.10	0.10	0.04	0.07	0.07	0.07	0.10	0.10	0.10	0.09	0.02	0.03	0.02	0.01	0.07	0.11	0.08
Al_2O_3	34.82	34.86	34.92	35.30	35.12	35.07	35.03	34.82	35.03	34.87	35.08	35.32	35.20	35.37	35.37	35.02	34.69	34.92
SiO_2	43.78	44.32	45.26	44.25	44.35	44.03	43.54	44.33	44.96	44.83	44.47	43.63	43.69	44.04	43.48	44.97	44.23	44.47
K_2O	b.d.	0.03	0.05	b.d.	b.d.	0.03	b.d.	0.04	0.04	b.d.	b.d.	b.d.	b.d.	b.d.	0.03	b.d.	b.d.	b.d.
CaO	19.57	19.21	19.16	19.38	19.48	19.04	19.46	19.26	19.01	18.96	19.21	19.66	19.61	19.47	19.78	19.20	19.05	19.06
FeO	0.15	0.13	0.13	0.10	0.06	0.12	0.09	0.08	0.12	0.08	0.10	0.08	0.08	0.07	0.09	0.12	0.17	0.16
Total	98.78	99.07	100.08	99.29	99.37	98.64	98.50	99.08	99.64	99.26	99.29	98.88	98.78	99.15	98.94	99.79	98.64	99.08

Table A7, ctd

Point #	43	44	45	46	47	48	49	51	52	53	54	55	56	57	58	59	60	61
Na_2O	0.39	0.42	0.34	0.38	0.37	0.33	0.34	0.37	0.36	0.39	0.35	0.40	0.33	0.34	0.34	0.35	0.39	0.32
MgO	0.07	0.07	0.07	0.08	0.09	0.08	0.08	0.08	0.10	0.11	0.11	0.08	0.09	0.09	0.10	0.07	0.11	0.07
Al_2O_3	34.77	34.91	35.37	35.04	35.16	35.14	35.06	35.13	34.86	35.33	34.88	34.64	34.92	35.04	34.93	35.12	34.93	35.02
SiO_2	44.09	44.32	44.48	44.22	44.27	43.63	43.89	44.41	44.31	44.70	44.35	44.15	43.90	44.24	44.00	44.03	45.00	43.91
K_2O	0.03	b.d.	0.03	b.d.	b.d.	b.d.	b.d.	0.03	0.04	0.03	0.04	0.06	0.03	b.d.	0.07	b.d.	0.06	b.d.
CaO	19.20	19.11	19.18	19.39	19.31	19.15	19.20	19.23	19.35	19.26	19.15	19.13	19.46	19.39	19.08	19.43	18.91	19.28
FeO	0.06	0.07	0.09	0.05	0.08	0.07	0.08	0.06	0.09	0.10	0.11	0.10	0.11	0.07	0.09	0.09	0.13	0.05
Total	98.62	98.91	99.56	99.15	99.27	98.42	98.66	99.31	99.11	99.92	98.98	98.55	98.84	99.18	98.61	99.09	99.53	98.65

Table A7, ctd

Point #	62	63	64	65	66	67	68	69	70	71	72	73	74	75	76	78	79	80
Na_2O	0.37	0.29	0.34	0.38	0.42	0.36	0.40	0.29	0.33	0.42	0.37	0.38	0.39	0.32	0.36	0.47	0.26	0.28
MgO	0.09	0.06	0.07	0.09	0.10	0.16	0.09	0.06	0.07	1.31	0.09	0.08	0.11	0.09	0.07	0.13	0.08	0.07
Al_2O_3	35.00	35.18	34.94	35.03	34.71	34.78	34.74	35.04	35.11	33.38	34.65	34.67	34.76	35.17	34.83	34.82	35.03	34.98
SiO_2	43.97	44.15	44.29	44.55	44.45	44.06	44.14	44.29	44.46	44.70	43.86	44.26	44.47	43.84	43.72	44.94	43.59	43.85
K_2O	0.04	b.d.	0.03	b.d.	b.d.	0.05	0.03	b.d.	b.d.	0.03	b.d.	0.03	b.d.	b.d.	b.d.	b.d.	b.d.	b.d.
CaO	19.25	19.44	19.55	19.28	19.07	19.05	19.07	19.21	19.16	18.93	19.11	19.08	19.08	18.93	19.28	19.05	19.38	19.21
FeO	0.08	0.05	0.09	0.10	0.09	0.06	0.06	0.08	0.09	0.56	0.07	0.06	0.03	0.09	0.10	0.09	0.06	0.11
Total	98.79	99.17	99.32	99.44	98.85	98.51	98.52	98.97	99.21	99.33	98.15	98.56	98.85	98.42	98.36	99.49	98.40	98.49

Table A7, ctd

Point #	81	82	83	84	85	86	87	88	89	90	91	93	94	96
Na_2O	0.40	0.36	0.40	0.32	0.44	0.45	0.37	0.38	0.34	0.42	0.37	0.38	0.40	0.42
MgO	0.10	0.06	0.05	0.04	0.06	0.09	0.06	0.08	0.13	0.07	0.15	0.08	0.07	0.08
Al_2O_3	34.86	35.04	34.93	34.66	34.86	34.98	34.78	34.95	34.85	34.63	34.78	34.79	34.65	34.66
SiO_2	44.48	43.70	44.12	43.46	44.47	44.71	43.82	43.78	43.66	43.57	43.55	43.51	43.15	44.00
K_2O	b.d.	b.d.	b.d.	b.d.	b.d.	0.04	b.d.	b.d.	0.07	0.06	0.03	b.d.	0.13	0.03
CaO	19.03	19.62	19.17	19.34	19.07	19.06	19.25	19.41	19.13	19.10	19.20	19.43	19.34	18.99
FeO	0.14	0.11	0.13	0.15	0.17	0.20	0.16	0.17	0.18	0.15	0.22	0.15	0.19	0.13
Total	99.01	98.89	98.80	97.97	99.07	99.52	98.45	98.76	98.36	98.00	98.30	98.35	97.92	98.32

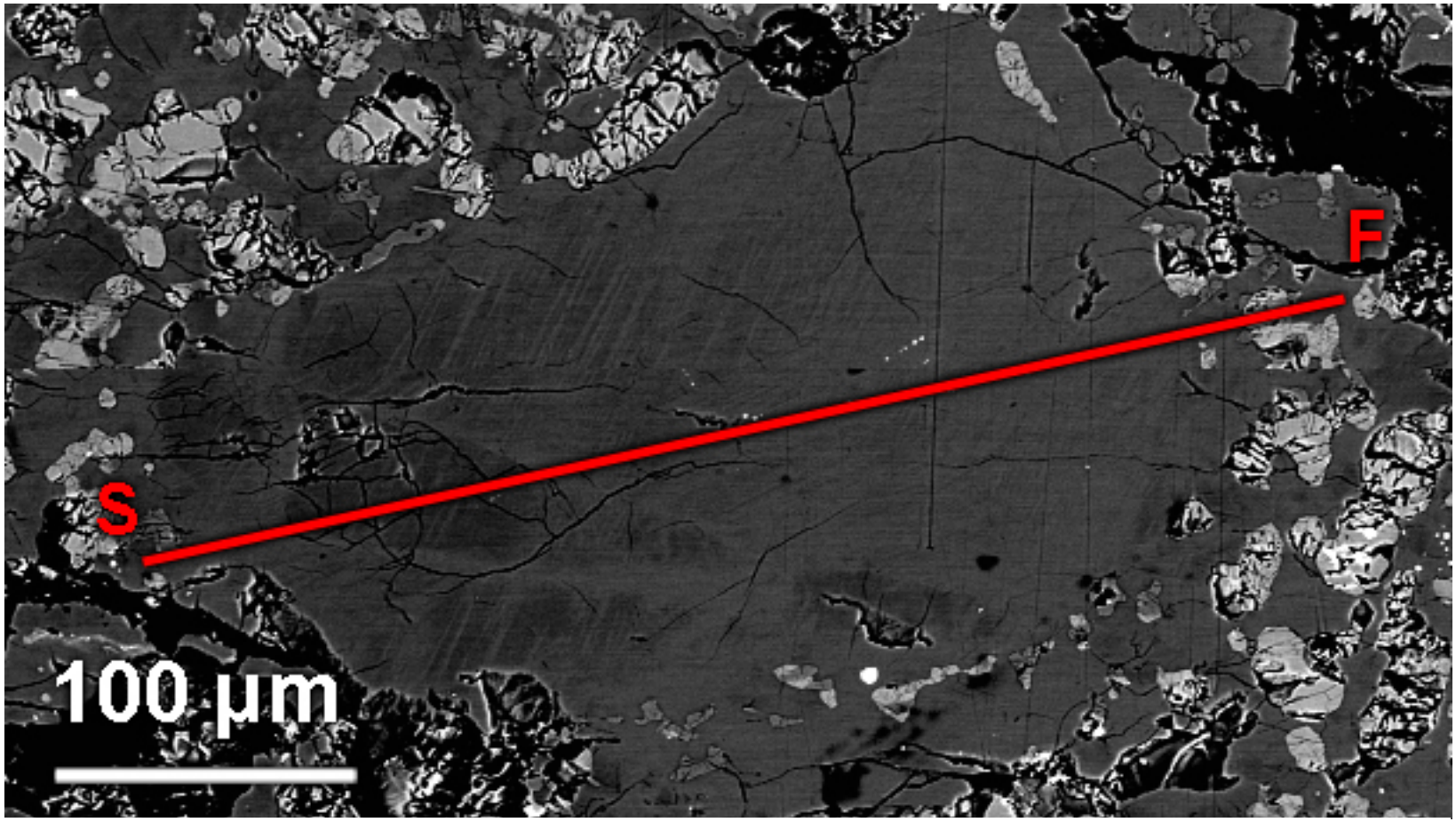

Figure A9: Map of Table A8 EMP plagioclase line location. The line scan is 400 µm in length and was configured to acquire 34 points with 12.1 µm spacing.

Table A8: Major element content of individual plagioclase points in the line scan shown in Figure A9

Point #	1σ	1	3	4	5	7	8	9	13	14	15	17	18	19	20	21	22	23
Na_2O	0.04	0.51	0.35	0.34	0.32	0.35	0.33	0.35	0.35	0.37	0.34	0.33	0.29	0.32	0.32	0.32	0.28	0.28
MgO	0.01	0.08	0.10	0.10	0.10	0.11	0.09	0.07	0.08	0.08	0.06	0.10	0.08	0.08	0.10	0.10	0.07	0.08
Al_2O_3	0.20	34.54	35.48	34.95	34.99	34.68	34.80	34.92	34.90	34.64	34.75	34.86	35.42	35.06	34.93	34.87	34.61	35.16
SiO_2	0.31	44.04	44.89	44.17	43.90	43.52	43.41	43.68	43.96	43.89	43.50	43.98	44.81	44.12	44.17	43.33	43.96	44.00
K_2O	0.02	0.04	0.03	b.d.	b.d.	0.05	b.d.	b.d.	b.d.	b.d.	b.d.	b.d.	b.d.	b.d.	b.d.	b.d.	b.d.	b.d.
CaO	0.30	18.90	19.09	19.26	19.17	19.17	19.50	19.02	19.26	19.14	19.37	19.18	19.21	19.09	19.18	19.22	19.26	19.30
FeO	0.05	0.26	0.15	0.16	0.16	0.14	0.11	0.10	0.09	0.07	0.07	0.06	0.09	0.10	0.09	0.11	0.08	0.07
Total		98.36	100.09	98.99	98.65	98.02	98.25	98.15	98.63	98.19	98.09	98.52	99.90	98.76	98.80	97.94	98.26	98.90

Table A8, ctd

Point #	24	25	26	27	28	29	30	31	33	34
Na_2O	0.28	0.28	0.29	0.24	0.22	0.19	0.41	0.36	0.42	0.43
MgO	0.07	0.06	0.05	0.06	0.05	0.03	0.25	0.20	0.07	0.07
Al_2O_3	35.30	35.25	35.34	35.43	35.33	35.46	34.55	34.96	34.99	35.08
SiO_2	44.26	44.22	44.66	43.90	43.88	43.85	44.26	44.38	44.14	44.38
K_2O	b.d.	b.d.	b.d.	b.d.	0.03	b.d.	b.d.	b.d.	b.d.	b.d.
CaO	19.36	19.36	19.33	18.99	19.31	19.31	18.93	18.93	18.96	18.86
FeO	0.04	0.07	0.06	0.12	0.10	0.16	0.25	0.37	0.30	0.34
Total	99.30	99.24	99.72	98.75	98.91	99.00	98.65	99.21	98.88	99.17

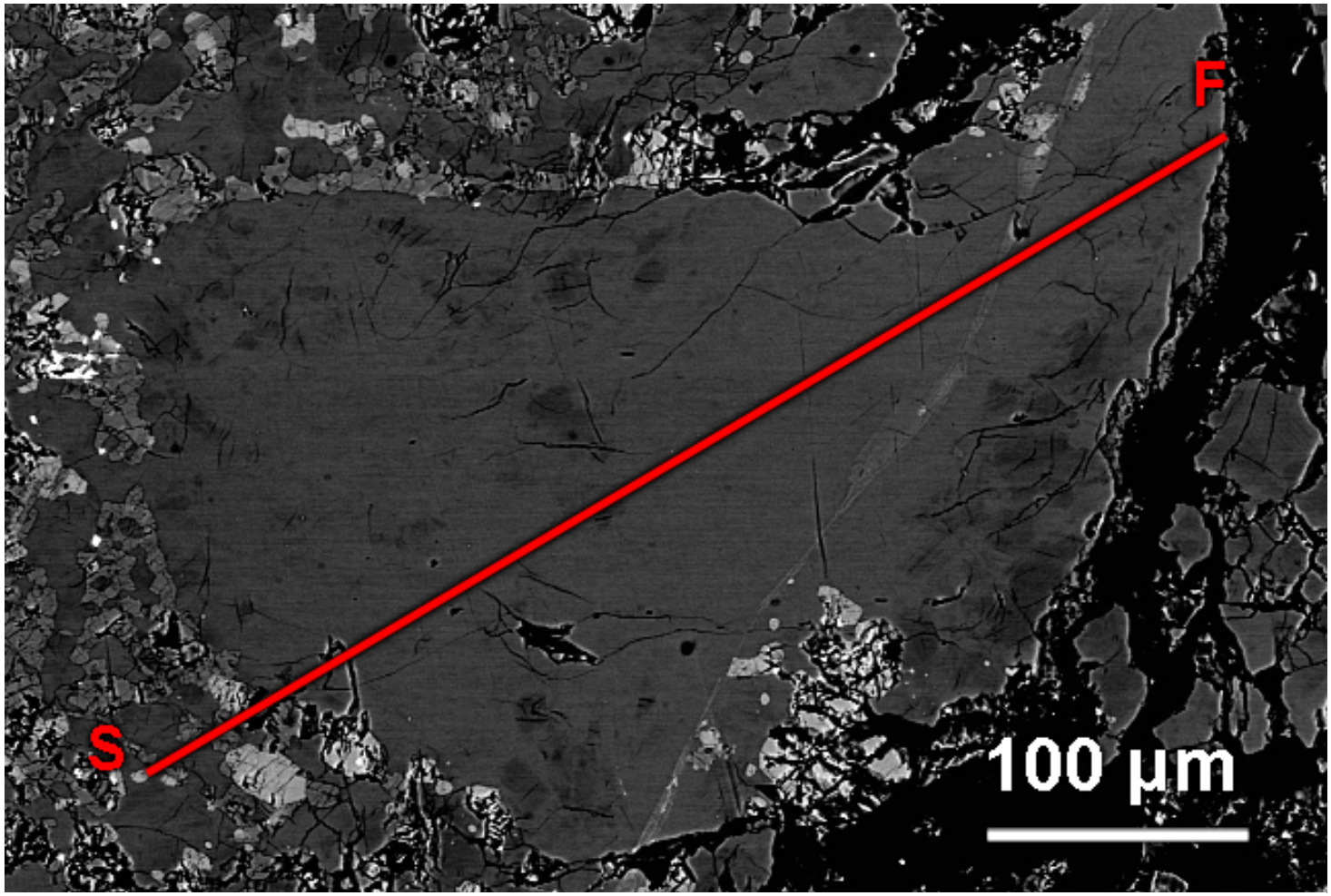

Figure A10: Map of Table A9 EMP plagioclase line location. The line scan is 471 µm in length and was configured to acquire 32 points with 15.2 µm spacing.

Table A9: Major element content of individual plagioclase points in the line scan shown in Figure A10

Point #	1σ	2	6	7	8	9	10	11	12	13	14	15	16	17	18	19	20	21
Na_2O	0.04	0.33	0.45	0.36	0.35	0.40	0.41	0.34	0.34	0.38	0.36	0.42	0.35	0.45	0.40	0.34	0.39	0.40
MgO	0.02	0.44	0.12	0.11	0.11	0.12	0.10	0.14	0.13	0.12	0.13	0.13	0.14	0.14	0.13	0.12	0.15	0.13
Al_2O_3	0.20	34.79	34.93	34.97	35.11	35.05	34.94	35.30	35.31	35.19	34.88	34.80	34.79	35.02	35.00	35.48	35.36	35.23
SiO_2	0.32	44.66	45.64	45.41	45.17	45.09	44.91	45.34	45.70	45.53	44.74	44.83	44.54	45.32	45.57	45.63	45.47	45.79
K_2O	0.02	b.d.	b.d.	b.d.	b.d.	0.03	b.d.	b.d.	b.d.	0.04	b.d.	0.03	b.d.	b.d.	b.d.	b.d.	b.d.	0.03
CaO	0.30	18.97	18.87	19.08	19.48	19.14	19.16	19.27	19.28	19.11	19.30	19.26	19.39	19.36	19.20	19.32	19.04	19.38
FeO	0.05	0.36	0.18	0.16	0.17	0.14	0.10	0.11	0.08	0.13	0.13	0.12	0.11	0.12	0.09	0.09	0.10	0.10
Total		99.55	100.19	100.08	100.39	99.96	99.63	100.50	100.84	100.50	99.54	99.60	99.32	100.42	100.40	100.99	100.50	101.06

Table A9, ctd

Point #	22	23	24	25	26	27	28	29	30	31
Na_2O	0.42	0.37	0.39	0.38	0.42	0.36	0.45	0.42	0.35	0.33
MgO	0.15	0.12	0.14	0.14	0.14	0.13	0.19	0.13	0.12	0.10
Al_2O_3	35.09	35.40	35.36	35.19	34.73	35.20	34.33	34.84	35.24	35.15
SiO_2	45.46	45.51	45.28	45.73	44.95	45.28	44.71	44.55	45.83	44.42
K_2O	b.d.	0.04	b.d.	0.03	0.03	b.d.	0.10	b.d.	b.d.	b.d.
CaO	19.14	19.21	19.13	19.29	19.06	19.06	18.80	19.27	19.24	19.23
FeO	0.14	0.14	0.14	0.11	0.14	0.13	0.17	0.14	0.12	0.12
Total	100.40	100.80	100.44	100.87	99.46	100.17	98.73	99.35	100.91	99.34

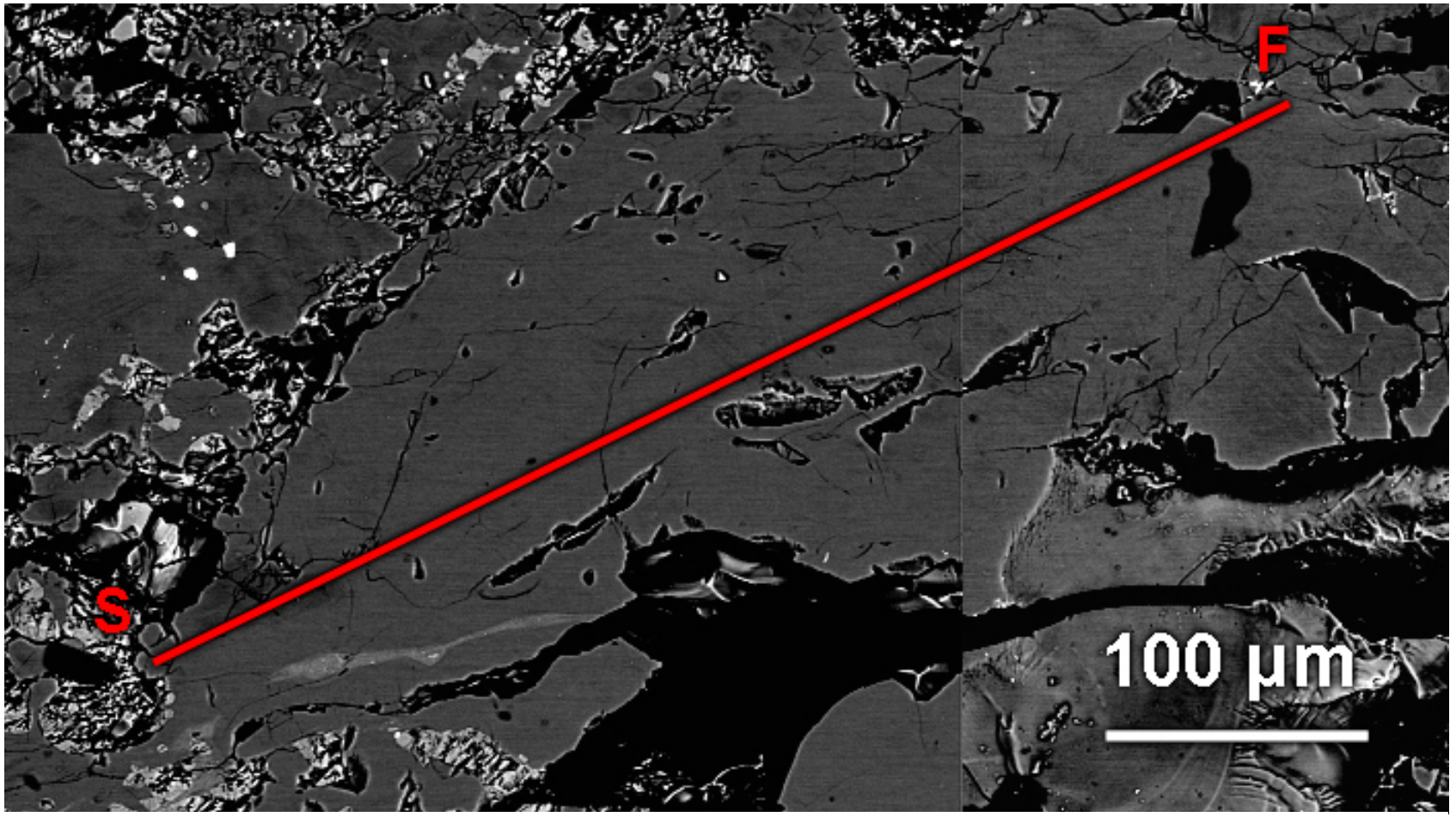

Figure A11: Map of Table A10 EMP plagioclase line location. The line scan is 496 µm in length and was configured to acquire 34 points with 15 µm spacing.

Table A10: Major element content of individual plagioclase points in the line scan shown in Figure A11

Point #	1σ	1	2	3	4	5	6	7	8	9	10	11	12	13	14	15	16	17
Na_2O	0.04	0.54	0.51	0.32	0.42	0.38	0.36	0.33	0.32	0.33	0.33	0.35	0.39	0.36	0.35	0.37	0.35	0.40
MgO	0.01	0.09	0.16	0.11	0.10	0.09	0.17	0.09	0.09	0.09	0.07	0.08	0.08	0.10	0.07	0.08	0.08	0.08
Al_2O_3	0.20	34.70	34.82	35.03	34.81	34.73	34.95	35.46	35.45	35.23	35.16	35.03	35.11	35.34	35.19	35.79	35.25	34.60
SiO_2	0.32	44.50	45.89	44.62	44.28	43.89	45.07	45.13	44.95	44.71	44.69	44.92	45.00	44.90	44.88	45.24	44.90	44.12
K_2O	0.02	0.08	0.04	0.03	0.05	b.d.	b.d.	b.d.	b.d.	b.d.	b.d.	b.d.	0.03	b.d.	b.d.	0.03	b.d.	0.04
CaO	0.30	18.82	18.86	19.22	19.39	18.97	18.98	19.13	19.25	19.31	19.32	19.39	19.15	19.30	19.44	19.12	19.39	18.95
FeO	0.05	0.31	0.31	0.22	0.16	0.15	0.15	0.14	0.14	0.12	0.10	0.10	0.13	0.10	0.13	0.10	0.07	0.15
Total		99.04	100.59	99.54	99.20	98.20	99.68	100.29	100.20	99.79	99.68	99.88	99.89	100.11	100.06	100.73	100.03	98.34

Table A10, ctd

Point #	18	19	20	21	22	23	24	25	26	27	28	29	30	31	32	33	34
Na_2O	0.36	0.39	0.37	0.39	0.36	0.33	0.36	0.39	0.40	0.34	0.36	0.36	0.38	0.36	0.37	0.38	0.34
MgO	0.07	0.09	0.07	0.07	0.08	0.07	0.08	0.08	0.08	0.08	0.09	0.07	0.11	0.09	0.08	0.08	0.09
Al_2O_3	35.00	35.43	35.25	35.38	35.02	35.21	35.10	35.11	35.10	34.87	35.30	35.29	35.20	35.40	35.28	35.07	35.50
SiO_2	44.45	45.34	45.14	45.29	44.84	44.52	44.91	44.52	44.64	44.36	44.88	44.87	44.94	44.89	44.69	44.82	44.83
K_2O	b.d.	0.03	b.d.	b.d.	b.d.	b.d.	0.03	b.d.	b.d.	b.d.	0.03	b.d.	b.d.	b.d.	b.d.	0.03	b.d.
CaO	18.99	19.38	19.35	19.44	19.24	19.34	19.22	19.46	19.04	19.30	19.07	19.12	19.22	19.32	19.29	19.11	19.07
FeO	0.09	0.14	0.09	0.10	0.08	0.09	0.10	0.08	0.09	0.12	0.08	0.09	0.07	0.07	0.08	0.12	0.11
Total	98.97	100.80	100.28	100.67	99.61	99.56	99.81	99.63	99.36	99.08	99.81	99.81	99.93	100.13	99.77	99.61	99.94

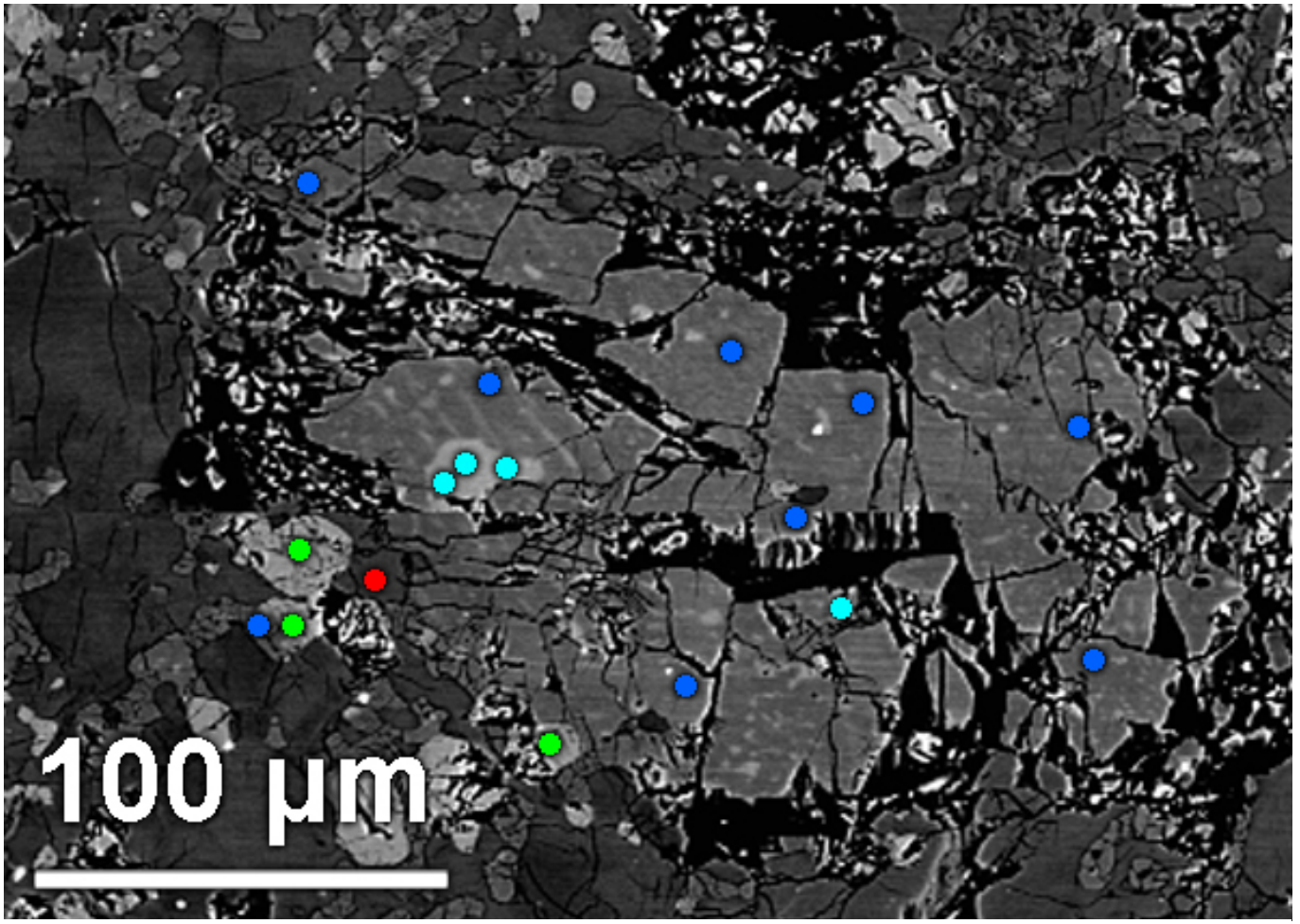

Figure A12: Map of Table A11 EMP point locations. Red, green, dark-blue, and light-blue dots respectively represent plagioclase, olivine, clinoenstatite, and augite measurement locations.

Table A11: Averaged major element content of minerals in Figure A12

	Plag	1σ	Olv	1σ	C-En 1	1σ	C-En 2	1σ	Aug	1σ
Points	1		3		8		1		4	
Na_2O	0.52	0.05	b.d.	-	b.d.	-	b.d.	-	0.05	0.03
MgO	0.13	0.02	42.22	0.35	28.28	0.32	29.26	0.33	17.91	0.21
Al_2O_3	34.64	0.20	0.06	0.01	0.88	0.02	1.15	0.03	2.29	0.04
SiO_2	45.10	0.32	38.41	0.24	55.33	0.24	54.97	0.24	51.88	0.23
P_2O_5	b.d.	-	b.d.	-	b.d.	-	b.d.	-	0.04	0.03
CaO	18.87	0.29	0.17	0.03	3.71	0.11	2.26	0.08	19.17	0.30
TiO_2	b.d.	-	0.14	0.02	0.37	0.02	0.69	0.03	1.19	0.04
MnO	b.d.	-	0.24	0.04	0.24	0.04	0.25	0.04	0.19	0.04
FeO	0.43	0.06	18.84	0.35	11.32	0.25	11.38	0.26	6.34	0.18
Total	99.69		100.07		100.12		99.96		99.06	

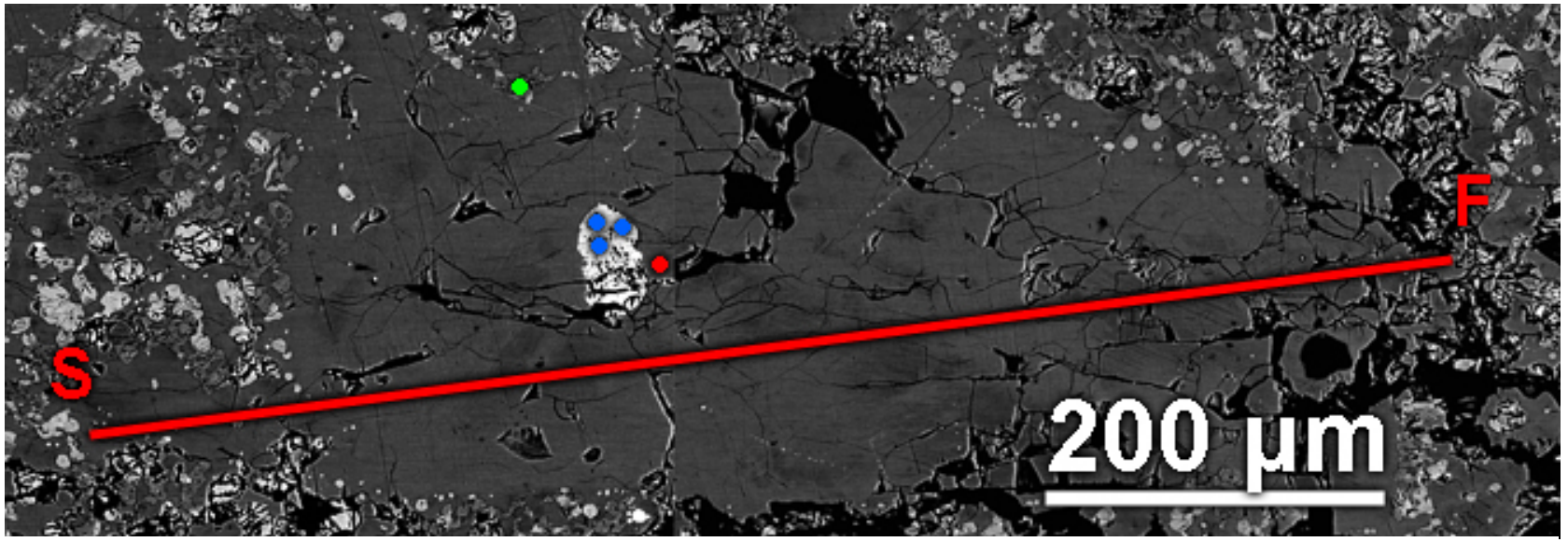

Figure A13: Map of Table A12 EMP point and Table A13 plagioclase line locations. Green and blue dots represent olivine and clinoenstatite, respectively. The line scan is 824 µm in length and was configured to acquire 50 points with 16.8 µm spacing.

Table A12: Averaged major element content of minerals in Figure A13

	Plag	1σ	Olv	1σ	C-En	1σ
Points	1		1		3	
Na_2O	0.30	0.04	b.d.	-	b.d.	-
MgO	0.07	0.01	41.81	0.34	22.84	0.26
Al_2O_3	35.53	0.21	0.07	0.01	1.13	0.03
SiO_2	44.79	0.32	37.96	0.23	53.06	0.23
CaO	19.31	0.30	0.19	0.03	2.04	0.08
TiO_2	b.d.	-	0.20	0.02	0.56	0.03
MnO	b.d.	-	0.24	0.04	0.38	0.04
FeO	0.16	0.05	18.02	0.34	19.30	0.35
Total	100.16		98.49		99.30	

Table A13: Major element content of individual plagioclase points in the line scan shown in Figure A13

Point #	1σ	3	4	5	7	8	10	11	12	13	14	15	16	17	18	19	20	21
Na_2O	0.04	0.34	0.36	0.34	0.63	0.72	0.35	0.38	0.35	0.36	0.35	0.39	0.30	0.32	0.28	0.33	0.33	0.34
MgO	0.01	0.07	0.14	0.07	0.18	0.19	0.11	0.10	0.11	0.07	0.09	0.10	0.09	0.09	0.09	0.11	0.10	0.09
Al_2O_3	0.20	35.24	35.24	35.14	34.25	34.67	35.11	35.34	35.22	35.24	35.43	35.21	35.42	35.21	35.19	35.31	35.14	35.33
SiO_2	0.32	44.71	44.76	44.33	45.82	46.15	44.47	44.51	44.90	44.62	44.91	44.32	44.71	44.25	43.89	44.67	44.40	44.83
K_2O	0.02	0.03	0.03	b.d.	0.03	0.04	b.d.	b.d.	b.d.	b.d.	0.03	0.03	b.d.	b.d.	b.d.	b.d.	b.d.	0.04
CaO	0.30	19.17	19.03	19.04	18.56	18.52	19.27	19.35	19.20	19.35	19.21	19.32	19.22	19.35	19.47	19.56	19.40	19.31
FeO	0.05	0.16	0.20	0.17	0.34	0.27	0.14	0.17	0.11	0.13	0.13	0.15	0.11	0.12	0.10	0.16	0.10	0.14
Total		99.75	99.83	99.14	99.81	100.65	99.51	99.90	99.93	99.81	100.16	99.54	99.93	99.40	99.06	100.16	99.57	100.10

Table A13, ctd

Point #	22	23	24	25	26	27	28	29	30	31	32	33	34	35	36	38	39	40
Na_2O	0.33	0.36	0.33	0.37	0.33	0.36	0.34	0.35	0.34	0.32	0.36	0.37	0.31	0.35	0.39	0.35	0.37	0.34
MgO	0.09	0.10	0.11	0.09	0.08	0.08	0.09	0.10	0.10	0.11	0.12	0.11	0.10	0.11	0.11	0.10	0.10	0.09
Al_2O_3	35.25	34.95	34.94	35.24	35.26	35.05	35.32	34.94	35.12	35.09	34.79	35.30	35.34	35.12	35.07	35.30	35.44	35.05
SiO_2	44.46	44.36	44.03	44.04	44.50	44.36	45.07	43.99	44.35	44.70	43.98	44.86	44.89	44.40	44.42	44.11	44.76	44.72
K_2O	b.d.	0.03	0.05	b.d.	b.d.	b.d.	b.d.	0.04	b.d.	b.d.	0.03	b.d.	b.d.	b.d.	b.d.	b.d.	b.d.	b.d.
CaO	19.45	19.44	19.29	19.20	19.34	19.31	19.22	19.34	19.24	19.15	19.26	19.43	19.02	19.37	19.18	19.08	19.38	19.17
FeO	0.14	0.09	0.11	0.14	0.11	0.12	0.11	0.13	0.21	0.15	0.10	0.14	0.14	0.17	0.18	0.14	0.11	0.13
Total	99.73	99.38	98.88	99.16	99.67	99.31	100.24	98.94	99.44	99.60	98.70	100.28	99.88	99.57	99.37	99.11	100.23	99.57

Table A13, ctd

Point #	41	42	44	45	46	48	49
Na_2O	0.39	0.34	0.34	0.33	0.32	0.43	0.32
MgO	0.10	0.10	0.11	0.10	0.12	0.43	0.04
Al_2O_3	34.99	34.97	35.41	34.98	35.17	34.57	35.53
SiO_2	44.45	44.53	44.95	44.36	44.09	44.85	44.40
K_2O	0.04	b.d.	b.d.	b.d.	b.d.	b.d.	b.d.
CaO	19.21	19.33	19.25	19.30	19.43	18.81	19.39
FeO	0.14	0.12	0.15	0.11	0.11	0.30	0.33
Total	99.38	99.44	100.26	99.26	99.30	99.52	100.09

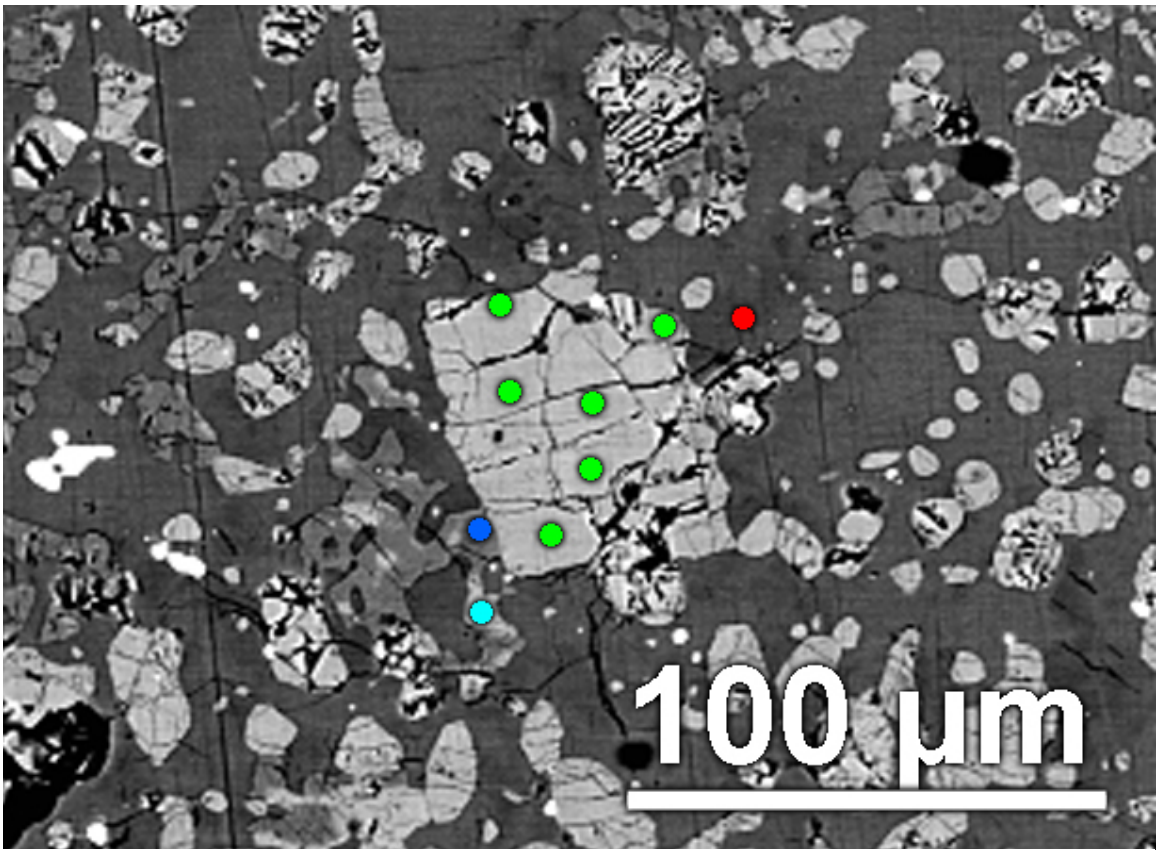

Figure A14: Map of Table A14 EMP point locations. Red, green, dark-blue, and light-blue represent plagioclase, olivine, clinoenstatite, and augite measurement locations, respectively.

Table A14: Averaged major element content of minerals in Figure A14

	Plag	1σ	Olv	1σ	C-En	1σ	Aug	1σ
Points	1		6		1		1	
Na_2O	0.29	0.04	b.d.	-	b.d.	-	0.05	0.03
MgO	0.07	0.01	41.53	0.34	29.22	0.33	17.49	0.21
Al_2O_3	35.40	0.21	0.06	0.01	1.01	0.03	1.51	0.03
SiO_2	44.36	0.31	37.71	0.23	55.36	0.24	52.75	0.23
CaO	19.14	0.30	0.10	0.03	1.93	0.08	21.01	0.32
TiO_2	b.d.	-	0.20	0.02	0.65	0.03	1.06	0.04
MnO	b.d.	-	0.24	0.04	0.23	0.04	0.16	0.04
FeO	0.35	0.06	19.33	0.35	11.68	0.26	5.29	0.17
Total	99.68		99.24		100.14		99.34	

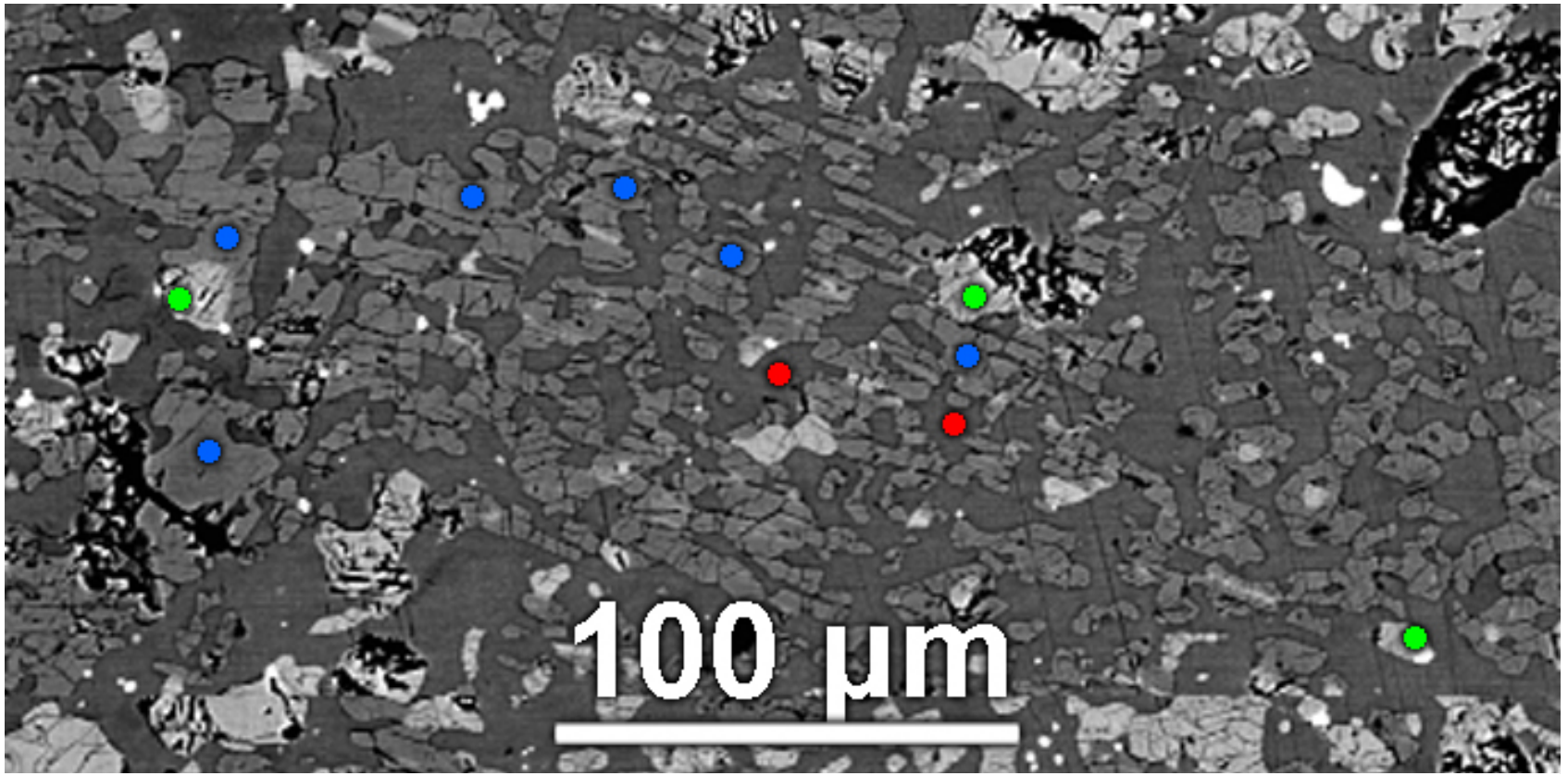

Figure A15: Map of Table A15 EMP point locations. Red, green, and dark-blue represent plagioclase, olivine, and clinoenstatite, respectively.

Table A15: Averaged major element content of minerals in Figure A15

	Plag	1σ	Olv	1σ	C-En	1σ
Points	2		3		6	
Na_2O	0.50	0.04	b.d.	-	b.d.	-
MgO	0.10	0.02	42.10	0.35	28.94	0.33
Al_2O_3	35.17	0.20	0.21	0.02	1.72	0.03
SiO_2	45.20	0.32	38.09	0.24	54.32	0.24
P_2O_5	0.05	0.03	b.d.	-	0.06	0.03
SO_2	b.d.	-	0.02	0.01	b.d.	-
CaO	18.78	0.29	0.21	0.03	2.02	0.08
TiO_2	0.04	0.02	0.17	0.02	0.83	0.03
MnO	b.d.	-	0.24	0.04	0.23	0.04
FeO	0.39	0.06	18.30	0.34	11.07	0.25
Total	100.27		99.39		99.25	

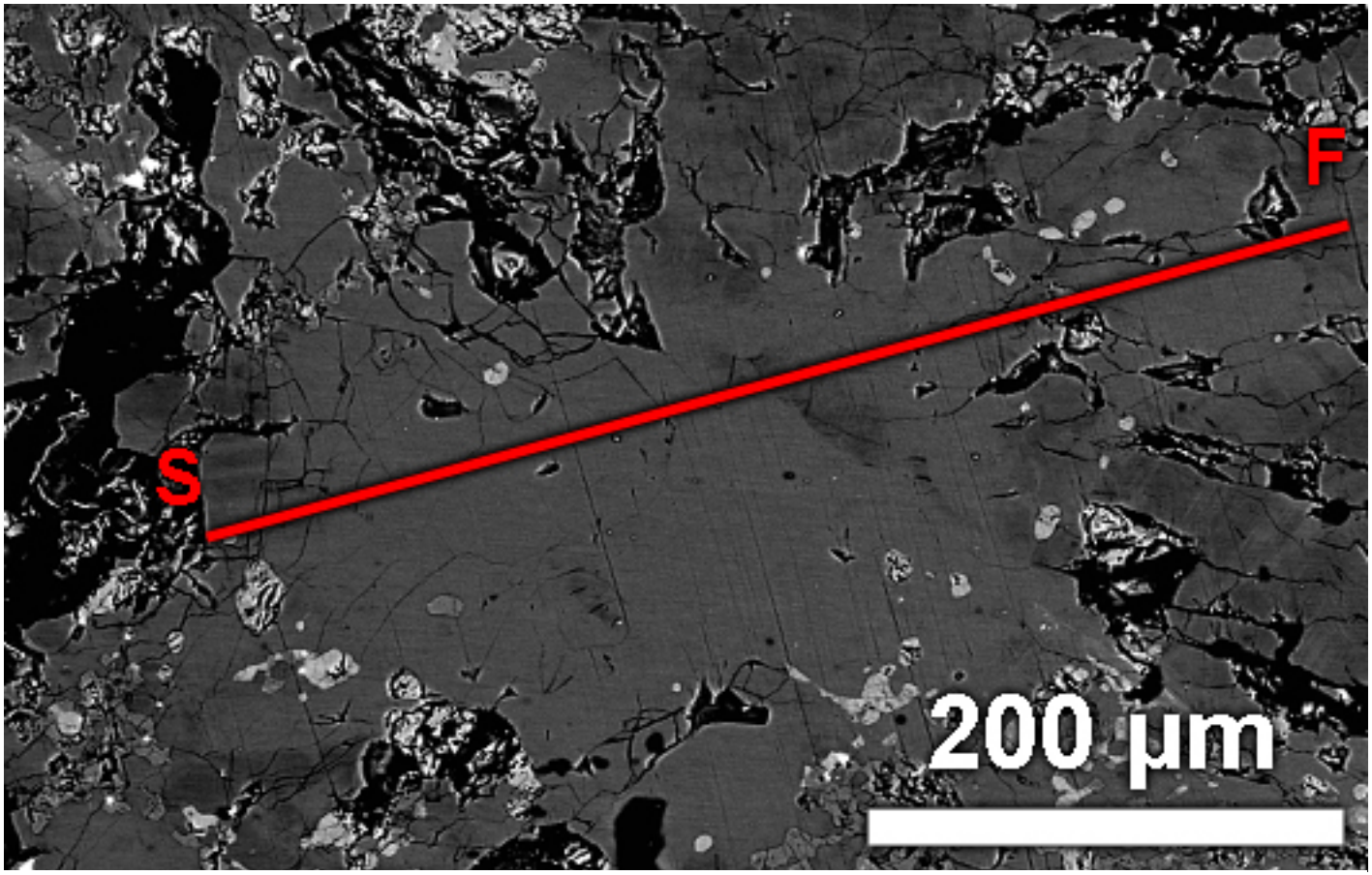

Figure A16: Map of Table A16 EMP plagioclase line location. The line scan is 420 µm in length and was configured to acquire 25 points with 17.5 µm spacing.

Table A16: Major element content of individual plagioclase points in the line scan shown in Figure A16

Point #	1σ	1	2	3	4	5	6	7	8	10	11	12	13	14	15	16	17	18
Na_2O	0.04	0.36	0.37	0.35	0.36	0.35	0.37	0.36	0.37	0.38	0.36	0.42	0.37	0.38	0.37	0.33	0.32	0.59
MgO	0.01	0.10	0.10	0.08	0.07	0.05	0.10	0.08	0.07	0.08	0.06	0.09	0.06	0.07	0.08	0.07	0.10	0.12
Al_2O_3	0.20	35.40	35.19	35.35	35.29	35.31	35.69	35.35	35.15	35.70	35.33	34.92	35.18	35.28	35.03	35.29	35.23	34.31
SiO_2	0.32	44.54	44.88	44.63	44.59	44.61	45.10	44.68	44.59	45.28	45.15	44.21	44.34	44.73	44.23	44.38	43.86	45.09
K_2O	0.02	b.d.	b.d.	b.d.	b.d.	b.d.	b.d.	b.d.	b.d.	b.d.	b.d.	b.d.	b.d.	b.d.	b.d.	b.d.	b.d.	0.06
CaO	0.30	19.20	19.17	19.35	19.22	19.15	19.19	19.20	19.20	19.32	19.12	19.42	19.49	19.18	19.07	18.83	19.12	18.99
FeO	0.05	0.13	0.10	0.12	0.09	0.06	0.10	0.05	0.09	0.11	b.d.	0.08	0.08	0.03	0.09	0.09	0.12	0.20
Total		99.84	99.88	99.89	99.65	99.56	100.63	99.74	99.52	100.90	100.14	99.16	99.56	99.76	98.93	99.03	98.82	99.39

Table A16, ctd

Point #	20	21	22	23	24	25
Na_2O	0.34	0.38	0.38	0.35	0.32	0.31
MgO	0.08	0.09	0.06	0.10	0.11	0.11
Al_2O_3	35.10	35.42	35.07	34.95	34.93	35.19
SiO_2	44.46	45.09	44.19	44.40	44.42	44.41
K_2O	b.d.	b.d.	b.d.	b.d.	b.d.	b.d.
CaO	19.17	19.09	19.34	19.23	19.20	19.46
FeO	0.24	0.14	0.12	0.09	0.15	0.17
Total	99.46	100.30	99.21	99.21	99.17	99.67

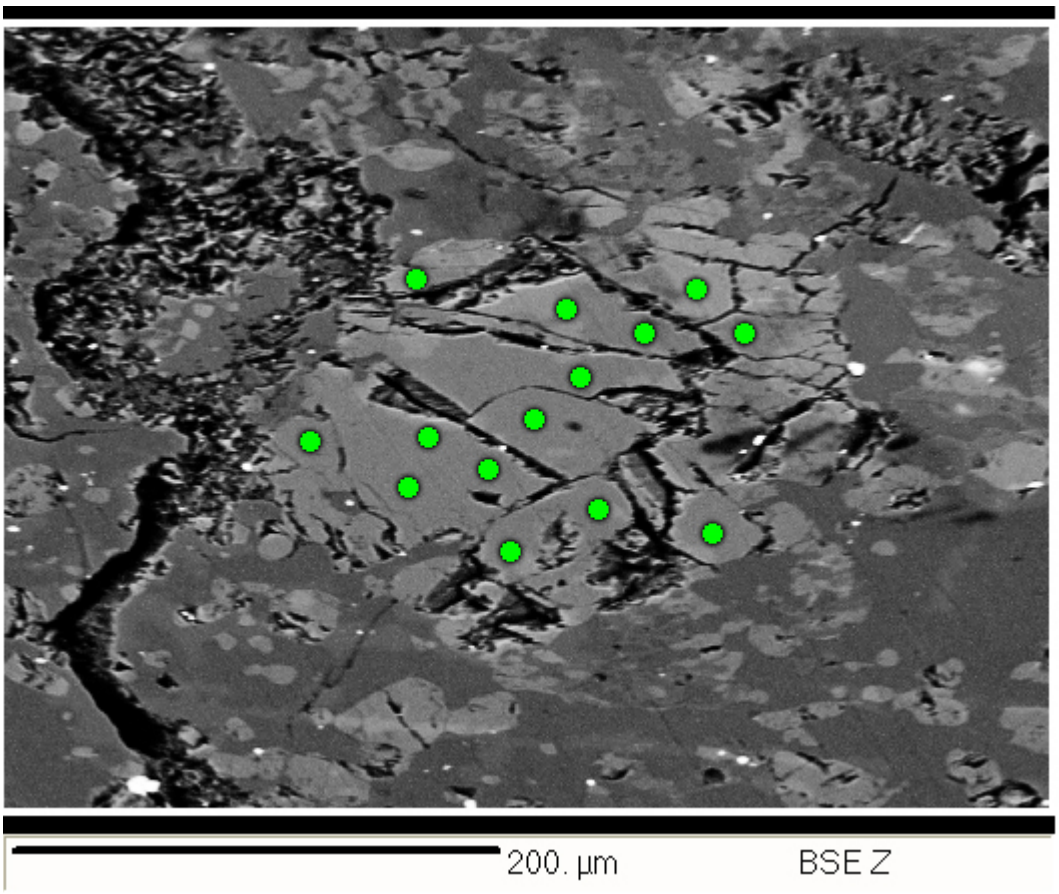

Figure A17: Map of Table A17 EMP point locations. Green dots represent olivine measurement locations.

Table A17: Averaged major element content of olivine in Figure A17

	Olv	1σ
Points	14	
MgO (wt %)	41.21	0.32
Al_2O_3	0.03	0.02
SiO_2	38.61	0.20
CaO	0.12	0.02
TiO_2	0.05	0.02
MnO	0.23	0.05
FeO	19.25	0.32
Total	99.50	

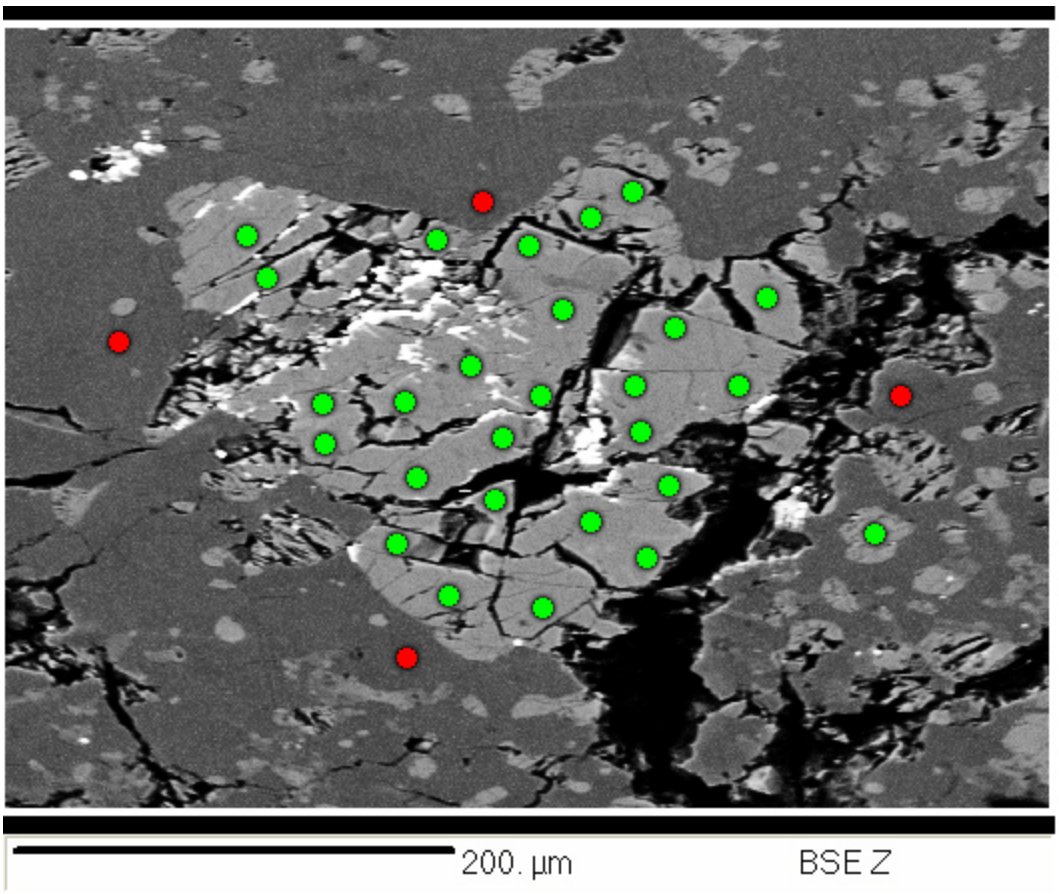

Figure A18: Map of Table A18 EMP point locations. Red and green dots represent plagioclase and olivine measurement locations, respectively. High density material within the cracks of this olivine was observed to contain significant amounts of Fe, Ni, and Cr, via EDS analysis.

Table A18: Averaged major element content of minerals in Figure A18

	Plag	1σ	Olv[1]	1σ	Olv[2]	1σ
Points	4		26		1	
Na_2O (wt %)	0.41	0.04	b.d.	-	b.d.	-
MgO	0.07	0.02	40.13	0.31	40.43	0.32
Al_2O_3	34.98	0.41	0.07	0.02	0.07	0.02
SiO_2	43.65	0.23	38.71	0.20	38.76	0.19
SO_2	0.04	0.03	b.d.	-	b.d.	-
CaO	19.29	0.39	0.12	0.02	0.34	0.03
TiO_2	b.d.	-	b.d.	-	0.06	0.02
Cr_2O_3	b.d.	-	b.d.	-	0.04	0.03
MnO	b.d.	-	0.25	0.05	0.24	0.05
FeO	0.35	0.06	20.21	0.32	19.97	0.32
Total	98.80		99.49		99.92	

[1]Large olivine grain centerd in Figure A18.
[2]Single matrix olivine grain on the right side of Figure A18

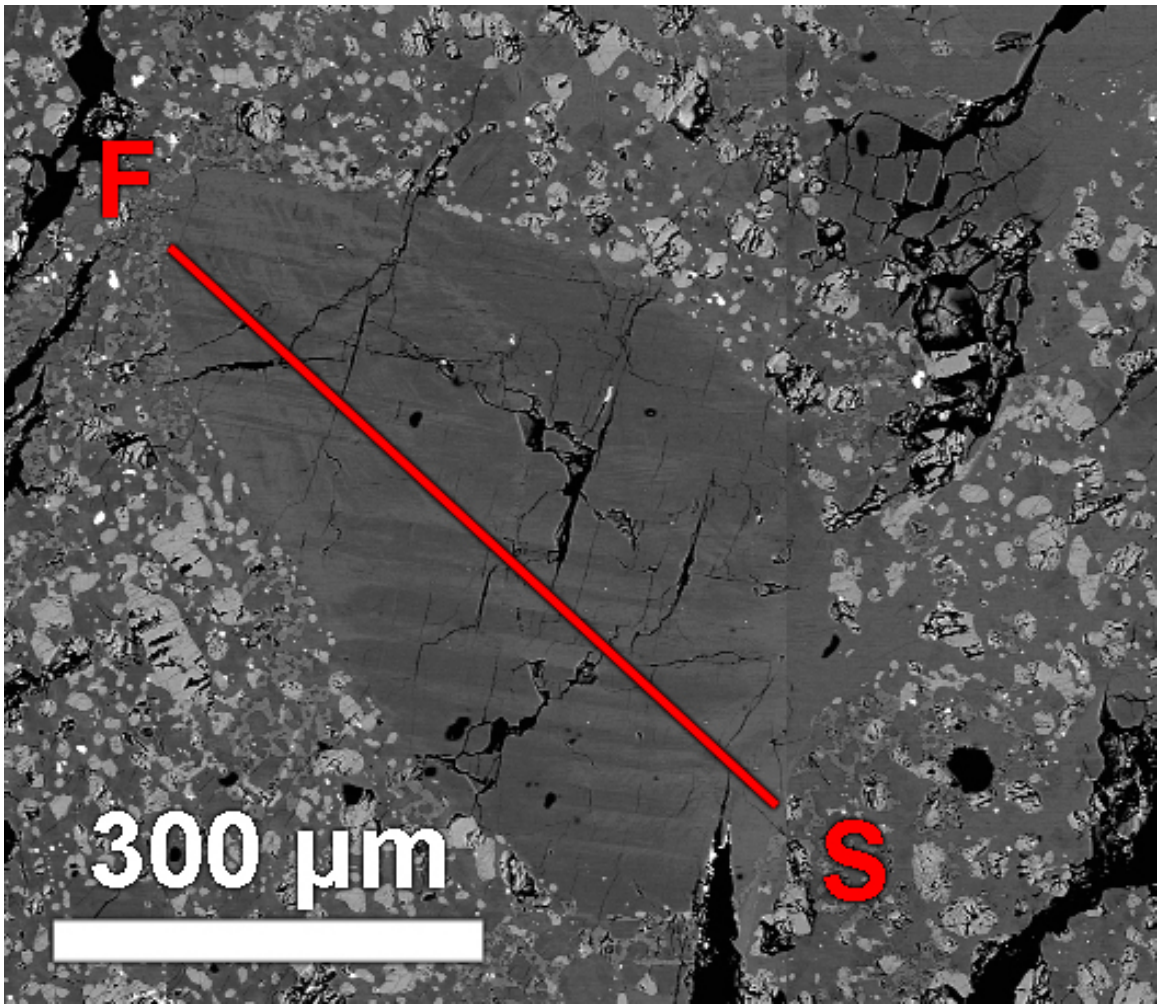

Figure A19: Map of Table A19 EMP plagioclase line location. The line scan is 550 µm in length and was configured to acquire 25 points with 22.9 µm spacing.

Table A19: Major element content of individual plagioclase points in the line scan shown in Figure A19

	1σ	1	2	3	4	5	6	7	8	9	10	11	13	14	15	16	17	18
Na_2O (wt %)	0.04	0.46	0.46	0.47	0.45	0.46	0.47	0.45	0.46	0.46	0.56	0.46	0.47	0.43	0.44	0.44	0.45	0.47
MgO	0.02	0.16	0.14	0.16	0.12	0.16	0.15	0.12	0.15	0.12	0.15	0.15	0.16	0.13	0.14	0.14	0.14	0.16
Al_2O_3	0.41	34.93	35.09	34.80	35.07	35.05	35.05	35.17	35.13	35.06	34.72	35.04	35.08	35.02	35.09	35.10	35.11	35.25
SiO_2	0.24	44.36	44.38	44.04	44.18	43.93	44.03	43.89	44.33	43.92	43.67	43.97	43.94	43.88	43.95	43.84	43.89	44.22
CaO	0.39	19.31	19.49	19.35	19.33	19.64	19.63	19.37	19.47	19.74	19.12	19.58	19.53	19.43	19.73	19.61	19.49	19.63
FeO	0.05	0.22	0.18	0.13	0.13	0.16	0.10	0.14	0.15	0.14	0.15	0.16	0.17	0.12	0.13	0.13	0.13	0.13
Total		99.44	99.73	98.95	99.28	99.39	99.43	99.15	99.68	99.45	98.38	99.35	99.34	99.01	99.49	99.25	99.19	99.85

Table A19, ctd

	19	20	21	22	23	24	25
Na_2O (wt %)	0.45	0.43	0.45	0.46	0.46	0.43	0.44
MgO	0.16	0.13	0.15	0.14	0.16	0.16	0.16
Al_2O_3	35.13	35.11	35.08	35.09	35.16	35.18	35.22
SiO_2	44.28	44.17	43.84	44.02	44.20	44.07	44.35
CaO	19.48	19.53	19.28	19.45	19.72	19.69	19.46
FeO	0.11	0.15	0.16	0.14	0.14	0.17	0.18
Total	99.62	99.52	98.96	99.30	99.84	99.71	99.82

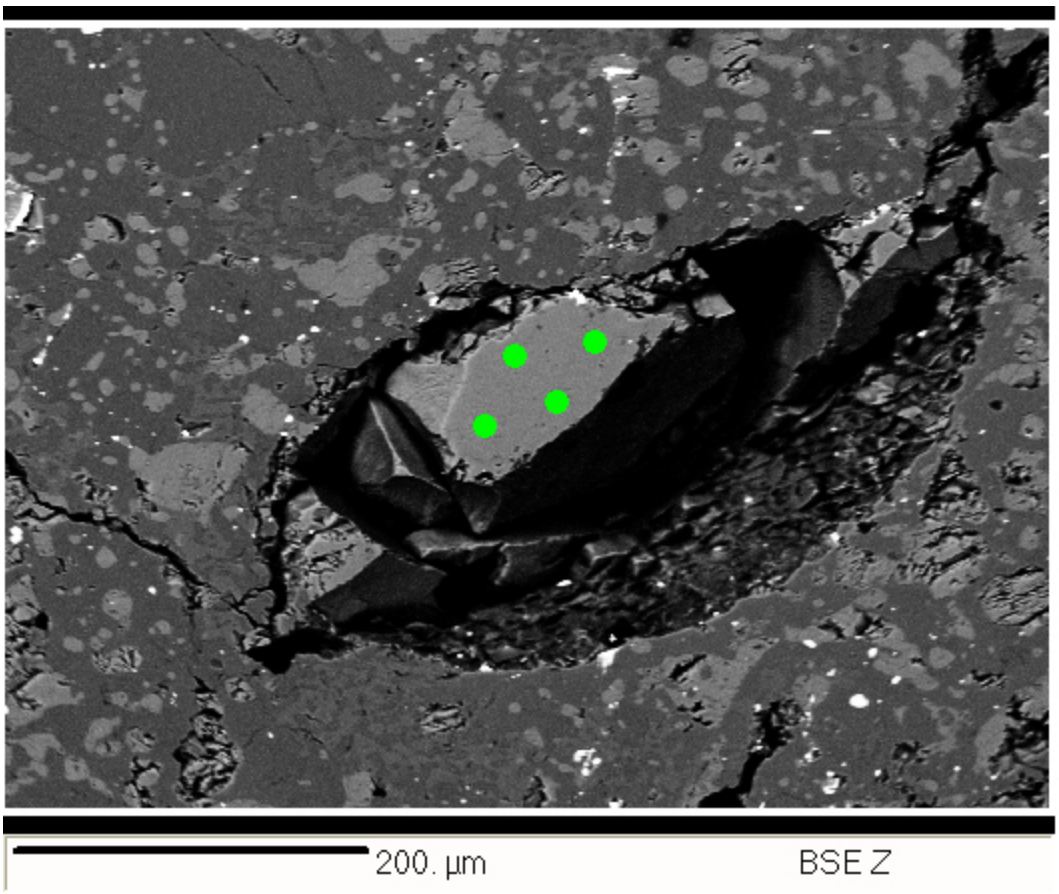

Figure A20: Map of Table A20 EMP point locations. Green dots represent olivine measurement locations.

Table A20: Averaged major element content of olivine in Figure A20

	Olv	1σ
Points	4	
MgO (wt %)	41.54	0.32
SiO_2	39.32	0.20
CaO	0.08	0.02
TiO_2	0.05	0.02
Cr_2O_3	0.05	0.03
MnO	0.25	0.05
FeO	19.70	0.32
Total	100.99	

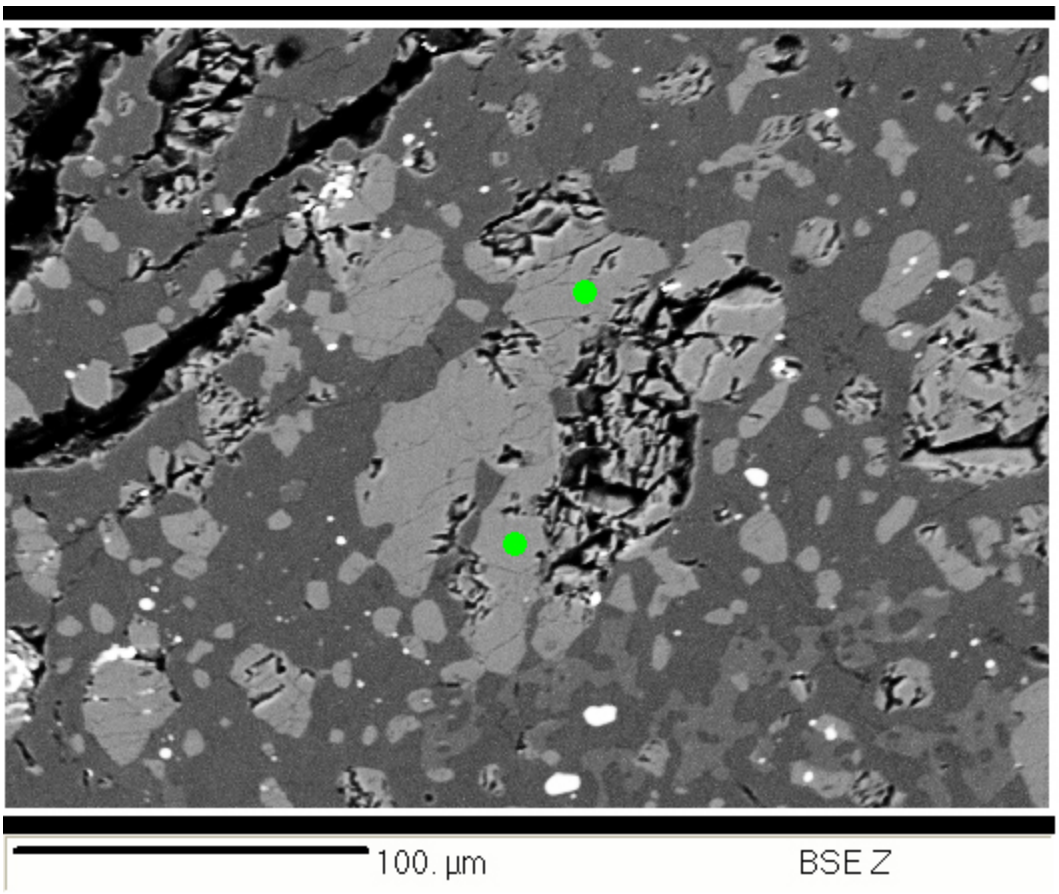

Figure A21: Map of Table A21 EMP point locations. Green dots represent olivine measurement locations.

Table A21: Averaged major element content of olivine in Figure A21

Points	Olv 2	1σ
MgO (wt %)	41.31	0.32
Al_2O_3	0.05	0.02
SiO_2	39.16	0.20
CaO	0.09	0.02
TiO_2	0.17	0.02
Cr_2O_3	0.08	0.03
MnO	0.27	0.05
FeO	19.65	0.32
Total	100.78	

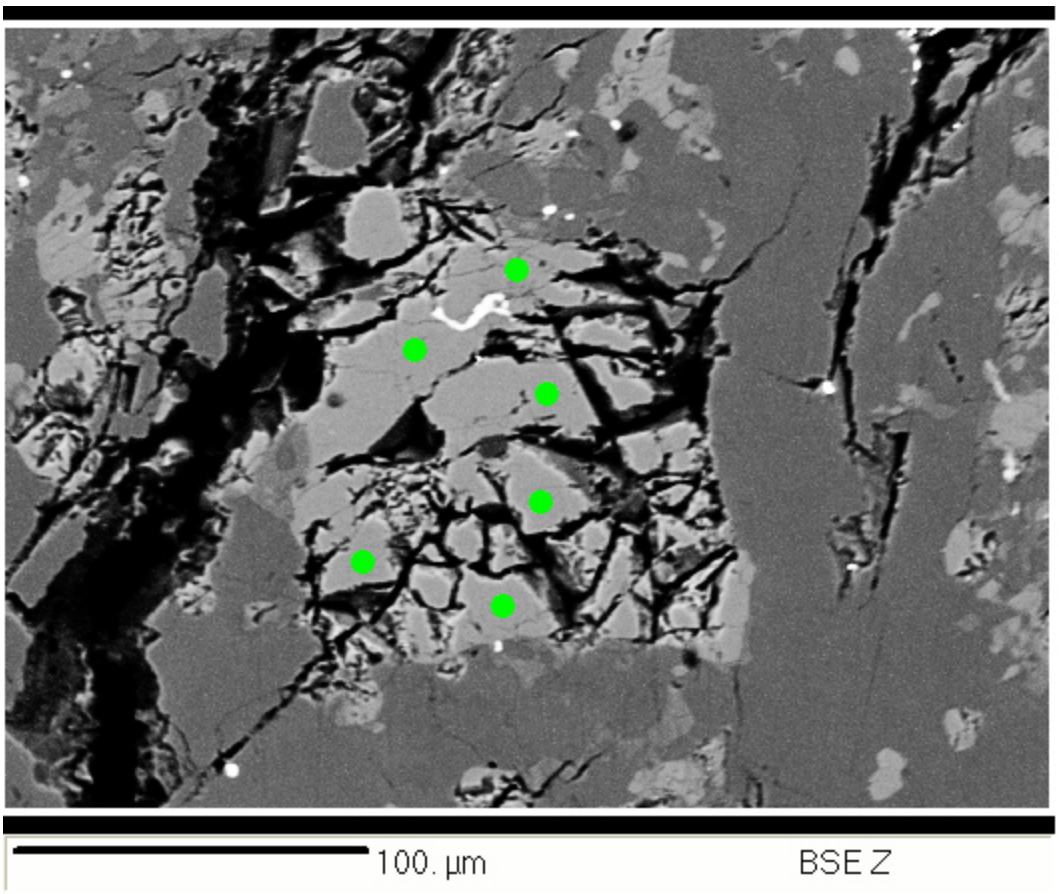

Figure A22: Map of Table A22 EMP point locations. Green dots represent olivine measurement locations.

Table A22: Averaged major element content of olivine in Figure A22

	Olv	1σ
Points	6	
MgO (wt %)	41.16	0.32
Al_2O_3	0.04	0.02
SiO_2	39.13	0.20
CaO	0.10	0.02
MnO	0.26	0.05
FeO	19.93	0.32
Total	100.62	

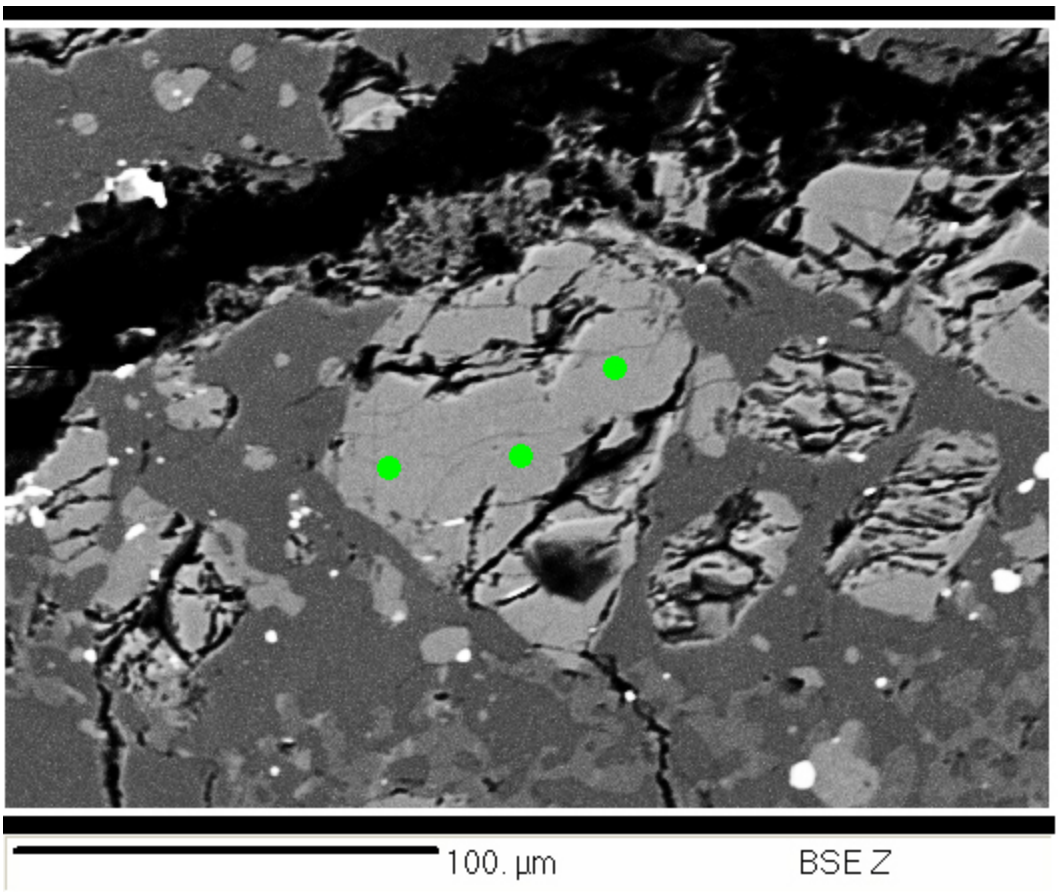

Figure A23: Map of Table A23 EMP point locations. Green dots represent olivine measurement locations.

Table A23: Averaged major element content of olivine in Figure A23

	Olv	1σ
Points	3	
MgO (wt %)	41.31	0.32
Al_2O_3	0.06	0.02
SiO_2	39.18	0.20
CaO	0.10	0.02
TiO_2	0.10	0.02
Cr_2O_3	0.06	0.03
MnO	0.24	0.06
FeO	20.05	0.32
Total	101.08	

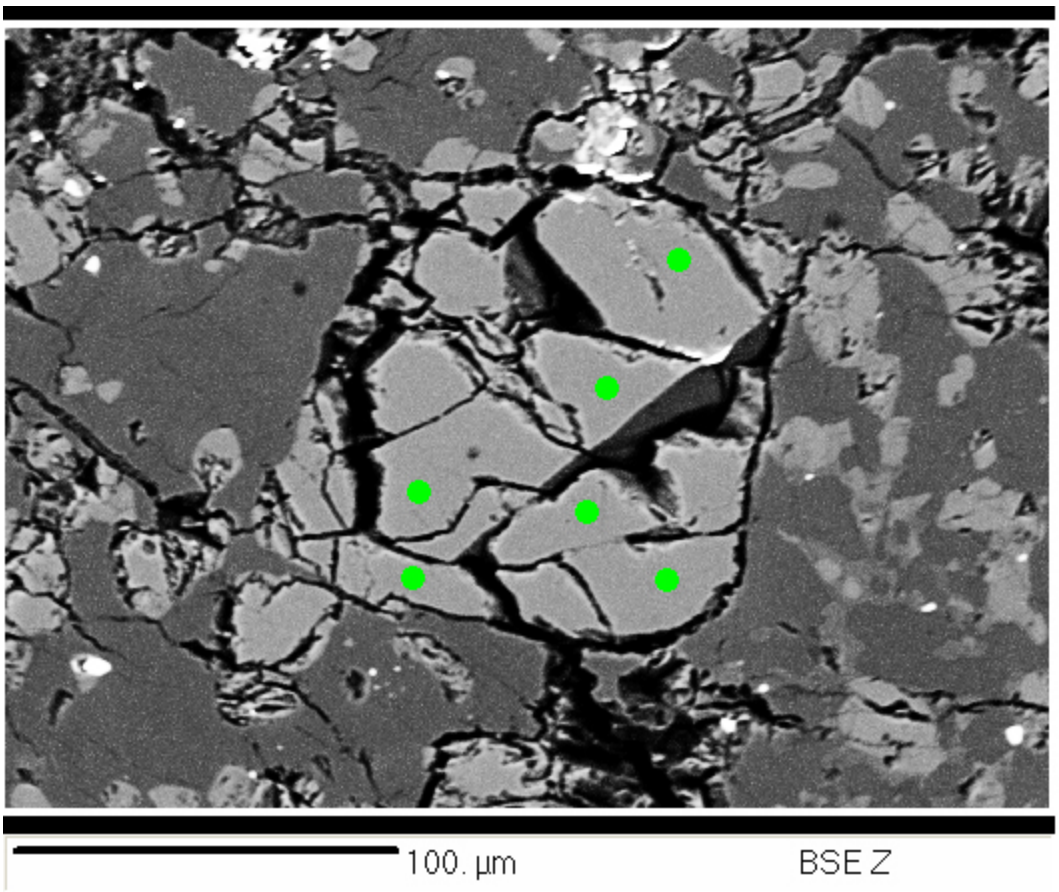

Figure A24: Map of Table A24 EMP point locations. Green dots represent olivine measurement locations.

Table A24: Averaged major element content of olivine in Figure A24

	Olv	1σ
Points	6	
MgO (wt %)	41.14	0.32
SiO_2	39.11	0.20
CaO	0.09	0.02
MnO	0.24	0.05
FeO	20.19	0.32
Total	100.78	

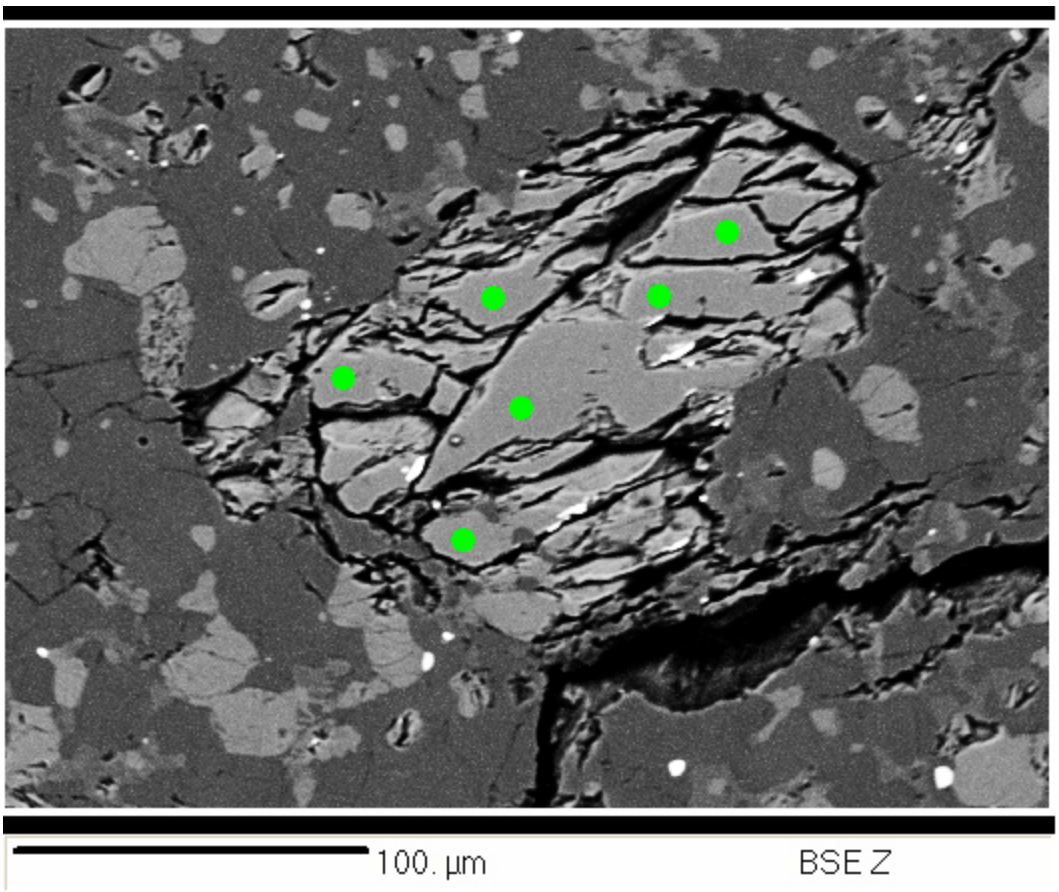

Figure A25: Map of Table A25 EMP point locations. Green dots represent olivine measurement locations.

Table A25: Averaged major element content of olivine in Figure A25

	Olv	1σ
Points	6	
MgO (wt %)	41.13	0.32
Al_2O_3	0.03	0.02
SiO_2	39.13	0.20
CaO	0.08	0.02
TiO_2	0.08	0.02
Cr_2O_3	0.04	0.03
MnO	0.25	0.05
FeO	20.40	0.32
Total	101.14	

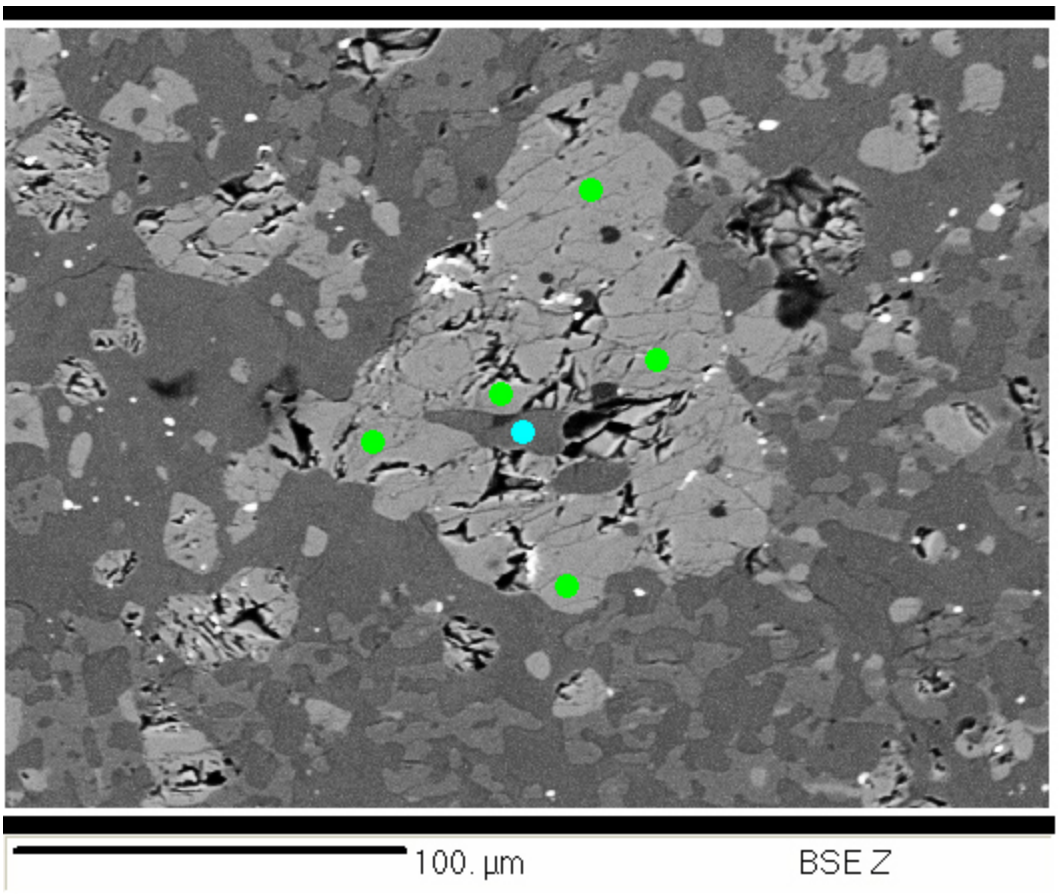

Figure A26: Map of Table A26 EMP point locations. Green and light-blue dots represent olivine and augite measurement locations, respectively.

Table A25: Averaged major element content of minerals in Figure A25

	Olv	1σ	Aug	1σ
Points	5		1	
Na_2O (wt %)	b.d.	-	0.64	0.05
MgO	41.43	0.32	0.27	0.03
Al_2O_3	0.09	0.02	34.88	0.42
SiO_2	39.37	0.20	46.08	0.24
K_2O	b.d.	-	0.04	0.02
CaO	0.12	0.02	17.93	0.24
TiO_2	0.04	0.02	b.d.	-
MnO	0.23	0.05	b.d.	-
FeO	19.43	0.32	0.88	0.08
Total	100.71		100.72	

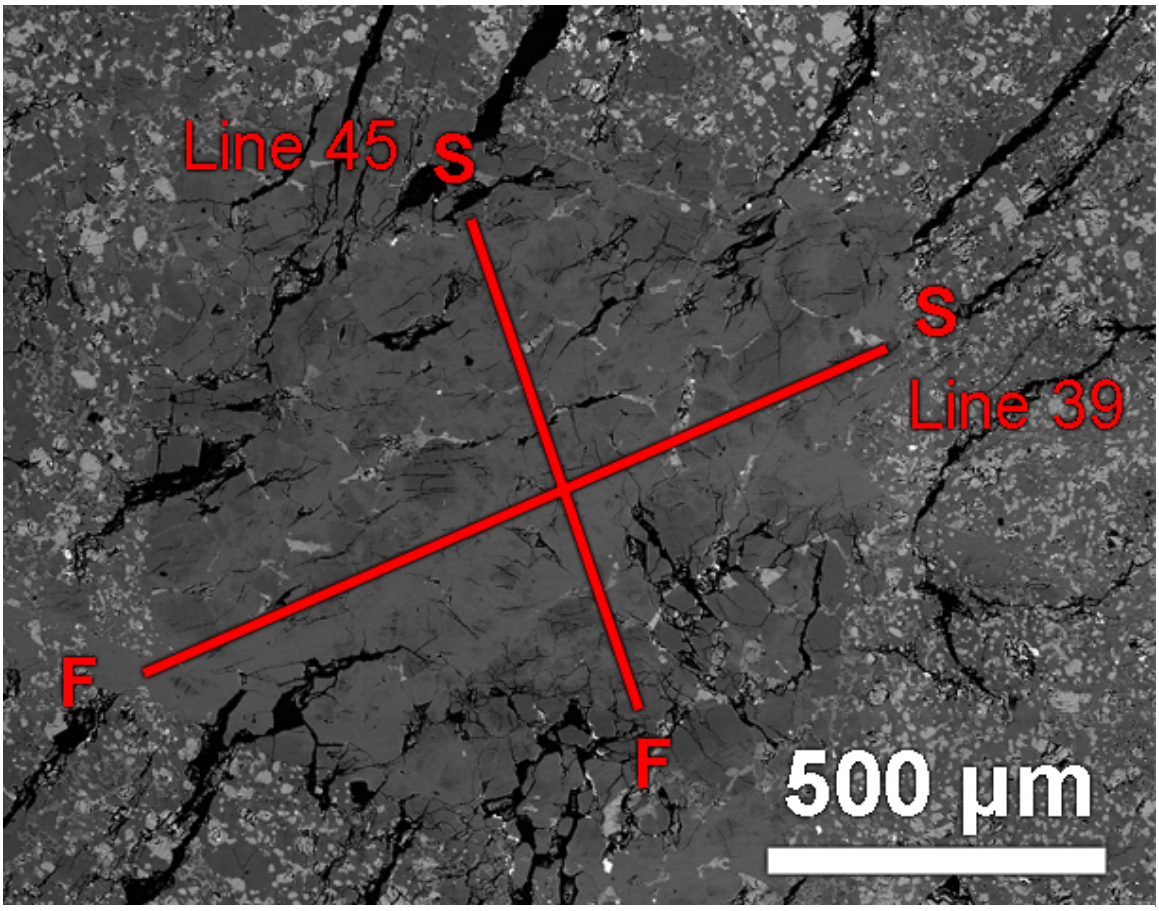

Figure A27: Map of EMP plagioclase Line 39 and 45 locations, respectively. Line scan 39 (Table A27) is 1124 µm in length and was configured to acquire 40 points with 28.8 µm spacing. Line scan 45 (Table A28) is 660 µm in length and was configured to acquire 30 points with 22.7 µm spacing.

Table A27: Major element content of individual plagioclase points in Line 39 shown in Figure A27

	1σ	1	2	3	4	5	6	7	8	9	10	12	13	15	16	18	19	20
Na_2O (wt %)	0.04	0.29	0.41	0.51	0.55	0.42	0.48	0.38	0.40	0.39	0.58	0.39	0.35	0.36	0.33	0.42	0.41	0.46
MgO	0.02	0.06	0.08	0.07	0.08	0.11	0.06	0.05	0.09	0.09	0.09	0.05	0.08	0.05	0.07	0.08	0.07	0.06
Al_2O_3	0.42	35.87	35.49	35.28	35.14	35.50	35.54	35.59	35.44	35.85	34.81	35.73	35.49	35.47	35.78	35.60	35.51	35.71
SiO_2	0.23	43.72	44.19	43.76	44.44	44.45	44.71	43.94	43.65	44.44	43.42	44.54	44.17	43.68	44.11	44.31	44.29	43.84
K_2O	0.02	0.04	b.d.	0.07	0.06	b.d.	0.03	b.d.	0.03	b.d.	0.11	b.d.	0.03	b.d.	b.d.	b.d.	0.03	0.04
CaO	0.39	19.66	19.68	19.60	19.39	19.43	19.49	19.58	19.60	19.58	19.33	19.50	19.65	19.63	19.78	19.59	19.43	19.66
FeO	0.05	0.17	0.14	0.10	0.07	0.12	0.07	0.11	0.10	0.10	0.10	0.13	0.11	0.09	0.06	0.10	0.13	0.08
Total		99.81	100.00	99.38	99.72	100.03	100.38	99.65	99.31	100.45	98.46	100.34	99.88	99.27	100.12	100.11	99.87	99.84

Table A27, ctd

	21	22	23	24	25	26	27	28	29	30	32	33	34	35	36	37	38	39
Na_2O (wt %)	0.40	0.39	0.46	0.40	0.43	0.44	0.43	0.42	0.59	0.52	0.36	0.42	0.44	0.39	0.38	0.40	0.33	0.36
MgO	0.08	0.07	0.11	0.07	0.08	0.06	0.07	0.07	0.09	0.09	0.08	0.08	0.04	0.09	0.10	0.14	0.31	0.08
Al_2O_3	35.52	35.51	35.75	35.49	35.15	35.48	35.18	35.37	34.99	34.86	35.42	35.05	35.45	35.41	35.46	35.49	35.25	35.49
SiO_2	44.23	44.09	45.09	43.87	44.11	43.88	43.83	43.82	43.54	44.03	43.72	44.12	43.96	43.81	44.52	44.43	43.82	44.25
K_2O	b.d.	0.04	b.d.	b.d.	0.11	b.d.	0.03	0.03	0.06	0.14	0.03	b.d.	b.d.	b.d.	b.d.	b.d.	b.d.	b.d.
CaO	19.70	19.70	19.70	19.63	19.45	19.77	19.27	19.60	19.41	18.98	19.52	19.46	19.48	19.71	19.52	19.45	19.63	19.60
FeO	0.09	0.07	0.10	0.11	0.08	0.04	0.08	0.07	0.11	0.07	0.15	0.10	0.09	0.11	0.15	0.17	0.18	0.16
Total	100.02	99.87	101.20	99.58	99.41	99.67	98.88	99.37	98.79	98.69	99.27	99.23	99.46	99.51	100.13	100.08	99.52	99.94

Table A27, ctd

	40
Na_2O (wt %)	0.38
MgO	0.07
Al_2O_3	35.53
SiO_2	44.31
K_2O	0.03
CaO	19.62
FeO	0.18
Total	100.12

Table A28: Major element content of individual plagioclase points in Line 45 shown in Figure A27

	1σ	1	2	3	4	5	6	7	8	9	10	11	12	13	14	15	16	17
Na_2O (wt %)	0.04	0.39	0.35	0.49	0.40	0.33	0.36	0.41	0.47	0.49	0.45	0.46	0.31	0.45	0.53	0.45	0.34	0.41
MgO	0.02	0.08	0.08	0.11	0.09	0.06	0.05	0.06	0.06	0.04	0.08	0.07	0.04	0.08	0.10	0.09	0.08	0.09
Al_2O_3	0.42	35.62	35.62	34.59	35.36	35.46	35.54	35.37	35.44	35.76	35.22	35.41	35.88	35.38	34.53	35.74	35.60	35.65
SiO_2	0.24	44.62	44.59	43.20	44.78	43.90	44.13	44.75	44.87	45.13	44.07	44.47	44.47	44.55	43.79	44.68	44.34	44.31
K_2O	0.02	0.03	0.03	0.06	0.03	0.05	0.05	0.03	0.04	b.d.	0.06	b.d.	b.d.	b.d.	0.03	b.d.	b.d.	b.d.
CaO	0.39	19.49	19.57	19.35	19.53	19.71	19.55	19.45	19.56	19.47	19.36	19.54	19.72	19.42	18.92	19.60	19.62	19.61
FeO	0.05	0.09	0.07	0.14	0.05	0.12	0.11	0.06	0.07	0.05	0.12	0.11	0.12	0.10	0.09	0.07	0.10	0.08
Total		100.32	100.32	97.93	100.25	99.63	99.79	100.13	100.51	100.94	99.36	100.06	100.53	99.96	97.98	100.63	100.08	100.15

Table A28, ctd

	18	19	20	21	22	24	25	26	27	28	29	30
Na_2O (wt %)	0.40	0.40	0.36	0.49	0.43	0.43	0.35	0.32	0.43	0.35	0.39	0.40
MgO	0.22	0.08	0.05	0.05	0.05	0.07	0.06	0.07	0.08	0.08	0.09	0.08
Al_2O_3	35.44	35.61	35.63	35.90	35.47	35.53	35.71	35.62	35.70	35.77	35.62	35.49
SiO_2	44.30	44.62	44.38	44.95	44.58	44.16	44.46	44.10	44.59	44.55	44.39	44.62
K_2O	0.03	b.d.	b.d.	b.d.	b.d.	b.d.	b.d.	b.d.	b.d.	b.d.	b.d.	b.d.
CaO	19.59	19.70	19.58	19.61	19.80	19.49	19.69	19.72	19.64	19.71	19.77	19.52
FeO	0.12	0.11	0.12	0.06	0.08	0.15	0.17	0.13	0.07	0.10	0.07	0.08
Total	100.10	100.51	100.14	101.06	100.41	99.83	100.45	99.95	100.50	100.56	100.33	100.18

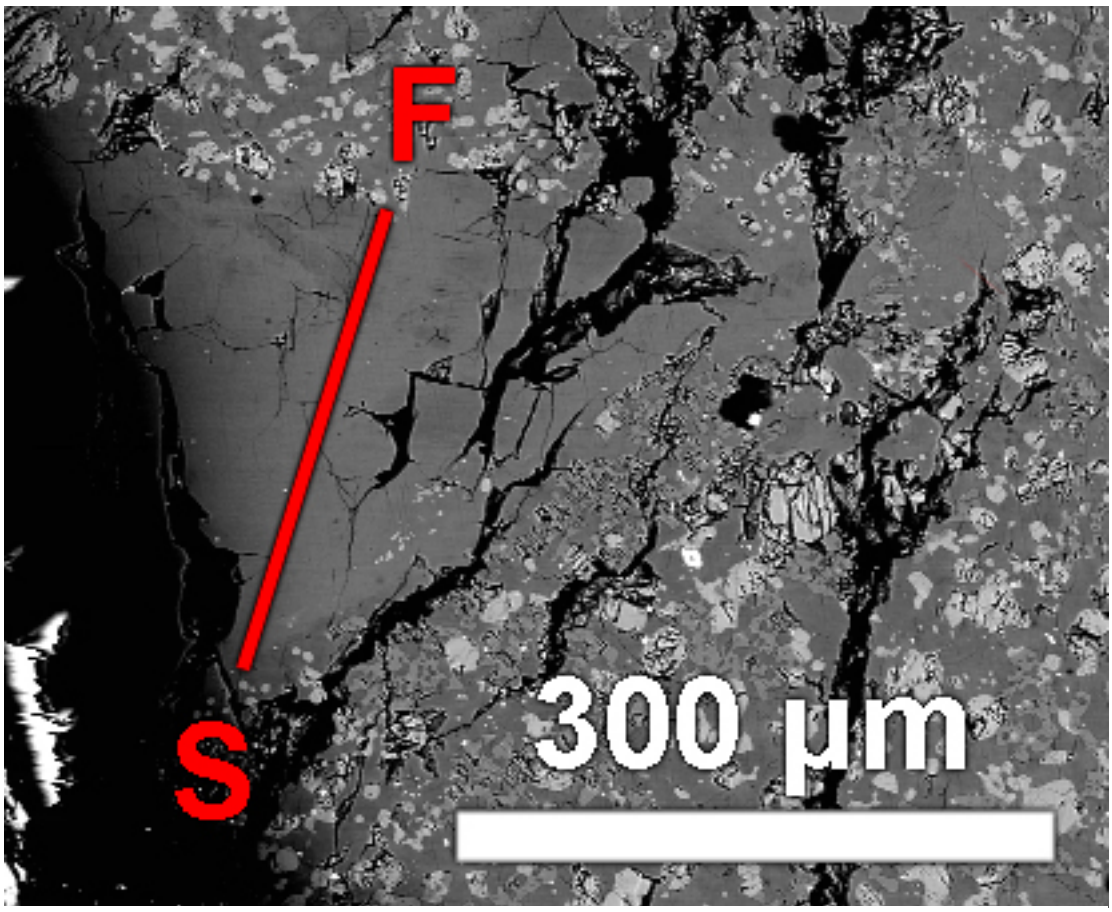

Figure A28: Map of Table A29 EMP plagioclase line location. The line scan is 267 µm in length and was configured to acquire 15 points with 19 µm spacing.

Table A29: Major element content of individual plagioclase points in the line scan shown in Figure A28

Point	1σ	1	2	3	4	5	6	7	8	9	10	11	12	14	15
Na_2O (wt %)	0.04	0.38	0.34	0.34	0.42	0.37	0.33	0.37	0.51	0.32	0.34	0.33	0.36	0.30	0.53
MgO	0.02	0.09	0.17	0.12	0.08	0.14	0.10	0.14	0.13	0.11	0.14	0.09	0.09	0.12	0.45
Al_2O_3	0.42	35.65	35.78	35.54	34.52	35.23	35.79	35.32	34.95	35.81	35.75	35.79	35.71	35.59	34.56
SiO_2	0.24	44.58	44.72	44.23	43.29	44.64	44.80	43.90	43.70	44.69	44.84	44.70	44.28	44.33	44.34
K_2O	0.02	b.d.	b.d.	b.d.	0.12	b.d.	b.d.	0.04	0.17	b.d.	b.d.	b.d.	b.d.	b.d.	b.d.
CaO	0.39	19.56	19.66	19.61	19.61	19.69	19.60	19.44	19.55	19.69	19.84	19.74	19.67	19.68	19.33
TiO_2	0.03	b.d.	b.d.	b.d.	b.d.	b.d.	b.d.	0.11	b.d.	b.d.	b.d.	b.d.	b.d.	b.d.	b.d.
FeO	0.05	0.14	0.11	0.10	0.11	0.06	0.10	0.61	0.09	0.13	0.09	0.14	0.10	0.17	0.25
NiO	0.06	b.d.	b.d.	b.d.	b.d.	b.d.	b.d.	0.18	b.d.	b.d.	0.07	b.d.	b.d.	b.d.	b.d.
Total		100.41	100.78	99.94	98.15	100.13	100.73	100.11	99.08	100.75	101.07	100.78	100.21	100.19	99.47

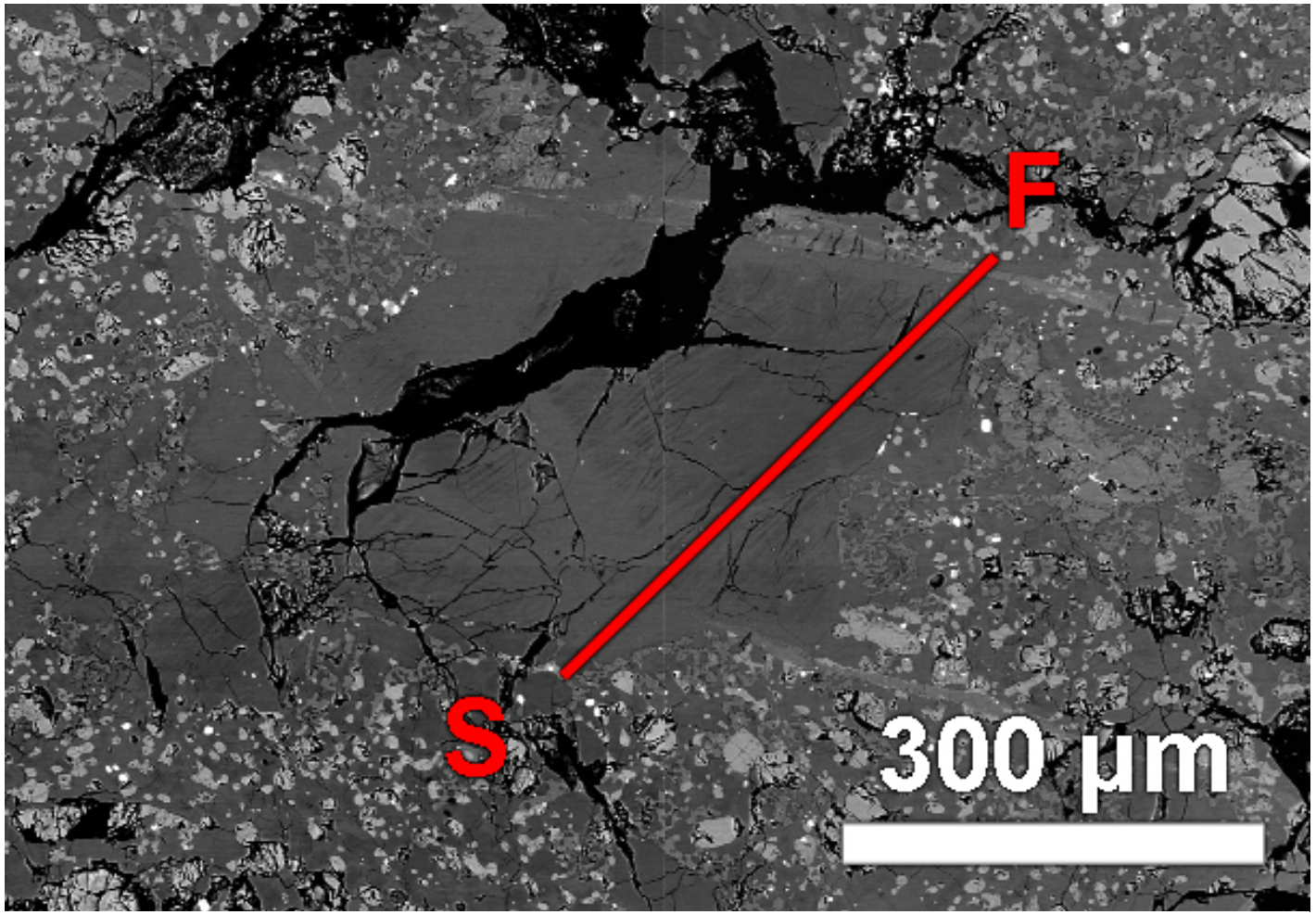

Figure A29: Map of Table A30 EMP plagioclase line location. The line scan is 413 µm in length and was configured to acquire 20 points with 21.7 µm spacing.

Table A30: Major element content of individual plagioclase points in the line scan shown in Figure A29

Point	1σ	1	2	3	4	5	6	7	8	9	10	11	12	13	14	15	17	18
Na_2O (wt %)	0.04	0.51	0.30	0.30	0.35	0.44	0.39	0.36	0.39	0.35	0.34	0.40	0.30	0.33	0.35	0.30	0.37	0.51
MgO	0.02	0.55	0.09	0.08	0.08	0.13	0.10	0.07	0.10	0.07	0.08	0.09	0.09	0.08	0.11	0.08	0.12	0.16
Al_2O_3	0.42	34.85	36.22	36.17	35.65	35.53	35.90	35.70	35.53	35.84	35.77	35.22	35.61	35.72	35.31	35.65	35.24	33.10
SiO_2	0.24	45.00	44.90	44.88	44.70	44.11	44.93	44.56	44.44	44.71	44.17	44.04	44.44	44.10	44.23	44.09	44.01	42.03
K_2O	0.02	0.05	b.d.	b.d.	b.d.	0.07	0.03	b.d.	b.d.	0.03	b.d.	0.04	b.d.	b.d.	b.d.	b.d.	0.05	0.13
CaO	0.39	19.14	19.84	19.89	19.82	19.45	19.60	19.68	19.76	19.58	19.64	19.87	19.72	19.73	19.76	19.84	19.75	19.33
FeO	0.05	0.24	0.14	0.09	0.14	0.13	0.09	0.10	0.13	0.14	0.13	0.10	0.11	0.13	0.15	0.13	0.15	0.31
Total		100.35	101.49	101.41	100.74	99.85	101.03	100.47	100.35	100.72	100.13	99.75	100.28	100.10	99.91	100.08	99.69	95.57

Table A30, ctd

Point	19	20	21	22	23
Na_2O (wt %)	0.36	0.35	0.31	0.37	0.39
MgO	0.08	0.09	0.11	0.09	0.07
Al_2O_3	35.53	35.63	35.73	35.65	35.67
SiO_2	43.94	44.04	44.77	44.82	44.62
K_2O	b.d.	b.d.	b.d.	b.d.	b.d.
CaO	19.89	19.82	19.65	19.66	19.78
FeO	0.13	0.15	0.18	0.20	0.21
Total	99.93	100.09	100.76	100.79	100.75

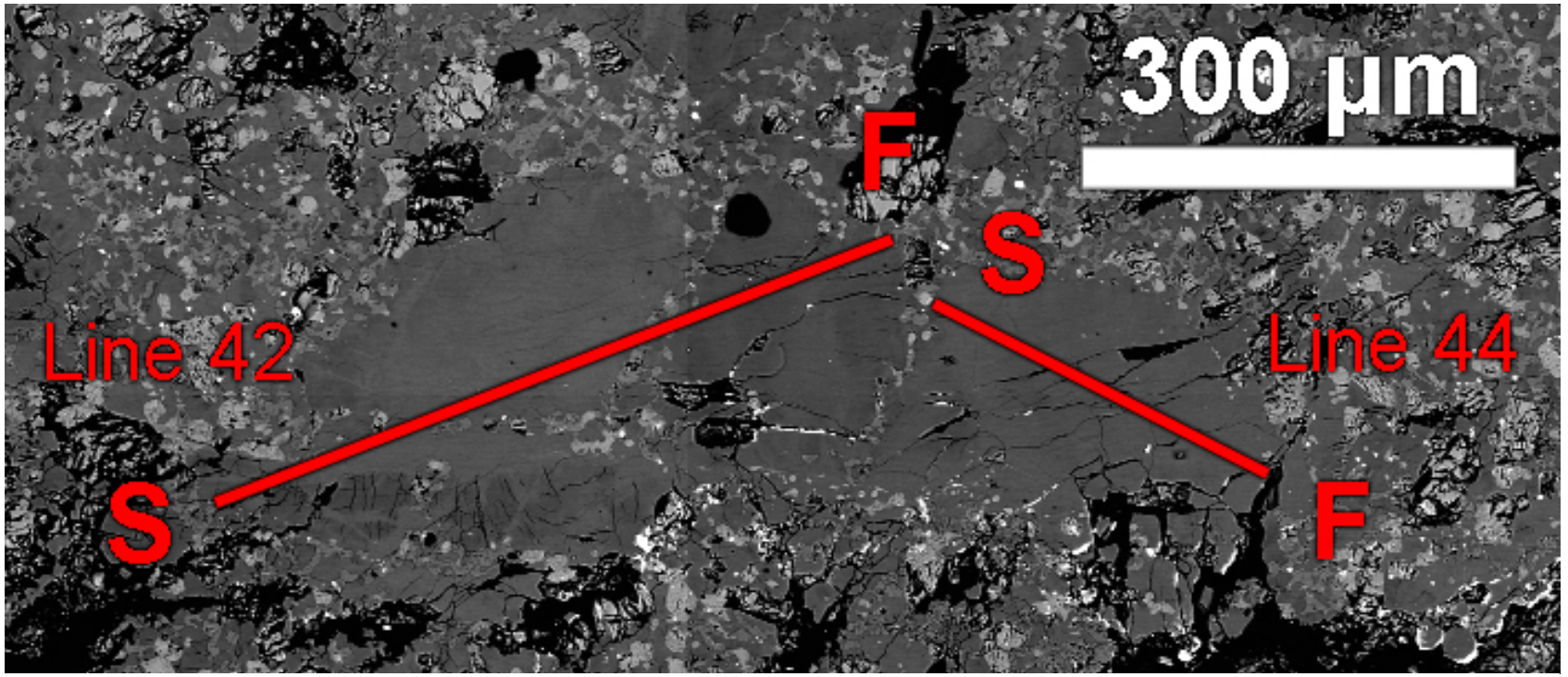

Figure A30: Map of EMP plagioclase Line 42 and 44 locations, respectively. Line scan 42 (Table A31) is 479 µm in length and was configured to acquire 25 points with 20 µm spacing. Line scan 44 (Table A32) is 242 µm in length and was configured to acquire 13 points with 20.2 µm spacing.

Table A31: Major element content of individual plagioclase points in Line 42 shown in Figure A30

Point	1σ	1	2	3	4	5	6	7	8	9	10	11	12	13	14	15	18
Na_2O (wt %)	0.04	0.28	0.39	0.42	0.53	0.43	0.37	0.30	0.47	0.30	0.32	0.42	0.29	0.31	0.34	0.44	0.33
MgO	0.02	0.06	0.07	0.13	0.58	0.08	1.22	0.04	0.08	0.06	0.05	0.08	0.10	0.06	0.06	0.06	0.09
Al_2O_3	0.42	36.22	36.06	35.53	34.71	35.43	31.86	35.82	35.52	36.07	36.03	35.24	35.69	35.86	35.67	35.72	35.60
SiO_2	0.24	44.44	44.38	44.21	45.35	44.79	43.95	44.17	44.08	44.56	44.67	43.89	44.61	44.58	44.60	44.38	43.99
K_2O	0.02	b.d.	b.d.	0.10	0.03	0.03	0.04	0.03	0.08	b.d.	b.d.	0.09	b.d.	b.d.	b.d.	0.06	b.d.
CaO	0.39	19.78	19.68	19.55	18.98	19.55	18.81	19.70	19.58	19.71	19.77	19.77	19.71	19.74	19.60	19.61	20.05
FeO	0.05	0.19	0.19	0.23	0.28	0.20	0.53	0.24	0.20	0.17	0.12	0.13	0.11	0.11	0.15	0.15	0.13
Total		100.97	100.77	100.18	100.47	100.51	96.77	100.28	100.00	100.87	100.96	99.63	100.50	100.66	100.42	100.42	100.20

Table 31, ctd

Point	19	20	21	22	23	24	25
Na_2O (wt %)	0.42	0.34	0.38	0.31	0.30	0.31	0.48
MgO	0.04	0.07	0.08	0.06	0.08	0.08	0.10
Al_2O_3	35.76	35.75	35.59	35.69	35.78	35.77	35.13
SiO_2	44.11	44.24	43.96	44.20	44.50	44.06	44.69
K_2O	b.d.	b.d.	b.d.	b.d.	b.d.	b.d.	0.03
CaO	19.86	19.72	19.84	19.89	19.71	19.66	19.48
FeO	0.10	0.12	0.17	0.10	0.13	0.15	0.26
Total	100.30	100.24	100.02	100.26	100.50	100.03	100.16

Table A32: Major element content of individual plagioclase points in Line 44 shown in Figure A30

Point	1σ	1	2	3	4	5	6	7	8	9	10	11	12	13
Na_2O (wt %)	0.04	0.31	0.30	0.34	0.34	0.34	0.37	0.42	0.39	0.34	0.32	0.31	0.27	0.32
MgO	0.02	0.06	0.08	0.10	0.11	0.08	0.08	0.09	0.07	0.08	0.08	0.10	0.07	0.08
Al_2O_3	0.42	35.53	35.58	35.60	35.73	35.53	35.78	35.94	35.99	35.78	36.03	35.54	35.73	35.81
SiO_2	0.24	44.18	44.22	44.24	44.21	44.23	44.41	43.89	44.37	44.37	44.52	44.11	44.36	44.77
K_2O	0.02	b.d.	b.d.	b.d.	b.d.	b.d.	b.d.	0.06	0.04	b.d.	b.d.	b.d.	b.d.	b.d.
CaO	0.39	19.70	19.85	19.73	19.71	19.78	19.78	19.42	19.76	19.61	19.69	19.71	20.03	19.61
FeO	0.05	0.20	0.12	0.13	0.09	0.10	0.10	0.17	0.11	0.08	0.15	0.12	0.17	0.22
Total		99.98	100.14	100.15	100.19	100.07	100.51	99.99	100.73	100.25	100.80	99.89	100.62	100.81

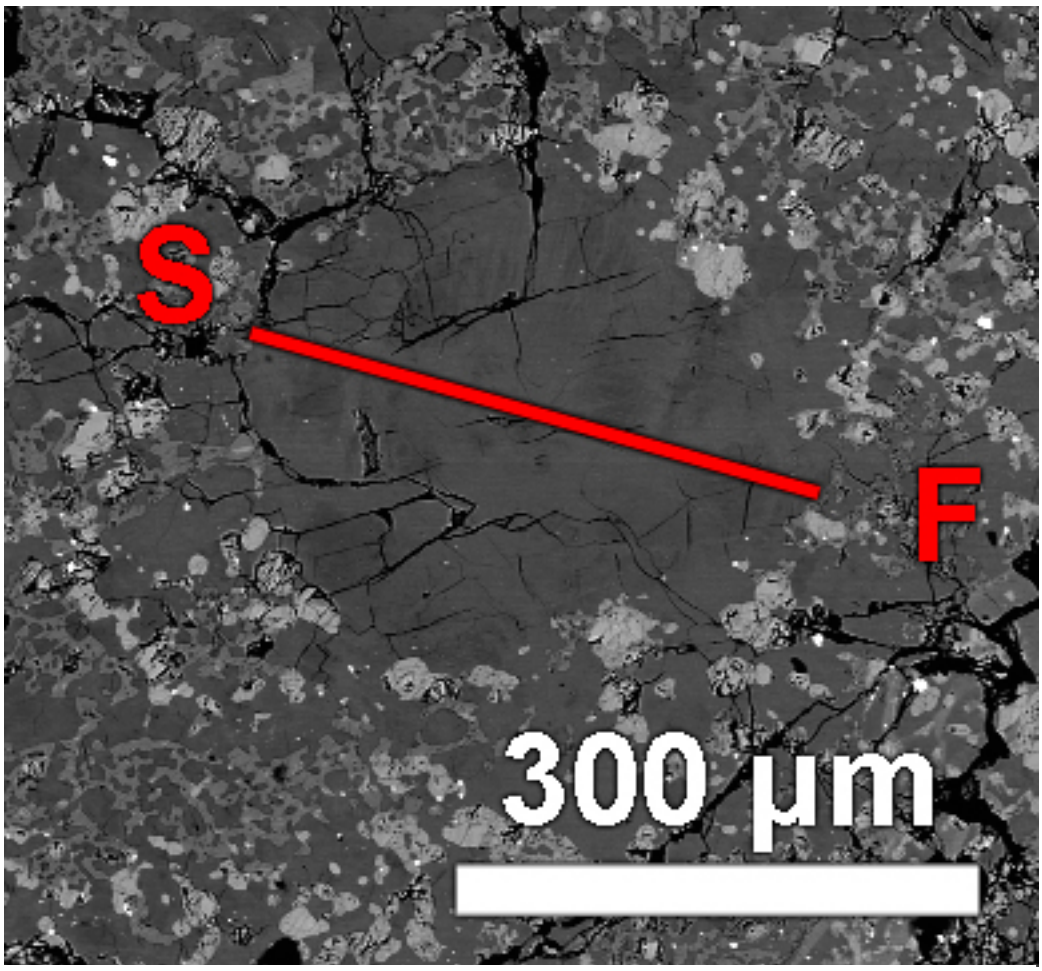

Figure A31: Map of Table A33 EMP plagioclase line location. The line scan is 320 µm in length and was configured to acquire 20 points with 16.8 µm spacing.

Table A33: Major element content of individual plagioclase points in the line scan shown in Figure A31

Point	1σ	1	2	3	4	5	6	7	8	9	10	11	12	13	14	15	16
Na_2O	0.04	0.32	0.30	0.33	0.28	0.29	0.33	0.34	0.34	0.34	0.32	0.29	0.30	0.35	0.32	0.34	0.32
MgO	0.02	0.11	0.15	0.14	0.13	0.13	0.14	0.14	0.14	0.14	0.15	0.13	0.15	0.16	0.15	0.15	0.14
Al_2O_3	0.42	35.44	35.34	35.64	35.52	35.65	35.45	35.38	35.14	35.42	35.42	35.44	35.34	35.25	35.62	35.65	35.62
SiO_2	0.24	44.48	44.02	44.01	44.32	44.48	44.47	44.51	44.12	44.38	44.57	44.35	43.95	43.75	44.56	44.72	44.35
K_2O	0.02	0.03	b.d.	0.04	b.d.	b.d.	b.d.	0.04	0.07	b.d.	b.d.	b.d.	0.04	0.09	b.d.	b.d.	b.d.
CaO	0.40	19.81	19.80	19.64	19.80	19.63	19.77	19.71	19.72	19.54	19.50	19.80	19.64	19.56	19.76	19.89	19.63
FeO	0.05	0.23	0.20	0.12	0.17	0.17	0.13	0.09	0.13	0.12	0.14	0.14	0.13	0.19	0.13	0.16	0.15
Total		100.50	99.89	100.01	100.33	100.40	100.42	100.32	99.66	99.97	100.27	100.19	99.59	99.49	100.58	101.03	100.27

Table 33A, ctd

Point	17	19	20
Na_2O	0.33	0.36	0.50
MgO	0.14	0.12	0.09
Al_2O_3	35.45	35.59	35.17
SiO_2	44.34	45.08	44.50
K_2O	0.03	b.d.	0.03
CaO	19.69	19.58	19.31
FeO	0.17	0.22	0.31
Total	100.21	101.03	100.01

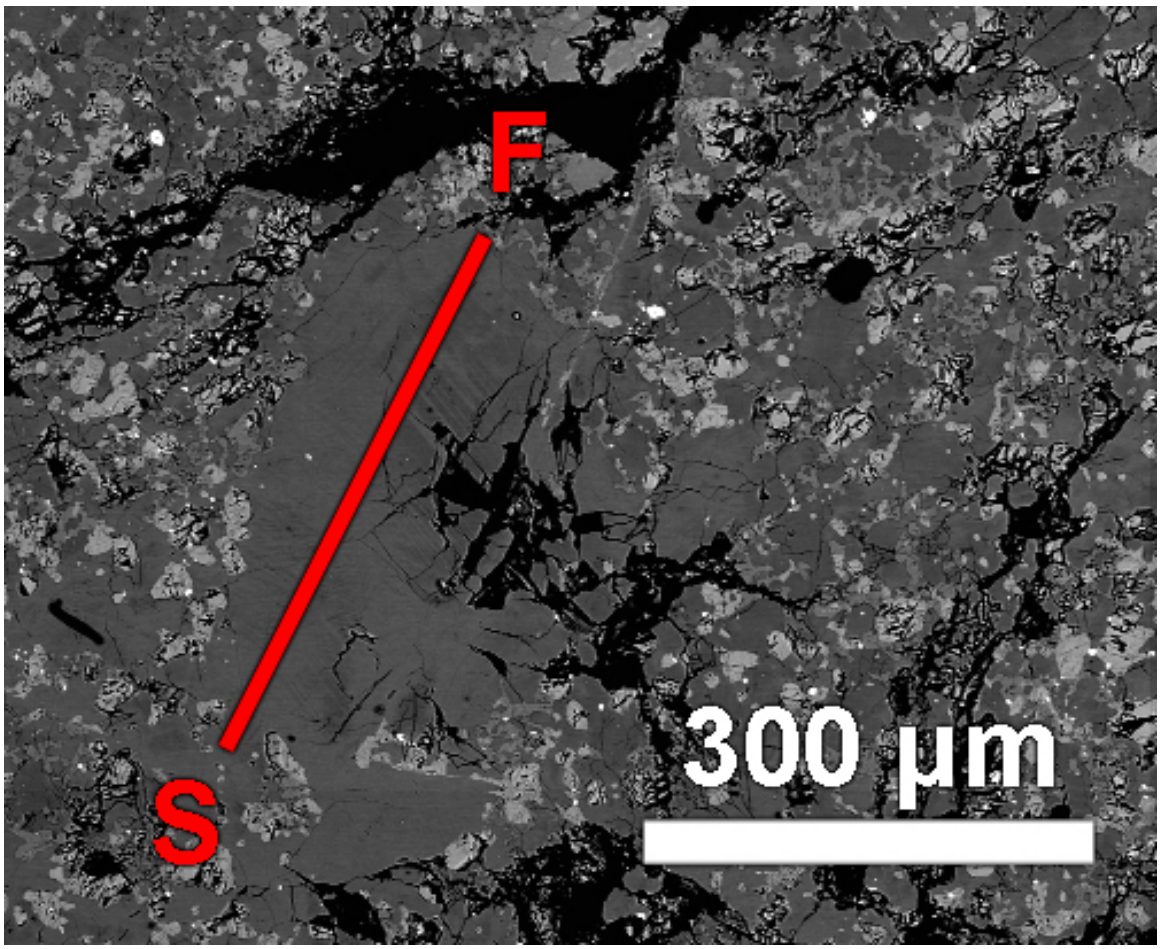

Figure A32: Map of Table A34 EMP plagioclase line location. The line scan is 376 µm in length and was configured to acquire 50 points with 7.7 µm spacing.

Table A34: Major element content of individual plagioclase points in the line scan shown in Figure A32

	1σ	1	2	5	6	8	9	10	11	13	16	18	19	20	21	22	23	24
Na_2O (wt %)	0.04	0.36	0.43	0.44	0.48	0.48	0.49	0.52	0.49	0.44	0.50	0.50	0.54	0.53	0.54	0.50	0.62	0.47
MgO	0.02	0.05	0.07	0.13	0.13	0.13	0.12	0.12	0.14	0.13	0.13	0.13	0.12	0.13	0.13	0.12	0.11	0.12
Al_2O_3	0.26	34.17	34.18	33.71	33.88	33.96	34.01	34.00	33.96	33.94	33.80	33.78	33.80	33.73	33.69	33.98	34.02	34.12
SiO_2	0.28	43.89	44.02	44.30	44.29	44.30	44.35	44.45	44.19	44.32	44.29	44.22	44.29	44.40	44.27	44.43	44.42	44.57
K_2O	0.02	b.d.	b.d.	b.d.	0.03	0.03	0.05	0.03	0.03	b.d.	b.d.	0.03	b.d.	b.d.	0.04	b.d.	0.03	0.03
CaO	0.43	19.66	19.34	19.48	19.22	19.24	19.24	19.30	19.17	19.21	19.21	19.33	19.05	19.33	19.24	19.29	19.31	19.30
TiO_2	0.03	b.d.	b.d.	b.d.	b.d.	0.05	b.d.	b.d.	b.d.	0.05	b.d.	b.d.	0.04	b.d.	0.04	b.d.	b.d.	0.05
FeO	0.05	0.16	0.17	0.15	0.15	0.17	0.18	0.15	0.12	0.17	0.14	0.11	0.14	0.14	0.16	0.14	0.14	0.11
Total		98.29	98.23	98.22	98.17	98.37	98.43	98.56	98.10	98.27	98.06	98.10	97.98	98.27	98.10	98.46	98.66	98.77

Table A34, ctd

	25	26	27	29	30	31	32	33	34	35	36	37	38	39	40	41	42	43
Na_2O (wt %)	0.48	0.49	0.48	0.49	0.49	0.49	0.51	0.52	0.50	0.50	0.50	0.55	0.47	0.50	0.47	0.48	0.48	0.50
MgO	0.13	0.11	0.12	0.17	0.14	0.13	0.11	0.16	0.12	0.13	0.13	0.13	0.14	0.16	0.17	0.15	0.14	0.14
Al_2O_3	34.05	34.09	34.03	33.79	34.26	34.06	34.13	34.01	34.13	34.09	34.13	34.05	33.99	34.22	34.26	34.32	34.15	34.26
SiO_2	44.34	44.23	44.39	44.86	44.62	44.51	44.61	44.51	44.59	44.37	44.55	44.55	44.70	44.42	44.72	44.36	44.42	44.56
K_2O	b.d.	b.d.	b.d.	0.03	b.d.	b.d.	b.d.	0.08	0.03	0.03	b.d.	0.05	0.04	0.04	b.d.	b.d.	0.03	b.d.
CaO	19.40	19.40	19.36	19.23	19.50	19.50	19.38	19.08	19.28	19.08	19.18	19.35	19.29	19.36	19.40	19.47	19.57	19.07
TiO_2	b.d.	0.04	b.d.	0.04	b.d.	0.04	b.d.	b.d.	0.07	b.d.	b.d.	b.d.	b.d.	b.d.	0.06	b.d.	0.05	b.d.
FeO	0.13	0.15	0.16	0.19	0.15	0.16	0.17	0.16	0.14	0.14	0.16	0.20	0.16	0.17	0.20	0.15	0.19	0.14
Total	98.53	98.50	98.53	98.80	99.16	98.90	98.92	98.53	98.85	98.34	98.66	98.88	98.79	98.87	99.27	98.94	99.04	98.67

Table A34, ctd

	44	45	46	47	48	49
Na_2O (wt %)	0.49	0.54	0.59	0.48	0.50	0.54
MgO	0.17	0.15	0.15	0.13	0.12	0.12
Al_2O_3	34.19	33.95	34.09	34.50	34.29	34.22
SiO_2	44.57	44.47	44.54	44.79	44.67	44.52
K_2O	b.d.	0.09	0.05	b.d.	0.03	0.07
CaO	19.54	19.24	19.12	19.32	19.26	19.22
TiO_2	b.d.	b.d.	b.d.	0.06	0.04	0.05
FeO	0.17	0.24	0.24	0.20	0.26	0.26
Total	99.13	98.68	98.78	99.49	99.18	98.99

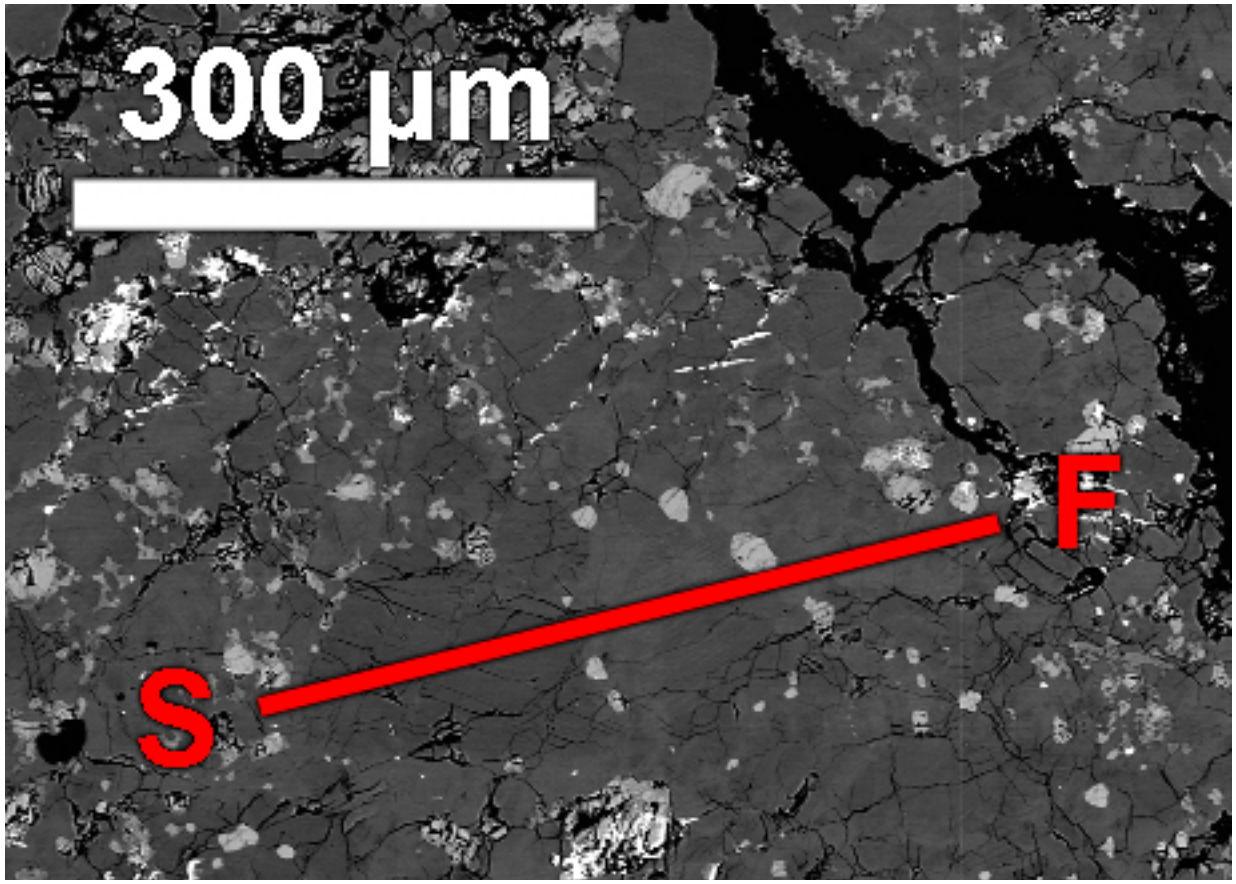

Figure A33: Map of Table A35 EMP plagioclase line location. The line scan is 420 µm in length and was configured to acquire 70 points with 6.1 µm spacing.

Table A35: Major element content of individual plagioclase points in the line scan shown in Figure A33

	1σ	1	2	3	9	11	14	18	19	20	21	23	25	26	27	29	30	31
Na_2O (wt %)	0.04	0.33	0.42	0.32	0.35	0.37	0.38	0.34	0.31	0.31	0.31	0.30	0.34	0.31	0.32	0.38	0.37	0.35
MgO	0.01	0.06	0.06	0.05	0.04	0.07	0.09	0.08	0.07	0.08	0.08	0.07	0.10	0.09	0.08	0.05	0.06	0.05
Al_2O_3	0.27	34.27	34.41	34.62	34.62	34.25	34.58	34.45	34.20	34.21	34.18	34.96	34.35	34.84	34.31	34.43	34.58	34.52
SiO_2	0.28	44.70	44.37	43.57	44.20	44.17	43.90	43.88	44.08	43.81	43.68	44.29	43.68	43.61	43.61	44.37	44.11	44.08
P_2O_5	0.03	0.05	b.d.	b.d.	b.d.	0.05	b.d.	0.04	b.d.	0.04	b.d.	0.04	b.d.	0.06	b.d.	b.d.	b.d.	0.04
K_2O	0.02	0.07	0.03	0.03	b.d.	0.05	0.09	b.d.	b.d.	b.d.	b.d.	b.d.	0.04	b.d.	b.d.	0.04	b.d.	b.d.
CaO	0.44	19.81	19.68	19.62	20.19	19.52	19.38	19.58	19.34	19.41	19.54	19.91	19.66	19.72	19.47	19.61	19.53	19.64
FeO	0.05	0.20	0.11	0.18	0.09	0.13	0.09	0.11	0.11	0.11	0.13	0.10	0.14	0.13	0.11	0.10	0.13	0.09
Total		99.49	99.09	98.40	99.48	98.61	98.51	98.48	98.12	97.97	97.92	99.67	98.30	98.77	97.90	98.99	98.78	98.77

Table A35, ctd

	32	33	34	35	36	37	38	39	40	41	42	43	44	45	46	47	48	49
Na_2O (wt %)	0.35	0.36	0.34	0.34	0.34	0.34	0.33	0.32	0.32	0.31	0.33	0.32	0.34	0.41	0.43	0.45	0.37	0.41
MgO	0.07	0.07	0.08	0.09	0.08	0.09	0.10	0.09	0.09	0.09	0.10	0.10	0.07	0.04	0.06	0.04	0.05	0.06
Al_2O_3	34.36	34.39	34.45	34.56	34.82	34.81	34.82	34.64	34.43	34.69	34.62	34.67	34.68	35.07	34.81	34.74	34.90	34.86
SiO_2	43.95	43.90	43.57	43.85	44.09	44.07	43.92	43.94	43.92	44.13	43.90	44.09	44.23	44.30	44.43	44.11	44.11	44.20
P_2O_5	b.d.	0.04	0.04	b.d.	b.d.	b.d.	b.d.	b.d.	b.d.	0.06	0.04	0.05	0.05	b.d.	b.d.	b.d.	0.08	b.d.
K_2O	b.d.	b.d.	b.d.	b.d.	0.03	b.d.	b.d.	b.d.	b.d.	b.d.	0.03	b.d.	b.d.	0.03	0.06	0.09	0.05	0.05
CaO	19.22	19.61	19.53	19.55	19.69	19.49	19.53	19.63	19.81	19.65	19.43	19.59	19.62	19.66	19.48	19.34	19.36	19.55
FeO	0.14	0.13	0.14	0.14	0.12	0.15	0.10	0.11	0.12	0.15	0.13	0.12	0.14	0.15	0.17	0.14	0.15	0.13
Total	98.08	98.49	98.16	98.52	99.16	98.96	98.80	98.72	98.69	99.08	98.58	98.94	99.14	99.67	99.44	98.91	99.08	99.25

Table A35, ctd

	50	51	52	53	54	55	56	57	58	59	60	61	62	63	64	65	66	67
Na_2O (wt %)	0.41	0.40	0.42	0.38	0.34	0.39	0.40	0.52	0.39	0.59	0.29	0.44	0.39	0.39	0.36	0.40	0.39	0.38
MgO	0.06	0.06	0.03	0.05	0.05	0.08	0.06	0.04	0.06	0.07	0.05	0.08	0.05	0.06	0.03	0.05	0.05	0.08
Al_2O_3	34.71	34.75	34.77	35.08	34.89	34.86	34.87	34.80	34.87	34.41	35.15	34.50	35.14	34.98	35.01	35.02	35.04	34.79
SiO_2	44.28	44.12	44.14	44.58	44.43	44.36	44.46	44.03	43.98	44.36	43.94	44.15	44.32	43.98	44.05	44.07	44.37	44.25
P_2O_5	b.d.	b.d.	b.d.	b.d.	b.d.	b.d.	b.d.	b.d.	b.d.	b.d.	b.d.	b.d.	0.05	b.d.	b.d.	b.d.	b.d.	b.d.
K_2O	0.07	0.05	0.03	b.d.	b.d.	0.03	b.d.	0.03	b.d.	0.07	0.04	0.10	0.03	0.04	0.05	b.d.	0.04	0.07
CaO	19.46	19.56	19.54	19.26	19.55	19.28	19.65	19.37	19.48	19.40	19.75	19.35	19.60	19.63	19.67	19.57	19.26	19.20
FeO	0.15	0.16	0.15	0.17	0.12	0.15	0.14	0.12	0.14	0.16	0.11	0.14	0.14	0.12	0.13	0.14	0.13	0.13
Total	99.13	99.10	99.08	99.52	99.38	99.16	99.60	98.91	98.91	99.07	99.33	98.76	99.72	99.21	99.29	99.25	99.28	98.90

Table A35, ctd

	68	69
Na_2O (wt %)	0.32	0.29
MgO	0.01	0.03
Al_2O_3	35.28	35.41
SiO_2	43.97	43.95
P_2O_5	b.d.	b.d.
K_2O	b.d.	b.d.
CaO	19.78	19.63
FeO	0.11	0.18
Total	99.46	99.49

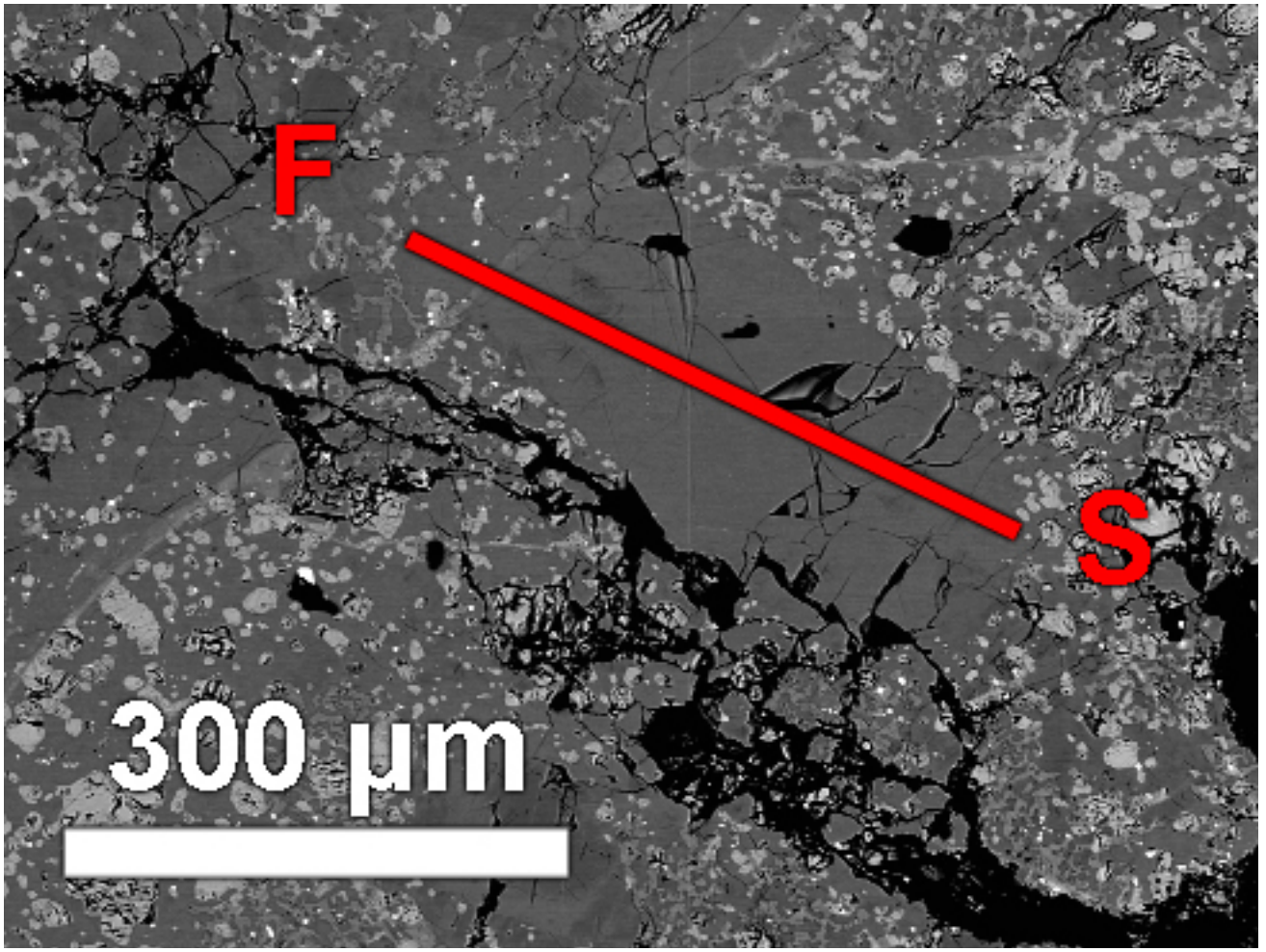

Figure A34: Map of Table A36 EMP plagioclase line location. The line scan is 390 µm in length and was configured to acquire 50 points with 8 µm spacing.

Table A36: Major element content of individual plagioclase points in the line scan shown in Figure A34

	1σ	2	3	23	24	25	26	29	30	31	32	33	34	35	36	37	45	46
Na_2O (wt %)	0.04	0.40	0.43	0.39	0.39	0.59	0.63	0.44	0.42	0.45	0.46	0.45	0.43	0.47	0.52	0.45	0.41	0.40
MgO	0.02	0.15	0.46	0.41	0.60	0.08	0.11	0.05	0.62	0.06	0.07	0.08	0.07	0.06	0.08	0.10	0.20	0.09
Al_2O_3	0.27	35.42	35.22	34.99	34.97	35.31	34.88	35.36	34.81	35.34	35.27	35.24	35.27	35.18	35.11	35.23	35.35	35.33
SiO_2	0.28	44.19	44.16	44.04	43.98	43.83	44.23	44.26	44.50	44.31	44.56	44.53	44.55	44.48	44.42	44.37	44.28	44.59
K_2O	0.02	0.03	b.d.	0.04	0.03	0.04	0.03	b.d.	0.03	0.03	b.d.	b.d.	b.d.	b.d.	b.d.	b.d.	0.03	b.d.
CaO	0.43	19.59	19.15	19.25	19.08	19.46	19.13	19.32	19.20	19.28	19.20	19.63	19.43	19.31	19.16	19.45	19.48	19.13
FeO	0.06	0.37	0.42	0.51	0.60	0.46	0.45	0.45	0.56	0.38	0.37	0.38	0.39	0.33	0.36	0.31	0.35	0.37
Total		100.16	99.85	99.64	99.65	99.78	99.46	99.88	100.15	99.85	99.93	100.31	100.15	99.83	99.64	99.91	100.10	99.90

Table A36, ctd

	47	48	49	50
Na_2O (wt %)	0.47	0.45	0.44	0.44
MgO	0.10	0.08	0.08	0.07
Al_2O_3	35.18	35.08	35.12	35.28
SiO_2	45.02	45.16	44.64	44.57
K_2O	0.05	0.04	0.03	b.d.
CaO	19.20	19.23	19.18	19.37
FeO	0.33	0.39	0.30	0.35
Total	100.35	100.42	99.80	100.08

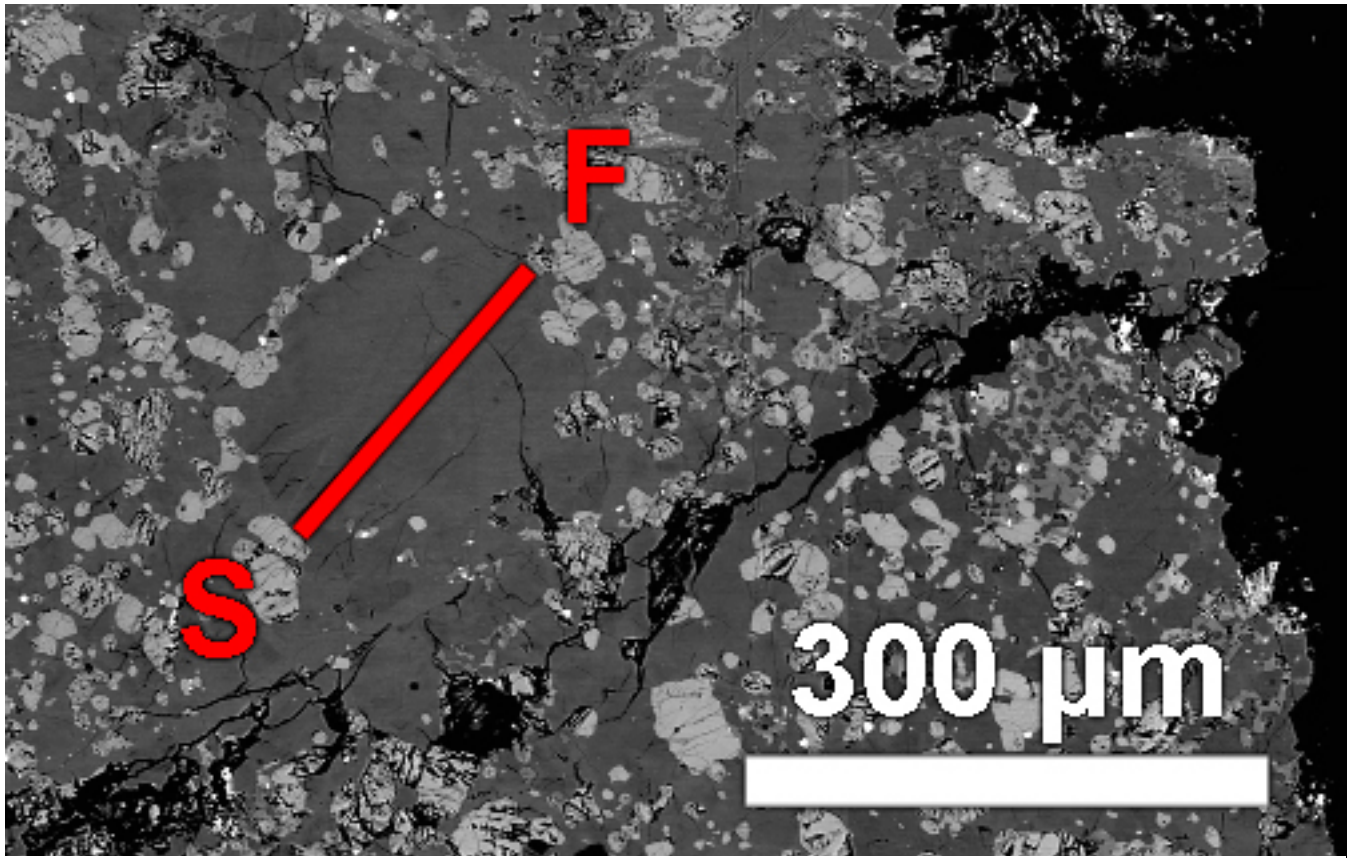

Figure A35: Map of Table A37 EMP plagioclase line location. The line scan is 189 µm in length and was configured to acquire 30 points with 6.5 µm spacing.

Table A37: Major element content of individual plagioclase points in the line scan shown in Figure A35

	1σ	1	2	3	4	5	6	7	8	9	10	11	12	14	15	16	17	18
Na_2O (wt %)	0.04	0.36	0.30	0.29	0.33	0.31	0.30	0.32	0.29	0.29	0.32	0.31	0.32	0.33	0.37	0.32	0.32	0.31
MgO	0.01	0.04	0.07	0.04	0.07	0.08	0.07	0.06	0.08	0.08	0.08	0.08	0.09	0.07	0.08	0.10	0.08	0.06
Al_2O_3	0.27	35.71	35.59	35.53	35.54	35.56	35.59	35.50	35.59	35.41	35.54	35.65	35.48	35.54	36.39	35.79	35.46	35.76
SiO_2	0.28	43.86	43.93	43.77	44.14	43.82	43.93	44.01	43.98	44.06	44.08	44.00	43.89	43.61	44.42	43.66	44.03	44.02
K_2O	0.02	b.d.	b.d.	b.d.	b.d.	b.d.	b.d.	0.03	b.d.	b.d.	b.d.	b.d.	b.d.	b.d.	b.d.	b.d.	0.03	0.03
CaO	0.44	19.92	19.74	19.71	19.81	19.89	19.76	19.83	19.84	19.69	19.70	19.85	19.91	19.48	20.26	19.75	19.71	20.05
FeO	0.05	0.15	0.17	0.14	0.11	0.17	0.10	0.14	0.08	0.06	0.09	0.08	0.12	0.16	0.10	0.12	0.11	0.10
Total		100.03	99.80	99.48	100.00	99.83	99.76	99.89	99.86	99.59	99.82	99.96	99.81	99.19	101.62	99.74	99.74	100.33

Table A37, ctd

	19	20	21	22	23	24	25	26	27	28	29
Na_2O (wt %)	0.33	0.36	0.33	0.41	0.29	0.36	0.35	0.36	0.39	0.40	0.37
MgO	0.08	0.06	0.07	0.09	0.07	0.08	0.06	0.04	0.06	0.07	0.07
Al_2O_3	35.56	35.78	35.52	35.55	35.57	35.54	35.91	35.97	35.27	35.60	35.23
SiO_2	44.14	43.61	44.30	44.01	43.42	43.81	44.03	44.28	43.65	44.19	43.91
K_2O	b.d.	0.05	0.03	0.06	b.d.	b.d.	0.04	0.03	0.04	0.03	0.06
CaO	19.67	19.47	19.98	19.85	19.57	19.77	19.93	19.97	19.49	19.74	19.57
FeO	0.12	0.12	0.13	0.09	0.13	0.16	0.15	0.17	0.19	0.26	0.26
Total	99.90	99.45	100.36	100.06	99.06	99.72	100.46	100.81	99.08	100.30	99.47

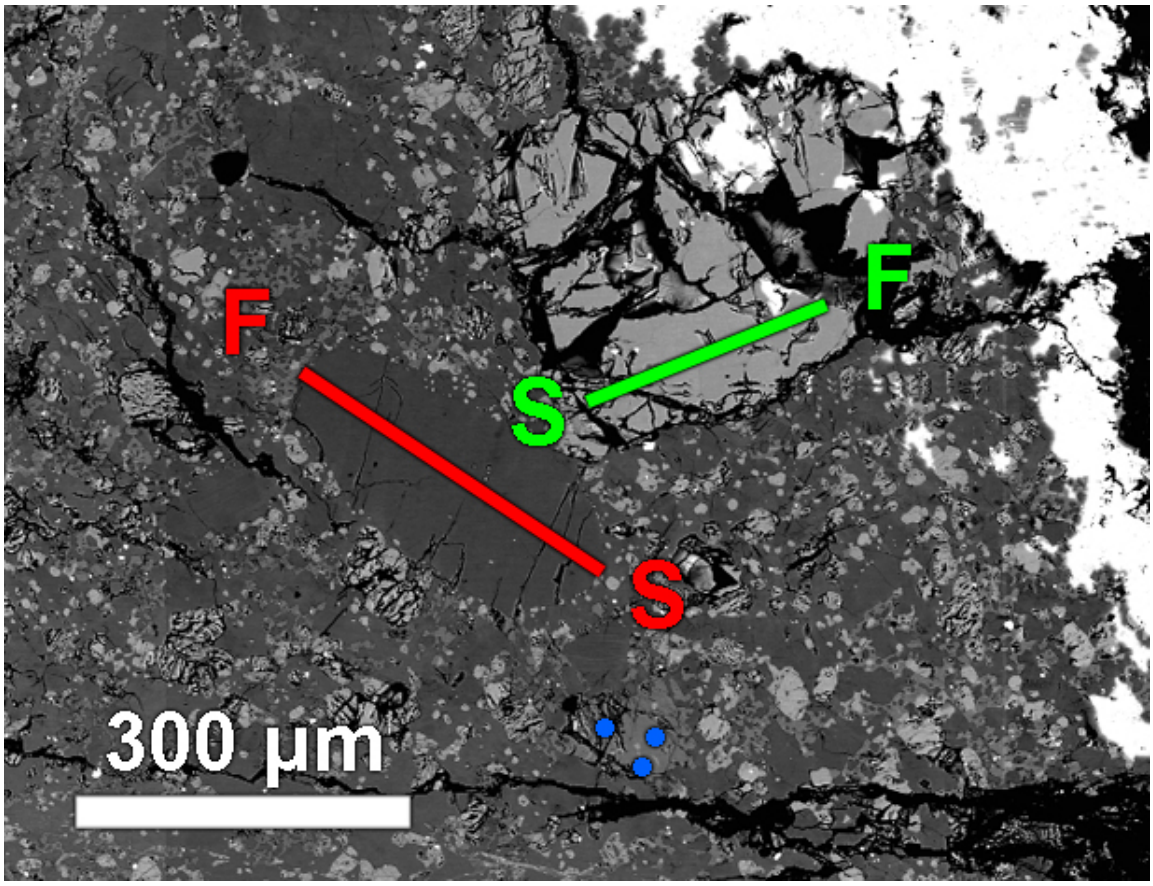

Figure A36: Map of Table A38 EMP clinoenstatite point locations in blue and Tables A39 and A40 of the pictured plagioclase and olivine line locations, respectively. The plagioclase line scan (shown in red) is 319 µm in length and was configured to acquire 50 points with 6.5 µm spacing. The olivine line scan (shown in green) is 225 µm in length and was configured to acquire 50 points with 4.6 µm spacing.

Table A38: Averaged major element content of clinoenstatite in Figure A36

	C-En	1σ
Points	3	
MgO (wt %)	28.87	0.38
Al_2O_3	1.15	0.03
SiO_2	54.53	0.32
CaO	2.67	0.09
TiO_2	0.46	0.04
Cr_2O_3	0.52	0.05
MnO	0.27	0.06
FeO	11.73	0.51
Total	100.20	

Table A39: Major element content of individual plagioclase points in the line scan shown in FigureA36

	1σ	1	2	3	4	5	6	8	10	12	13	14	15	16	17	18	19	20
Na_2O (wt %)	0.04	0.38	0.41	0.44	0.27	0.29	0.27	0.30	0.29	0.34	0.32	0.30	0.31	0.32	0.33	0.30	0.32	0.32
MgO	0.01	0.16	0.10	0.08	0.06	0.06	0.07	0.07	0.07	0.07	0.06	0.05	0.06	0.07	0.07	0.09	0.08	0.07
Al_2O_3	0.27	35.47	35.16	35.19	36.08	35.77	35.77	35.69	35.71	35.70	35.66	35.56	35.65	35.63	35.48	35.43	35.40	35.54
SiO_2	0.27	43.86	43.52	43.75	43.56	43.38	43.49	43.28	43.66	43.58	43.41	43.61	43.45	43.88	43.58	43.96	43.42	43.66
P_2O_5	0.03	0.06	b.d.	0.06	b.d.	b.d.	b.d.	b.d.	b.d.	b.d.	b.d.	0.08	b.d.	b.d.	b.d.	b.d.	b.d.	b.d.
K_2O	0.02	b.d.	b.d.	b.d.	b.d.	b.d.	0.03	b.d.	b.d.	b.d.	b.d.	b.d.	0.03	b.d.	b.d.	b.d.	b.d.	b.d.
CaO	0.44	19.79	19.63	19.65	19.86	19.93	19.77	19.70	19.84	19.59	19.62	19.89	19.94	19.91	19.98	19.71	19.68	19.64
FeO	0.05	0.33	0.28	0.26	0.17	0.21	0.18	0.16	0.16	0.13	0.13	0.14	0.15	0.17	0.10	0.14	0.11	0.14
Total		100.03	99.10	99.42	100.00	99.63	99.58	99.20	99.74	99.42	99.21	99.63	99.59	99.97	99.56	99.62	99.00	99.37

Table A39, ctd

	21	22	23	24	25	26	27	28	29	30	31	32	33	34	35	36	37	38
Na_2O (wt %)	0.32	0.51	0.28	0.33	0.35	0.31	0.35	0.32	0.34	0.31	0.38	0.32	0.30	0.33	0.33	0.27	0.31	0.33
MgO	0.05	0.07	0.07	0.08	0.09	0.05	0.04	0.07	0.06	0.06	0.09	0.07	0.07	0.06	0.05	0.06	0.09	0.09
Al_2O_3	35.72	35.27	35.26	35.73	35.59	35.70	35.74	35.73	35.66	35.73	35.63	35.75	35.51	35.62	35.60	35.58	35.57	35.63
SiO_2	43.78	43.67	43.36	43.37	43.73	43.88	43.63	43.34	43.80	43.17	43.54	43.86	43.83	43.23	43.91	43.76	43.72	43.78
P_2O_5	b.d.	b.d.	b.d.	b.d.	b.d.	b.d.	b.d.	b.d.	b.d.	b.d.	b.d.	b.d.	b.d.	0.04	b.d.	b.d.	0.08	b.d.
K_2O	0.03	b.d.	0.03	b.d.	b.d.	0.03	0.03	b.d.	b.d.	b.d.	b.d.	b.d.	b.d.	b.d.	0.11	b.d.	b.d.	b.d.
CaO	19.85	19.77	19.60	19.80	19.80	19.78	19.75	19.66	19.82	19.78	19.51	19.79	19.77	19.96	19.66	19.90	19.96	19.90
FeO	0.14	0.16	0.12	0.15	0.15	0.11	0.12	0.10	0.15	0.15	0.08	0.13	0.12	0.14	0.11	0.12	0.15	0.15
Total	99.88	99.46	98.73	99.46	99.69	99.86	99.66	99.22	99.84	99.19	99.23	99.92	99.59	99.37	99.78	99.70	99.88	99.87

Table A39, ctd:

	39	40	41	42	43	44	45	46	47	48	49	50
Na_2O (wt %)	0.28	0.31	0.33	0.29	0.31	0.28	0.30	0.30	0.26	0.24	0.25	0.25
MgO	0.06	0.07	0.07	0.05	0.06	0.07	0.06	0.06	0.05	0.03	0.04	0.04
Al_2O_3	35.70	35.40	35.57	35.76	35.64	35.74	35.61	35.70	35.71	35.84	35.81	35.89
SiO_2	43.80	43.73	43.82	43.77	43.65	42.30	42.54	42.87	42.47	42.87	43.48	43.24
P_2O_5	b.d.	b.d.	b.d.	b.d.	b.d.	b.d.	b.d.	b.d.	b.d.	b.d.	b.d.	b.d.
K_2O	b.d.	0.05	b.d.	b.d.	0.03	0.03	b.d.	b.d.	b.d.	b.d.	b.d.	b.d.
CaO	19.69	19.54	19.76	19.93	19.74	19.71	19.53	19.90	19.96	20.00	19.86	19.92
FeO	0.16	0.18	0.14	0.11	0.20	0.15	0.16	0.21	0.22	0.21	0.24	0.28
Total	99.70	99.28	99.69	99.91	99.62	98.28	98.19	99.03	98.68	99.20	99.69	99.62

Table A40: Major element content of individual olivine points in the line scan shown in FigureA36

	1σ	1	5	6	9	10	11	12	13	14	15	16	17	18	19	20	21
MgO (wt %)	0.21	50.16	41.50	41.10	41.70	41.24	41.32	41.51	41.43	41.34	41.39	41.62	41.37	41.72	41.58	41.38	41.47
Al_2O_3	0.01	0.10	0.04	0.24	b.d.	0.05	b.d.	0.02	0.03	0.02	0.02	b.d.	0.02	b.d.	b.d.	0.04	0.07
SiO_2	0.22	29.63	37.94	38.17	38.01	38.74	38.76	38.33	38.53	38.43	38.68	38.66	38.73	38.66	38.73	38.71	38.74
P_2O_5	0.03	b.d.	b.d.	0.04	0.04	b.d.	b.d.	b.d.	b.d.	0.06	b.d.	b.d.	b.d.	b.d.	b.d.	b.d.	b.d.
CaO	0.02	0.10	0.07	0.08	0.05	0.07	0.08	0.05	0.08	0.09	0.07	0.07	0.06	0.06	0.07	0.08	0.11
TiO_2	0.02	0.05	0.03	0.07	0.06	0.05	0.06	0.04	0.04	0.03	0.03	0.07	0.05	0.06	0.06	0.05	0.05
Cr_2O_3	0.03	b.d.	0.07	0.08	0.05	0.04	b.d.	b.d.	0.05	b.d.	b.d.	0.05	b.d.	b.d.	b.d.	b.d.	b.d.
MnO	0.06	0.25	0.27	0.26	0.29	0.25	0.25	0.29	0.29	0.26	0.25	0.28	0.24	0.25	0.24	0.26	0.26
FeO	0.34	19.82	20.41	20.27	20.10	20.36	20.37	20.18	20.11	20.25	20.61	20.39	20.35	20.61	20.44	20.28	20.03
Total		100.11	100.34	100.30	100.30	100.80	100.83	100.40	100.55	100.48	101.05	101.15	100.81	101.35	101.13	100.81	100.72

Table A40, ctd

	22	26	27	28	29	30	31	32	33	36	37	38	39	40	41	42	43
MgO (wt %)	41.41	41.53	41.62	41.68	41.52	41.51	41.73	41.38	41.66	39.03	41.73	41.72	41.82	41.80	41.77	41.79	41.87
Al_2O_3	0.04	b.d.	b.d.	0.02	0.05	0.04	0.04	0.08	0.02	0.99	0.02	0.02	0.03	b.d.	0.02	0.02	b.d.
SiO_2	38.88	38.62	38.61	38.83	38.79	38.76	38.82	38.91	38.89	36.95	38.75	38.78	39.01	38.84	38.98	38.86	38.92
P_2O_5	b.d.	0.06	b.d.	b.d.	0.05	b.d.	b.d.	b.d.	b.d.	0.09	b.d.	b.d.	b.d.	b.d.	0.04	b.d.	b.d.
CaO	0.08	0.05	0.07	0.05	0.09	0.07	0.09	0.10	0.06	0.24	0.08	0.07	0.08	0.05	0.07	0.06	0.04
TiO_2	0.04	0.04	0.06	0.05	0.05	0.03	0.03	0.05	0.02	0.10	0.05	0.04	0.04	0.06	0.03	0.04	0.04
Cr_2O_3	b.d.	b.d.	0.06	b.d.	b.d.	b.d.	b.d.	0.04	0.06	0.46	b.d.	0.04	0.04	0.04	0.04	0.05	b.d.
MnO	0.25	0.26	0.22	0.27	0.22	0.27	0.30	0.29	0.22	0.23	0.26	0.28	0.24	0.30	0.26	0.29	0.23
FeO	20.48	20.17	20.34	20.25	20.28	20.40	20.48	20.41	20.37	19.75	20.37	20.12	20.14	20.32	20.08	20.24	20.40
Total	101.17	100.73	100.97	101.14	101.05	101.08	101.48	101.27	101.31	97.83	101.25	101.06	101.39	101.40	101.28	101.36	101.50

Table A40, ctd

	44	45	46	47
MgO (wt %)	41.83	40.84	41.93	41.97
Al_2O_3	0.05	0.10	b.d.	b.d.
SiO_2	39.01	38.78	38.98	38.93
P_2O_5	b.d.	b.d.	b.d.	b.d.
CaO	0.07	0.11	0.07	0.07
TiO_2	0.04	0.05	0.02	0.05
Cr_2O_3	b.d.	b.d.	b.d.	b.d.
MnO	0.28	0.22	0.28	0.24
FeO	20.38	20.21	20.31	20.31
Total	101.65	100.31	101.61	101.58

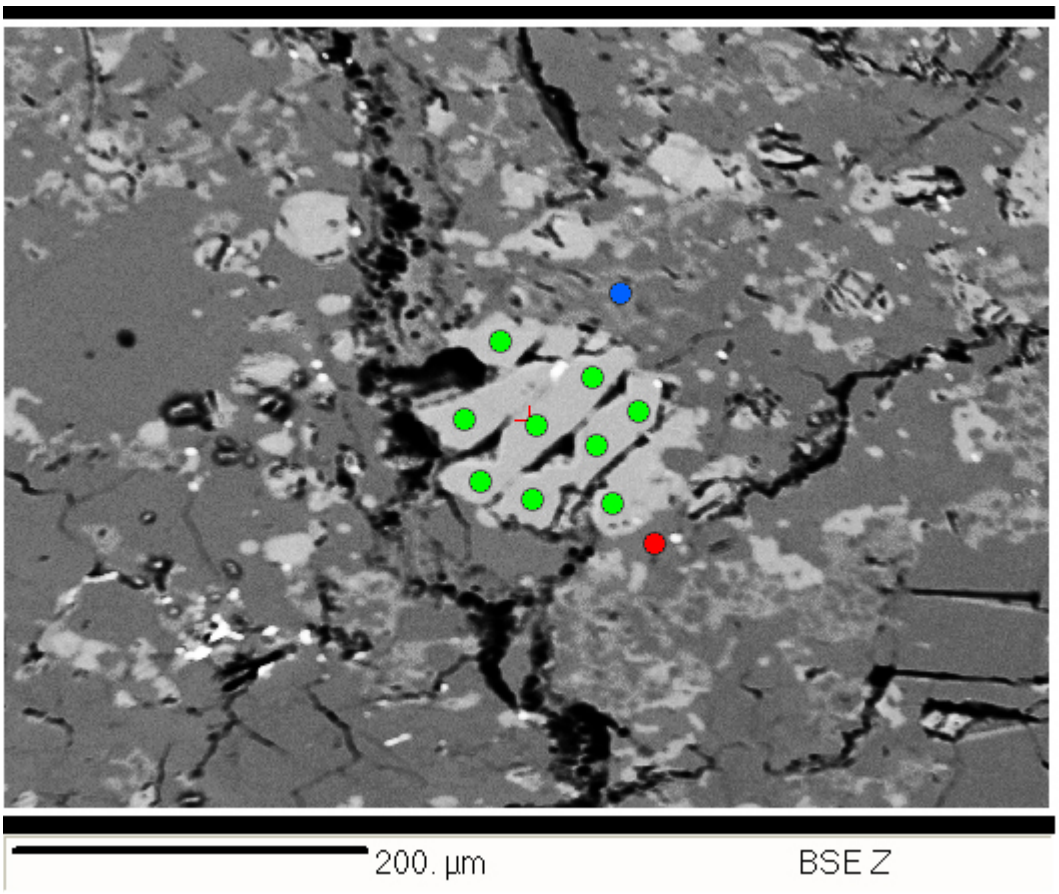

Figure A37: Map of Table A41 EMP point locations. Red, green, and blue dots represent plagioclase, olivine, and clinoenstatite measurement locations, respectively.

Table A41: Averaged major element content of minerals in Figure A37

	Plag	1σ	Olv	1σ	C-En	1σ
Points	1		9		1	
Na_2O (wt %)	0.39	0.04	b.d.	-	0.04	0.03
MgO	0.06	0.01	41.36	0.21	27.70	0.36
Al_2O_3	34.97	0.27	0.03	0.01	4.15	0.06
SiO_2	44.46	0.28	37.92	0.22	54.19	0.32
K_2O	0.03	0.02	b.d.	-	b.d.	-
CaO	19.57	0.44	0.13	0.02	2.52	0.09
TiO_2	0.06	0.03	0.05	0.02	0.59	0.04
Cr_2O_3	b.d.	-	b.d.	-	0.26	0.04
MnO	0.05	0.04	0.25	0.06	0.25	0.05
FeO	0.33	0.06	20.10	0.34	11.34	0.50
Total	99.93		99.84		101.04	

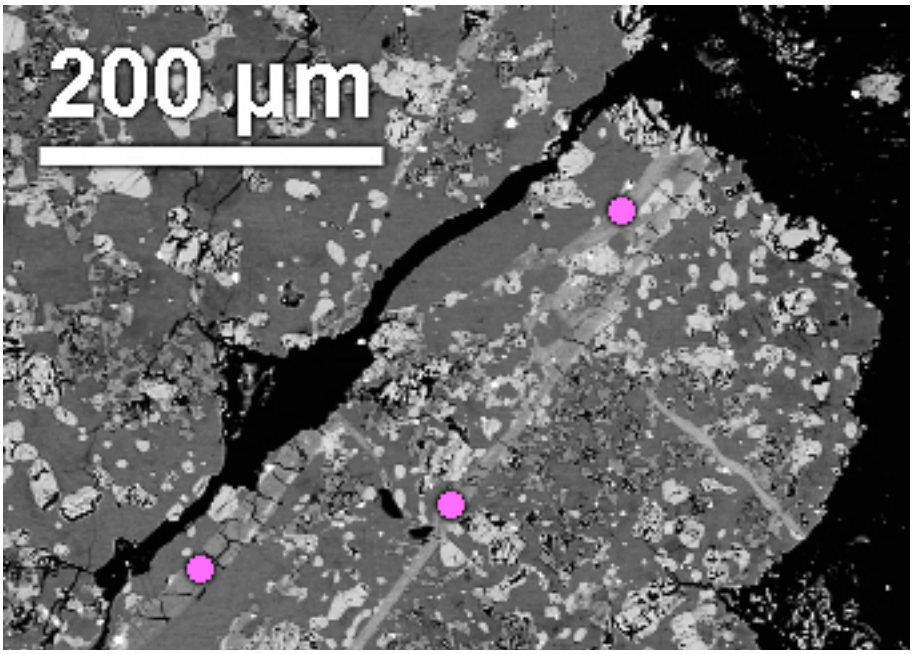

Figure A38: Map of Table A42 EMP point locations for shock vein measurement locations, shown with pink dots.

Table A42: Averaged major element content of shock veins in Figure A38

	SV	1σ
Points	3	
Na_2O (wt %)	0.28	0.04
MgO	9.85	0.14
Al_2O_3	25.67	0.21
SiO_2	44.90	0.28
CaO	14.79	0.35
SO_2	0.08	0.03
TiO_2	0.13	0.03
Cr_2O_3	0.10	0.04
MnO	0.06	0.05
FeO	4.64	0.24
Total	100.51	

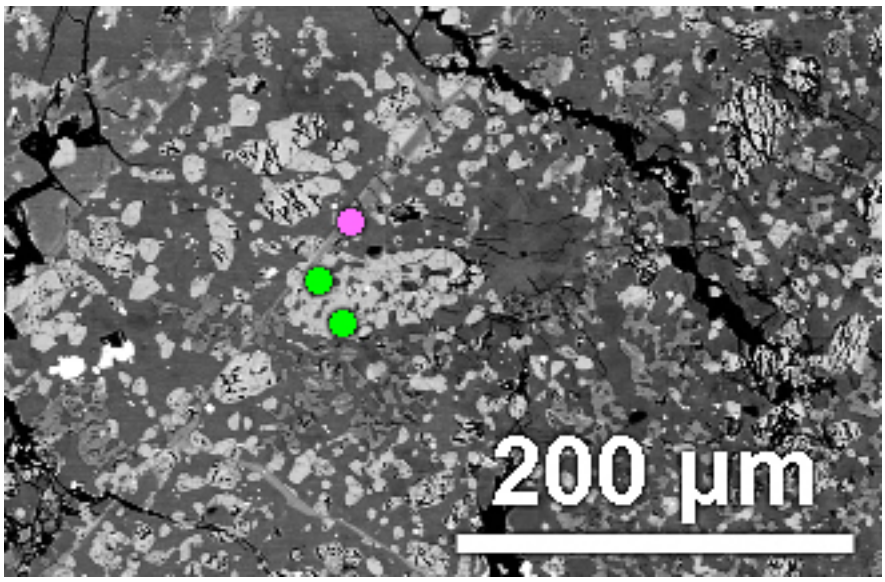

Figure A39: Map of Table A43 EMP point locations for olivine and shock vein measurement locations, shown with green and pink dots respectively.

Table A43: Averaged major element content of minerals in Figure A39

	Olv	1σ	SV	1σ
Points	2		1	
Na_2O (wt %)	b.d.	-	0.34	0.04
MgO	41.02	0.21	10.45	0.15
Al_2O_3	0.11	0.02	24.20	0.20
SiO_2	38.75	0.22	45.06	0.28
P_2O_5	b.d.	-	0.04	0.03
K_2O	0.06	0.03	0.07	0.03
CaO	0.16	0.03	14.54	0.34
SO_2	b.d.	-	0.09	0.03
TiO_2	0.03	0.02	0.14	0.03
Cr_2O_3	b.d.	-	0.07	0.04
MnO	0.22	0.06	0.06	0.05
FeO	20.10	0.34	5.02	0.25
Total	100.44		100.07	

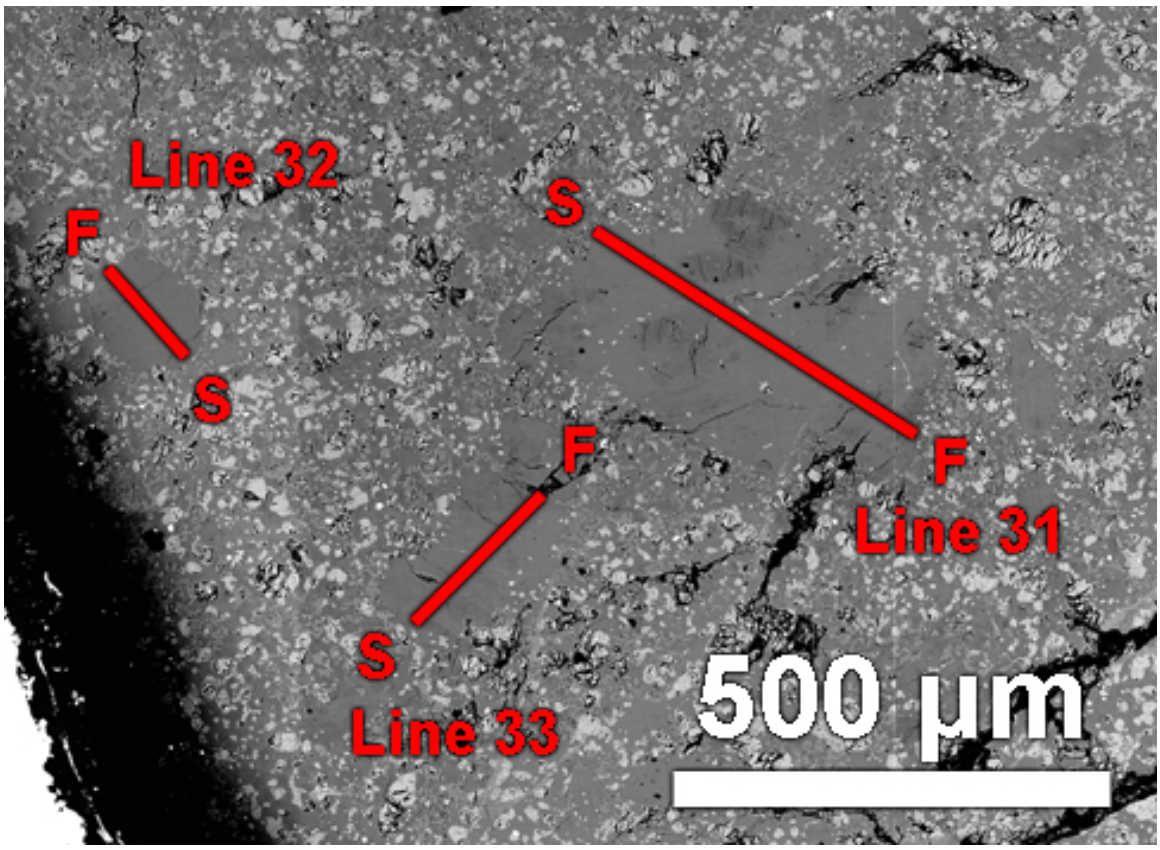

Figure A40: Map of EMP plagioclase Line 31, 32, and 33 locations. Line scan 31 (Table A44) is 495 µm in length and was configured to acquire 50 points with 10.1 µm spacing. Line scan 32 (Table A45) is 154 µm in length and was configured to acquire 20 points with 8.1 µm spacing. Line scan 33 (Table A46) is 235 µm in length and was configured to acquire 25 points with 9.8 µm spacing.

Table A44: Major element content of individual plagioclase points in Line 31 shown in Figure A40

	1σ	1	2	3	4	5	6	7	8	9	10	11	12	13	14	15	16
Na_2O (wt %)	0.04	0.35	0.35	0.38	0.37	0.40	0.40	0.36	0.37	0.38	0.39	0.39	0.38	0.39	0.38	0.37	0.41
MgO	0.02	0.10	0.10	0.10	0.08	0.08	0.09	0.10	0.10	0.09	0.10	0.09	0.07	0.07	0.08	0.08	0.07
Al_2O_3	0.27	34.55	34.75	34.36	34.55	34.48	34.38	34.65	34.59	34.58	34.49	34.50	34.62	34.64	34.70	34.75	34.45
SiO_2	0.28	43.97	44.31	44.10	44.15	43.98	44.25	44.30	43.92	44.06	44.31	44.13	44.17	43.96	44.07	44.09	44.17
P_2O_5	0.03	b.d.	b.d.	b.d.	0.04	0.04	b.d.	b.d.	b.d.	b.d.	b.d.	0.06	0.05	0.04	b.d.	b.d.	0.09
CaO	0.43	19.58	19.43	19.53	19.50	19.42	19.38	19.28	19.51	19.58	19.35	19.58	19.82	19.63	19.55	19.68	19.49
FeO	0.05	0.27	0.25	0.24	0.20	0.18	0.14	0.16	0.11	0.15	0.13	0.11	0.07	0.13	0.09	0.09	0.14
Total		98.82	99.20	98.71	98.88	98.59	98.64	98.85	98.62	98.84	98.76	98.86	99.18	98.86	98.87	99.07	98.81

Table A44, ctd

	17	18	19	20	21	22	23	24	25	26	27	28	29	30	31	32	33
Na_2O (wt %)	0.40	0.33	0.36	0.38	0.46	0.35	0.39	0.40	0.38	0.36	0.37	0.35	0.35	0.32	0.41	0.36	0.37
MgO	0.07	0.09	0.08	0.08	0.09	0.08	0.06	0.05	0.08	0.08	0.09	0.09	0.08	0.08	0.09	0.11	0.10
Al_2O_3	34.60	34.73	34.77	34.80	34.71	34.80	34.76	34.66	34.68	34.77	34.77	34.69	34.78	34.94	34.63	34.53	34.59
SiO_2	44.17	44.11	44.15	44.38	44.28	44.23	44.04	44.17	44.11	44.17	44.25	44.15	44.27	44.43	44.14	44.05	44.39
P_2O_5	b.d.	b.d.	b.d.	b.d.	b.d.	b.d.	b.d.	0.05	b.d.	b.d.	b.d.	b.d.	b.d.	b.d.	b.d.	b.d.	b.d.
CaO	19.42	19.63	19.28	19.43	19.63	19.39	19.45	19.39	19.48	19.54	19.60	19.76	19.36	19.52	19.35	19.53	19.50
FeO	0.10	0.12	0.13	0.14	0.10	0.09	0.07	0.11	0.11	0.09	0.11	0.11	0.09	0.11	0.14	0.10	0.09
Total	98.77	99.01	98.77	99.21	99.28	98.95	98.77	98.85	98.85	99.00	99.19	99.15	98.94	99.41	98.77	98.67	99.03

Table A44, ctd

	34	35	36	37	38	39	40	41	42	43	44	45	46	47	48	50
Na_2O (wt %)	0.39	0.37	0.34	0.42	0.40	0.42	0.39	0.34	0.38	0.36	0.38	0.35	0.36	0.38	0.41	0.53
MgO	0.10	1.58	0.07	0.11	0.06	0.08	0.09	0.07	0.07	0.08	0.08	0.10	0.10	0.09	0.08	1.06
Al_2O_3	34.89	33.23	34.81	34.87	34.76	34.86	34.79	34.87	34.93	34.93	34.82	35.00	35.00	34.92	34.91	34.87
SiO_2	44.13	44.80	43.97	44.21	44.17	44.28	44.40	44.30	44.22	44.33	44.40	44.19	44.38	44.29	43.98	44.71
P_2O_5	0.04	b.d.	0.04	b.d.	0.05	0.07	b.d.	0.04	b.d.	b.d.	b.d.	b.d.	b.d.	b.d.	0.04	0.04
CaO	19.46	18.76	19.69	19.60	19.42	19.40	19.58	19.54	19.49	19.56	19.52	19.71	19.65	19.63	19.36	18.80
FeO	0.08	0.75	0.13	0.10	0.06	0.10	0.12	0.14	0.09	0.13	0.14	0.16	0.17	0.19	0.22	0.60
Total	99.09	99.49	99.05	99.30	98.93	99.20	99.37	99.31	99.18	99.39	99.34	99.51	99.67	99.50	99.00	100.62

Table A45: Major element content of individual plagioclase points in Line 32 shown in Figure A40

	1σ	1	2	3	4	7	8	9	10	11	12	13	14	15	16	17
Na_2O (wt %)	0.04	0.54	0.30	0.33	0.35	0.32	0.29	0.30	0.35	0.31	0.33	0.33	0.28	0.34	0.32	0.29
MgO	0.02	0.31	0.06	0.06	0.09	0.05	0.08	0.08	0.10	0.09	0.10	0.10	0.08	0.10	0.10	0.08
Al_2O_3	0.27	34.18	35.04	34.88	34.80	35.00	35.13	34.98	35.09	35.20	35.01	34.66	35.05	35.05	34.83	34.63
SiO_2	0.28	44.87	43.91	43.84	43.99	43.84	44.04	44.00	44.13	44.16	43.98	44.04	44.12	44.22	44.14	43.83
K_2O	0.02	b.d.	b.d.	b.d.	0.03	b.d.	b.d.	b.d.	b.d.	0.03	b.d.	b.d.	b.d.	b.d.	0.03	b.d.
CaO	0.44	18.89	19.61	19.87	19.53	19.68	19.84	19.52	19.86	19.93	19.67	19.65	19.29	19.54	19.71	19.42
FeO	0.05	0.35	0.28	0.22	0.20	0.16	0.13	0.17	0.18	0.20	0.13	0.17	0.20	0.19	0.16	0.18
Total		99.15	99.20	99.20	98.99	99.06	99.51	99.04	99.71	99.91	99.21	98.94	99.02	99.43	99.29	98.43

Table A45, ctd

	18	19	20
Na_2O (wt %)	0.31	0.32	0.42
MgO	0.08	0.08	0.13
Al_2O_3	34.79	35.32	34.48
SiO_2	43.87	44.03	44.57
K_2O	b.d.	0.04	0.04
CaO	19.85	19.61	19.25
FeO	0.21	0.22	0.28
Total	99.12	99.61	99.16

Table A46: Major element content of individual plagioclase points in Line 33 shown in Figure A40

	1σ	1	2	3	4	5	6	7	8	9	10	11	12	13	14	15
Na_2O (wt %)	0.04	0.32	0.34	0.37	0.38	0.43	0.40	0.36	0.40	0.40	0.43	0.45	0.40	0.37	0.41	0.44
MgO	0.01	0.06	0.04	0.05	0.03	0.04	0.03	0.05	0.04	0.04	0.04	0.03	0.05	0.07	0.08	0.09
Al_2O_3	0.27	35.62	35.34	35.50	35.60	35.45	35.55	35.59	35.35	35.53	35.20	35.24	35.31	35.31	35.14	35.00
SiO_2	0.28	44.14	44.29	44.43	44.05	44.02	44.26	44.02	43.92	44.25	44.29	44.23	44.10	44.29	44.13	44.30
K_2O	0.02	b.d.	b.d.	b.d.	b.d.	b.d.	b.d.	b.d.	b.d.	b.d.	0.04	0.04	b.d.	b.d.	b.d.	b.d.
CaO	0.44	19.66	19.55	19.67	19.60	19.46	19.43	19.54	19.55	19.66	19.61	19.55	19.74	19.51	19.79	19.42
FeO	0.05	0.18	0.15	0.15	0.15	0.16	0.13	0.14	0.18	0.14	0.11	0.11	0.14	0.16	0.15	0.14
Total		99.99	99.71	100.16	99.81	99.55	99.80	99.68	99.45	100.01	99.72	99.65	99.74	99.71	99.70	99.39

Table A46, ctd

	16	17	18	19	20	22	23	24
Na_2O (wt %)	0.34	0.34	0.40	0.37	0.34	0.40	0.31	0.35
MgO	0.08	0.10	0.11	0.10	0.08	0.07	0.08	0.05
Al_2O_3	35.29	35.35	34.86	35.12	35.17	35.52	35.47	35.22
SiO_2	44.25	44.18	44.15	44.25	44.13	44.40	44.26	44.07
K_2O	b.d.	b.d.	0.03	b.d.	b.d.	b.d.	b.d.	b.d.
CaO	19.72	19.62	19.51	19.44	19.47	19.87	19.68	19.55
FeO	0.15	0.15	0.25	0.17	0.17	0.20	0.19	0.22
Total	99.84	99.74	99.30	99.44	99.36	100.46	99.98	99.46

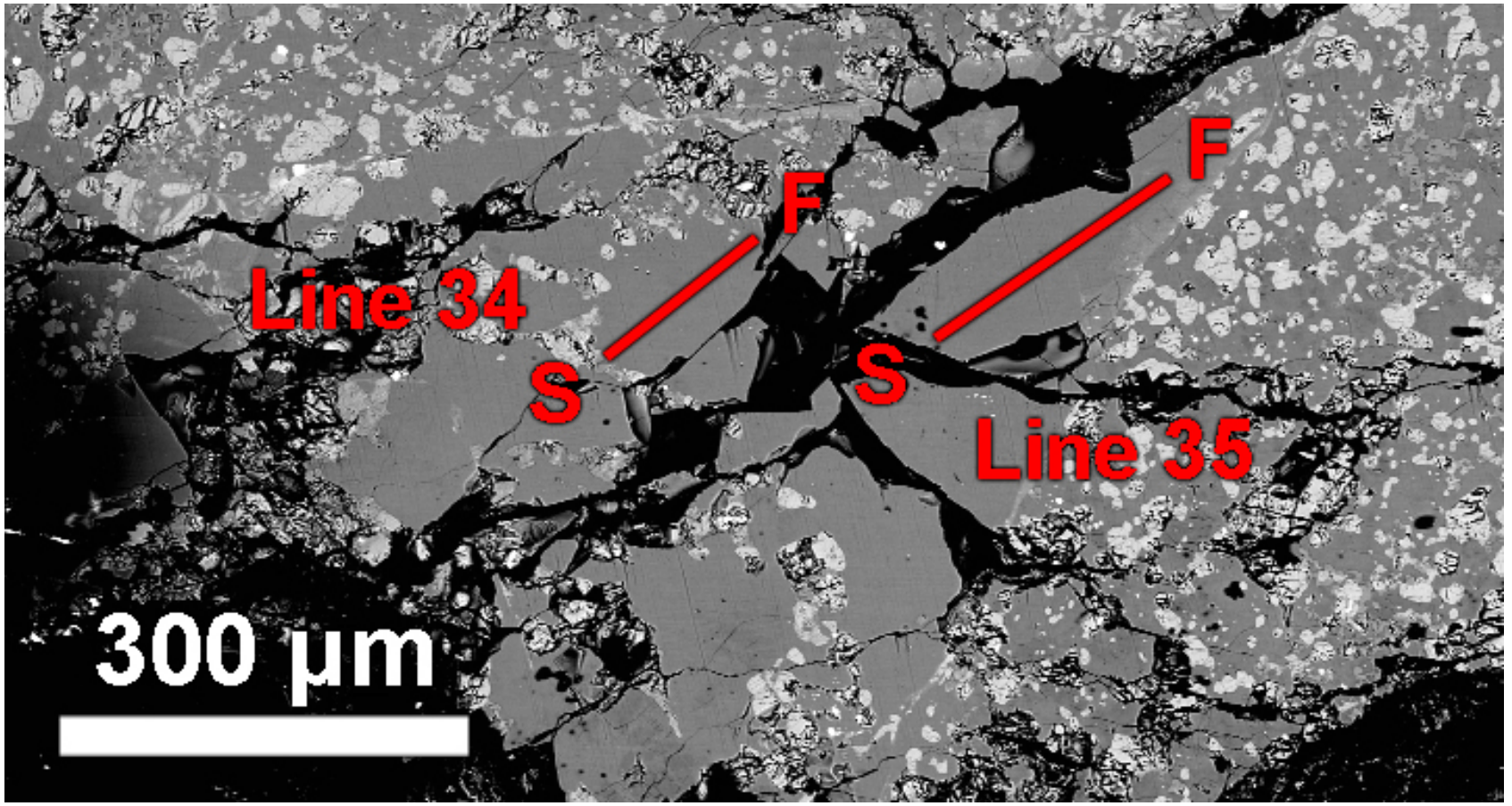

Figure A41: Map of EMP plagioclase Line 34 and 35 locations. Line scan 34 (Table A47) is 113 µm in length and was configured to acquire 13 points with 9.4 µm spacing. Line scan 35 (Table A48) is 197 µm in length and was configured to acquire 20 points with 10.4 µm spacing.

Table A47: Major element content of individual plagioclase points in Line 34 shown in Figure A41

	1σ	1	2	3	4	5	6	7	8	9	10	11	12
Na_2O (wt %)	0.04	0.25	0.29	0.28	0.30	0.26	0.29	0.29	0.31	0.26	0.27	0.30	0.29
MgO	0.02	0.08	0.09	0.08	0.10	0.09	0.08	0.09	0.07	0.07	0.07	0.07	0.08
Al_2O_3	0.27	35.78	35.30	35.51	35.53	34.81	35.38	35.61	35.38	35.63	35.56	35.70	35.64
SiO_2	0.28	44.60	43.78	44.20	44.02	43.61	43.72	43.94	44.06	44.29	44.20	44.13	43.69
K_2O	0.02	b.d.	b.d.	b.d.	b.d.	0.03	b.d.	b.d.	0.03	b.d.	b.d.	b.d.	b.d.
CaO	0.44	19.90	19.74	19.73	19.49	19.46	19.93	19.76	19.75	19.70	19.77	19.57	19.75
FeO	0.05	0.22	0.22	0.19	0.17	0.14	0.19	0.16	0.20	0.18	0.22	0.23	0.22
Total		100.82	99.42	99.99	99.61	98.40	99.59	99.85	99.79	100.13	100.10	99.99	99.66

Table A48: Major element content of individual plagioclase points in Line 35 shown in Figure A41

	1σ	1	2	3	4	5	6	7	8	9	10	11	12	13	14	15	16
Na_2O (wt %)	0.04	0.31	0.30	0.28	0.30	0.29	0.30	0.29	0.27	0.28	0.26	0.28	0.29	0.28	0.26	0.28	0.30
MgO	0.02	0.10	0.09	0.08	0.09	0.08	0.09	0.07	0.07	0.08	0.09	0.09	0.07	0.07	0.09	0.08	0.09
Al_2O_3	0.27	35.63	35.27	35.68	35.37	35.59	35.42	35.77	35.61	35.41	35.46	35.23	35.46	35.61	35.38	35.03	35.24
SiO_2	0.28	44.56	44.05	44.04	43.99	44.52	43.88	44.57	44.72	44.05	43.85	44.05	44.36	43.93	43.99	43.67	44.25
K_2O	0.02	0.03	b.d.	0.04	0.03	b.d.	0.03	b.d.	b.d.	b.d.	b.d.	b.d.	b.d.	b.d.	b.d.	0.03	b.d.
CaO	0.44	20.06	19.60	19.70	19.56	19.57	19.47	20.09	19.77	19.72	19.76	19.46	19.58	19.65	19.60	19.66	19.50
FeO	0.05	0.17	0.16	0.16	0.47	0.12	0.08	0.16	0.11	0.17	0.15	0.16	0.12	0.15	0.16	0.19	0.26
Total		100.87	99.47	99.98	99.82	100.18	99.27	100.95	100.55	99.70	99.58	99.27	99.86	99.69	99.48	98.93	99.63

Table A48, ctd

	17	18	19	20
Na_2O (wt %)	0.30	0.30	0.32	0.33
MgO	0.07	0.13	0.11	0.10
Al_2O_3	35.62	35.01	35.55	35.70
SiO_2	43.63	43.87	44.18	43.97
K_2O	0.03	b.d.	0.03	0.03
CaO	19.34	19.57	19.73	19.75
FeO	0.25	0.18	0.20	0.29
Total	99.23	99.06	100.11	100.16

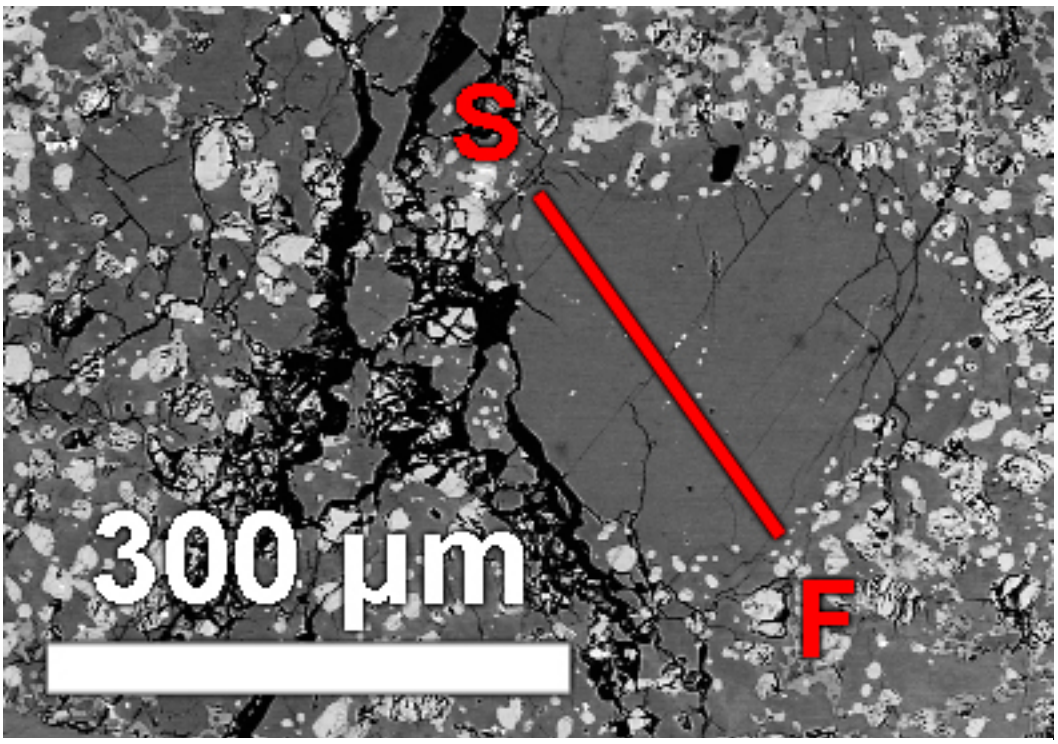

Figure A42: Map of Table A49 EMP plagioclase line location. The line scan is 24 µm in length and was configured to acquire 30 points with 8.5 µm spacing.

Table A49: Major element content of individual plagioclase points in the line scan shown in Figure A42

	1σ	1	2	3	4	5	6	7	8	9	10	11	12	13	14	15	16
Na_2O (wt %)	0.04	0.28	0.29	0.28	0.29	0.28	0.31	0.27	0.28	0.26	0.29	0.28	0.25	0.29	0.27	0.38	0.29
MgO	0.02	0.08	0.08	0.09	0.09	0.08	0.10	0.09	0.09	0.08	0.09	0.09	0.08	0.08	0.09	0.08	0.08
Al_2O_3	0.27	35.79	35.23	35.48	35.50	35.42	35.59	35.08	35.43	35.72	34.98	35.77	35.27	35.57	35.14	34.65	35.47
SiO_2	0.28	44.21	44.01	43.95	44.45	44.41	44.05	43.89	44.12	44.60	44.04	44.64	43.96	44.60	43.99	43.42	43.99
K_2O	0.02	0.03	b.d.	b.d.	b.d.	b.d.	b.d.	b.d.	b.d.	b.d.	b.d.	b.d.	b.d.	b.d.	b.d.	0.09	b.d.
CaO	0.44	20.00	20.02	19.93	20.11	20.02	19.79	19.69	20.02	20.02	19.98	19.89	19.81	20.13	19.77	19.27	19.60
FeO	0.05	0.25	0.25	0.21	0.22	0.19	0.24	0.20	0.16	0.15	0.17	0.14	0.16	0.18	0.18	0.13	0.16
Total		100.62	99.88	99.94	100.65	100.42	100.09	99.22	100.11	100.83	99.56	100.80	99.54	100.85	99.44	98.02	99.60

Table A49, ctd

	17	18	19	20	21	22	23	24	25	26	27	28	29	30
Na_2O (wt %)	0.31	0.29	0.30	0.35	0.29	0.29	0.27	0.32	0.29	0.26	0.31	0.31	0.31	0.53
MgO	0.09	0.07	0.09	0.11	0.10	0.11	0.09	0.09	0.10	0.08	0.10	0.09	0.09	0.20
Al_2O_3	35.56	35.37	35.56	34.95	35.56	35.36	35.15	35.05	35.39	35.11	35.80	35.38	35.41	34.73
SiO_2	44.20	43.89	44.49	43.98	44.78	44.12	43.92	43.83	44.06	43.99	44.71	44.37	44.05	44.41
K_2O	b.d.	b.d.	b.d.	b.d.	b.d.	b.d.	b.d.	0.03	b.d.	b.d.	0.03	b.d.	b.d.	b.d.
CaO	19.88	19.74	19.75	19.73	20.28	19.86	19.68	19.50	19.83	19.79	19.99	19.75	19.70	19.49
FeO	0.15	0.15	0.12	0.13	0.17	0.16	0.17	0.13	0.20	0.18	0.21	0.24	0.32	0.37
Total	100.19	99.52	100.30	99.24	101.17	99.90	99.28	98.94	99.87	99.41	101.14	100.14	99.88	99.74

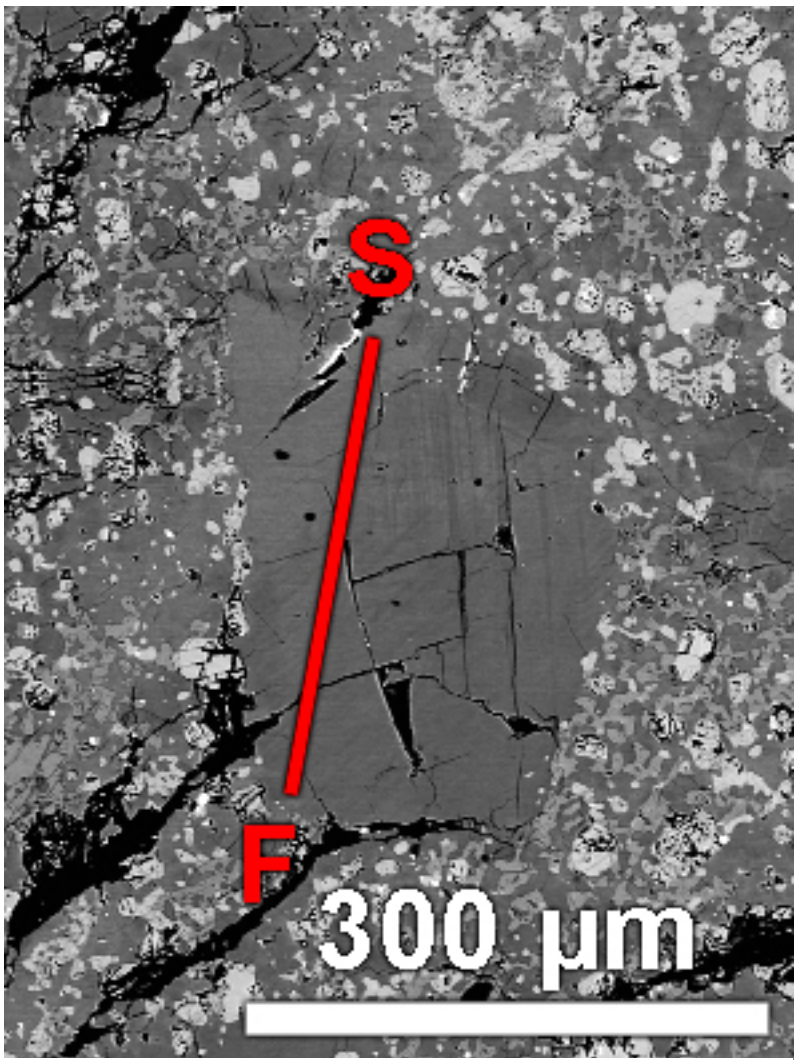

Figure A43: Map of Table A50 EMP plagioclase line location. The line scan is 269 µm in length and was configured to acquire 30 points with 9.3 µm spacing.

Table A50: Major element content of individual plagioclase points in the line scan shown in Figure A43

	1σ	1	2	3	4	6	7	8	9	10	11	12	13	14	15
Na_2O (wt %)	0.04	0.29	0.30	0.37	0.49	0.35	0.36	0.36	0.35	0.26	0.33	0.39	0.38	0.35	0.37
MgO	0.01	0.07	0.07	0.06	0.06	0.03	0.03	0.03	0.05	0.01	0.04	0.04	0.03	0.03	0.04
Al_2O_3	0.27	35.50	35.39	35.39	34.34	35.29	35.38	35.24	35.06	35.66	35.56	35.71	35.52	35.42	34.78
SiO_2	0.28	44.08	44.45	44.41	42.55	43.42	43.95	44.33	44.24	43.78	44.24	44.32	44.11	44.30	43.82
K_2O	0.02	0.02	0.01	0.01	0.08	0.06	0.02	0.00	0.03	0.03	0.02	0.01	0.02	0.02	0.02
CaO	0.44	19.62	19.70	19.56	18.78	19.56	19.49	19.84	19.69	20.00	19.67	19.59	19.66	19.80	19.62
FeO	0.05	0.18	0.13	0.13	0.66	0.07	0.07	0.07	0.09	0.05	0.07	0.08	0.07	0.08	0.10
Total		99.76	100.06	99.92	96.97	98.78	99.30	99.87	99.51	99.79	99.92	100.15	99.79	100.00	98.75

Table A50, ctd

	16	17	18	19	20	21	22	23	24	25	26	27	28	29	30
Na_2O (wt %)	0.46	0.40	0.38	0.39	0.38	0.37	0.36	0.35	0.37	0.36	0.36	0.36	0.38	0.48	0.36
MgO	0.04	0.03	0.03	0.04	0.03	0.04	0.05	0.04	0.03	0.03	0.03	0.03	0.02	0.05	0.05
Al_2O_3	35.26	35.55	35.32	35.36	35.60	35.39	35.51	35.46	35.50	35.56	35.61	35.51	35.75	35.09	35.47
SiO_2	45.93	44.18	44.20	44.29	44.22	44.01	44.35	44.30	44.03	44.07	44.35	44.10	44.05	43.96	44.35
K_2O	0.05	0.02	0.02	0.03	0.00	0.03	0.03	0.02	0.04	0.02	0.02	0.02	0.03	0.07	0.02
CaO	19.50	19.76	19.55	19.51	19.51	19.58	19.58	19.53	19.71	19.65	19.45	19.59	19.66	19.21	19.76
FeO	0.10	0.07	0.07	0.06	0.09	0.11	0.10	0.11	0.10	0.10	0.13	0.10	0.16	0.20	0.20
Total	101.35	100.01	99.57	99.69	99.85	99.53	99.99	99.81	99.79	99.79	99.95	99.70	100.04	99.07	100.20

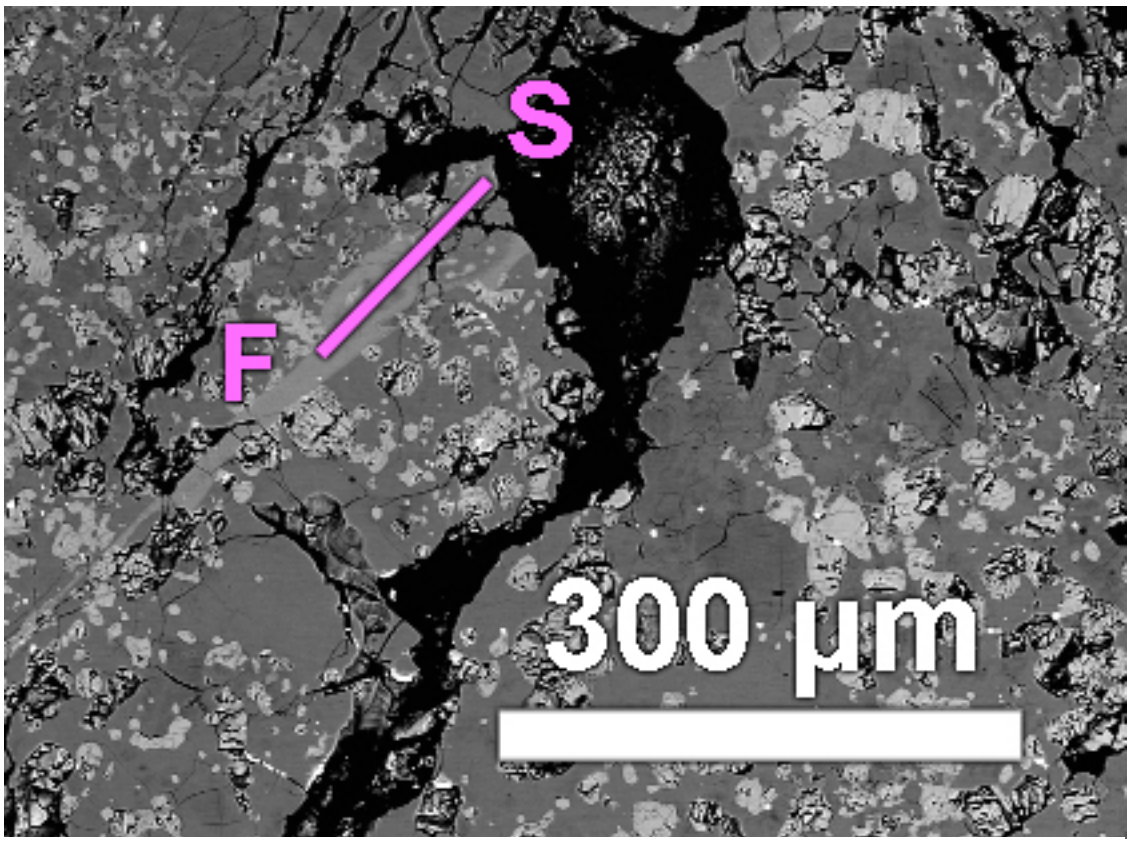

Figure A44: Map of Table A51 shock vein EMP line location. The line scan is 136 µm in length and was configured to acquire 9 points with 17 µm spacing.

Table A51: Averaged major element content of shock vein in Figure A44

	SV	1σ
Points	7	
Na_2O (wt %)	0.33	0.05
MgO	7.33	0.12
SiO_2	43.84	0.37
Al_2O_3	28.56	0.21
P_2O_5	b.d.	-
K_2O	b.d.	-
CaO	15.95	0.33
SO_2	0.08	0.03
TiO_2	0.10	0.03
Cr_2O_3	0.08	0.06
MnO	0.07	0.07
FeO	3.42	0.19
CoO	b.d.	-
NiO	b.d.	-
Total	99.90	

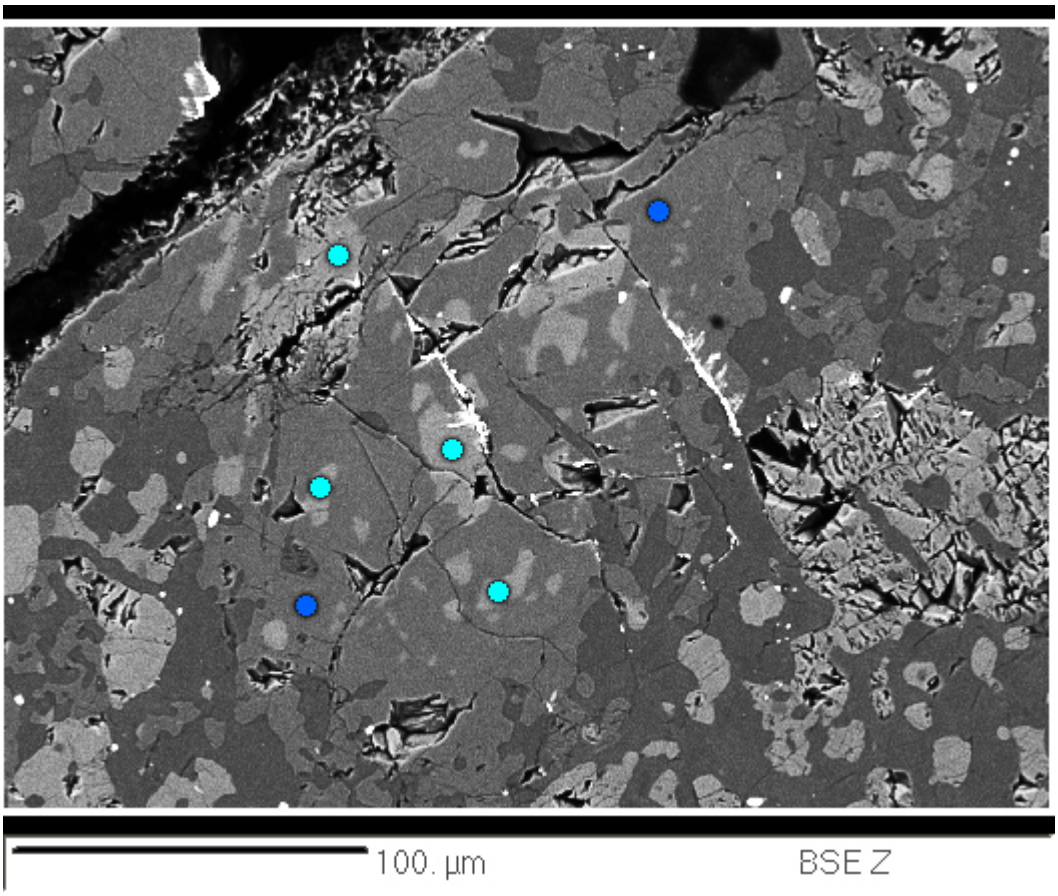

Figure A45: Map of Table A52 EMP point locations. Dark-blue and light-blue dots represent clinoenstatite and augite measurement locations, respectively.

Table A52: Averaged major element content of minerals in Figure A45

	Aug	1σ	C-En	1σ
Points	4		2	
Na_2O (wt %)	0.14	0.05	0.08	0.05
MgO	10.29	0.18	17.58	0.27
Al_2O_3	1.08	0.04	0.92	0.04
SiO_2	49.01	0.42	49.66	0.43
P_2O_5	b.d.	-	0.06	0.05
CaO	15.45	0.36	5.29	0.19
TiO_2	0.97	0.07	0.72	0.06
Cr_2O_3	0.37	0.06	0.32	0.06
MnO	0.39	0.09	0.42	0.09
FeO	22.32	0.59	25.46	0.64
Total	100.03		100.51	

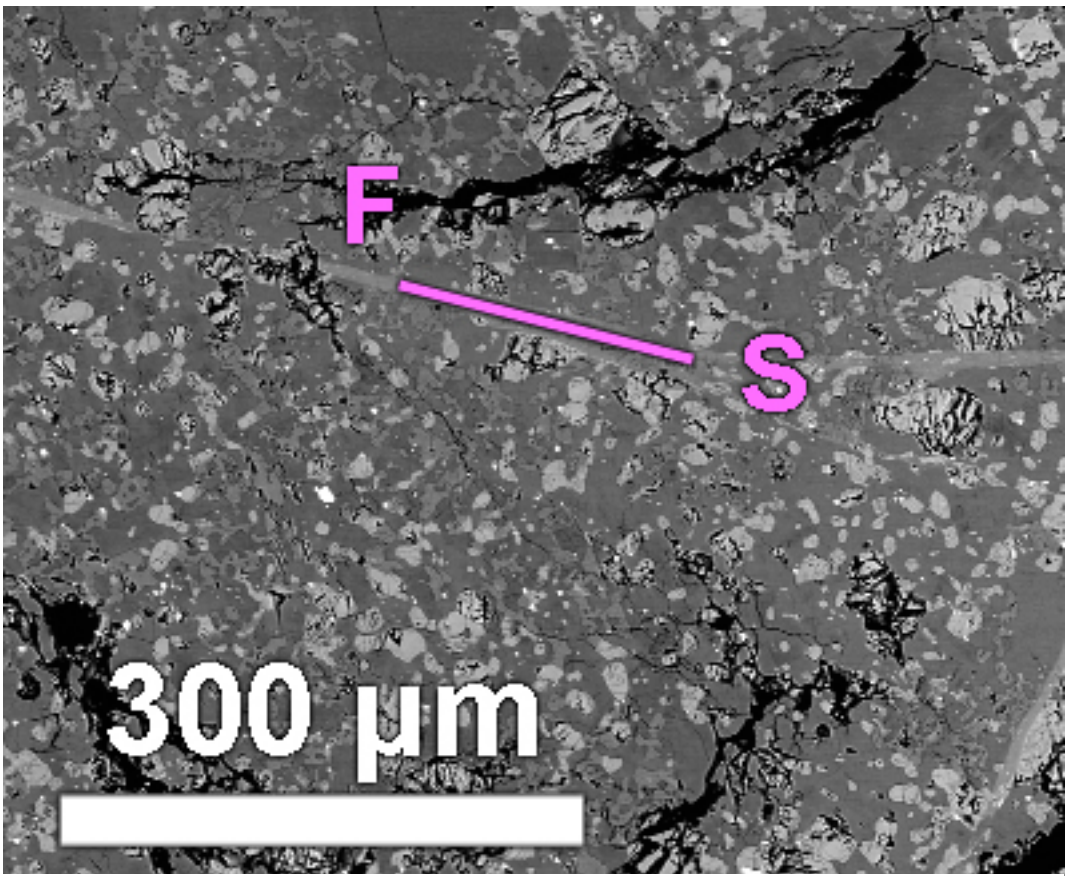

Figure A46: Map of Table A51 shock vein EMP line location. The line scan is 188 µm in length and was configured to acquire 24 points with 8.2 µm spacing.

Table A53: Averaged major element content of shock vein in Figure A46

	SV	1σ
Points	20	
Na_2O (wt %)	0.28	0.05
MgO	10.02	0.15
SiO_2	44.64	0.38
Al_2O_3	25.60	0.20
P_2O_5	0.06	0.05
K_2O	0.09	0.04
CaO	14.12	0.30
SO_2	0.09	0.04
TiO_2	0.14	0.03
Cr_2O_3	0.16	0.06
MnO	0.13	0.07
FeO	4.69	0.22
CoO	0.08	0.07
NiO	b.d.	-
Total	100.10	

Appendix B:

NWA 5744 Trace Element Data

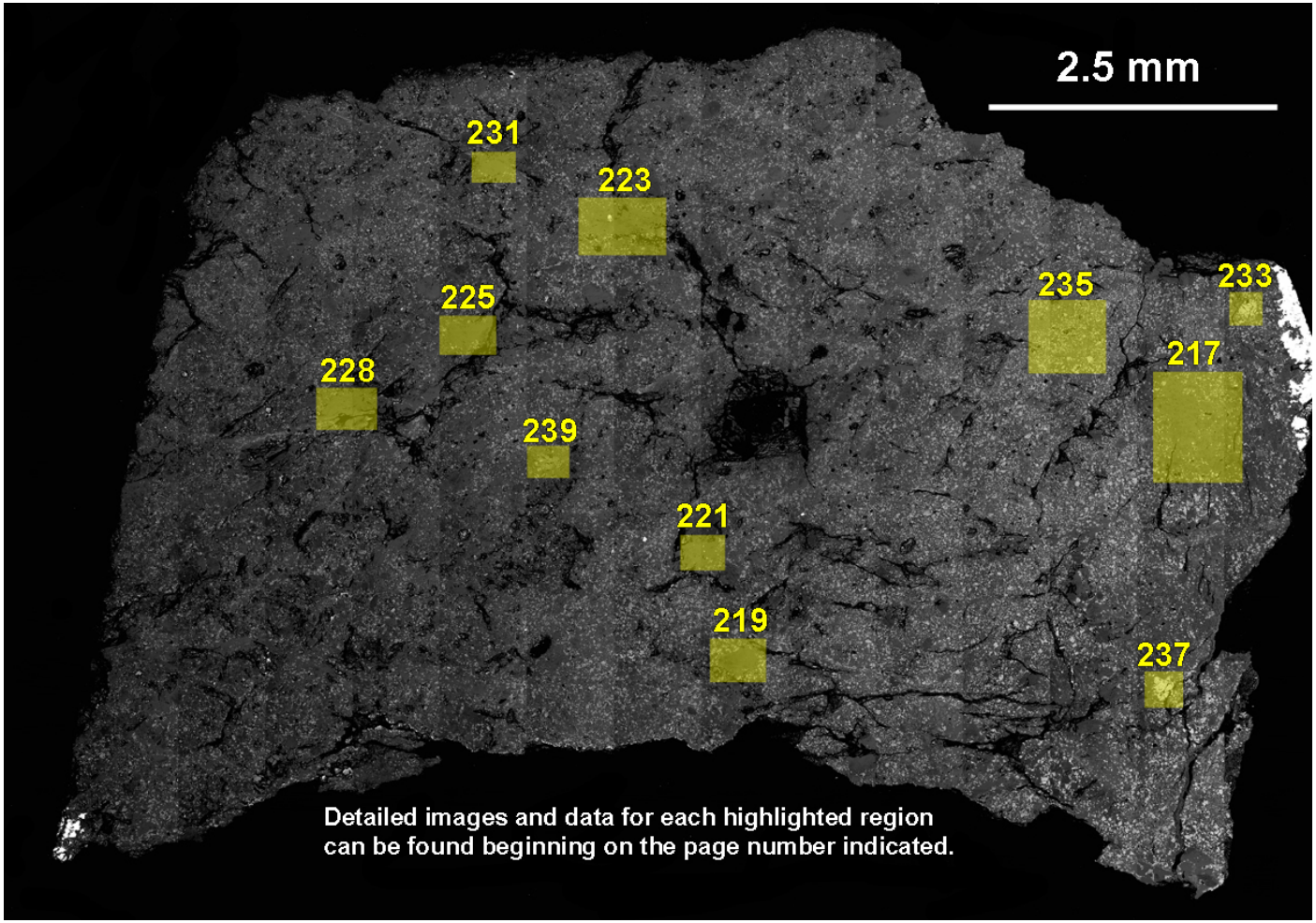

Figure B1: Map of slab piece 1 indicating the regions I obtained trace element data via LA-ICP-MS. The number beside each reagion indicates the page that data can be found on.

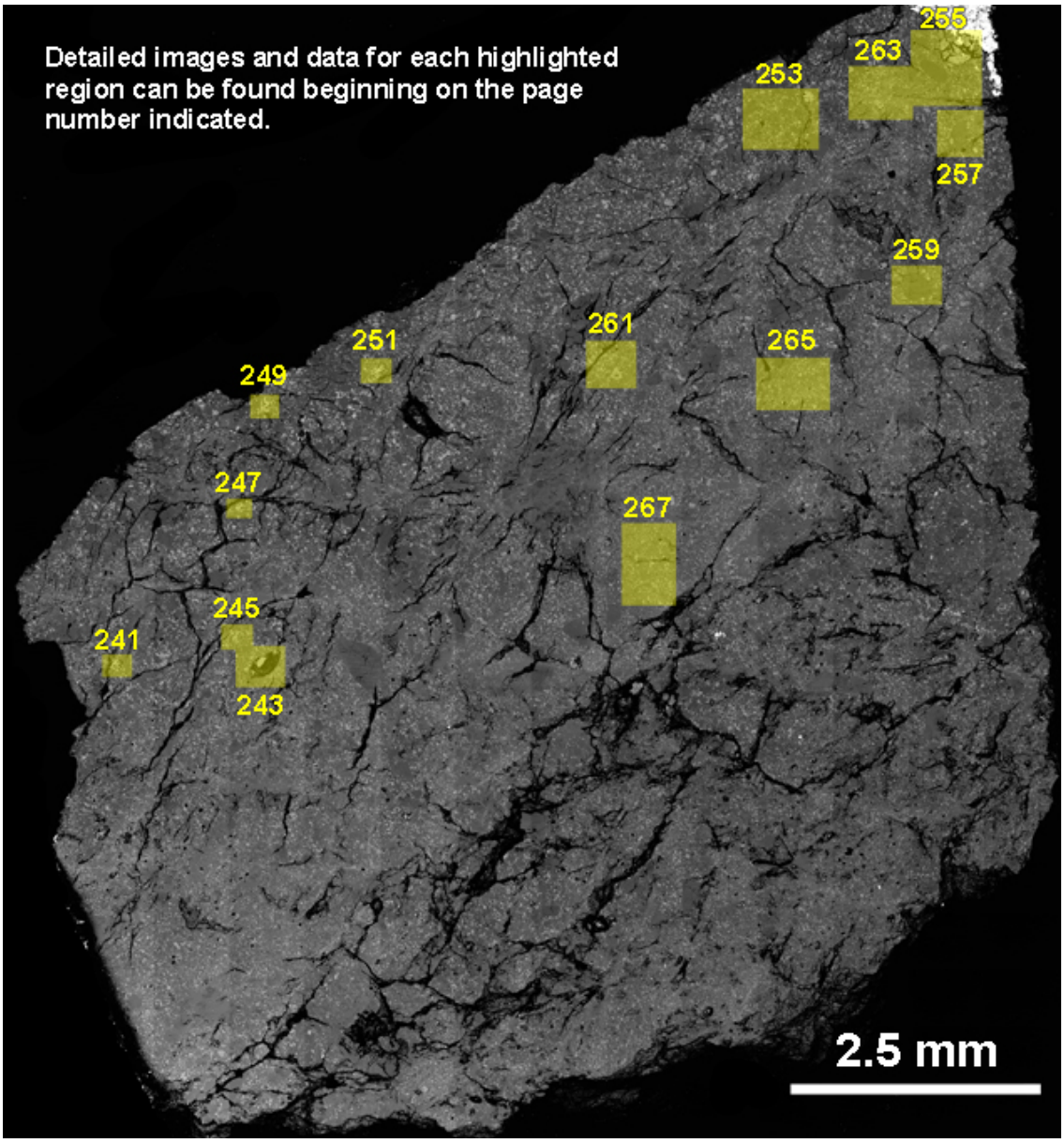

Figure B2: Map of slab piece 2 indicating the regions I obtained trace element data via LA-ICP-MS. The number beside each reagion indicates the page that data can be found on.

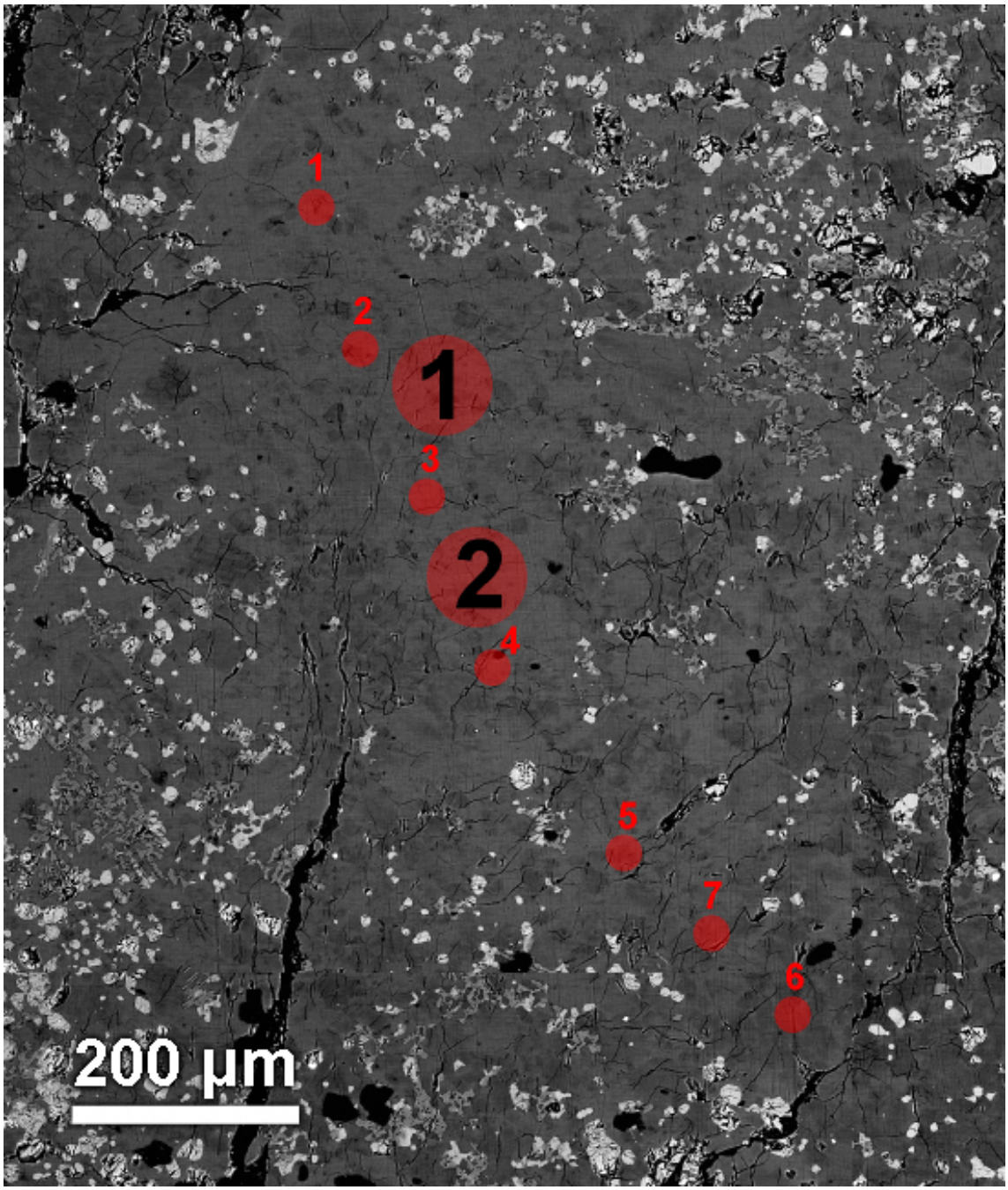

Figure B3: Detailed locations of 30 µm plagioclase ablation spots 1 through 7, and 84 µm plagioclase ablation spots 1 and 2.

Table B1: Trace element content (ppm) from areas shown in Figure B3

Spot	plag 1	1σ	plag 2	1σ	plag 3	1σ	plag 4	1σ	plag 5	1σ	plag 6	1σ	plag 7	1σ	plag 1	1σ	plag 2	1σ
Size	30µm		30µm		30µm		30µm		30µm		30µm		30µm		84µm		84µm	
Co	b.d.	-	0.26	0.11	b.d.	-	b.d.	-	b.d.	-	10.29	0.52	0.34	0.12	0.12	0.035	0.12	0.02
Ni	b.d.	-	b.d.	-	b.d.	-	b.d.	-	b.d.	-	45.96	19.54	b.d.	-	b.d.	-	3.09	1.06
Cu	b.d.	-	b.d.	-	b.d.	-	3.89	1.65	b.d.	-	b.d.	-	b.d.	-	0.45	0.092	0.13	0.05
Ga	2.59	0.33	2.45	0.32	2.45	0.32	2.93	0.36	3.33	0.36	3.11	0.37	2.94	0.35	2.39	0.13	1.22	0.066
Sr	181.50	8.52	181.34	8.5	177.66	8.32	188.91	8.84	183.43	8.58	182.39	8.57	181.07	8.54	143.74	6.79	78.98	3.77
Y	0.449	0.05	0.467	0.051	0.240	0.055	0.418	0.058	0.437	0.051	0.343	0.06	0.631	0.057	0.395	0.023	0.259	0.015
Zr	1.47	0.2	1.83	0.21	1.27	0.22	1.45	0.23	1.86	0.22	8.40	0.45	7.70	0.42	1.17	0.098	0.57	0.053
Nb	0.108	0.029	0.077	0.034	0.084	0.033	b.d.	-	0.086	0.036	0.414	0.049	0.165	0.034	0.147	0.0099	0.061	0.0046
Ba	16.51	0.93	21.00	1.16	23.37	1.29	22.07	1.24	20.74	1.17	35.21	1.94	21.07	1.19	16.43	0.73	8.59	0.39
Hf	0.147	0.035	b.d.	-	b.d.	-	b.d.	-	b.d.	-	0.155	0.045	0.120	0.041	0.021	0.0058	0.016	0.0031
Ta	0.0183	0.0086	b.d.	-	0.0283	0.0087	b.d.	-	b.d.	-	b.d.	-	0.0340	0.011	0.0054	0.002	0.0046	0.0012
Th	0.0174	0.0092	0.0175	0.011	0.0314	0.013	b.d.	-	0.0291	0.015	b.d.	-	0.0402	0.014	0.0218	0.0029	0.0097	0.0015
U	0.0434	0.011	b.d.	-	b.d.	-	b.d.	-	b.d.	-	b.d.	-	0.0408	0.0094	0.0036	0.00096	0.0024	0.0006
La	0.962	0.053	0.940	0.052	1.076	0.058	0.934	0.053	1.026	0.056	0.815	0.049	0.872	0.05	0.771	0.034	0.406	0.018
Ce	2.42	0.12	2.44	0.12	2.49	0.13	2.45	0.13	2.35	0.12	1.95	0.1	2.26	0.12	1.83	0.072	0.97	0.039
Pr	0.300	0.025	0.308	0.026	0.283	0.025	0.299	0.027	0.259	0.024	0.241	0.025	0.278	0.024	0.237	0.012	0.126	0.0064
Nd	1.45	0.12	1.25	0.11	1.36	0.12	1.46	0.13	1.24	0.11	0.80	0.11	1.04	0.098	0.99	0.056	0.55	0.031
Sm	0.258	0.05	0.280	0.056	b.d.	-	b.d.	-	b.d.	-	0.146	0.06	0.328	0.06	0.168	0.018	0.101	0.011
Eu	0.892	0.069	0.961	0.074	0.833	0.069	0.878	0.072	0.799	0.069	0.738	0.068	0.799	0.07	0.660	0.036	0.365	0.02
Gd	0.226	0.042	0.228	0.04	b.d.	-	0.191	0.052	0.203	0.046	0.131	0.049	0.219	0.044	0.133	0.015	0.078	0.0083
Tb	0.0308	0.0094	0.0159	0.0075	0.0243	0.0088	b.d.	-	0.0199	0.0091	b.d.	-	0.0170	0.0074	0.0194	0.0025	0.0092	0.0014
Dy	0.269	0.055	b.d.	-	0.197	0.053	b.d.	-	b.d.	-	b.d.	-	b.d.	-	0.069	0.011	0.043	0.0066
Ho	0.0155	0.0074	0.0277	0.0081	0.0233	0.0092	b.d.	-	b.d.	-	0.0261	0.011	0.0165	0.0078	0.0148	0.0022	0.0088	0.0013
Er	b.d.	-	b.d.	-	0.114	0.041	b.d.	-	b.d.	-	b.d.	-	b.d.	-	0.029	0.0068	0.030	0.0049
Tm	b.d.	-	b.d.	-	b.d.	-	b.d.	-	b.d.	-	b.d.	-	b.d.	-	0.0035	0.0015	b.d.	-
Yb	b.d.	-	b.d.	-	0.104	0.041	b.d.	-	0.073	0.033	b.d.	-	0.091	0.03	0.036	0.0075	0.022	0.0044
Lu	b.d.	-	b.d.	-	b.d.	-	b.d.	-	b.d.	-	b.d.	-	0.0249	0.0097	b.d.	-	0.0024	0.00078

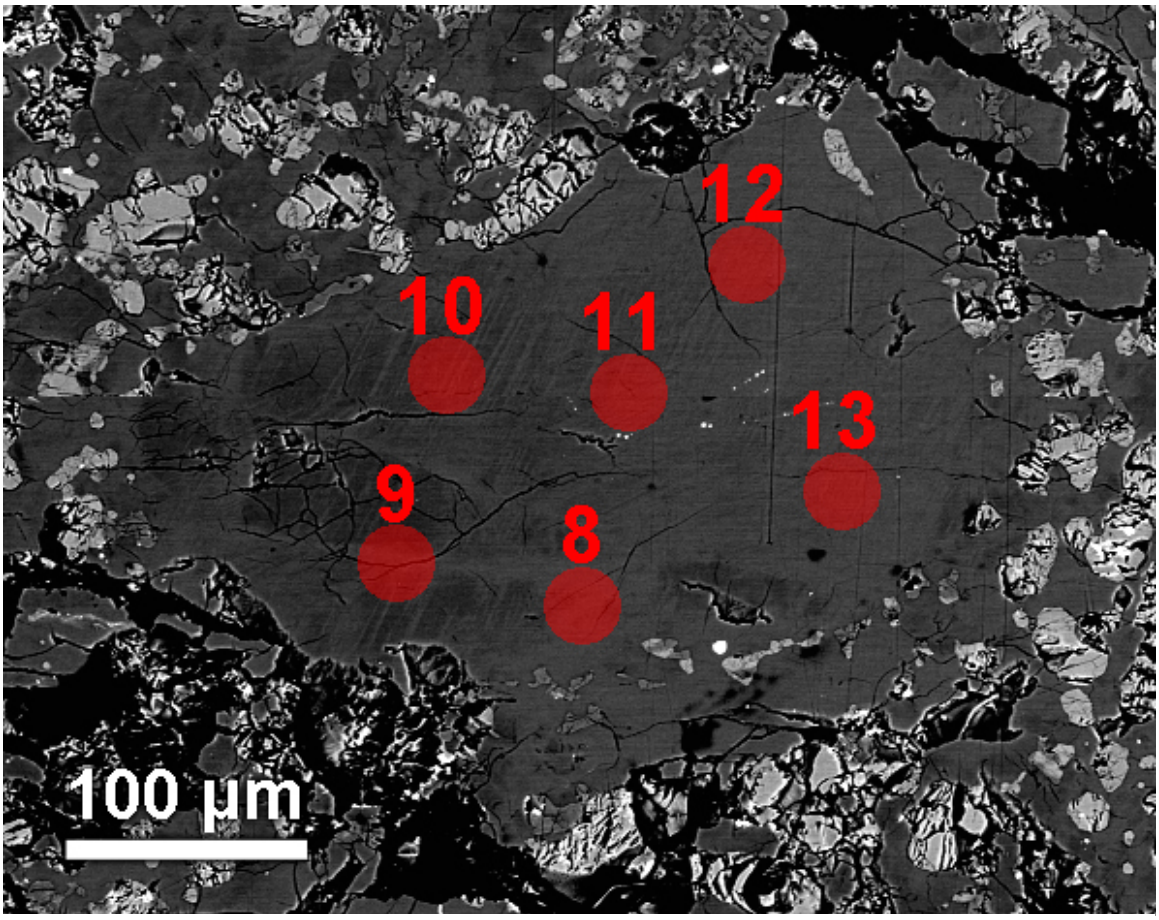

Figure B4: Detailed locations of 30 µm plagioclase ablation spots 8 through 13.

Table B2: Trace element content (ppm) from areas shown in Figure B4

Spot	plag 8	1σ	plag 9	1σ	plag 10	1σ	plag 11	1σ	plag 12	1σ	plag 13	1σ
Size	30µm		30µm		30µm		30µm		30µm		30µm	
Co	1.15	0.14	b.d.	-	b.d.	-	0.39	0.12	b.d.	-	1.94	0.17
Ni	b.d.	-	60.69	19.39	46.37	18.36	b.d.	-	b.d.	-	99.13	21.89
Cu	6.82	1.67	4.34	1.6	b.d.	-	b.d.	-	b.d.	-	b.d.	-
Ga	2.19	0.34	2.28	0.34	2.19	0.34	1.96	0.32	2.04	0.33	2.24	0.34
Sr	157.10	7.45	167.86	7.99	168.99	8.09	161.42	7.9	162.49	7.99	161.46	7.97
Y	0.513	0.056	0.187	0.041	0.311	0.047	0.278	0.044	0.306	0.045	0.309	0.048
Zr	1.82	0.23	b.d.	-	b.d.	-	b.d.	-	b.d.	-	0.59	0.21
Nb	b.d.	-	b.d.	-	b.d.	-	b.d.	-	b.d.	-	b.d.	-
Ba	11.40	0.69	14.55	0.84	10.61	0.63	11.47	0.66	12.67	0.72	10.14	0.6
Hf	b.d.	-	b.d.	-	b.d.	-	b.d.	-	b.d.	-	b.d.	-
Ta	b.d.	-	b.d.	-	b.d.	-	b.d.	-	b.d.	-	0.0342	0.0093
Th	b.d.	-	b.d.	-	b.d.	-	b.d.	-	b.d.	-	b.d.	-
U	0.0324	0.0094	b.d.	-	b.d.	-	b.d.	-	b.d.	-	b.d.	-
La	0.374	0.029	0.254	0.023	0.316	0.026	0.285	0.023	0.281	0.024	0.303	0.025
Ce	1.06	0.064	0.63	0.042	0.75	0.047	0.63	0.042	0.68	0.044	0.78	0.05
Pr	0.135	0.016	0.087	0.012	0.105	0.013	0.104	0.012	0.090	0.012	0.096	0.014
Nd	0.81	0.092	0.51	0.066	0.54	0.073	0.46	0.062	0.38	0.059	0.58	0.071
Sm	b.d.	-	0.081	0.042	0.268	0.055	0.107	0.041	0.130	0.051	0.106	0.047
Eu	0.640	0.059	0.795	0.067	0.788	0.067	0.758	0.063	0.786	0.065	0.709	0.062
Gd	0.137	0.041	b.d.	-	0.130	0.037	b.d.	-	b.d.	-	b.d.	-
Tb	b.d.	-	b.d.	-	b.d.	-	0.0239	0.0079	b.d.	-	b.d.	-
Dy	0.101	0.044	b.d.	-	b.d.	-	b.d.	-	b.d.	-	0.101	0.045
Ho	0.0151	0.0075	b.d.	-	0.0231	0.0089	0.0164	0.0073	b.d.	-	b.d.	-
Er	b.d.	-	b.d.	-	0.127	0.037	b.d.	-	0.096	0.032	b.d.	-
Tm	0.0158	0.0065	b.d.	-	b.d.	-	0.0133	0.0065	b.d.	-	b.d.	-
Yb	b.d.	-	b.d.	-	b.d.	-	b.d.	-	b.d.	-	b.d.	-
Lu	b.d.	-	b.d.	-	b.d.	-	0.0198	0.0067	b.d.	-	b.d.	-

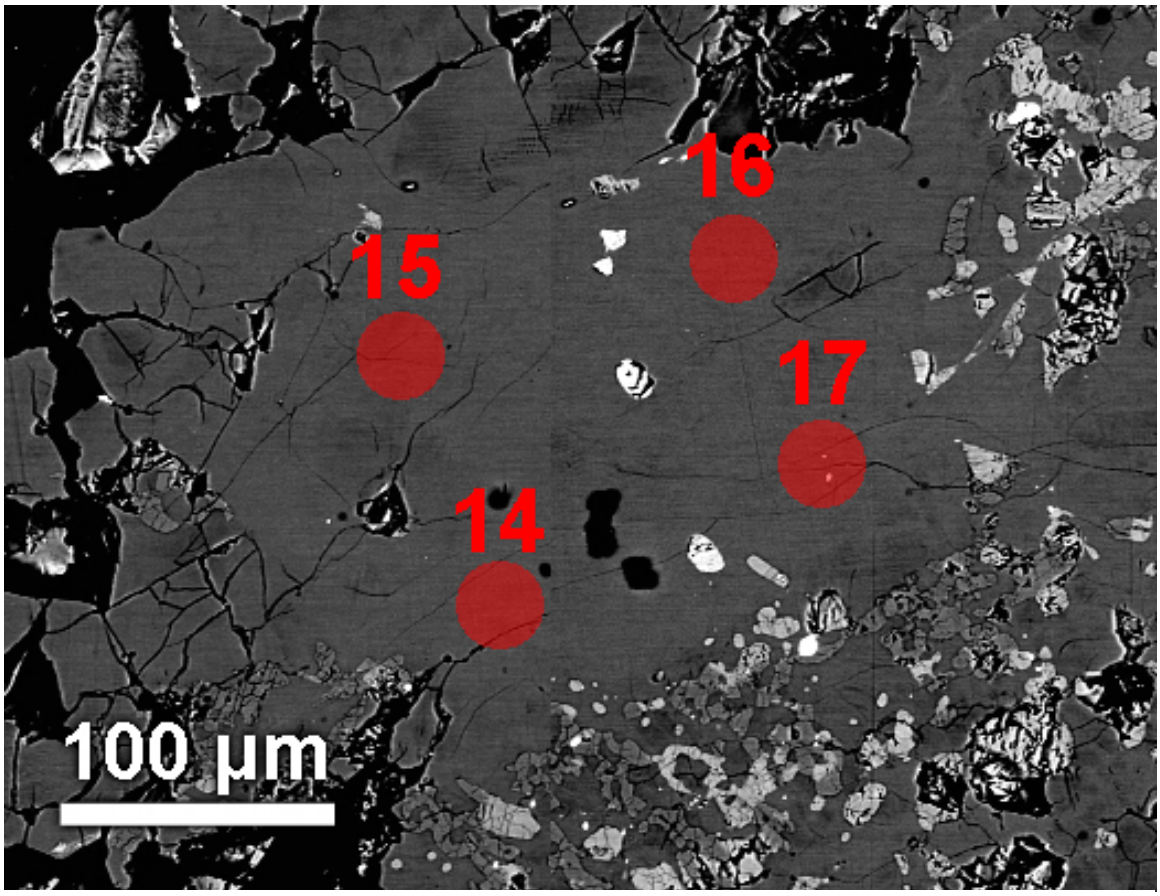

Figure B5: Detailed location of 30 µm plagioclase ablation spots 14 through 17.

Table B3: Trace element content (ppm) from areas shown in Figure B5

Spot	plag 14 30μm	1σ	plag 15 30μm	1σ	plag 16 30μm	1σ	plag 17 30μm	1σ
Co	1.88	0.17	b.d.	-	0.32	0.12	0.48	0.13
Ni	b.d.	-	b.d.	-	b.d.	-	b.d.	-
Cu	b.d.	-	b.d.	-	4.05	1.62	b.d.	-
Ga	2.04	0.37	2.41	0.39	2.39	0.38	2.20	0.38
Sr	170.71	8.47	157.06	7.84	156.00	7.93	166.01	8.44
Y	0.835	0.067	b.d.	-	0.272	0.046	2.080	0.12
Zr	1.51	0.24	b.d.	-	1.21	0.23	28.52	1.31
Nb	0.106	0.032	b.d.	-	b.d.	-	6.982	0.36
Ba	15.36	0.88	15.71	0.92	7.49	0.49	11.43	0.7
Hf	0.079	0.033	b.d.	-	b.d.	-	0.413	0.064
Ta	b.d.	-	b.d.	-	b.d.	-	0.2948	0.033
Th	b.d.	-	b.d.	-	b.d.	-	0.6447	0.085
U	0.0527	0.011	b.d.	-	b.d.	-	0.2938	0.036
La	1.054	0.061	0.226	0.025	0.217	0.022	1.095	0.064
Ce	2.09	0.12	0.46	0.037	0.56	0.04	2.89	0.16
Pr	0.230	0.022	0.055	0.011	0.092	0.013	0.419	0.034
Nd	1.28	0.12	0.36	0.065	0.31	0.062	2.11	0.17
Sm	0.271	0.061	0.169	0.051	b.d.	-	0.407	0.077
Eu	0.831	0.072	0.700	0.066	0.713	0.066	0.823	0.075
Gd	0.153	0.045	b.d.	-	b.d.	-	0.439	0.067
Tb	0.0312	0.0091	b.d.	-	b.d.	-	0.0579	0.011
Dy	0.131	0.046	b.d.	-	b.d.	-	0.367	0.073
Ho	b.d.	-	b.d.	-	0.0377	0.0087	0.0535	0.011
Er	0.090	0.038	b.d.	-	b.d.	-	0.129	0.04
Tm	0.0214	0.0095	b.d.	-	b.d.	-	0.0273	0.011
Yb	0.155	0.043	b.d.	-	b.d.	-	0.120	0.045
Lu	b.d.	-	b.d.	-	b.d.	-	b.d.	-

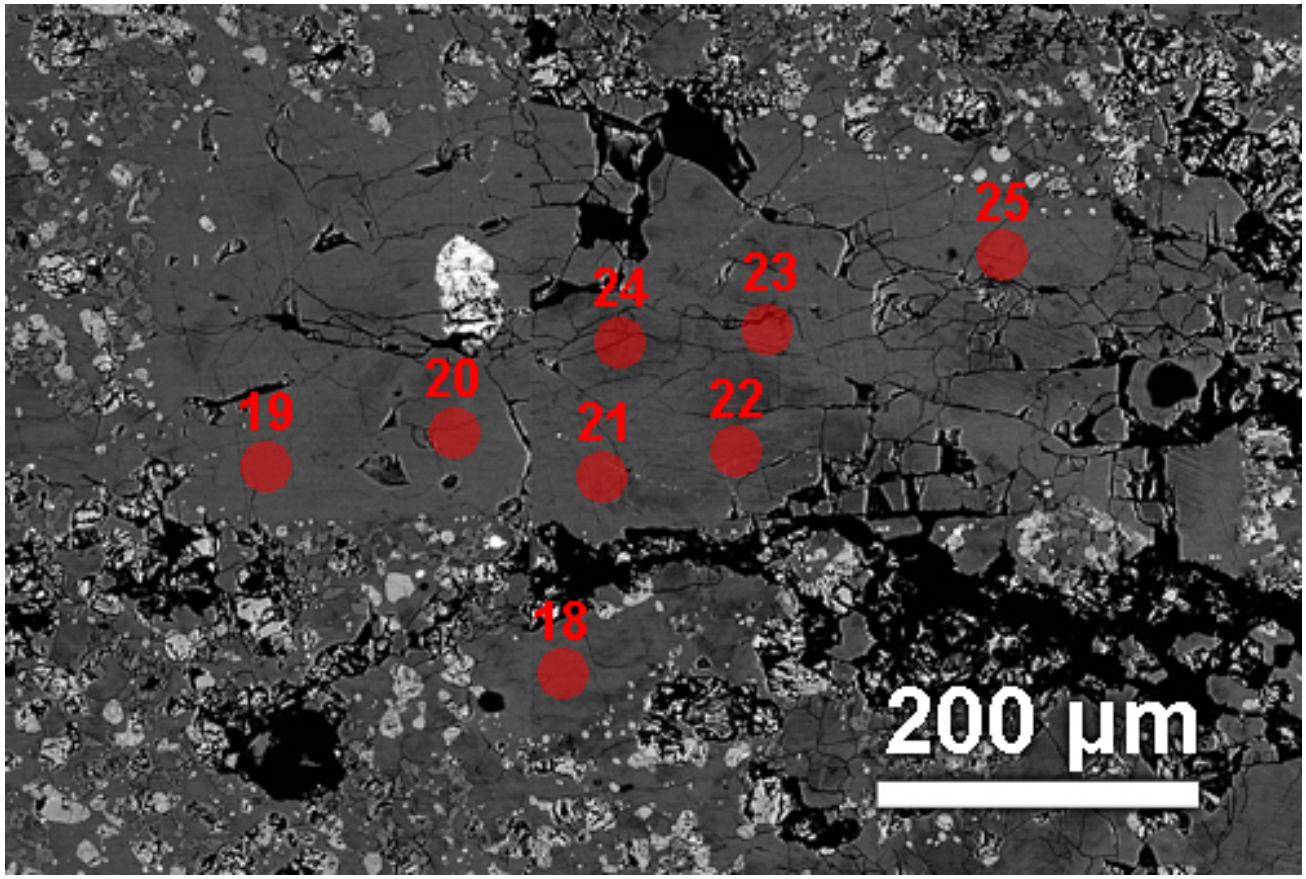

Figure B6: Detailed location of 30 µm plagioclase ablation spots 18 through 25.

Table B4: Trace element content (ppm) from areas shown in Figure B6

Spot	plag 18	1σ	plag 19	1σ	plag 20	1σ	plag 21	1σ	plag 22	1σ	plag 23	1σ	plag 24	1σ	plag 25	1σ
Size	30µm		30µm		30µm		30µm		30µm		30µm		30µm		30µm	
Co	b.d.	-	1.36	0.16	b.d.	-	4.11	0.26	b.d.	-	0.34	0.13	0.68	0.13	0.45	0.12
Ni	b.d.	-	b.d.	-	b.d.	-	159.25	30.76	b.d.	-	50.27	19.44	70.39	20.1	b.d.	-
Cu	b.d.	-	b.d.	-	b.d.	-	4.00	1.63	b.d.	-	b.d.	-	b.d.	-	3.12	1.46
Ga	2.38	0.4	1.96	0.4	2.07	0.38	2.46	0.39	2.18	0.37	2.09	0.38	1.41	0.35	1.96	0.35
Sr	169.15	8.6	164.36	8.36	154.05	7.84	154.09	7.91	157.25	8.08	156.65	8.07	150.27	7.76	155.24	8.03
Y	0.412	0.055	0.488	0.057	0.623	0.062	0.456	0.054	0.407	0.051	0.548	0.056	0.529	0.054	0.479	0.05
Zr	b.d.	-	b.d.	-	b.d.	-	b.d.	-	b.d.	-	b.d.	-	b.d.	-	b.d.	-
Nb	b.d.	-	b.d.	-	b.d.	-	b.d.	-	b.d.	-	b.d.	-	b.d.	-	b.d.	-
Ba	15.90	0.93	9.98	0.63	8.92	0.57	8.88	0.56	10.18	0.62	10.83	0.65	9.77	0.59	9.85	0.59
Hf	b.d.	-	b.d.	-	b.d.	-	b.d.	-	b.d.	-	b.d.	-	b.d.	-	b.d.	-
Ta	-	0.0095	0.0240	0.01	b.d.	-	b.d.	-	b.d.	-	b.d.	-	b.d.	-	b.d.	-
Th	b.d.	-	b.d.	-	b.d.	-	b.d.	-	b.d.	-	b.d.	-	b.d.	-	b.d.	-
U	0.0236	0.0078	b.d.	-	b.d.	-	b.d.	-	b.d.	-	b.d.	-	b.d.	-	b.d.	-
La	0.324	0.028	0.214	0.022	0.209	0.022	0.240	0.023	0.261	0.023	0.275	0.025	0.265	0.023	0.336	0.026
Ce	0.83	0.055	0.59	0.043	0.54	0.04	0.59	0.042	0.59	0.042	0.59	0.043	0.69	0.047	0.64	0.044
Pr	0.125	0.015	0.092	0.013	0.083	0.013	0.088	0.013	0.065	0.011	0.094	0.013	0.079	0.011	0.096	0.012
Nd	0.36	0.067	0.43	0.069	0.41	0.067	0.51	0.07	0.26	0.056	0.42	0.069	0.37	0.06	0.47	0.062
Sm	0.218	0.057	0.214	0.062	0.115	0.047	0.152	0.043	0.166	0.048	b.d.	-	0.167	0.054	b.d.	-
Eu	0.823	0.075	0.675	0.065	0.626	0.062	0.645	0.062	0.642	0.062	0.663	0.063	0.698	0.064	0.657	0.06
Gd	0.085	0.04	0.210	0.049	b.d.	-	0.136	0.043	0.167	0.042	b.d.	-	0.084	0.034	0.143	0.04
Tb	0.0210	0.0074	0.0144	0.0062	0.0249	0.011	b.d.	-	0.0172	0.0081	b.d.	-	0.0252	0.0095	b.d.	-
Dy	0.165	0.041	0.214	0.049	b.d.	-	0.132	0.043	b.d.	-	0.131	0.038	0.136	0.045	0.190	0.049
Ho	b.d.	-	b.d.	-	b.d.	-	0.0460	0.0096	0.0202	0.0093	0.0406	0.0099	0.0156	0.0074	b.d.	-
Er	b.d.	-	b.d.	-	b.d.	-	b.d.	-	0.068	0.034	0.076	0.035	0.091	0.04	0.068	0.029
Tm	b.d.	-	b.d.	-	b.d.	-	b.d.	-	b.d.	-	b.d.	-	b.d.	-	b.d.	-
Yb	b.d.	-	b.d.	-	b.d.	-	b.d.	-	b.d.	-	b.d.	-	b.d.	-	b.d.	-
Lu	b.d.	-	b.d.	-	b.d.	-	b.d.	-	b.d.	-	b.d.	-	b.d.	-	b.d.	-

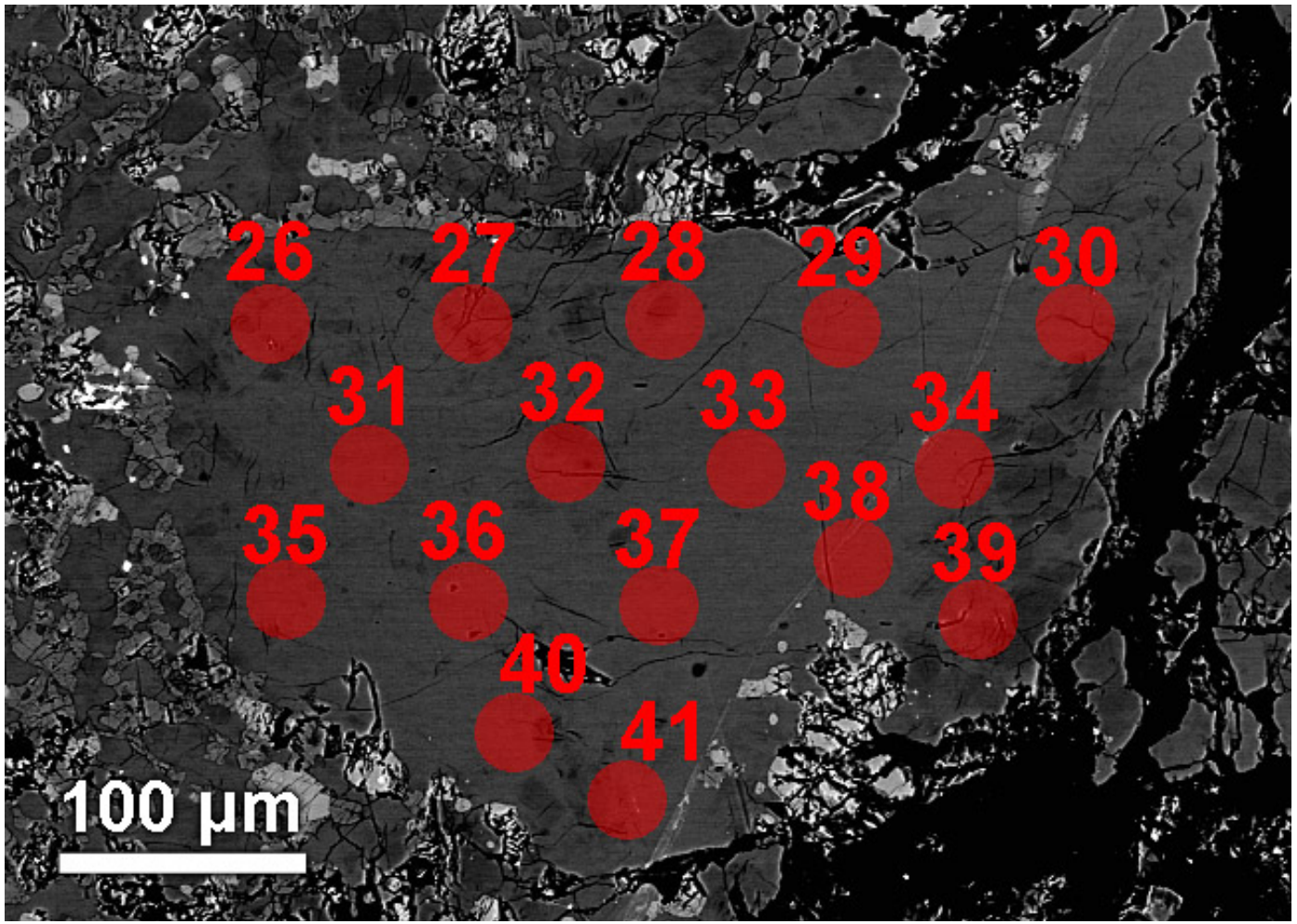

Figure B7: Detailed location of 30 µm plagioclase ablation spots 26 through 41. Spot 41 was excluded from this study.

Table B5: Trace element content (ppm) from areas shown in Figure B7

Spot	plag 26	1σ	plag 27	1σ	plag 28	1σ	plag 29	1σ	plag 30	1σ	plag 31	1σ	plag 32	1σ	plag 33	1σ
Size	30µm		30µm		30µm		30µm		30µm		30µm		30µm		30µm	
Co	0.31	0.13	1.75	0.17	b.d.	-	0.32	0.12	b.d.	-	0.26	0.12	b.d.	-	0.31	0.11
Ni	b.d.	-	b.d.	-	b.d.	-	b.d.	-	b.d.	-	b.d.	-	b.d.	-	b.d.	-
Cu	b.d.	-	b.d.	-	b.d.	-	b.d.	-	b.d.	-	b.d.	-	b.d.	-	b.d.	-
Ga	2.73	0.44	4.62	0.53	4.37	0.51	4.27	0.48	3.01	0.42	3.35	0.44	3.40	0.44	3.03	0.42
Sr	183.23	9.67	187.13	9.95	187.17	10.04	178.86	9.66	181.93	9.91	179.82	10.13	183.91	10.4	185.14	10.52
Y	0.524	0.058	0.297	0.053	0.594	0.061	0.534	0.055	0.500	0.054	0.416	0.055	0.487	0.05	0.445	0.053
Zr	1.70	0.26	1.29	0.24	2.19	0.27	2.06	0.25	1.66	0.23	1.00	0.22	1.10	0.22	0.86	0.22
Nb	0.281	0.045	0.160	0.038	0.300	0.043	0.197	0.039	0.167	0.036	0.089	0.036	0.133	0.035	0.079	0.034
Ba	20.20	1.14	18.09	1.03	18.46	1.07	17.63	1.02	23.58	1.35	16.87	1.02	17.31	1.05	17.47	1.05
Hf	0.072	0.033	b.d.	-	b.d.	-	0.148	0.04	b.d.	-	0.074	0.03	b.d.	-	b.d.	-
Ta	b.d.	-	b.d.	-	0.0266	0.011	b.d.	-	b.d.	-	b.d.	-	b.d.	-	b.d.	-
Th	0.0409	0.014	b.d.	-	b.d.	-	0.0409	0.013	0.0369	0.012	b.d.	-	0.0262	0.011	b.d.	-
U	0.0247	0.0094	b.d.	-	0.0158	0.0082	b.d.	-	0.0185	0.0088	b.d.	-	0.0135	0.0066	0.0107	0.0054
La	0.952	0.058	1.035	0.061	1.080	0.064	1.049	0.061	1.119	0.064	1.022	0.06	1.056	0.062	1.065	0.063
Ce	2.12	0.12	2.29	0.13	2.48	0.14	2.38	0.14	2.58	0.15	2.50	0.15	2.54	0.15	2.53	0.15
Pr	0.270	0.026	0.264	0.025	0.287	0.027	0.273	0.026	0.327	0.029	0.261	0.024	0.302	0.027	0.253	0.026
Nd	0.94	0.1	0.99	0.11	1.13	0.11	1.17	0.11	1.14	0.11	1.02	0.11	1.32	0.12	0.98	0.1
Sm	b.d.	-	0.201	0.062	0.220	0.056	0.290	0.064	0.154	0.054	0.137	0.058	0.237	0.058	0.171	0.062
Eu	0.930	0.084	0.910	0.082	0.862	0.08	0.811	0.076	0.837	0.079	0.772	0.078	0.865	0.085	0.843	0.083
Gd	0.157	0.046	b.d.	-	0.178	0.044	0.241	0.049	0.116	0.045	0.153	0.04	0.179	0.041	b.d.	-
Tb	0.0421	0.009	b.d.	-	0.0282	0.0097	b.d.	-	0.0260	0.0098	0.0253	0.0088	0.0334	0.0086	b.d.	-
Dy	0.121	0.047	b.d.	-	b.d.	-	0.136	0.039	0.155	0.047	b.d.	-	b.d.	-	0.118	0.051
Ho	0.0234	0.0079	b.d.	-	0.0234	0.0089	b.d.	-	0.0233	0.0081	b.d.	-	b.d.	-	b.d.	-
Er	b.d.	-	b.d.	-	b.d.	-	b.d.	-	0.111	0.037	b.d.	-	b.d.	-	0.071	0.027
Tm	b.d.	-	b.d.	-	b.d.	-	b.d.	-	b.d.	-	b.d.	-	b.d.	-	b.d.	-
Yb	b.d.	-	b.d.	-	b.d.	-	b.d.	-	b.d.	-	b.d.	-	0.074	0.036	b.d.	-
Lu	b.d.	-	b.d.	-	b.d.	-	b.d.	-	b.d.	-	b.d.	-	0.0159	0.0067	b.d.	-

Table B5, ctd

Spot	plag 34	1σ	plag 35	1σ	plag 36	1σ	plag 37	1σ	plag 38	1σ	plag 39	1σ	plag 40	1σ
Size	30µm		30µm		30µm		30µm		30µm		30µm		30µm	
Co	0.91	0.13	b.d.	-	b.d.	-	0.33	0.11	b.d.	-	b.d.	-	b.d.	-
Ni	b.d.	-	b.d.	-	b.d.	-	b.d.	-	b.d.	-	b.d.	-	b.d.	-
Cu	b.d.	-	b.d.	-	3.00	1.39	b.d.	-	b.d.	-	b.d.	-	b.d.	-
Ga	3.00	0.41	2.92	0.42	2.31	0.39	2.70	0.41	3.12	0.44	3.08	0.43	5.52	0.59
Sr	175.02	9.99	179.77	10.3	180.94	10.57	182.27	10.67	186.26	10.93	182.40	10.72	183.60	10.81
Y	0.587	0.057	0.424	0.048	0.385	0.046	0.558	0.054	0.547	0.055	0.394	0.048	0.476	0.048
Zr	1.25	0.22	1.40	0.23	0.77	0.2	1.07	0.22	1.06	0.22	1.92	0.23	2.67	0.26
Nb	0.171	0.036	0.225	0.039	0.073	0.031	0.142	0.038	0.201	0.038	0.265	0.039	0.134	0.035
Ba	17.36	1.05	21.82	1.3	17.50	1.07	19.04	1.17	16.98	1.06	22.75	1.41	18.56	1.17
Hf	b.d.	-	b.d.	-	b.d.	-	b.d.	-	b.d.	-	b.d.	-	b.d.	-
Ta	b.d.	-	b.d.	-	b.d.	-	b.d.	-	0.0230	0.0098	0.0316	0.01	b.d.	-
Th	b.d.	-	0.0324	0.012	b.d.	-	0.0359	0.013	0.0262	0.011	b.d.	-	b.d.	-
U	b.d.	-	b.d.	-	b.d.	-	b.d.	-	b.d.	-	b.d.	-	b.d.	-
La	1.042	0.062	0.882	0.055	0.929	0.057	1.013	0.062	1.029	0.063	1.072	0.064	1.059	0.063
Ce	2.51	0.15	2.15	0.13	2.36	0.14	2.64	0.16	2.63	0.16	2.42	0.15	2.23	0.14
Pr	0.306	0.027	0.260	0.024	0.270	0.024	0.361	0.031	0.346	0.03	0.314	0.028	0.272	0.025
Nd	1.38	0.12	1.07	0.1	1.09	0.1	1.05	0.1	1.24	0.12	1.43	0.12	1.08	0.1
Sm	0.271	0.058	0.206	0.048	0.241	0.051	0.281	0.055	0.209	0.059	0.329	0.059	0.213	0.051
Eu	0.847	0.083	0.890	0.086	0.852	0.082	0.811	0.08	0.939	0.092	0.893	0.088	0.865	0.087
Gd	0.189	0.04	0.207	0.043	0.228	0.049	0.142	0.041	0.262	0.051	0.167	0.045	0.159	0.042
Tb	b.d.	-	0.0190	0.0084	b.d.	-	0.0217	0.0072	0.0228	0.0081	b.d.	-	0.0203	0.008
Dy	0.123	0.046	b.d.	-	0.252	0.055	0.162	0.044	0.149	0.048	0.268	0.053	0.110	0.039
Ho	0.0174	0.0072	b.d.	-	b.d.	-	0.0157	0.0073	0.0293	0.0082	b.d.	-	0.0318	0.0084
Er	b.d.	-	0.123	0.041	b.d.	-	b.d.	-	b.d.	-	b.d.	-	b.d.	-
Tm	b.d.	-	b.d.	-	b.d.	-	b.d.	-	b.d.	-	0.0177	0.0075	b.d.	-
Yb	0.125	0.037	0.082	0.034	b.d.	-	0.072	0.032	b.d.	-	b.d.	-	b.d.	-
Lu	0.0196	0.0079	b.d.	-	b.d.	-	0.0249	0.0086	b.d.	-	b.d.	-	b.d.	-

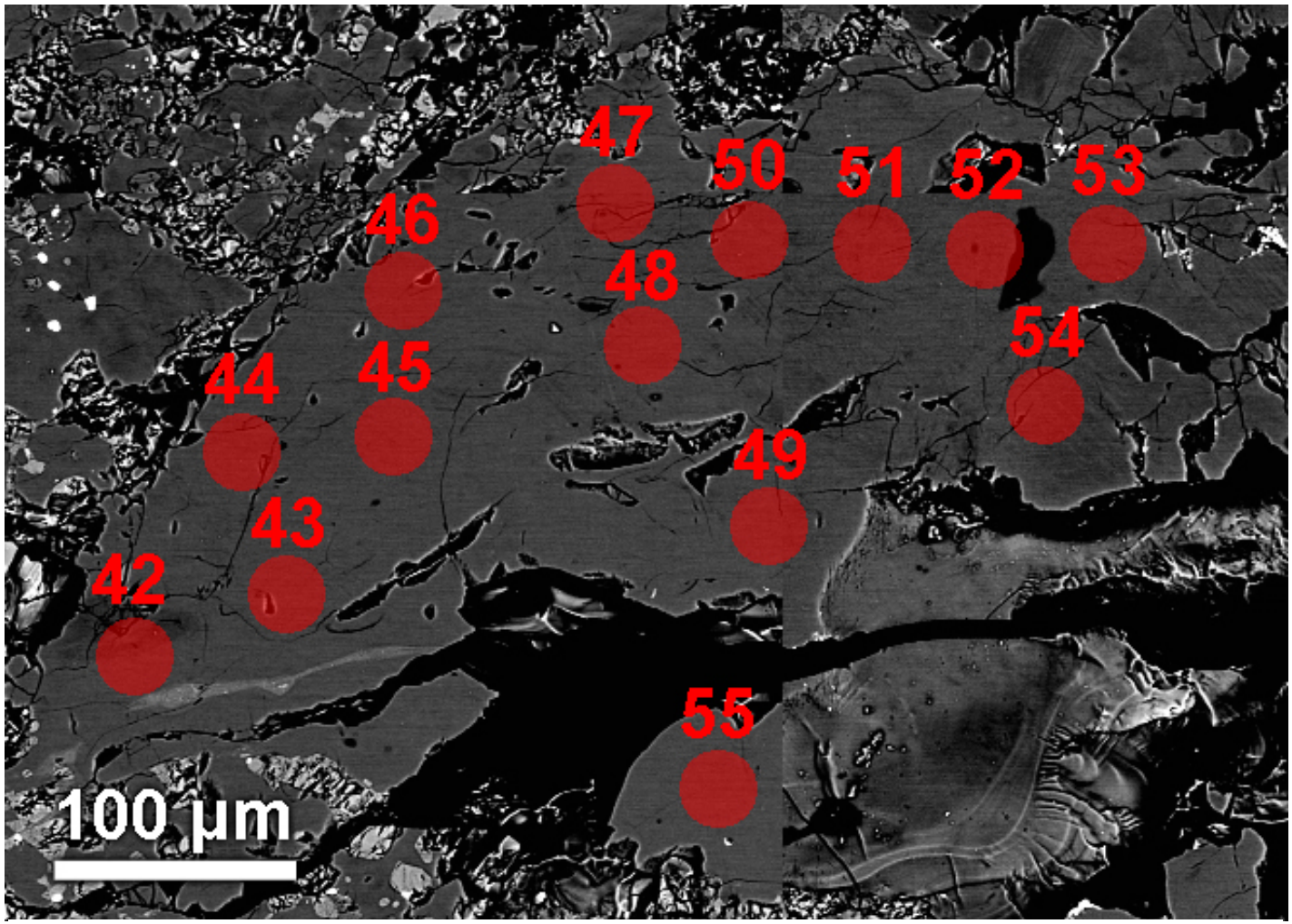

Figure B8: Detailed location of 30 µm plagioclase ablation spots 42 through 55.

Table B6: Trace element content (ppm) from areas shown in Figure B8

Spot	plag 42	1σ	plag 43	1σ	plag 44	1σ	plag 45	1σ	plag 46	1σ	plag 47	1σ	plag 48	1σ	plag 49	1σ
Size	30µm		30µm		30µm		30µm		30µm		30µm		30µm		30µm	
Co	2.32	0.2	1.29	0.15	b.d.	-	b.d.	-	b.d.	-	b.d.	-	b.d.	-	b.d.	-
Ni	38.14	17.78	b.d.	-	b.d.	-	b.d.	-	b.d.	-	b.d.	-	41.91	17.63	b.d.	-
Cu	b.d.	-	b.d.	-	b.d.	-	b.d.	-	b.d.	-	19.85	2.43	b.d.	-	b.d.	-
Ga	1.98	0.4	2.51	0.41	2.36	0.4	2.40	0.4	1.42	0.37	2.04	0.42	2.23	0.4	2.12	0.39
Sr	166.69	10.1	162.39	9.93	161.63	9.96	165.69	10.3	161.84	10.44	163.13	10.59	159.20	10.4	158.40	10.4
Y	0.433	0.053	0.299	0.044	0.172	0.039	0.200	0.042	0.203	0.038	0.143	0.039	0.248	0.043	0.233	0.037
Zr	0.72	0.23	b.d.	-	b.d.	-	b.d.	-	b.d.	-	b.d.	-	b.d.	-	b.d.	-
Nb	b.d.	-	b.d.	-	b.d.	-	b.d.	-	b.d.	-	b.d.	-	b.d.	-	b.d.	-
Ba	12.03	0.83	7.71	0.56	9.08	0.65	7.27	0.54	8.59	0.63	10.23	0.75	7.10	0.54	12.11	0.87
Hf	b.d.	-	b.d.	-	0.085	0.03	0.051	0.02	b.d.	-	b.d.	-	0.050	0.024	b.d.	-
Ta	b.d.	-	0.0260	0.011	b.d.	-	b.d.	-	b.d.	-	b.d.	-	b.d.	-	b.d.	-
Th	b.d.	-	b.d.	-	b.d.	-	b.d.	-	b.d.	-	b.d.	-	0.0204	0.0088	b.d.	-
U	b.d.	-	b.d.	-	b.d.	-	b.d.	-	b.d.	-	b.d.	-	b.d.	-	b.d.	-
La	0.359	0.029	0.199	0.02	0.215	0.021	0.170	0.019	0.164	0.019	0.217	0.023	0.188	0.019	0.178	0.018
Ce	0.77	0.055	0.44	0.036	0.53	0.04	0.44	0.034	0.47	0.037	0.51	0.04	0.43	0.035	0.40	0.033
Pr	0.090	0.012	0.066	0.011	0.056	0.01	0.024	0.0096	0.049	0.0097	0.071	0.011	0.062	0.0096	0.044	0.0087
Nd	0.50	0.068	0.27	0.052	0.19	0.053	0.29	0.05	0.20	0.047	0.32	0.058	0.14	0.048	0.21	0.05
Sm	b.d.	-	0.133	0.043	b.d.	-	0.088	0.039	0.098	0.042	b.d.	-	b.d.	-	b.d.	-
Eu	0.720	0.078	0.715	0.077	0.627	0.069	0.720	0.077	0.659	0.072	0.744	0.082	0.749	0.082	0.697	0.077
Gd	0.136	0.041	b.d.	-	0.097	0.035	b.d.	-	0.096	0.037	b.d.	-	0.110	0.037	0.091	0.029
Tb	b.d.	-	b.d.	-	b.d.	-	b.d.	-	0.0138	0.007	b.d.	-	b.d.	-	b.d.	-
Dy	0.082	0.041	b.d.	-	0.100	0.044	b.d.	-	b.d.	-	b.d.	-	b.d.	-	b.d.	-
Ho	b.d.	-	b.d.	-	b.d.	-	0.0187	0.0074	b.d.	-	b.d.	-	0.0176	0.0074	b.d.	-
Er	0.088	0.038	0.080	0.038	b.d.	-	b.d.	-	b.d.	-	b.d.	-	b.d.	-	0.088	0.037
Tm	b.d.	-	b.d.	-	b.d.	-	b.d.	-	b.d.	-	b.d.	-	b.d.	-	b.d.	-
Yb	0.111	0.036	0.095	0.033	b.d.	-	b.d.	-	b.d.	-	b.d.	-	b.d.	-	b.d.	-
Lu	b.d.	-	b.d.	-	b.d.	-	b.d.	-	b.d.	-	b.d.	-	b.d.	-	b.d.	-

Table B6, ctd

Spot	plag 50	1σ	plag 51	1σ	plag 52	1σ	plag 53	1σ	plag 54	1σ	plag 55	1σ
Size	30µm		30µm		30µm		30µm		30µm		30µm	
Co	b.d.	-	b.d.	-	b.d.	-	b.d.	-	b.d.	-	b.d.	-
Ni	b.d.	-	b.d.	-	b.d.	-	b.d.	-	b.d.	-	b.d.	-
Cu	b.d.	-	b.d.	-	b.d.	-	b.d.	-	b.d.	-	b.d.	-
Ga	2.47	0.42	2.28	0.4	2.37	0.4	2.36	0.4	1.43	0.35	2.01	0.38
Sr	155.66	10.29	158.41	10.72	159.53	10.8	153.82	10.42	159.28	10.8	163.36	11.08
Y	0.169	0.037	0.248	0.039	0.195	0.039	0.120	0.037	0.186	0.037	0.157	0.038
Zr	b.d.	-	b.d.	-	0.71	0.21	b.d.	-	b.d.	-	b.d.	-
Nb	b.d.	-	b.d.	-	b.d.	-	b.d.	-	b.d.	-	b.d.	-
Ba	7.94	0.59	8.17	0.62	7.45	0.57	7.11	0.55	12.76	0.93	7.37	0.57
Hf	b.d.	-	0.061	0.027	b.d.	-	0.104	0.034	b.d.	-	b.d.	-
Ta	b.d.	-	b.d.	-	b.d.	-	b.d.	-	b.d.	-	b.d.	-
Th	b.d.	-	b.d.	-	b.d.	-	b.d.	-	b.d.	-	b.d.	-
U	b.d.	-	b.d.	-	b.d.	-	b.d.	-	b.d.	-	b.d.	-
La	0.211	0.02	0.187	0.02	0.181	0.019	0.218	0.02	0.199	0.02	0.169	0.018
Ce	0.45	0.036	0.41	0.035	0.46	0.038	0.49	0.04	0.43	0.036	0.40	0.034
Pr	0.057	0.011	0.057	0.01	0.049	0.009	0.058	0.011	0.068	0.011	0.064	0.011
Nd	0.34	0.052	0.24	0.05	0.14	0.044	0.21	0.046	0.24	0.052	0.29	0.055
Sm	0.072	0.04	b.d.	-	b.d.	-	b.d.	-	b.d.	-	b.d.	-
Eu	0.710	0.079	0.754	0.086	0.729	0.084	0.681	0.08	0.669	0.079	0.730	0.086
Gd	0.078	0.038	b.d.	-	b.d.	-	b.d.	-	b.d.	-	b.d.	-
Tb	b.d.	-	b.d.	-	0.0192	0.008	0.0149	0.0068	b.d.	-	b.d.	-
Dy	b.d.	-	b.d.	-	0.118	0.039	b.d.	-	b.d.	-	0.082	0.035
Ho	b.d.	-	b.d.	-	0.0191	0.008	b.d.	-	b.d.	-	0.0151	0.007
Er	-	0.024	b.d.	-	b.d.	-	0.121	0.033	b.d.	-	b.d.	-
Tm	b.d.	-	b.d.	-	b.d.	-	b.d.	-	b.d.	-	b.d.	-
Yb	b.d.	-	b.d.	-	b.d.	-	b.d.	-	0.059	0.03	b.d.	-
Lu	b.d.	-	b.d.	-	b.d.	-	b.d.	-	b.d.	-	b.d.	-

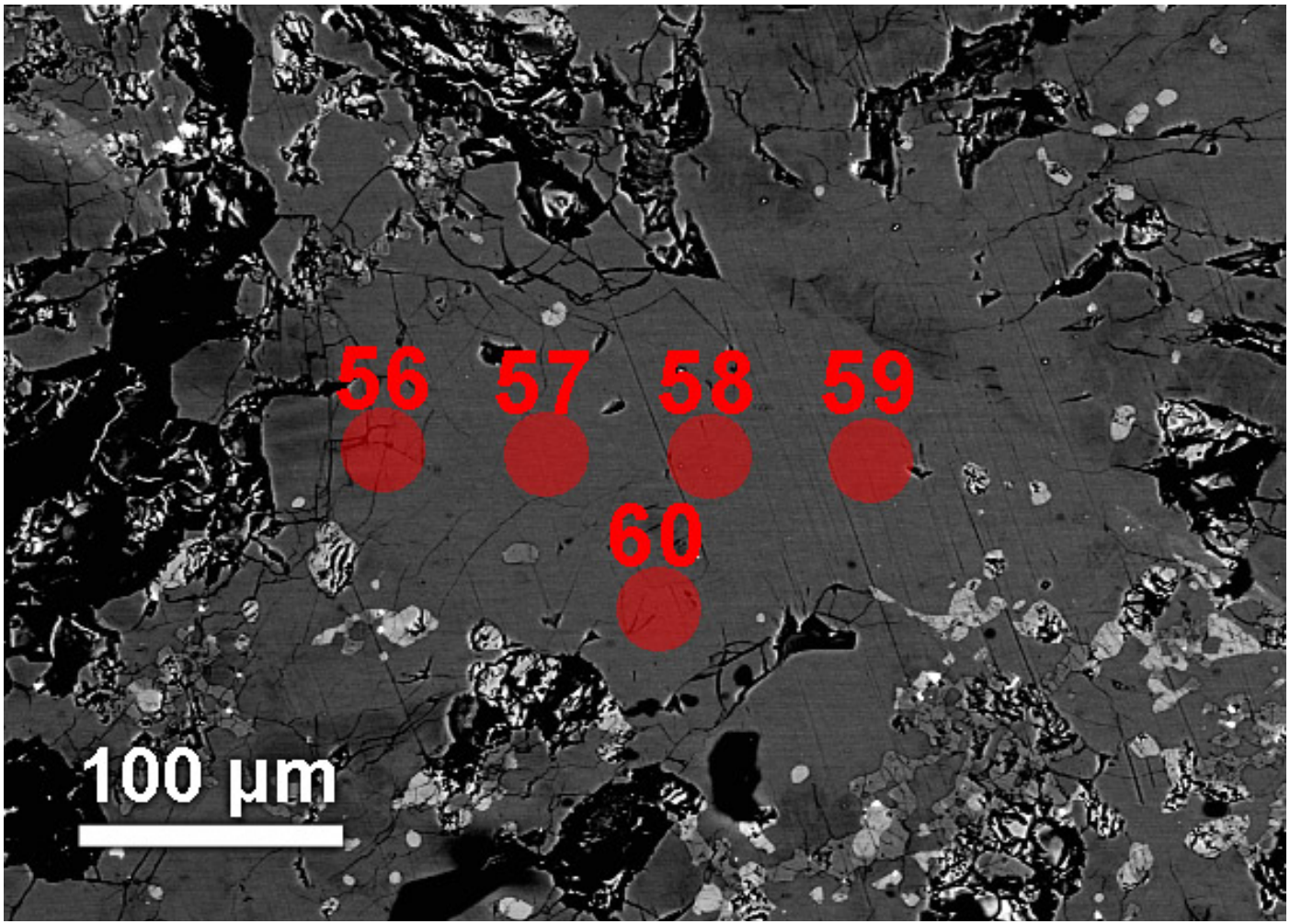

Figure B9: Detailed location of 30 µm plagioclase ablation spots 56 through 60.

Table B7: Trace element content (ppm) from areas shown in Figure B9

	plag		plag		plag		plag		plag	
Spot	56	1σ	57	1σ	58	1σ	59	1σ	60	1σ
Size	30µm		30µm		30µm		30µm		30µm	
Co	0.50	0.13	-	0.12	-	0.12	-	0.12	-	0.13
Ni	-	17.08	-	16.64	-	16.24	-	16.86	-	16.22
Cu	4.13	1.51	-	1.45	-	1.48	-	1.45	-	1.49
Ga	0.82	0.38	2.04	0.42	1.48	0.39	2.56	0.46	1.60	0.4
Sr	166.87	11.48	153.90	10.65	153.74	10.7	154.50	10.82	160.14	11.29
Y	0.809	0.07	0.482	0.053	0.480	0.053	0.414	0.052	0.729	0.069
Zr	0.67	0.23	-	0.22	0.67	0.23	-	0.23	1.48	0.26
Nb	-	0.035	-	0.036	-	0.034	-	0.035	-	0.038
Ba	11.93	0.9	8.83	0.68	7.78	0.61	7.97	0.62	10.09	0.78
Hf	-	0.025	-	0.025	-	0.026	-	0.025	-	0.028
Ta	-	0.0077	-	0.0065	-	0.0099	-	0.0079	-	0.0087
Th	-	0.011	-	0.0095	-	0.01	-	0.0092	-	0.01
U	0.0290	0.0091	0.0130	0.0071	-	0.0073	-	0.0074	-	0.0066
La	0.259	0.024	0.212	0.021	0.210	0.021	0.215	0.022	0.254	0.024
Ce	0.63	0.051	0.50	0.042	0.52	0.043	0.56	0.046	0.50	0.043
Pr	0.098	0.013	0.081	0.012	0.086	0.012	0.071	0.011	0.087	0.013
Nd	0.28	0.064	0.37	0.063	0.35	0.061	0.33	0.054	0.35	0.062
Sm	0.116	0.047	0.133	0.043	-	0.05	0.154	0.052	0.154	0.052
Eu	0.725	0.088	0.729	0.088	0.617	0.075	0.674	0.08	0.716	0.085
Gd	0.137	0.04	0.113	0.037	0.098	0.04	0.088	0.035	0.116	0.042
Tb	-	0.0081	-	0.0089	-	0.0072	-	0.008	0.0326	0.01
Dy	0.136	0.049	0.273	0.054	-	0.044	-	0.039	0.372	0.063
Ho	-	0.0072	0.0292	0.0088	-	0.0074	0.0245	0.0084	0.0334	0.009
Er	-	0.037	0.072	0.034	-	0.033	-	0.039	0.102	0.044
Tm	-	0.0077	-	0.0074	-	0.0083	-	0.0079	-	0.0094
Yb	-	0.032	-	0.041	-	0.037	-	0.034	-	0.029
Lu	-	0.0079	-	0.0083	-	0.0097	-	0.0081	0.0190	0.009

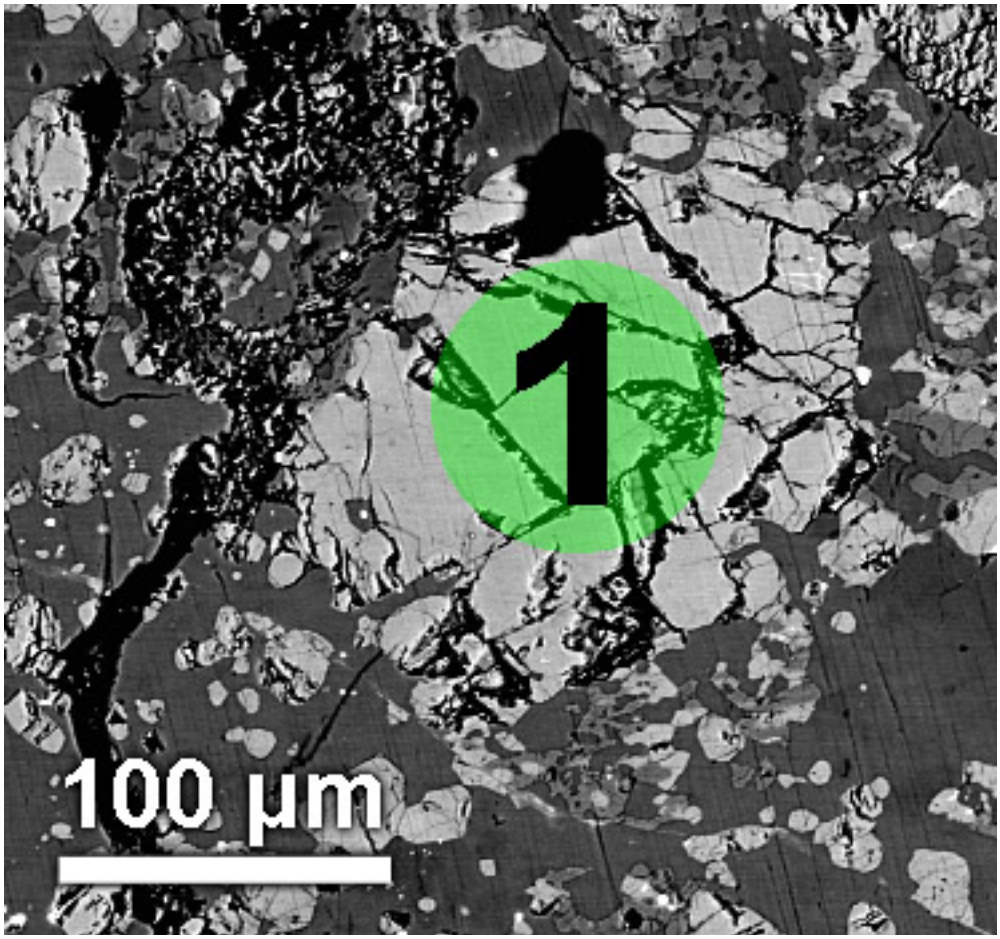

Figure B10: Detailed location of 84 µm olivine ablation spot 1.

Table B8: Trace element content (ppm) from area shown in Figure B10

Spot Size	olv 1 84μm	1σ
Co	70.36	2.55
Ni	123.26	6
Cu	5.77	0.28
Ga	26.54	1.18
Sr	9.05	0.38
Y	0.974	0.048
Zr	4.17	0.19
Nb	0.254	0.015
Ba	11.64	0.48
Hf	0.109	0.013
Ta	0.0156	0.003
Th	0.0240	0.0037
U	0.0194	0.0023
La	0.085	0.0065
Ce	0.36	0.016
Pr	0.041	0.0038
Nd	0.25	0.023
Sm	0.093	0.015
Eu	0.011	0.0029
Gd	0.089	0.014
Tb	0.0212	0.003
Dy	0.133	0.018
Ho	0.0365	0.0043
Er	0.109	0.015
Tm	0.0210	0.0032
Yb	0.199	0.02
Lu	0.0389	0.0047

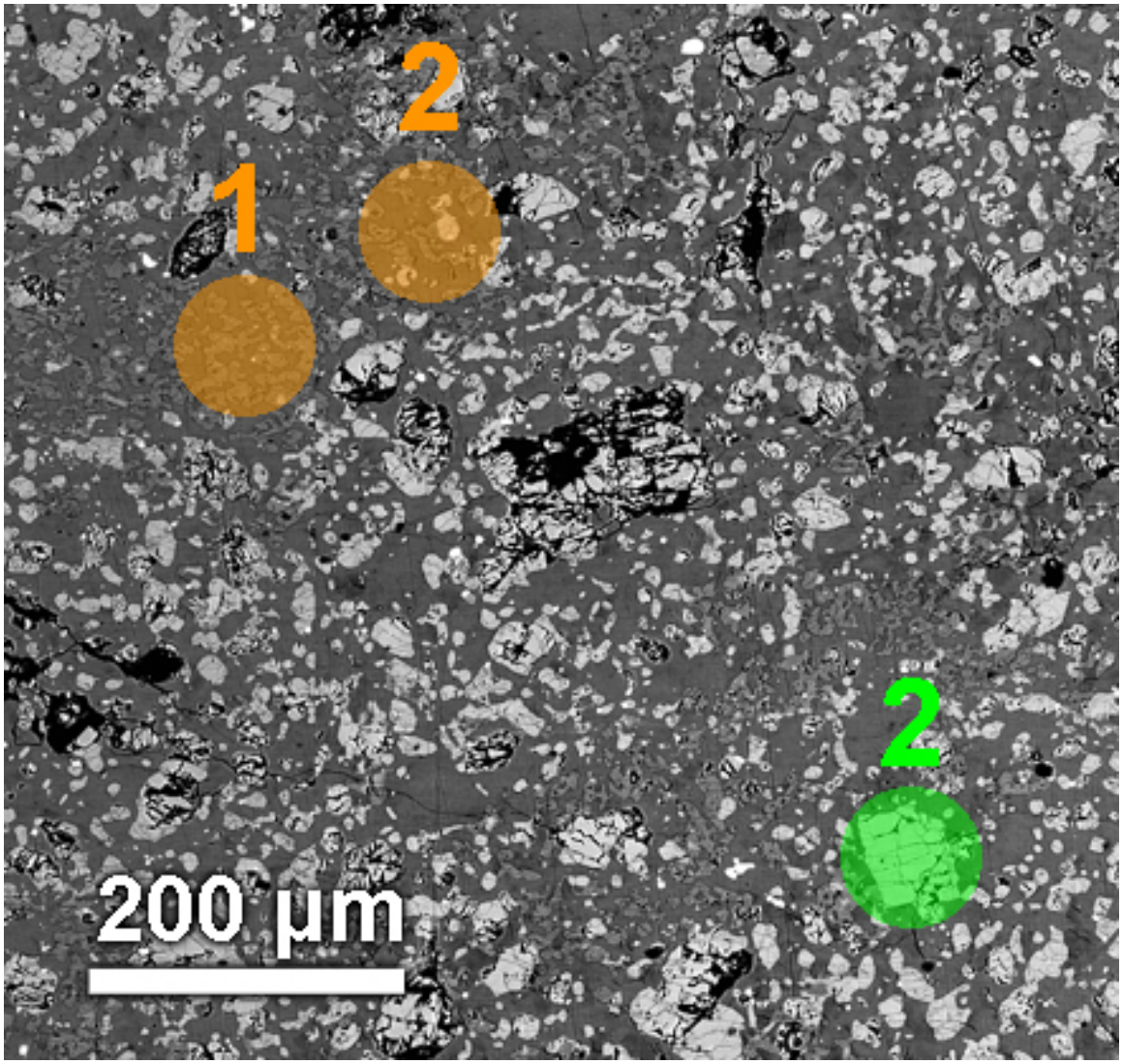

Figure B11: Detailed locations of 84 µm olivine ablation spot 2 and bulk ablation spots 1 and 2. Bulk spots 1 and 2 contain an excess of pyroxene and low levels of olivine. They are not reflective of overall bulk NWA 5744 and were not used in bulk calculations in this study. Olivine 2 ablation spot included some surrounding plagioclase and pyroxene, and also was not used in this study.

Table B9: Unused trace element content (ppm) from areas shown in Figure B11

Spot	olv 2 84µm	1σ	bulk 1 84µm	1σ	bulk 2 84µm	1σ
Co	73.01	2.66	17.55	0.72	19.43	0.81
Ni	210.41	9.84	45.72	2.78	122.30	7.13
Cu	12.15	0.53	4.87	0.25	6.45	0.34
Ga	1.38	0.068	1.73	0.092	1.97	0.11
Sr	52.52	2.2	79.04	3.82	104.25	5.11
Y	3.303	0.14	5.213	0.25	5.400	0.26
Zr	8.85	0.35	11.64	0.5	12.15	0.53
Nb	0.622	0.025	1.381	0.054	0.711	0.03
Ba	30.04	1.19	29.35	1.3	28.63	1.29
Hf	0.252	0.016	0.345	0.021	0.330	0.021
Ta	0.0347	0.0032	0.0949	0.0063	0.0479	0.0038
Th	0.0493	0.0043	0.0725	0.0059	0.0901	0.0074
U	0.0141	0.0014	0.0187	0.0015	0.0170	0.0015
La	0.352	0.015	0.455	0.02	0.556	0.025
Ce	1.12	0.042	1.20	0.047	1.47	0.058
Pr	0.154	0.0074	0.160	0.0078	0.203	0.0099
Nd	0.78	0.04	0.81	0.043	0.98	0.052
Sm	0.263	0.021	0.293	0.022	0.296	0.023
Eu	0.229	0.013	0.373	0.021	0.516	0.029
Gd	0.427	0.027	0.444	0.029	0.479	0.032
Tb	0.0734	0.0048	0.0902	0.0055	0.1039	0.0064
Dy	0.581	0.038	0.752	0.052	0.838	0.059
Ho	0.1223	0.0077	0.1889	0.012	0.2017	0.013
Er	0.406	0.028	0.654	0.047	0.677	0.05
Tm	0.0673	0.0049	0.1112	0.0078	0.1115	0.0081
Yb	0.528	0.03	0.787	0.044	0.789	0.046
Lu	0.1017	0.0074	0.1224	0.0096	0.1300	0.01

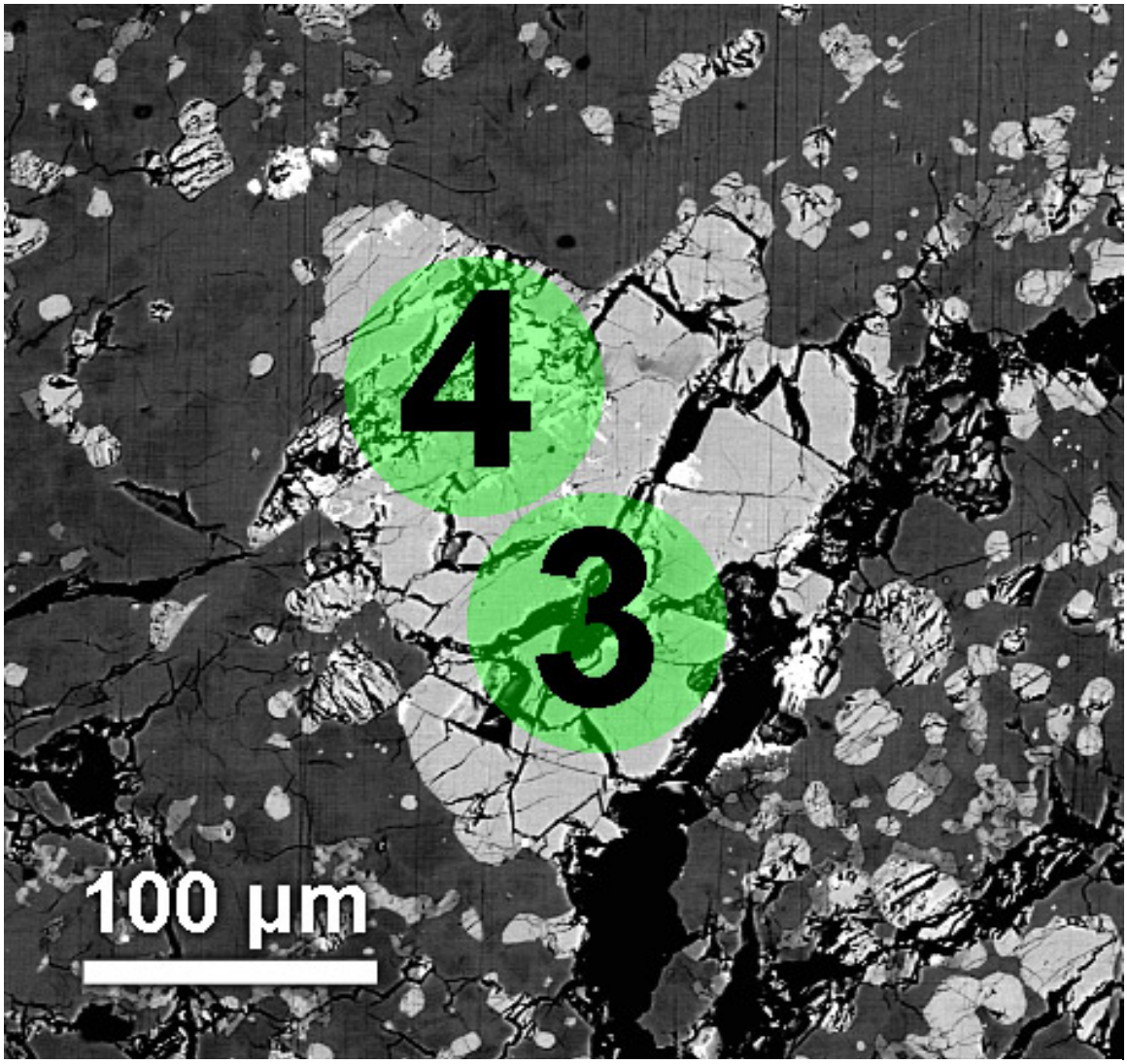

Figure B12: Detailed locations of 84 µm olivine ablation spots 3 and 4. These spots contained an excess of chromite and also appeared to include some plagioclase. Ablation data were not used in this study.

Table B10: Unused trace element content (ppm) from areas shown in Figure B12

Spot Size	olv 3 84μm	1σ	olv 4 84μm	1σ
Co	76.65	2.82	111.10	4.33
Ni	129.35	6.35	155.08	8.73
Cu	6.59	0.31	8.47	0.45
Ga	0.13	0.022	0.19	0.042
Sr	14.18	0.61	11.95	0.56
Y	0.537	0.028	14.082	0.65
Zr	0.95	0.08	27.23	1.15
Nb	0.147	0.0096	0.430	0.025
Ba	38.55	1.56	37.22	1.62
Hf	0.017	0.0051	0.869	0.057
Ta	0.0082	0.002	0.0258	0.0046
Th	0.0300	0.0035	0.1504	0.014
U	0.0271	0.0024	0.0528	0.0048
La	0.113	0.0068	0.338	0.019
Ce	0.40	0.017	1.69	0.068
Pr	0.039	0.0031	0.324	0.017
Nd	0.31	0.023	2.19	0.12
Sm	0.050	0.0097	1.088	0.082
Eu	0.007	0.0023	0.020	0.0046
Gd	0.068	0.01	1.662	0.11
Tb	0.0067	0.0016	0.3540	0.021
Dy	0.036	0.0081	2.549	0.17
Ho	0.0157	0.0023	0.5199	0.034
Er	0.067	0.01	1.563	0.11
Tm	0.0147	0.0024	0.2346	0.018
Yb	0.107	0.012	1.321	0.083
Lu	0.0355	0.0038	0.2071	0.018

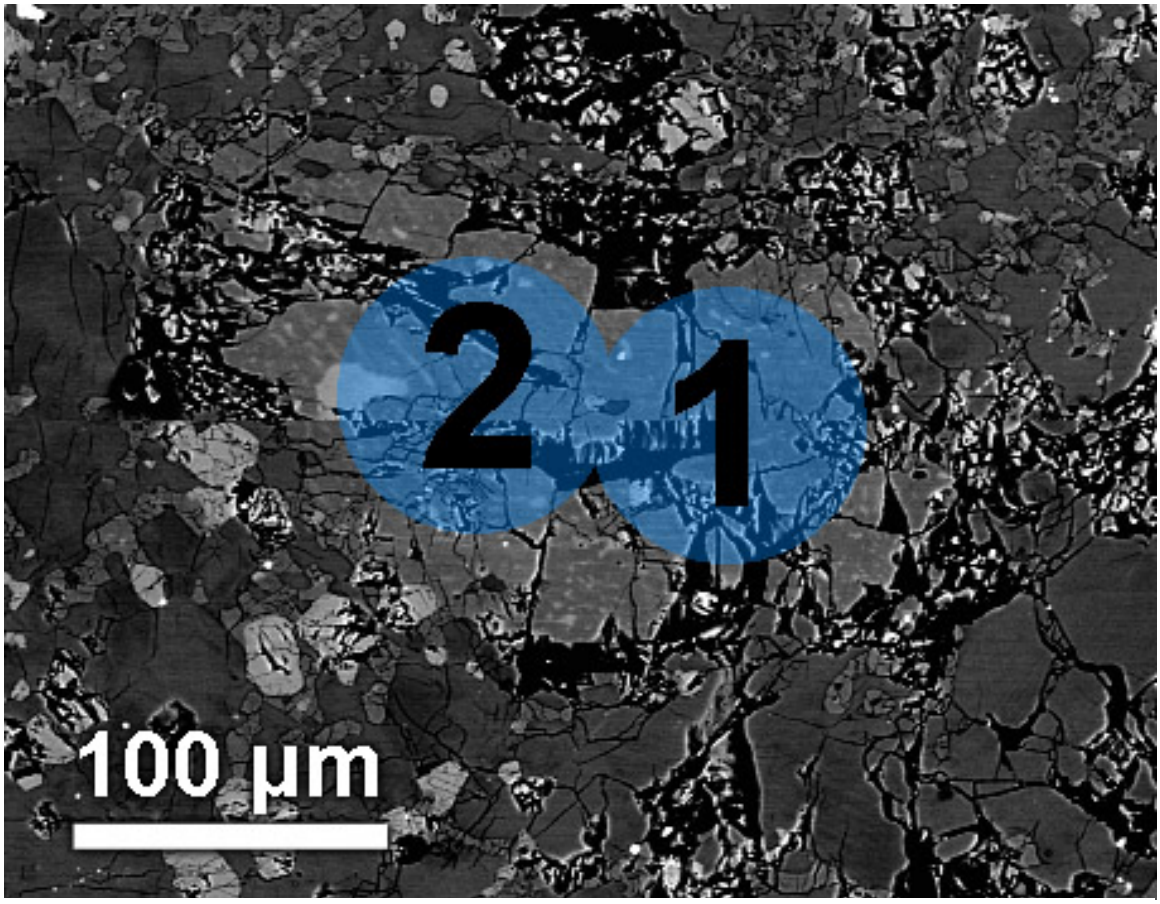

Figure B13: Detailed locations of 84 µm pyroxene ablation spots 1 and 2.

Table B11: Trace element content (ppm) from areas shown in Figure B13

Spot Size	pyx 1 84µm	1σ	pyx 2 84µm	1σ
Co	32.81	1.17	33.18	1.19
Ni	54.59	2.62	85.97	4.01
Cu	8.25	0.35	10.75	0.45
Ga	0.70	0.036	0.75	0.038
Sr	13.75	0.55	22.59	0.92
Y	17.103	0.68	16.903	0.68
Zr	55.95	2.04	45.02	1.66
Nb	0.769	0.028	1.008	0.036
Ba	28.08	1.07	23.76	0.92
Hf	1.661	0.073	1.331	0.06
Ta	0.0530	0.0036	0.0671	0.0044
Th	0.2767	0.015	0.2525	0.015
U	0.0727	0.0038	0.0574	0.0032
La	0.321	0.013	0.417	0.017
Ce	1.63	0.058	1.98	0.07
Pr	0.315	0.013	0.373	0.015
Nd	1.95	0.083	2.30	0.099
Sm	0.964	0.051	1.066	0.057
Eu	0.050	0.0035	0.101	0.0059
Gd	1.631	0.077	1.650	0.08
Tb	0.3281	0.015	0.3401	0.016
Dy	2.534	0.13	2.667	0.14
Ho	0.6251	0.031	0.6303	0.032
Er	1.987	0.11	2.057	0.11
Tm	0.3008	0.016	0.2989	0.016
Yb	2.169	0.095	2.032	0.091
Lu	0.3259	0.019	0.3061	0.019

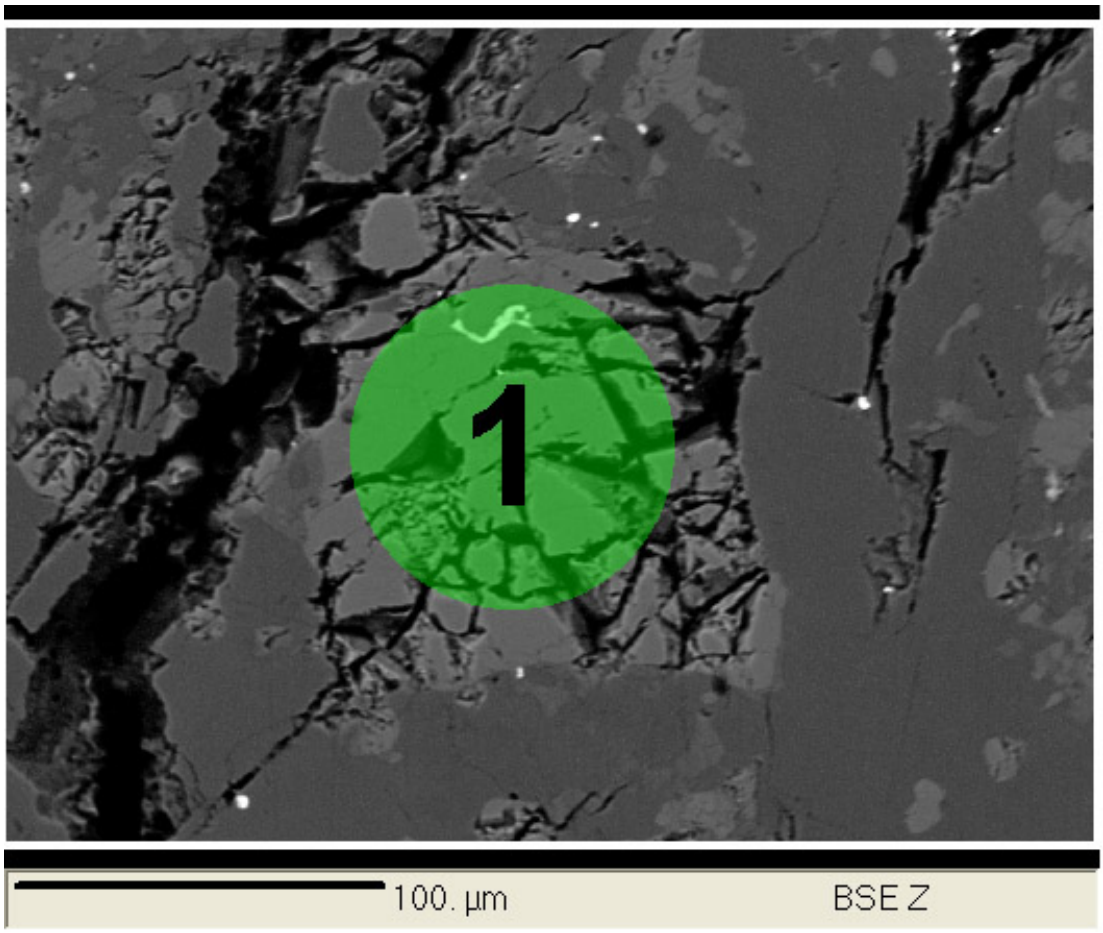

Figure B14: Detailed location of 84 µm olivine ablation point 1.

Table B12: Trace element content (ppm) from area shown in Figure B14

Spot Size	olv 1 84μm	1σ
Co	80.18	3.01
Ni	204.34	8.11
Cu	8.61	0.38
Ga	0.18	0.014
Sr	6.37	0.27
Y	0.505	0.029
Zr	2.14	0.12
Nb	0.427	0.021
Ba	28.05	1.01
Hf	0.076	0.0069
Ta	0.0410	0.0032
Th	0.0476	0.0043
U	0.0154	0.0013
La	0.055	0.0044
Ce	0.209	0.012
Pr	0.024	0.0021
Nd	0.099	0.0094
Sm	0.028	0.0057
Eu	0.006	0.0014
Gd	0.051	0.0059
Tb	0.009	0.0011
Dy	0.067	0.0071
Ho	0.016	0.0017
Er	0.067	0.0071
Tm	0.015	0.0017
Yb	0.147	0.01
Lu	0.029	0.0025

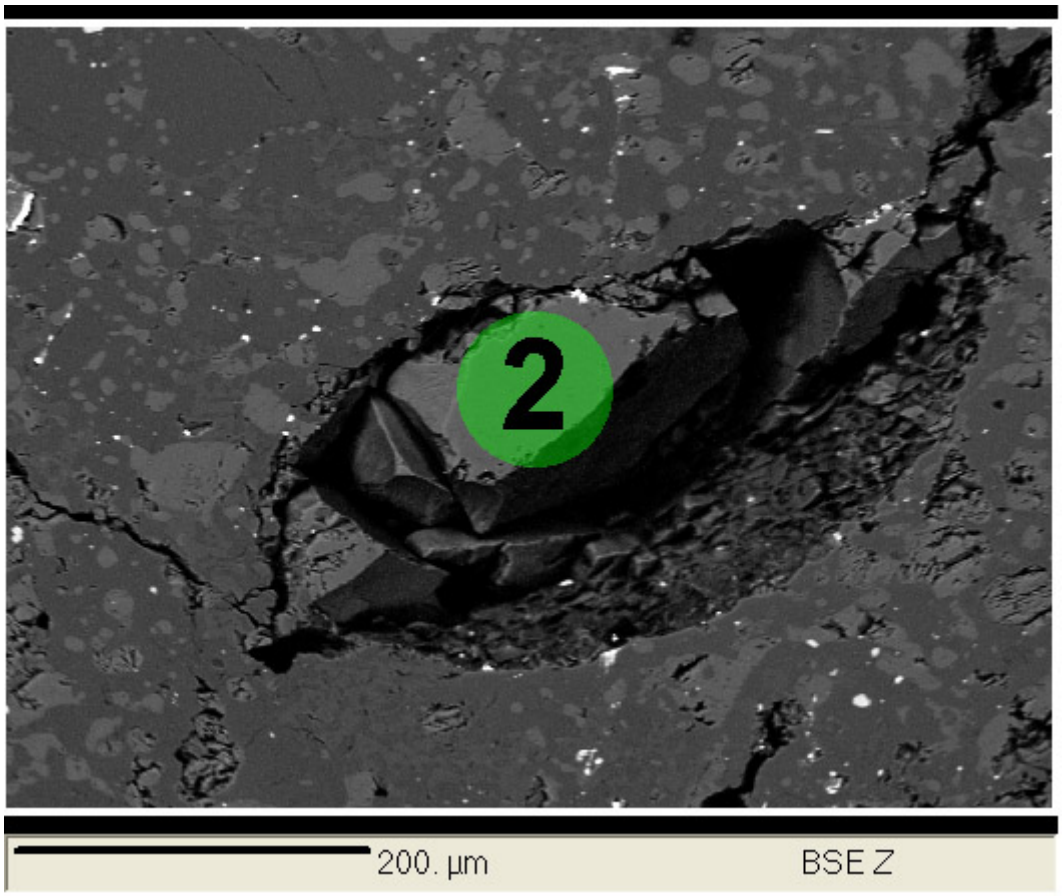

Figure B15: Detailed location of 84 µm olivine ablation point 2.

Table B13: Trace element content (ppm) from area shown in Figure B15

Spot	olv 2	1σ
Size	84µm	
Co	75.34	2.84
Ni	125.54	5.11
Cu	6.30	0.28
Ga	0.70	0.036
Sr	5.10	0.22
Y	0.416	0.025
Zr	2.44	0.15
Nb	0.224	0.013
Ba	74.75	2.69
Hf	0.041	0.0055
Ta	0.0144	0.0019
Th	0.0151	0.0021
U	0.0108	0.0011
La	0.016	0.0024
Ce	0.142	0.0086
Pr	0.010	0.0013
Nd	0.031	0.0062
Sm	b.d.	-
Eu	0.007	0.0015
Gd	0.018	0.0042
Tb	0.002	0.00078
Dy	0.037	0.0057
Ho	0.014	0.0016
Er	0.053	0.0067
Tm	0.014	0.0018
Yb	0.154	0.011
Lu	0.041	0.0032

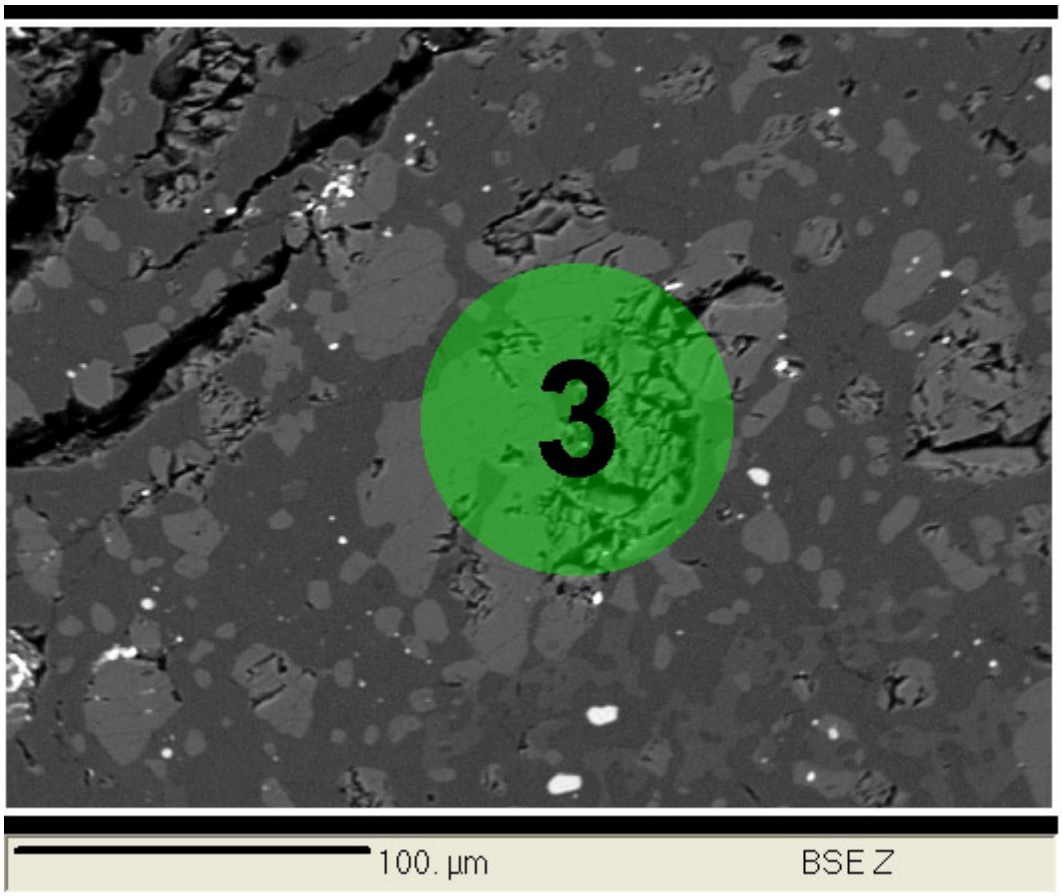

Figure B16: Detailed location of 84 µm olivine ablation point 3.

Table B14: Trace element content (ppm) from area shown in Figure B16

Spot	olv 3	1σ
Size	84μm	
Co	71.95	2.72
Ni	160.90	6.61
Cu	8.78	0.4
Ga	2.02	0.098
Sr	31.14	1.35
Y	0.723	0.043
Zr	2.69	0.17
Nb	0.326	0.019
Ba	13.94	0.52
Hf	0.052	0.007
Ta	0.0165	0.0025
Th	0.0254	0.0034
U	0.0081	0.0012
La	0.174	0.012
Ce	0.442	0.025
Pr	0.054	0.0042
Nd	0.181	0.017
Sm	0.051	0.0091
Eu	0.134	0.0084
Gd	0.058	0.0081
Tb	0.009	0.0016
Dy	0.101	0.011
Ho	0.021	0.0025
Er	0.116	0.012
Tm	0.027	0.003
Yb	0.281	0.019
Lu	0.062	0.0048

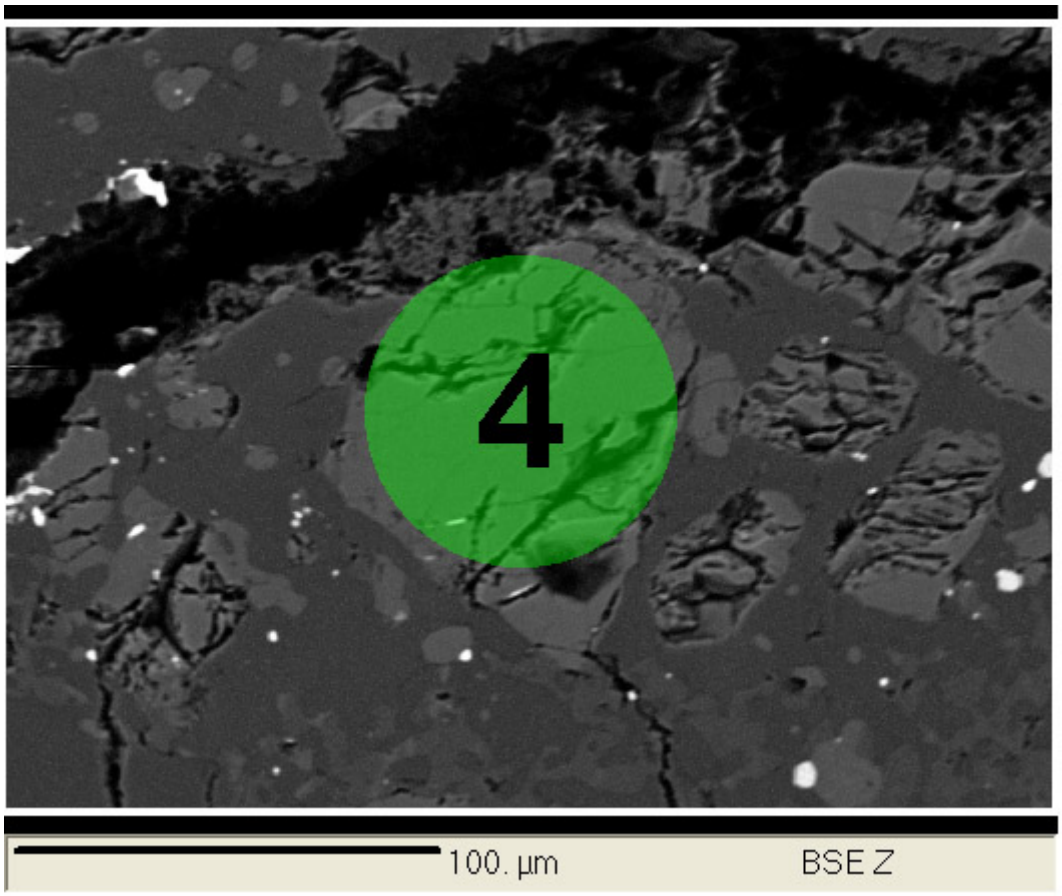

Figure B17: Detailed location of 84 µm olivine ablation point 4.

Table B15: Trace element content (ppm) from area shown in Figure B17

Spot	olv 4	1σ
Size	84µm	
Co	74.06	2.81
Ni	148.20	6.17
Cu	8.22	0.38
Ga	0.29	0.022
Sr	22.22	0.97
Y	0.892	0.052
Zr	1.59	0.13
Nb	0.165	0.011
Ba	35.08	1.28
Hf	0.021	0.005
Ta	0.0067	0.0017
Th	0.0339	0.004
U	0.0221	0.002
La	0.239	0.015
Ce	0.571	0.031
Pr	0.079	0.0056
Nd	0.398	0.028
Sm	0.085	0.011
Eu	0.058	0.005
Gd	0.097	0.011
Tb	0.016	0.002
Dy	0.104	0.012
Ho	0.026	0.0028
Er	0.129	0.013
Tm	0.021	0.0026
Yb	0.272	0.019
Lu	0.043	0.0038

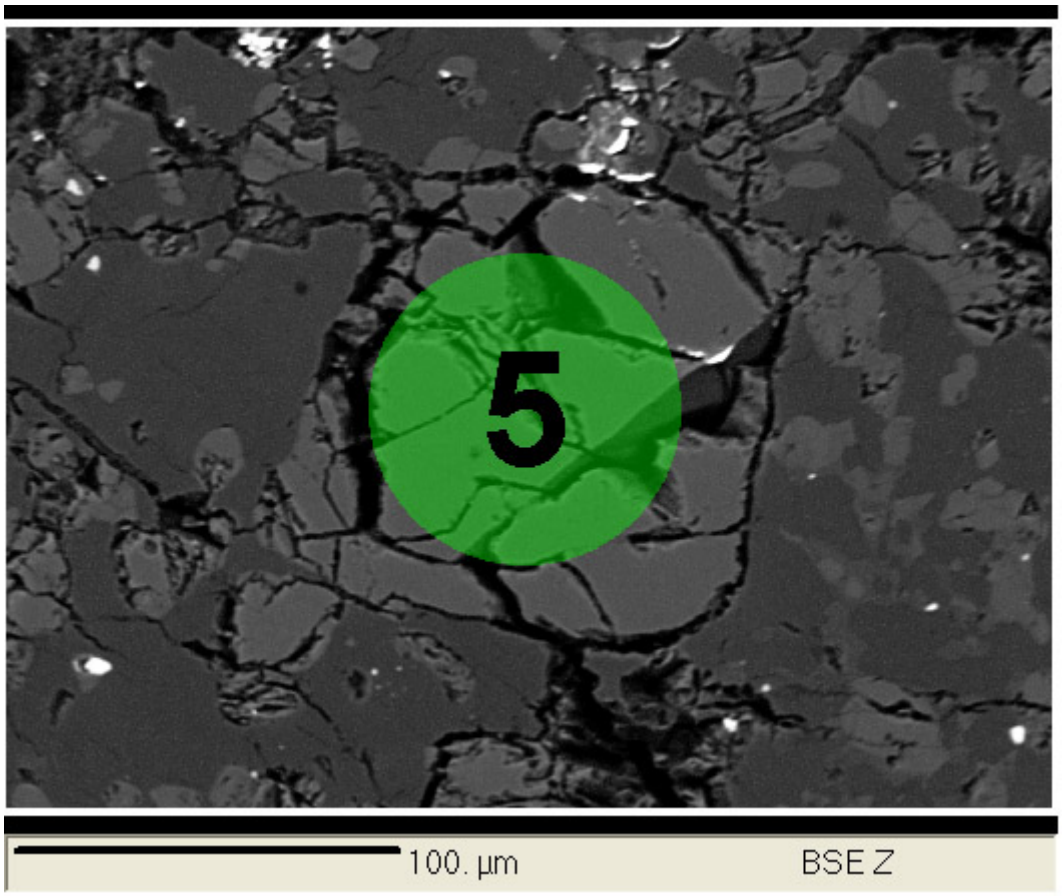

Figure B18: Detailed location of 84 µm olivine ablation point 5.

Table B16: Trace element content (ppm) from area shown in Figure B18

Spot	olv 5	1σ
Size	84µm	
Co	77.23	2.94
Ni	140.65	5.79
Cu	6.41	0.29
Ga	0.24	0.015
Sr	2.97	0.13
Y	0.250	0.016
Zr	0.79	0.068
Nb	0.029	0.0031
Ba	7.91	0.3
Hf	0.022	0.0035
Ta	b.d.	-
Th	0.0075	0.0013
U	0.0198	0.0014
La	0.028	0.0026
Ce	0.091	0.0058
Pr	0.008	0.001
Nd	0.039	0.0053
Sm	0.022	0.0042
Eu	0.003	0.001
Gd	0.016	0.0036
Tb	0.001	0.00057
Dy	0.028	0.0045
Ho	0.009	0.0012
Er	0.038	0.0048
Tm	0.012	0.0014
Yb	0.122	0.0087
Lu	0.029	0.0023

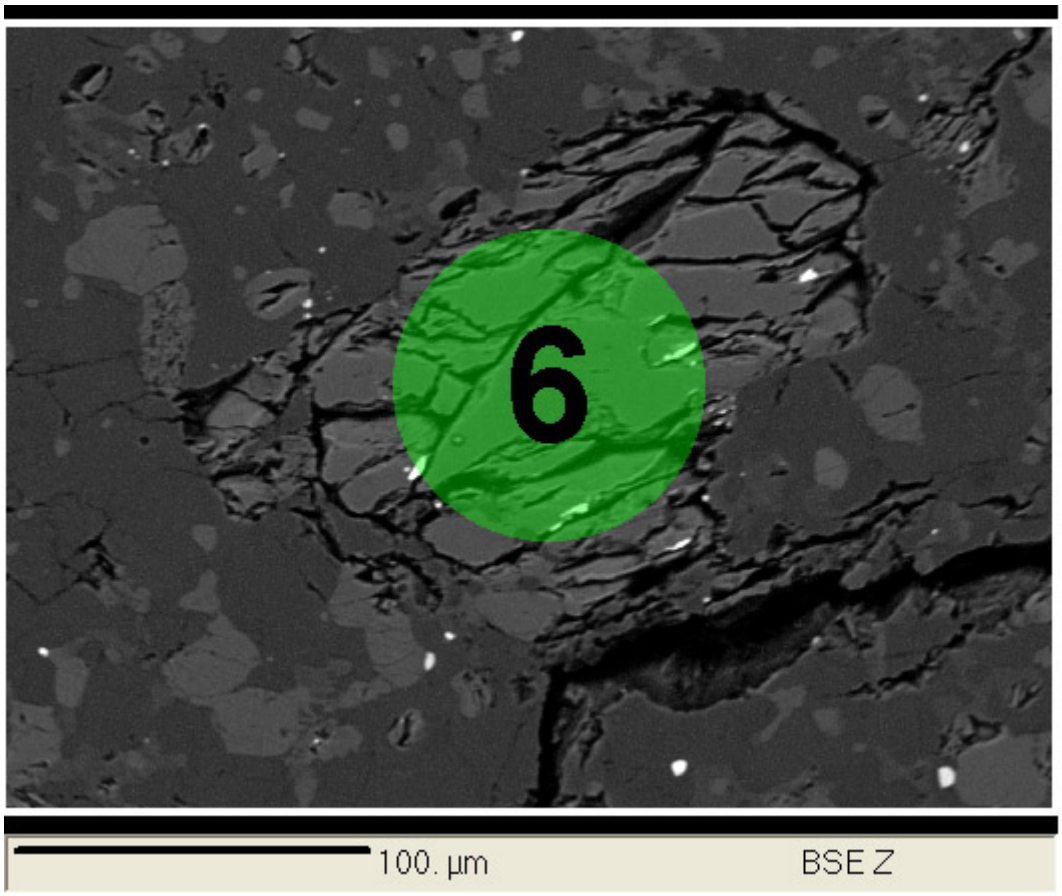

Figure B19: Detailed location of 84 µm olivine ablation point 6.

Table B17: Trace element content (ppm) from area shown in Figure B19

Spot	olv 6	1σ
Size	84μm	
Co	82.26	3.21
Ni	137.13	6
Cu	6.88	0.32
Ga	0.55	0.031
Sr	5.07	0.24
Y	0.469	0.03
Zr	3.42	0.21
Nb	0.301	0.017
Ba	5.14	0.2
Hf	0.086	0.0082
Ta	0.0177	0.0021
Th	0.0293	0.0033
U	0.0133	0.0013
La	0.057	0.0049
Ce	0.173	0.011
Pr	0.018	0.0019
Nd	0.188	0.015
Sm	0.017	0.0056
Eu	0.018	0.0023
Gd	0.037	0.0058
Tb	0.003	0.001
Dy	0.046	0.0066
Ho	0.019	0.0021
Er	0.090	0.0098
Tm	0.017	0.0021
Yb	0.165	0.012
Lu	0.045	0.0037

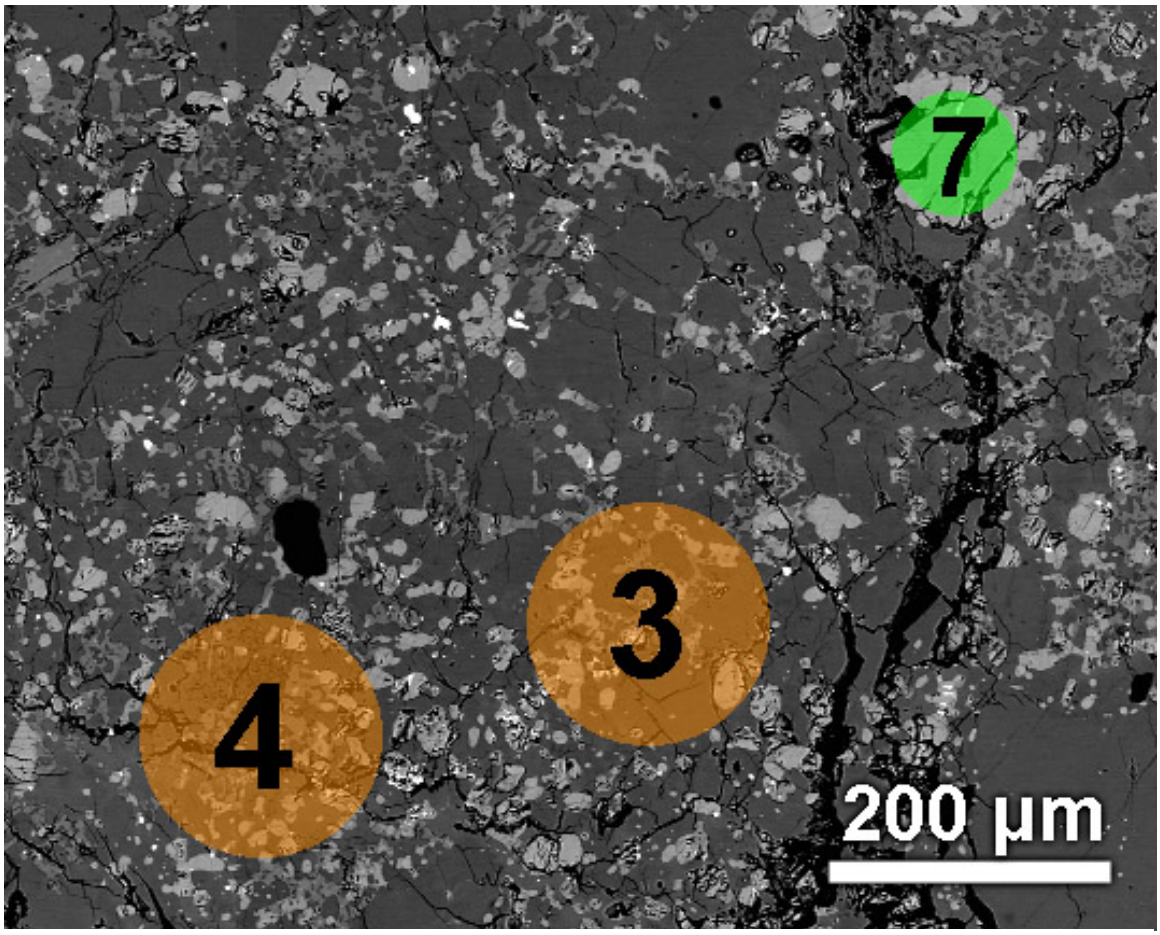

Figure B20: Detailed locations of 84 µm olivine ablation point 7 and 176 µm bulk ablation points 3 and 4.

Table B18: Trace element content (ppm) from areas shown in Figure B20

Spot	olv 7	1σ	bulk 3	1σ	bulk 4	1σ
Size	84μm		176μm		176μm	
Co	79.97	3.18	26.25	1.37	22.14	1.26
Ni	137.70	6.23	56.24	3.23	73.94	4.54
Cu	11.87	0.56	5.89	0.36	8.12	0.54
Ga	2.68	0.13	2.91	0.19	2.65	0.19
Sr	25.07	1.21	128.12	6.54	144.99	8.05
Y	1.333	0.084	8.385	0.72	6.820	0.65
Zr	3.18	0.2	20.17	1.76	16.58	1.61
Nb	0.296	0.017	1.003	0.062	0.863	0.058
Ba	40.89	1.59	38.16	1.99	76.69	4.31
Hf	0.066	0.0074	0.553	0.056	0.459	0.051
Ta	0.0168	0.0022	0.0541	0.005	0.0465	0.0044
Th	0.0592	0.0056	0.1514	0.014	0.1309	0.013
U	0.0642	0.0039	0.0420	0.0028	0.0758	0.0048
La	0.422	0.026	1.022	0.075	0.942	0.076
Ce	1.093	0.063	2.867	0.14	2.509	0.13
Pr	0.135	0.0087	0.445	0.027	0.381	0.025
Nd	0.624	0.038	2.412	0.16	2.012	0.14
Sm	0.148	0.014	0.884	0.065	0.664	0.052
Eu	0.048	0.0042	0.610	0.044	0.582	0.045
Gd	0.190	0.015	1.157	0.096	0.848	0.077
Tb	0.030	0.0026	0.211	0.019	0.164	0.016
Dy	0.175	0.015	1.423	0.12	1.142	0.11
Ho	0.045	0.0041	0.297	0.026	0.247	0.024
Er	0.130	0.013	0.900	0.079	0.766	0.074
Tm	0.023	0.0027	0.119	0.012	0.105	0.012
Yb	0.217	0.016	0.864	0.069	0.722	0.063
Lu	0.036	0.0033	0.113	0.011	0.108	0.011

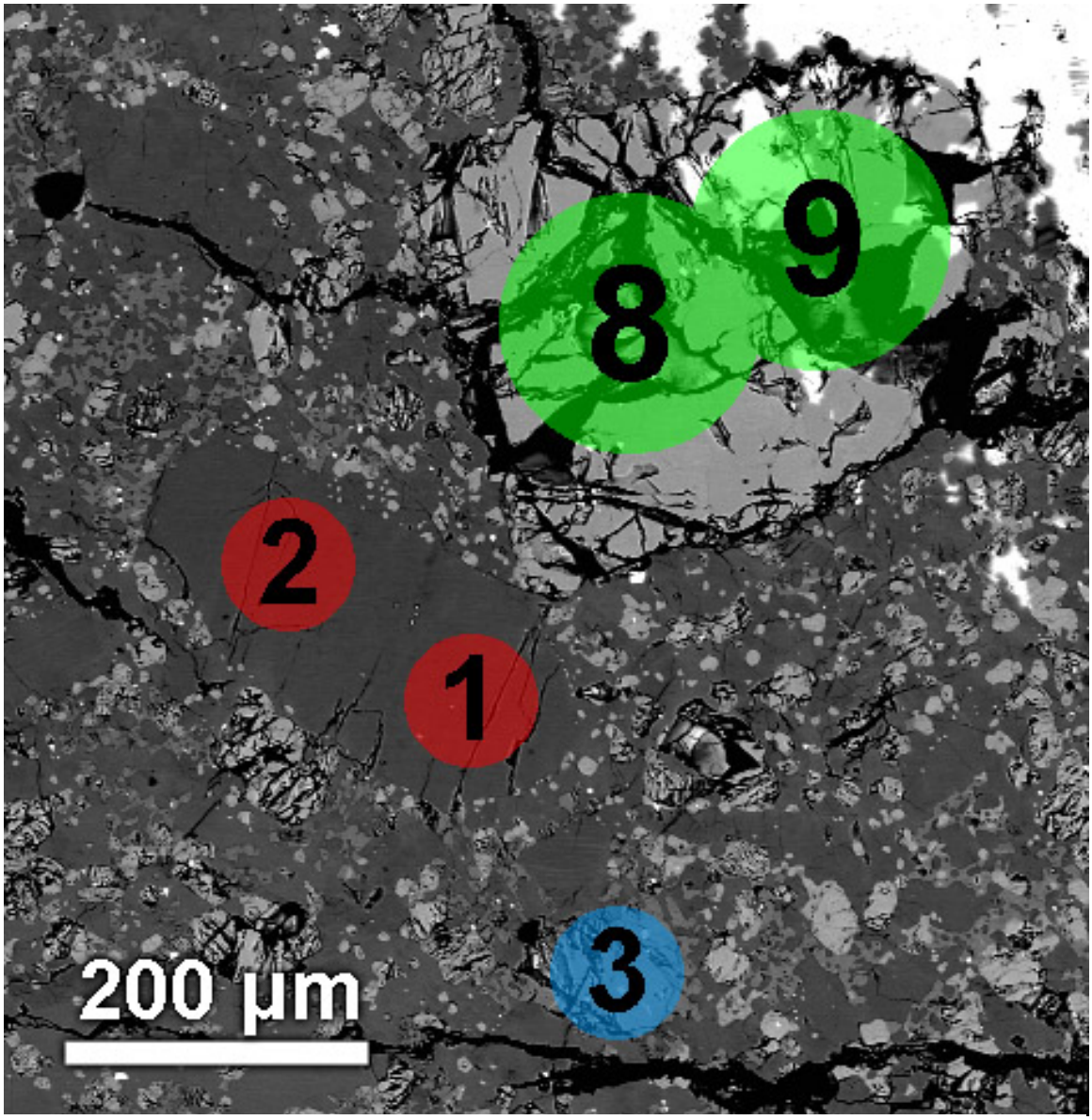

Figure B21: Detailed locations of 176 µm olivine ablation spots 8 and 9, 84 µm plagioclase spots 1 and 2, and 84 µm pyroxene ablation spot 3.

Table B19: Trace element content (ppm) from areas shown in Figure B21

Spot	pyx 3	1σ	plag 1	1σ	plag 2	1σ	olv 8	1σ	olv 9	1σ
Size	84µm		84µm		84µm		176µm		176µm	
Co	32.63	1.31	0.11	0.01	0.22	0.019	77.01	3.79	77.33	3.85
Ni	35.13	1.83	1.98	0.43	3.55	0.81	118.78	6.14	122.34	6.41
Cu	8.22	0.4	0.19	0.022	0.55	0.049	6.38	0.36	6.28	0.36
Ga	1.33	0.068	0.89	0.047	1.52	0.08	0.34	0.022	1.04	0.066
Sr	16.72	0.82	63.35	3.3	115.60	6.12	7.39	0.36	3.96	0.19
Y	13.806	0.85	0.132	0.0099	0.277	0.021	1.214	0.098	1.280	0.1
Zr	27.19	1.58	0.33	0.037	0.47	0.064	3.25	0.27	3.79	0.32
Nb	0.527	0.029	0.064	0.0045	0.030	0.0035	0.472	0.027	0.419	0.024
Ba	19.31	0.76	3.41	0.14	8.96	0.37	13.11	0.65	7.80	0.39
Hf	0.646	0.038	0.007	0.0016	b.d.	-	0.085	0.0083	0.089	0.0088
Ta	0.0448	0.0039	0.0014	0.00052	0.0034	0.00087	0.0240	0.002	0.0205	0.0018
Th	0.1909	0.015	0.0064	0.00091	0.0067	0.0013	0.0450	0.0039	0.0850	0.0073
U	0.0443	0.0029	0.0018	0.00028	0.0018	0.00039	0.0228	0.0013	0.0205	0.0012
La	0.309	0.019	0.117	0.0077	0.327	0.021	0.106	0.0074	0.096	0.0069
Ce	1.198	0.07	0.287	0.017	0.760	0.046	0.312	0.015	0.290	0.014
Pr	0.215	0.013	0.038	0.0027	0.089	0.006	0.039	0.0024	0.039	0.0024
Nd	1.193	0.067	0.183	0.012	0.413	0.026	0.205	0.014	0.195	0.013
Sm	0.527	0.035	0.040	0.0046	0.101	0.0099	0.060	0.0052	0.063	0.0054
Eu	0.065	0.005	0.302	0.015	0.554	0.028	0.009	0.00091	0.005	0.00068
Gd	0.993	0.055	0.033	0.0038	0.091	0.0081	0.093	0.008	0.098	0.0084
Tb	0.226	0.013	0.006	0.00069	0.012	0.0013	0.017	0.0015	0.021	0.0019
Dy	1.990	0.12	0.024	0.0033	0.066	0.007	0.132	0.011	0.158	0.013
Ho	0.492	0.034	0.006	0.00076	0.010	0.0013	0.040	0.0034	0.044	0.0038
Er	1.715	0.11	0.009	0.002	0.020	0.004	0.157	0.013	0.172	0.015
Tm	0.252	0.021	0.003	0.00053	0.002	0.00078	0.033	0.0032	0.035	0.0035
Yb	1.834	0.1	0.011	0.0019	0.025	0.0036	0.269	0.02	0.277	0.021
Lu	0.307	0.02	0.001	0.00041	0.003	0.00071	0.062	0.0052	0.065	0.0055

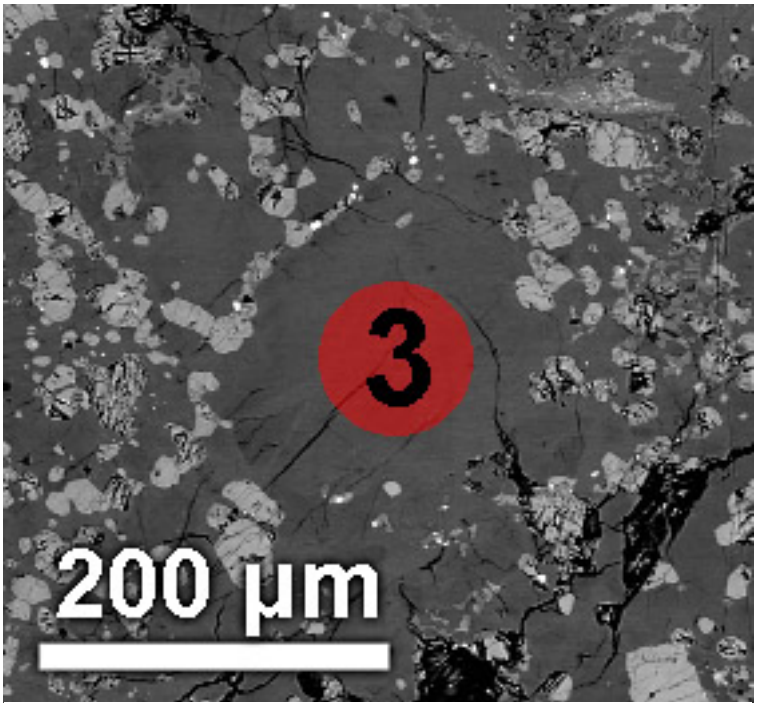

Figure B22: Detailed location of 84 µm plagioclase spot 3.

Table B20: Trace element content (ppm) from area shown in Figure B22

Spot Size	plag 3 84μm	1σ
Co	0.21	0.016
Ni	6.39	0.72
Cu	0.34	0.035
Ga	1.63	0.086
Sr	104.10	5.6
Y	0.152	0.012
Zr	b.d.	-
Nb	0.026	0.0029
Ba	8.38	0.35
Hf	b.d.	-
Ta	b.d.	-
Th	0.0026	0.00073
U	0.0008	0.00028
La	0.189	0.013
Ce	0.382	0.024
Pr	0.050	0.0036
Nd	0.232	0.016
Sm	0.040	0.0057
Eu	0.521	0.027
Gd	0.037	0.005
Tb	0.005	0.00078
Dy	0.033	0.0046
Ho	0.005	0.00087
Er	0.016	0.0034
Tm	b.d.	-
Yb	0.019	0.0031
Lu	0.002	0.00064

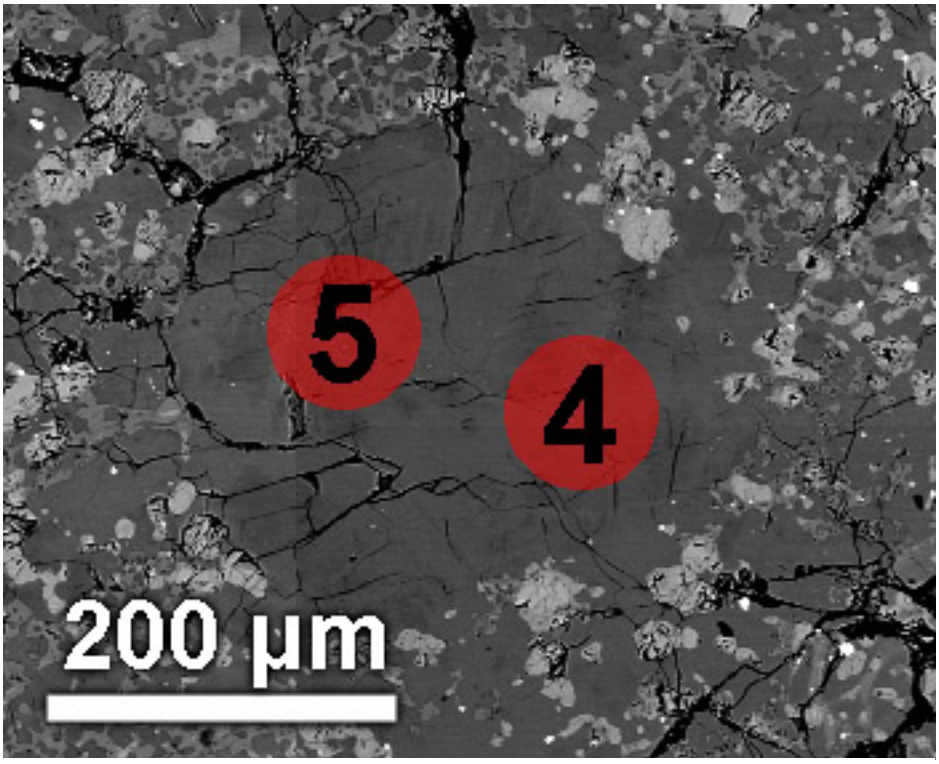

Figure B23: Detailed locations of 84 µm plagioclase ablation spots 4 and 5.

Table B21: Trace element content (ppm) from areas shown in Figure B23

Spot Size	plag 4 84μm	1σ	plag 5 84μm	1σ
Co	0.40	0.027	0.37	0.026
Ni	20.86	1.43	13.38	1.18
Cu	0.90	0.068	1.00	0.071
Ga	2.45	0.13	2.01	0.11
Sr	132.85	7.26	143.82	7.98
Y	0.097	0.0098	0.109	0.011
Zr	0.52	0.075	0.21	0.067
Nb	0.010	0.0029	0.014	0.0036
Ba	17.56	0.74	24.77	1.06
Hf	0.053	0.0062	0.011	0.0043
Ta	b.d.	-	b.d.	-
Th	0.0037	0.0011	0.0052	0.0013
U	0.0035	0.00058	0.0030	0.00057
La	0.078	0.0063	0.086	0.007
Ce	0.169	0.012	0.216	0.015
Pr	0.031	0.0027	0.027	0.0025
Nd	0.096	0.01	0.089	0.011
Sm	0.030	0.0059	b.d.	-
Eu	0.602	0.032	0.658	0.035
Gd	0.025	0.0047	0.046	0.0065
Tb	0.004	0.00095	b.d.	-
Dy	b.d.	-	0.028	0.0058
Ho	0.006	0.0011	0.004	0.00099
Er	b.d.	-	b.d.	-
Tm	b.d.	-	b.d.	-
Yb	b.d.	-	0.022	0.0042
Lu	b.d.	-	b.d.	-

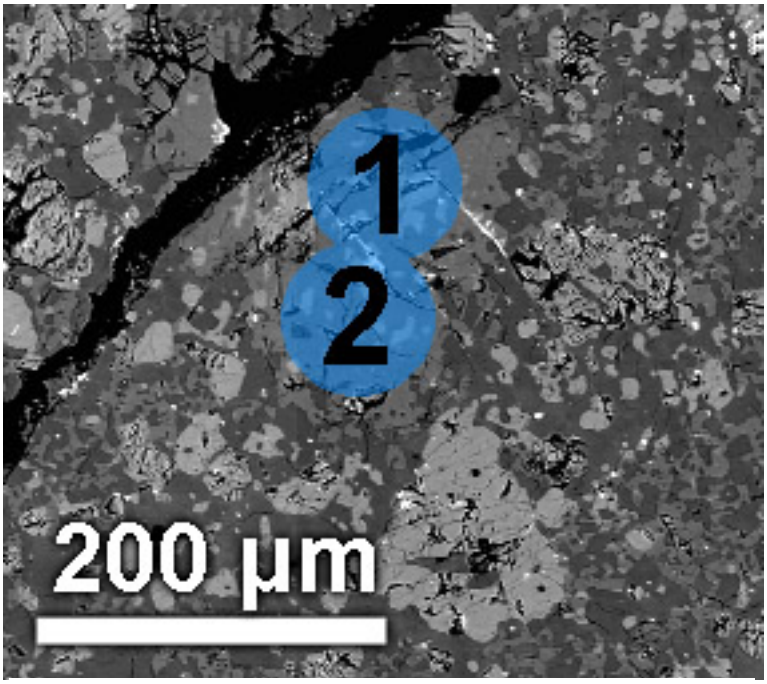

Figure B24: Detailed locations of 84 µm pyroxene ablation locations 1 and 2.

Table B22: Trace element content (ppm) from areas shown in Figure B24

Spot Size	pyx 1 84µm	1σ	pyx 2 84µm	1σ
Co	39.76	1.56	33.21	1.31
Ni	166.85	7.3	37.31	1.86
Cu	8.74	0.41	5.62	0.27
Ga	2.27	0.11	1.24	0.063
Sr	7.84	0.37	9.40	0.45
Y	17.680	1.04	23.325	1.39
Zr	39.19	2.19	55.87	3.15
Nb	0.646	0.033	0.870	0.044
Ba	12.92	0.5	9.54	0.38
Hf	1.224	0.064	1.942	0.1
Ta	0.0410	0.0034	0.0572	0.0044
Th	0.3426	0.025	0.2258	0.017
U	0.0809	0.0046	0.0526	0.0033
La	0.532	0.031	0.538	0.032
Ce	2.130	0.12	2.803	0.16
Pr	0.400	0.022	0.541	0.03
Nd	2.215	0.11	3.346	0.17
Sm	0.933	0.055	1.620	0.091
Eu	0.038	0.0033	0.055	0.0041
Gd	1.695	0.085	2.517	0.13
Tb	0.345	0.018	0.502	0.025
Dy	2.805	0.15	3.712	0.2
Ho	0.627	0.041	0.834	0.055
Er	1.988	0.12	2.663	0.16
Tm	0.334	0.025	0.385	0.03
Yb	2.244	0.12	2.561	0.14
Lu	0.365	0.022	0.387	0.024

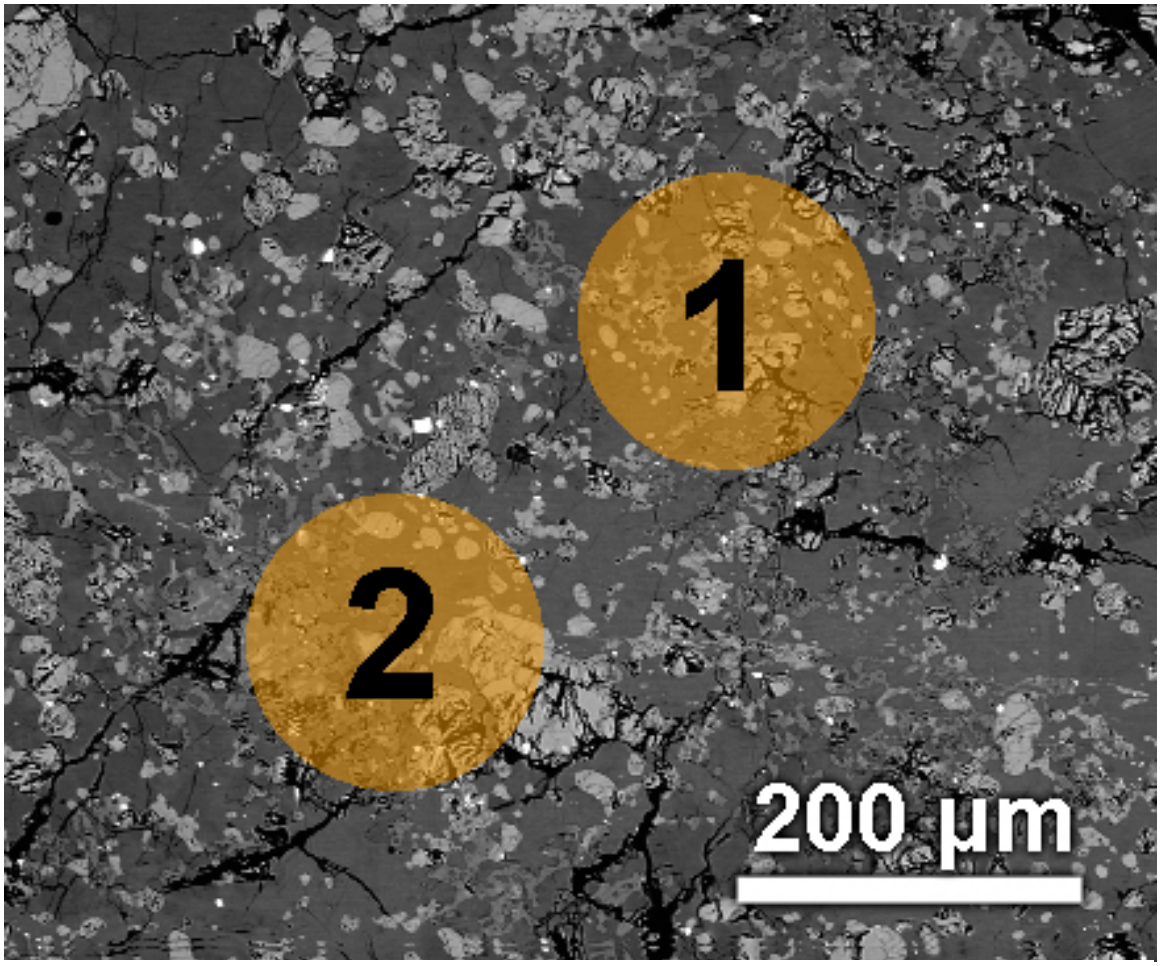

Figure B25: Detailed locations of 176 µm bulk NWA 5744 ablation locations 1 and 2.

Table B23: Trace element content (ppm) from areas shown in Figure B25

Spot Size	bulk 1 176µm	1σ	bulk 2 176µm	1σ
Co	23.74	1.2	20.94	1.08
Ni	63.47	3.41	53.67	2.98
Cu	5.43	0.32	6.09	0.36
Ga	1.73	0.11	1.76	0.12
Sr	93.41	4.63	72.00	3.62
Y	4.293	0.36	7.034	0.59
Zr	11.27	0.95	16.59	1.42
Nb	0.653	0.039	0.763	0.046
Ba	24.63	1.25	28.12	1.45
Hf	0.301	0.029	0.442	0.044
Ta	0.0324	0.0028	0.0450	0.004
Th	0.0994	0.0088	0.1403	0.013
U	0.0189	0.0012	0.0228	0.0016
La	0.759	0.053	0.680	0.049
Ce	1.744	0.082	1.885	0.09
Pr	0.263	0.015	0.306	0.018
Nd	1.253	0.079	1.675	0.11
Sm	0.442	0.031	0.601	0.043
Eu	0.455	0.031	0.344	0.024
Gd	0.586	0.047	0.893	0.073
Tb	0.103	0.0089	0.167	0.015
Dy	0.741	0.061	1.131	0.095
Ho	0.162	0.014	0.249	0.022
Er	0.474	0.04	0.771	0.066
Tm	0.070	0.007	0.104	0.011
Yb	0.463	0.035	0.773	0.06
Lu	0.070	0.0062	0.118	0.011

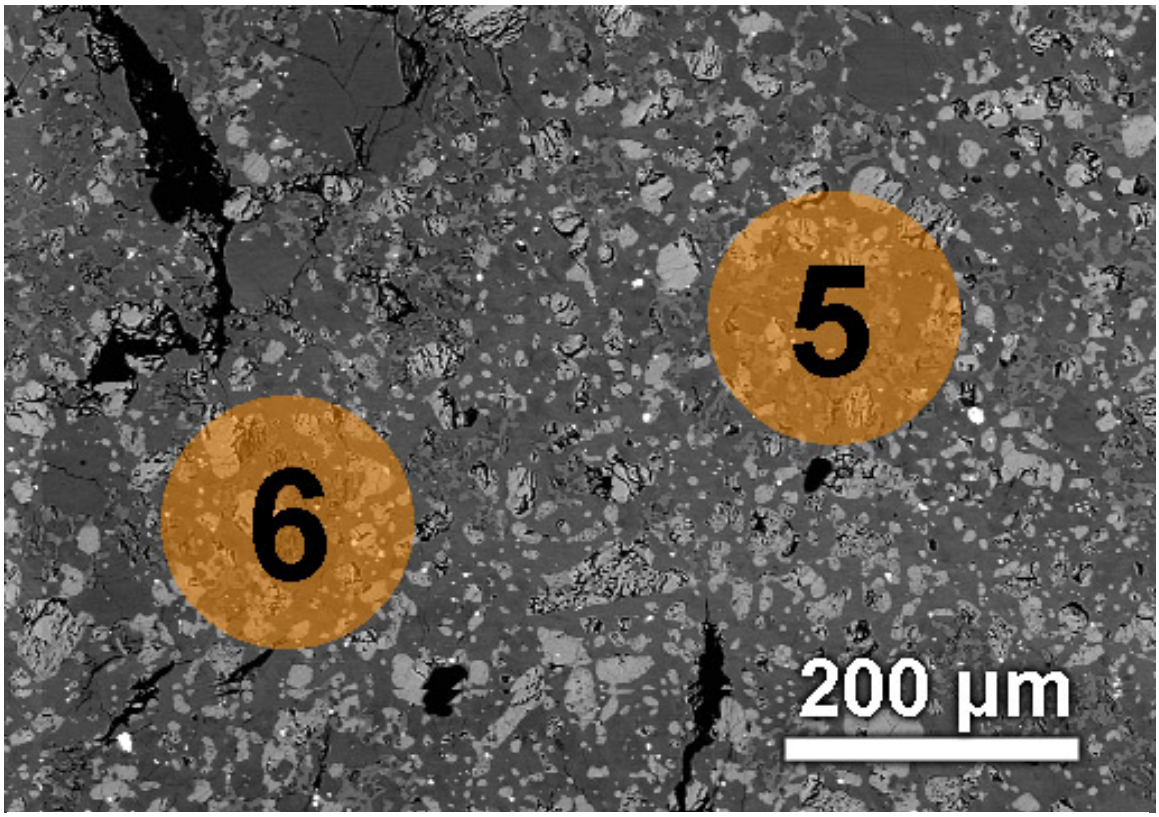

Figure B26: Detailed locations of 176 µm bulk NWA 5744 ablation locations 5 and 6.

Table B24: Trace element content (ppm) from areas shown in Figure B26

Spot Size	bulk 5 176µm	1σ	bulk 6 176µm	1σ
Co	21.27	1.23	25.26	1.49
Ni	82.66	5.16	118.93	7.54
Cu	5.47	0.37	5.21	0.36
Ga	2.14	0.16	1.68	0.13
Sr	107.32	6.07	79.19	4.57
Y	4.370	0.43	2.934	0.3
Zr	11.04	1.09	8.38	0.85
Nb	0.736	0.051	0.546	0.038
Ba	27.59	1.58	18.74	1.1
Hf	0.290	0.033	0.196	0.023
Ta	0.0367	0.0036	0.0252	0.0026
Th	0.1017	0.011	0.0609	0.0066
U	0.0262	0.0018	0.0137	0.0011
La	0.696	0.058	0.518	0.044
Ce	1.816	0.096	1.416	0.076
Pr	0.266	0.018	0.194	0.013
Nd	1.174	0.086	0.904	0.068
Sm	0.338	0.028	0.299	0.025
Eu	0.518	0.041	0.403	0.033
Gd	0.469	0.044	0.355	0.035
Tb	0.092	0.0093	0.069	0.0073
Dy	0.727	0.071	0.482	0.049
Ho	0.161	0.016	0.111	0.012
Er	0.531	0.053	0.317	0.032
Tm	0.081	0.0094	0.046	0.0056
Yb	0.595	0.053	0.348	0.032
Lu	0.089	0.0092	0.052	0.0056

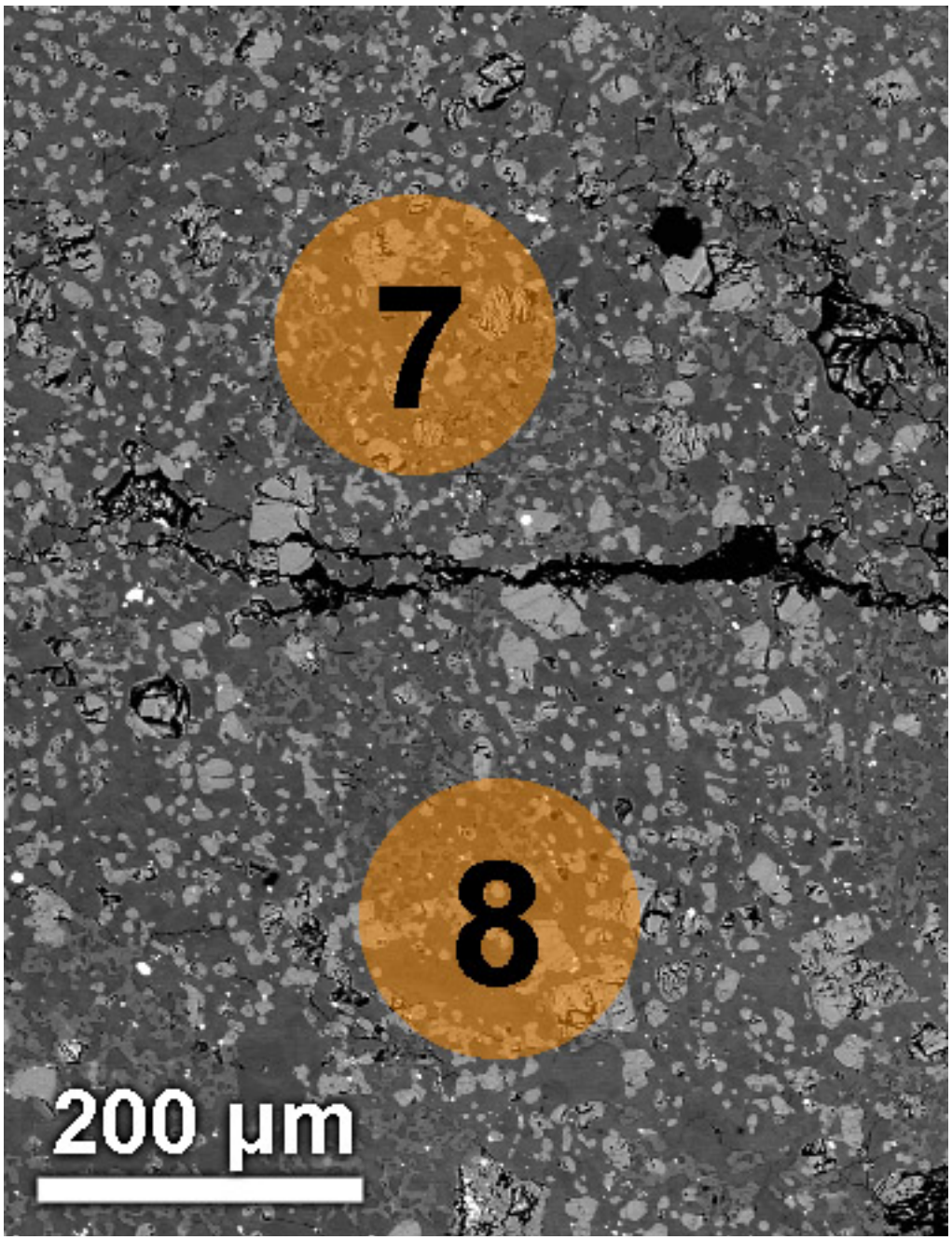

Figure B27: Detailed locations of 176 µm bulk NWA 5744 ablation locations 7 and 8.

Table B25: Trace element content (ppm) from areas shown in Figure B27

Spot Size	bulk 7 176µm	1σ	bulk 8 176µm	1σ
Co	23.99	1.44	23.93	1.46
Ni	73.45	4.77	112.11	7.41
Cu	4.68	0.33	6.43	0.47
Ga	1.78	0.14	1.60	0.13
Sr	85.14	5.01	78.70	4.72
Y	4.899	0.51	7.084	0.75
Zr	13.66	1.42	18.73	1.98
Nb	0.647	0.046	0.761	0.055
Ba	20.79	1.24	23.22	1.41
Hf	0.377	0.045	0.507	0.062
Ta	0.0342	0.0035	0.0405	0.0041
Th	0.0725	0.0079	0.1125	0.013
U	0.0237	0.0017	0.0288	0.0021
La	0.573	0.05	0.625	0.055
Ce	1.868	0.1	2.099	0.11
Pr	0.277	0.019	0.344	0.024
Nd	1.407	0.11	1.886	0.15
Sm	0.534	0.045	0.727	0.061
Eu	0.409	0.034	0.370	0.031
Gd	0.713	0.069	0.994	0.098
Tb	0.126	0.013	0.186	0.02
Dy	0.852	0.087	1.290	0.13
Ho	0.185	0.019	0.259	0.028
Er	0.552	0.057	0.776	0.081
Tm	0.075	0.0091	0.106	0.013
Yb	0.476	0.044	0.682	0.064
Lu	0.065	0.007	0.100	0.011

Appendix C:

QUE 93069 Major and Trace Element Data

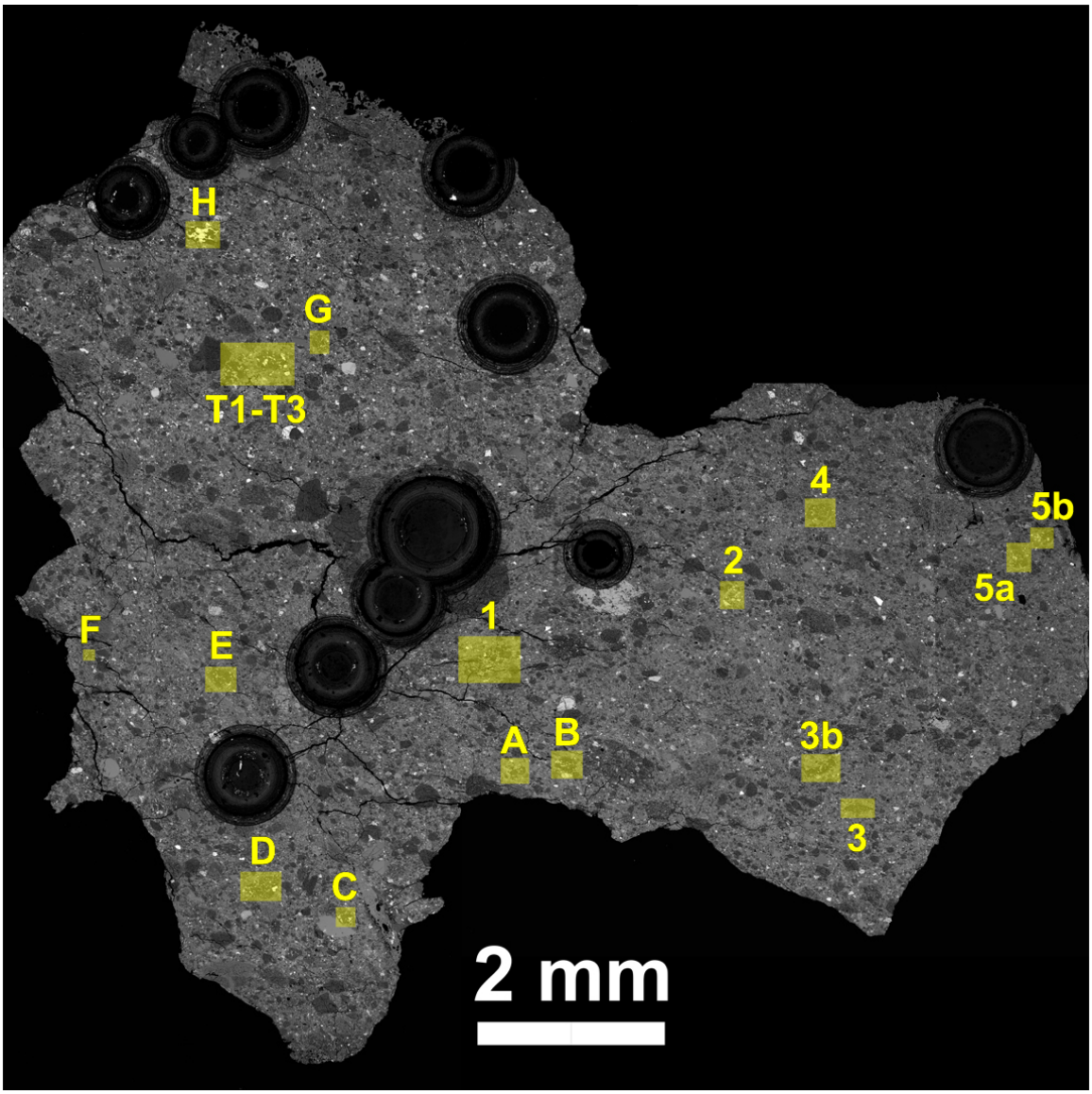

Figure C1: BSE map of thick section QUE 93069,52 with the locations labeled for each clast analyzed in this study. Included are clasts 4, 5b, A, H, and T2, which were analyzed but determined to be either primary igneous clasts or impact melt clasts, and on that basis were excluded from the study.

Table C1: Major element composition of each clast analyzed in QUE 93069,58

Clast	1									
	Plag	1σ	Olv	1σ	OPX	1σ	Ti-Chrm	1σ	Ilm	1σ
Analyses	12		11		13		3		1	
SiO_2 (wt %)	43.78	0.26	37.19	0.29	52.77	0.38	0.07	0.02	19.56	0.17
TiO_2	0.04	0.03	0.05	0.03	0.76	0.04	12.90	0.14	29.41	0.22
Al_2O_3	34.97	0.38	b.d.	-	0.78	0.03	7.72	0.12	0.26	0.03
FeO	0.35	0.06	26.45	0.46	16.24	0.33	37.40	0.58	29.55	0.49
MgO	0.04	0.02	35.66	0.35	24.47	0.33	4.34	0.09	13.54	0.18
CaO	19.55	0.37	0.17	0.03	3.48	0.10	0.21	0.03	1.03	0.06
Na_2O	0.34	0.04	b.d.	-	b.d.	-	b.d.	-	b.d.	-
K_2O	0.05	0.02	b.d.	-	b.d.	-	b.d.	-	b.d.	-
P_2O_5	b.d.	-	b.d.	-	b.d.	-	b.d.	-	b.d.	-
MnO	b.d.	-	0.26	0.06	0.31	0.06	0.29	0.07	0.47	0.07
Cr_2O_3	b.d.	-	0.07	0.05	0.37	0.06	33.19	0.38	0.96	0.07
Total	99.11		99.83		99.18		96.12		94.77	
An	96.6									
Mg#	16.4		70.6		72.9		17.1		45.0	
En					67.8					
Fs					25.2					
Wo					6.9					

Table C1, ctd: Major element composition of each clast analyzed in QUE 93069,58

Clast	2										3					
	Plag	1σ	Olv	1σ	OPX-M[1]	1σ	CPX-B[2]	1σ	Ilm	1σ	Plag	1σ	Olv	1σ	CPX	1σ
Analyses	3		4		2		3		2		3		2		1	
SiO_2 (wt %)	43.24	0.43	36.00	0.22	51.93	0.44	49.32	0.42	0.34	0.03	43.56	0.43	34.61	0.21	51.25	0.44
TiO_2	b.d.	-	0.08	0.03	0.82	0.06	1.02	0.07	51.50	0.51	b.d.	-	0.04	0.03	0.72	0.06
Al_2O_3	34.77	0.26	0.04	0.02	1.09	0.04	1.17	0.04	0.62	0.04	35.41	0.26	0.08	0.02	1.38	0.05
FeO	0.44	0.09	31.20	0.75	18.47	0.52	19.27	0.53	40.31	1.00	0.26	0.08	40.77	0.92	10.71	0.37
MgO	0.08	0.02	32.38	0.45	22.41	0.33	9.85	0.17	4.86	0.12	0.02	0.02	24.60	0.35	14.61	0.23
CaO	19.56	0.43	0.20	0.04	4.63	0.18	18.17	0.40	0.35	0.06	19.68	0.43	0.34	0.05	20.26	0.44
Na_2O	0.41	0.06	b.d.	-	b.d.	-	0.16	0.05	b.d.	-	0.37	0.06	b.d.	-	b.d.	-
K_2O	0.05	0.03	b.d.	-	b.d.	-	b.d.	-	b.d.	-	b.d.	-	b.d.	-	b.d.	-
P_2O_5	b.d.	-	0.08	0.05	b.d.	-	b.d.	-	b.d.	-	b.d.	-	b.d.	-	b.d.	-
MnO	b.d.	-	0.31	0.09	0.31	0.09	0.35	0.08	0.46	0.12	b.d.	-	0.48	0.09	0.28	0.08
Cr_2O_3	b.d.	-	0.07	0.04	0.43	0.06	0.40	0.06	0.61	0.07	b.d.	-	b.d.	-	0.35	0.06
Total	98.55		100.37		100.10		99.70		99.05		99.30		100.92		99.54	
An	96.1										96.6					
Mg#	24.7		64.9		68.4		47.7		17.7		13.0		51.8		70.9	
En					62.1		29.2								41.5	
Fs					28.7		32.1								17.1	
Wo					9.2		38.7								41.4	

[1]OPX-M refers to the pigeonite present throughout the main portion of the clast

[2]CPX-B refers to the augite present only in the dual pyroxene attached to the bottom of the clast

Table C1, ctd: Major element composition of each clast analyzed in QUE 93069,58

Clast	3b						4							
	Plag	1σ	OPX	1σ	CPX	1σ	Plag	1σ	Olv	1σ	OPX	1σ	CPX	1σ
Analyses	4		2		2		2		2		1		2	
SiO_2 (wt %)	43.98	0.44	51.94	0.44	50.58	0.30	42.97	0.43	36.28	0.22	50.67	0.43	50.62	0.43
TiO_2	b.d.	-	0.51	0.05	1.14	0.07	b.d.	-	0.05	0.03	0.78	0.06	0.78	0.06
Al_2O_3	35.23	0.26	0.44	0.03	1.57	0.24	35.14	0.26	0.11	0.02	1.70	0.05	1.90	0.06
FeO	0.20	0.08	22.91	0.61	10.39	0.27	0.27	0.08	30.78	0.74	16.04	0.48	12.70	0.41
MgO	0.05	0.02	21.03	0.31	14.84	0.14	0.08	0.02	33.12	0.46	20.22	0.30	18.40	0.28
CaO	19.70	0.44	2.49	0.13	19.73	0.25	19.54	0.43	0.25	0.04	7.94	0.24	13.92	0.34
Na_2O	0.38	0.06	b.d.	-	b.d.	-	0.35	0.05	b.d.	-	0.06	0.04	0.05	0.04
K_2O	b.d.	-	b.d.	-	b.d.	-	b.d.	-	b.d.	-	b.d.	-	b.d.	-
P_2O_5	b.d.	-	0.05	0.05	b.d.	-	b.d.	-	b.d.	-	b.d.	-	b.d.	-
MnO	b.d.	-	0.46	0.09	b.d.	-	b.d.	-	0.31	0.08	0.30	0.08	0.26	0.08
Cr_2O_3	b.d.	-	0.14	0.05	0.40	0.07	b.d.	-	0.10	0.04	0.34	0.06	0.66	0.07
Total	99.54		99.97		98.65		98.35		101.01		98.03		99.29	
An	96.5						96.7							
Mg#	30.6		62.1		71.8		35.9		65.7		69.2		72.1	
En			58.9		42.6						57.9		51.8	
Fs			36.0		16.7						25.8		20.1	
Wo			5.0		40.7						16.3		28.1	

Table C1, ctd: Major element composition of each clast analyzed in QUE 93069,58

Clast	5a						5b						A	
	Plag	1σ	Olv	1σ	OPX	1σ	Plag	1σ	Olv	1σ	OPX	1σ	Plag	1σ
Analyses	1		1		1		2		1		1		3	
SiO_2 (wt %)	44.12	0.44	37.01	0.22	52.26	0.45	43.67	0.43	36.52	0.22	52.50	0.45	43.24	0.24
TiO_2	b.d.	-	0.04	0.03	0.91	0.07	b.d.	-	0.06	0.03	0.81	0.06	0.03	0.03
Al_2O_3	34.85	0.26	0.05	0.02	0.96	0.04	35.12	0.26	0.09	0.02	0.98	0.04	35.20	0.41
FeO	0.26	0.08	30.17	0.73	18.16	0.52	0.32	0.08	29.23	0.72	16.77	0.49	0.25	0.06
MgO	0.07	0.02	33.46	0.46	23.28	0.34	0.09	0.02	35.12	0.48	23.08	0.34	b.d.	-
CaO	19.71	0.44	0.20	0.04	3.81	0.16	19.35	0.43	0.27	0.04	5.65	0.20	19.16	0.40
Na_2O	0.53	0.07	b.d.	-	b.d.	-	0.51	0.06	b.d.	-	b.d.	-	b.d.	-
K_2O	0.05	0.04	b.d.	-	b.d.	-	0.07	0.04	b.d.	-	b.d.	-	0.04	0.02
P_2O_5	b.d.	-	b.d.	-	b.d.	-	0.06	0.05	b.d.	-	b.d.	-	b.d.	-
MnO	b.d.	-	0.27	0.08	0.31	0.08	b.d.	-	0.31	0.08	0.29	0.09	b.d.	-
Cr_2O_3	b.d.	-	0.12	0.04	0.40	0.06	b.d.	-	0.07	0.04	0.43	0.06	b.d.	-
Total	99.59		101.32		100.09		99.19		101.68		100.50		97.92	
An	95.1						95.0						95.9	
Mg#	31.5		66.4		69.6		32.1		68.2		71.1		52.0	
En					64.3						63.1			
Fs					28.1						25.7			
Wo					7.6						11.1			

Table C1, ctd: Major element composition of each clast analyzed in QUE 93069,58

Clast	B						C									
	Plag	1σ	Olv	1σ	OPX	1σ	Plag	1σ	Olv	1σ	CPX	1σ	OPX	1σ	Ilm	1σ
Analyses	6		2		5		2		1		1		4		1	
SiO_2 (wt %)	43.67	0.25	34.95	0.29	52.96	0.31	42.72	0.24	35.42	0.29	51.07	0.30	52.02	0.31	1.49	0.03
TiO_2	b.d.	-	0.04	0.02	0.23	0.03	b.d.	-	0.05	0.02	0.70	0.04	0.49	0.04	51.27	0.33
Al_2O_3	35.86	0.42	0.08	0.02	0.69	0.03	35.90	0.42	0.05	0.02	1.43	0.04	0.98	0.03	0.12	0.02
FeO	0.30	0.06	39.16	0.55	24.13	0.48	0.28	0.06	40.33	0.57	13.12	0.31	20.64	0.43	42.09	0.72
MgO	0.03	0.01	26.15	0.21	19.86	0.27	0.02	0.01	25.26	0.21	14.59	0.21	18.76	0.26	2.62	0.05
CaO	19.59	0.41	0.25	0.03	2.24	0.09	19.56	0.41	0.22	0.03	17.64	0.31	6.66	0.16	0.44	0.03
Na_2O	0.36	0.04	0.05	0.03	b.d.	-	0.39	0.04	0.06	0.03	0.04	0.03	b.d.	-	0.08	0.04
K_2O	b.d.	-	b.d.	-	b.d.	-	0.03	0.02	0.04	0.03	b.d.	-	b.d.	-	b.d.	-
P_2O_5	b.d.	-	0.07	0.03	b.d.	-	b.d.	-	b.d.	-	b.d.	-	b.d.	-	b.d.	-
MnO	b.d.	-	0.44	0.06	0.46	0.06	b.d.	-	0.45	0.07	0.29	0.06	0.34	0.06	0.48	0.07
Cr_2O_3	b.d.	-	b.d.	-	0.11	0.05	b.d.	-	b.d.	-	0.42	0.06	0.28	0.06	0.07	0.04
Total	99.81		101.19		100.67		98.89		101.88		99.32		100.17		98.66	
An	96.7						96.4									
Mg#	12.6		54.3		59.5		11.3		52.7		66.5		61.8		10.0	
En					56.7						42.1		53.4			
Fs					38.7						21.3		33.0			
Wo					4.6						36.6		13.7			

Table C1, ctd: Major element composition of each clast analyzed in QUE 93069,58

Clast	D								E							
	Plag	1σ	OPX	1σ	CPX	1σ	Ilm	1σ	Plag	1σ	Olv	1σ	OPX	1σ	CPX	1σ
Analyses	2		1		1		1		2		3		1		1	
SiO_2 (wt %)	43.00	0.24	51.43	0.31	51.02	0.30	1.45	0.03	42.21	0.24	35.73	0.29	51.86	0.31	50.52	0.30
TiO_2	b.d.	-	0.33	0.04	0.44	0.04	51.10	0.33	0.03	0.03	0.07	0.02	0.88	0.05	1.29	0.05
Al_2O_3	35.66	0.42	0.38	0.02	0.89	0.03	0.80	0.03	35.77	0.42	0.10	0.02	1.13	0.03	2.04	0.05
FeO	0.32	0.06	27.11	0.53	13.57	0.32	42.77	0.73	0.32	0.06	35.13	0.51	20.15	0.42	11.84	0.29
MgO	0.14	0.01	17.54	0.24	13.66	0.19	2.13	0.05	0.09	0.01	28.55	0.23	19.77	0.27	15.38	0.22
CaO	19.17	0.40	2.78	0.10	18.84	0.33	0.74	0.04	19.53	0.41	0.33	0.03	5.51	0.14	17.69	0.31
Na_2O	0.49	0.04	b.d.	-	0.05	0.03	b.d.	-	0.28	0.04	b.d.	-	b.d.	-	0.05	0.03
K_2O	0.05	0.02	b.d.	-	b.d.	-	b.d.	-	0.03	0.02	b.d.	-	b.d.	-	b.d.	-
P_2O_5	b.d.	-	b.d.	-	b.d.	-	b.d.	-	b.d.	-	b.d.	-	0.05	0.03	b.d.	-
MnO	b.d.	-	0.50	0.07	0.29	0.06	0.45	0.07	0.05	0.04	0.42	0.06	0.37	0.06	0.24	0.06
Cr_2O_3	b.d.	-	0.11	0.05	0.27	0.06	b.d.	-	b.d.	-	0.08	0.04	0.42	0.06	0.57	0.07
Total	98.83		100.16		99.03		99.43		98.31		100.41		100.14		99.60	
An	95.3								97.3							
Mg#	21.7		53.6		64.2		8.1		33.7		59.2		63.6		69.9	
En			50.5		39.2								56.4		44.3	
Fs			43.8		21.9								32.3		19.1	
Wo			5.7		38.9								11.3		36.6	

Table C1, ctd: Major element composition of each clast analyzed in QUE 93069,58

Clast	F								G					
	Plag	1σ	OPX	1σ	Olv	1σ	Ilm	1σ	Plag	1σ	Olv	1σ	OPX	1σ
Analyses	1		1		1		1		3		3		2	
SiO_2 (wt %)	41.85	0.24	52.27	0.31	37.10	0.30	2.69	0.04	42.67	0.24	37.48	0.31	52.01	0.31
TiO_2	0.07	0.03	0.85	0.04	0.05	0.02	51.16	0.33	0.03	0.03	0.08	0.02	0.89	0.05
Al_2O_3	35.47	0.41	1.21	0.04	0.14	0.02	0.35	0.02	35.83	0.42	0.29	0.02	1.60	0.04
FeO	0.31	0.06	16.30	0.36	26.37	0.42	35.78	0.64	0.28	0.06	29.34	0.45	17.50	0.38
MgO	0.11	0.01	23.29	0.31	36.53	0.28	7.45	0.12	0.08	0.01	33.18	0.26	21.96	0.30
CaO	19.34	0.40	4.66	0.13	0.26	0.03	0.59	0.04	19.45	0.40	0.36	0.03	4.74	0.13
Na_2O	0.38	0.04	b.d.	-	b.d.	-	0.10	0.04	0.34	0.04	b.d.	-	0.04	0.03
K_2O	0.04	0.02	b.d.	-	b.d.	-	b.d.	-	b.d.	-	b.d.	-	b.d.	-
P_2O_5	b.d.	-	b.d.	-	b.d.	-	b.d.	-	b.d.	-	0.09	0.04	b.d.	-
MnO	b.d.	-	0.34	0.06	0.33	0.06	0.33	0.06	b.d.	-	0.32	0.06	0.34	0.06
Cr_2O_3	b.d.	-	0.40	0.06	0.06	0.04	0.82	0.06	b.d.	-	0.10	0.04	0.39	0.06
Total	97.59		99.31		100.84		99.25		98.67		101.25		99.47	
An	96.3								96.8					
Mg#	39.1		71.8		71.2		27.1		35.1		66.8		69.1	
En			65.1										62.4	
Fs			25.6										27.9	
Wo			9.4										9.7	

Table C1, ctd: Major element composition of each clast analyzed in QUE 93069,58

Clast	H								T1			
	Plag	1σ	OPX	1σ	CPX 1	1σ	CPX 2	1σ	Plag	1σ	OPX	1σ
Analyses	4		37		19		1		1		1	
SiO_2 (wt %)	42.35	0.24	48.19	0.29	48.26	0.29	50.94	0.30	43.86	0.28	52.46	0.31
TiO_2	b.d.	-	0.71	0.04	0.80	0.05	0.96	0.05	0.06	0.03	0.65	0.04
Al_2O_3	35.83	0.42	0.90	0.03	1.59	0.04	1.54	0.04	34.09	0.26	1.02	0.03
FeO	0.58	0.07	31.78	0.60	27.05	0.53	15.44	0.35	0.48	0.07	17.44	0.73
MgO	b.d.		8.41	0.13	7.91	0.12	15.36	0.22	0.15	0.02	22.90	0.31
CaO	19.47	0.40	8.37	0.18	12.98	0.25	14.27	0.27	19.16	0.43	4.49	0.12
Na_2O	0.36	0.04	0.04	0.03	0.04	0.03	b.d.	-	0.44	0.04	0.04	0.03
K_2O	b.d.	-	b.d.	-	b.d.	-	b.d.	-	0.05	0.03	0.03	0.02
P_2O_5	b.d.	-	b.d.	-	b.d.	-	b.d.	-	b.d.	-	b.d.	-
MnO	b.d.	-	0.48	0.07	0.40	0.06	0.31	0.06	b.d.	-	0.35	0.06
Cr_2O_3	b.d.	-	0.24	0.05	0.31	0.06	0.43	0.06	b.d.	-	0.34	0.04
Total	98.59		99.12		99.32		99.25		98.29		99.72	
An	96.7								95.7			
Mg#			32.1		34.3		64.0		35.9		70.1	
En			26.1		24.4		44.8				63.8	
Fs			55.3		46.8		25.3				27.2	
Wo			18.7		28.8		29.9				9.0	

Table C1, ctd: Major element composition of each clast analyzed in QUE 93069,58

Clast	T2		T3					
	Plag	1σ	Plag	1σ	OPX	1σ	CPX	1σ
Analyses	1		3		1		2	
SiO_2 (wt %)	43.25	0.27	44.00	0.28	50.14	0.30	49.68	0.30
TiO_2	b.d.	-	b.d.	-	0.78	0.04	1.07	0.05
Al_2O_3	34.47	0.26	34.57	0.27	0.87	0.03	1.29	0.03
FeO	0.29	0.06	0.39	0.06	24.22	1.00	16.40	0.69
MgO	0.10	0.02	0.04	0.01	14.98	0.21	11.55	0.17
CaO	19.05	0.43	19.05	0.43	7.57	0.16	17.83	0.26
Na_2O	0.32	0.04	0.48	0.04	0.03	0.03	0.05	0.03
K_2O	0.03	0.02	b.d.	-	b.d.	-	b.d.	-
P_2O_5	b.d.	-	b.d.	-	b.d.	-	b.d.	-
MnO	b.d.	-	b.d.	-	0.46	0.07	0.28	0.06
Cr_2O_3	b.d.	-	b.d.	-	0.49	0.04	0.42	0.05
Total	97.51		98.55		99.54		98.55	
An	96.9		95.5					
Mg#	37.2		16.0		52.5		55.7	
En					44.1		34.4	
Fs					40.0		27.4	
Wo					16.0		38.2	

Table C2: Bulk trace element abundance for each clast analyzed in QUE 93069,58

	BIR Ref	BIR Avg	%RSD	1	1σ	2	1σ	3	1σ	3b	1σ	4	1σ	5a	1σ
Spot (μm)				176		84		84		30		176		84	
Ablations		21		3		2		1		3		1		2	
Co (ppm)	52.5	58.22	4.04	35.36	3.44	32.92	4.74	6.71	1.00	4.31	0.98	6.19	0.61	14.86	2.45
Ni	179	174.72	3.62	164.81	13.90	330.83	41.11	17.82	3.51	14.34	6.05	41.44	3.79	82.25	11.84
Cu	121	128.91	3.58	8.95	0.94	10.26	1.56	2.63	0.45	1.17	0.44	2.62	0.30	2.57	0.47
Ga	14	17.33	3.53	2.61	0.31	2.02	0.35	2.68	0.48	2.43	0.66	2.64	0.31	2.73	0.54
Sr	112	115.46	3.78	123.49	7.98	88.39	7.85	164.01	14.89	137.12	18.58	161.79	10.57	140.96	13.74
Y	15.8	14.33	2.54	27.39	1.48	48.32	3.14	4.28	0.28	10.62	1.03	16.54	0.90	23.06	1.61
Zr	15.3	14.03	2.79	51.87	2.89	117.52	7.84	8.86	0.61	30.51	3.01	48.18	2.70	66.99	4.82
Nb	0.564	0.531	3.808	1.336	0.085	1.506	0.125	0.108	0.018	b.d.	-	1.598	0.100	0.837	0.078
Ba	6.6	6.91	2.90	39.30	3.13	20.70	2.20	12.53	1.37	9.35	1.47	34.56	2.78	40.19	4.70
La	0.623	0.600	3.868	3.044	0.183	1.901	0.145	0.694	0.056	0.616	0.071	3.015	0.180	1.706	0.145
Ce	1.93	2.029	3.271	8.411	0.540	6.525	0.550	1.815	0.160	2.035	0.247	8.246	0.530	4.656	0.435
Pr	0.381	0.377	2.994	1.132	0.065	1.082	0.080	0.301	0.024	0.393	0.044	1.210	0.069	0.797	0.064
Nd	2.49	2.335	3.553	5.213	0.307	6.457	0.480	1.359	0.110	2.255	0.253	5.694	0.330	4.177	0.340
Sm	1.14	1.073	3.852	1.785	0.109	2.986	0.215	0.477	0.046	1.028	0.117	1.866	0.110	1.791	0.145
Eu	0.537	0.515	3.155	0.631	0.041	0.473	0.040	0.795	0.066	0.654	0.081	0.861	0.054	0.813	0.071
Gd	1.91	1.721	3.825	2.577	0.160	5.279	0.390	0.566	0.051	1.410	0.167	2.309	0.140	2.584	0.205
Tb	0.369	0.334	3.621	0.545	0.032	1.066	0.077	0.108	0.010	0.276	0.031	0.416	0.025	0.508	0.041
Dy	2.73	2.428	2.885	4.464	0.253	8.060	0.555	0.703	0.060	2.073	0.223	3.018	0.170	3.946	0.300
Ho	0.599	0.541	3.826	1.029	0.056	1.722	0.110	0.160	0.013	0.401	0.041	0.623	0.034	0.880	0.063
Er	1.79	1.576	3.780	3.347	0.203	5.741	0.410	0.503	0.045	1.161	0.133	1.801	0.110	2.698	0.210
Tm	0.26	0.240	3.968	0.531	0.034	0.862	0.065	0.078	0.008	0.156	0.020	0.267	0.018	0.427	0.035
Yb	1.79	1.618	3.801	3.844	0.280	5.449	0.495	0.494	0.053	1.019	0.149	1.829	0.140	2.792	0.275
Lu	0.27	0.236	4.317	0.582	0.040	0.836	0.072	0.072	0.008	0.134	0.019	0.261	0.019	0.409	0.038
Hf	0.609	0.530	2.944	1.972	0.116	3.299	0.235	0.255	0.026	0.863	0.099	1.093	0.067	2.015	0.155
Ta	0.038	0.035	8.391	0.044	0.005	0.045	0.006	b.d.	-	b.d.	-	0.062	0.005	0.030	0.004
Th	0.03	0.029	11.968	0.163	0.012	0.738	0.063	0.076	0.009	0.084	0.012	0.547	0.035	0.101	0.011
U	0.016	0.016	12.640	0.016	0.002	0.149	0.025	0.019	0.004	0.028	0.007	0.127	0.014	0.094	0.018

Table C2, ctd: Bulk trace element abundance for each clast analyzed in QUE 93069,58

	5b	1σ	A	1σ	B	1σ	C	1σ	D	1σ	E	1σ	F	1σ	G	1σ
Spot (μm)	84		84		84		84		176		84		30		84	
Ablations	1		1		1		1		2		1		1		2	
Co (ppm)	50.17	8.48	7.95	1.09	19.81	2.76	7.79	1.34	34.93	3.51	4.00	0.43	14.84	3.44	28.53	5.57
Ni	1036.43	149.72	102.38	12.38	50.10	6.63	35.13	5.80	86.39	7.76	6.50	1.47	188.62	40.92	305.43	51.51
Cu	6.93	1.22	2.98	0.46	6.58	0.99	1.59	0.33	77.42	8.27	0.72	0.12	5.71	1.43	4.55	0.94
Ga	3.09	0.62	3.14	0.51	2.44	0.41	2.64	0.54	2.59	0.31	2.27	0.28	3.94	1.06	2.84	0.66
Sr	159.67	15.85	156.65	13.45	141.44	12.31	153.51	15.42	162.14	10.87	155.45	10.69	164.74	22.56	157.59	17.35
Y	7.04	0.50	14.55	0.92	6.68	0.43	8.18	0.59	13.42	0.75	3.31	0.19	23.69	2.32	16.03	1.25
Zr	24.14	1.77	35.99	2.34	10.53	0.70	18.54	1.38	18.82	1.08	8.54	0.50	46.62	4.69	46.06	3.68
Nb	0.612	0.059	0.896	0.075	0.046	0.015	0.172	0.023	0.852	0.057	0.558	0.039	0.434	0.064	1.167	0.123
Ba	43.94	5.22	37.09	3.78	8.22	0.86	18.95	2.28	34.24	2.82	11.27	0.95	48.52	7.69	34.10	4.50
La	1.877	0.160	2.737	0.200	0.439	0.035	1.327	0.120	2.720	0.170	0.566	0.037	3.371	0.390	2.964	0.280
Ce	4.257	0.410	6.501	0.530	1.184	0.099	3.475	0.340	7.395	0.485	1.451	0.099	8.422	1.040	7.929	0.850
Pr	0.626	0.052	0.965	0.069	0.205	0.016	0.568	0.048	1.126	0.066	0.229	0.015	1.202	0.130	1.213	0.110
Nd	2.722	0.230	4.952	0.360	1.122	0.091	2.780	0.240	5.302	0.320	1.015	0.067	5.829	0.650	5.914	0.540
Sm	0.779	0.067	1.407	0.110	0.420	0.041	1.039	0.091	1.621	0.097	0.326	0.026	2.044	0.220	1.854	0.160
Eu	0.855	0.076	0.856	0.067	0.643	0.052	0.816	0.074	0.933	0.060	0.674	0.045	0.874	0.110	0.843	0.084
Gd	1.032	0.088	2.051	0.160	0.597	0.052	1.304	0.110	2.155	0.140	0.419	0.032	2.866	0.340	2.409	0.220
Tb	0.178	0.015	0.336	0.025	0.135	0.011	0.208	0.018	0.361	0.023	0.073	0.006	0.557	0.062	0.454	0.039
Dy	1.198	0.097	2.473	0.170	0.992	0.078	1.460	0.120	2.450	0.145	0.536	0.038	3.829	0.410	2.865	0.240
Ho	0.266	0.020	0.533	0.036	0.240	0.018	0.314	0.024	0.507	0.029	0.122	0.008	0.880	0.088	0.599	0.047
Er	0.771	0.067	1.634	0.120	0.726	0.060	0.896	0.079	1.457	0.093	0.322	0.025	2.658	0.300	1.724	0.155
Tm	0.119	0.011	0.241	0.019	0.123	0.011	0.129	0.012	0.202	0.014	0.059	0.005	0.440	0.052	0.245	0.024
Yb	0.753	0.080	1.676	0.150	0.976	0.094	0.898	0.097	1.399	0.110	0.364	0.033	2.659	0.380	1.598	0.175
Lu	0.120	0.012	0.225	0.020	0.144	0.014	0.117	0.013	0.191	0.015	0.057	0.005	0.426	0.056	0.240	0.026
Hf	0.648	0.054	0.824	0.064	0.268	0.026	0.505	0.046	0.647	0.043	0.212	0.017	1.099	0.130	1.296	0.111
Ta	0.026	0.004	0.032	0.005	b.d.	-	0.014	0.003	0.039	0.004	0.026	0.003	0.017	0.005	0.045	0.006
Th	0.155	0.016	0.518	0.044	0.118	0.012	0.081	0.009	0.305	0.021	0.066	0.006	0.632	0.072	0.579	0.054
U	0.060	0.012	0.071	0.011	0.030	0.005	0.016	0.004	0.051	0.006	0.020	0.003	0.067	0.017	0.075	0.017

Table C2, ctd: Bulk trace element abundance for each clast analyzed in QUE 93069,58

	H	1σ	T1	1σ	T2	1σ	T3	1σ
Spot (μm)	84		176		30		176	
Ablations	2		1		1		2	
Co (ppm)	12.98	2.30	11.03	1.19	1.82	0.44	10.07	1.10
Ni	b.d.	-	38.33	3.78	13.93	5.66	15.07	1.98
Cu	2.11	0.40	2.30	0.28	2.39	0.66	2.70	0.33
Ga	2.19	0.46	2.97	0.37	3.69	1.00	2.89	0.37
Sr	62.06	6.35	144.82	10.05	174.81	24.12	175.99	12.37
Y	27.63	2.01	16.80	0.95	36.58	3.59	9.28	0.54
Zr	30.19	2.28	34.93	2.03	173.94	17.58	17.59	1.03
Nb	0.065	0.011	0.828	0.058	10.407	1.320	0.572	0.042
Ba	7.55	0.93	32.84	2.78	77.06	12.31	36.22	3.10
La	0.505	0.046	1.845	0.120	15.524	1.780	2.450	0.160
Ce	2.116	0.210	4.892	0.340	33.502	4.170	5.938	0.415
Pr	0.455	0.039	0.703	0.043	4.251	0.480	0.790	0.050
Nd	2.952	0.250	3.442	0.210	17.346	1.930	3.632	0.225
Sm	1.513	0.120	1.329	0.084	4.388	0.450	1.070	0.070
Eu	0.363	0.034	0.736	0.049	0.961	0.120	1.036	0.070
Gd	2.657	0.220	1.912	0.130	5.007	0.580	1.303	0.087
Tb	0.557	0.045	0.368	0.023	0.991	0.110	0.230	0.016
Dy	4.311	0.330	2.866	0.170	6.522	0.680	1.688	0.107
Ho	1.055	0.076	0.657	0.038	1.371	0.130	0.363	0.022
Er	3.340	0.275	2.000	0.130	4.183	0.470	1.051	0.071
Tm	0.523	0.044	0.292	0.020	0.629	0.073	0.162	0.012
Yb	3.747	0.385	2.066	0.160	4.048	0.570	1.116	0.094
Lu	0.559	0.054	0.309	0.023	0.584	0.076	0.158	0.013
Hf	0.990	0.081	0.935	0.060	3.640	0.390	0.481	0.034
Ta	b.d.	-	0.028	0.003	0.509	0.062	0.016	0.002
Th	0.028	0.004	0.275	0.019	1.689	0.190	0.074	0.006
U	0.027	0.005	0.072	0.008	0.742	0.180	0.045	0.005